DESIGN AND APPLICATION OF INNOVATIVE LOCAL TREATMENTS IN GLIOBLASTOMA AND OTHER CANCERS

EDITED BY: Emmanuel Garcion and Carmen Alvarez-Lorenzo
PUBLISHED IN: Frontiers in Pharmacology and Frontiers in Oncology

frontiers Research Topics

ISSN 1664-8714
ISBN 978-2-88966-658-4
DOI 10.3389/978-2-88966-658-4

About Frontiers

Frontiers is more than just an open-access publisher of scholarly articles: it is a pioneering approach to the world of academia, radically improving the way scholarly research is managed. The grand vision of Frontiers is a world where all people have an equal opportunity to seek, share and generate knowledge. Frontiers provides immediate and permanent online open access to all its publications, but this alone is not enough to realize our grand goals.

Frontiers Journal Series

The Frontiers Journal Series is a multi-tier and interdisciplinary set of open-access, online journals, promising a paradigm shift from the current review, selection and dissemination processes in academic publishing. All Frontiers journals are driven by researchers for researchers; therefore, they constitute a service to the scholarly community. At the same time, the Frontiers Journal Series operates on a revolutionary invention, the tiered publishing system, initially addressing specific communities of scholars, and gradually climbing up to broader public understanding, thus serving the interests of the lay society, too.

Dedication to Quality

Each Frontiers article is a landmark of the highest quality, thanks to genuinely collaborative interactions between authors and review editors, who include some of the world's best academicians. Research must be certified by peers before entering a stream of knowledge that may eventually reach the public - and shape society; therefore, Frontiers only applies the most rigorous and unbiased reviews.
Frontiers revolutionizes research publishing by freely delivering the most outstanding research, evaluated with no bias from both the academic and social point of view. By applying the most advanced information technologies, Frontiers is catapulting scholarly publishing into a new generation.

What are Frontiers Research Topics?

Frontiers Research Topics are very popular trademarks of the Frontiers Journals Series: they are collections of at least ten articles, all centered on a particular subject. With their unique mix of varied contributions from Original Research to Review Articles, Frontiers Research Topics unify the most influential researchers, the latest key findings and historical advances in a hot research area! Find out more on how to host your own Frontiers Research Topic or contribute to one as an author by contacting the Frontiers Editorial Office: frontiersin.org/about/contact

DESIGN AND APPLICATION OF INNOVATIVE LOCAL TREATMENTS IN GLIOBLASTOMA AND OTHER CANCERS

Topic Editors:
Emmanuel Garcion, Institut National de la Santé et de la Recherche Médicale (INSERM), France
Carmen Alvarez-Lorenzo, University of Santiago de Compostela, Spain

Citation: Garcion, E., Alvarez-Lorenzo, C., eds. (2021). Design and Application of Innovative Local Treatments in Glioblastoma and Other Cancers. Lausanne: Frontiers Media SA. doi: 10.3389/978-2-88966-658-4

Table of Contents

frontiers in Pharmacology

ORIGINAL RESEARCH
published: 29 November 2018
doi: 10.3389/fphar.2018.01372

Tolerance, Variability and Pharmacokinetics of Albumin-Bound Paclitaxel in Chinese Breast Cancer Patients

*Qingmei Li[1], Hong Zhang[2], Xiaoxue Zhu[2], Chengjiao Liu[2], Min Wu[2], Cuiyun Li[2], Xiaojiao Li[2], Lei Gao[2] and Yanhua Ding[2]**

[1] The First Hospital of Jilin University, Changchun, China, [2] Phase I Clinical Research Center, The First Hospital of Jilin University, Changchun, China

OPEN ACCESS

Edited by:
Carmen Alvarez-Lorenzo,
Universidade de Santiago de Compostela, Spain

Reviewed by:
Marcello Locatelli,
Università degli Studi G. d'Annunzio Chieti e Pescara, Italy
Ayesha N. Shajahan-Haq,
Georgetown University, United States

***Correspondence:**
Yanhua Ding
dingyanhua2003@126.com

Specialty section:
This article was submitted to Pharmacology of Anti-Cancer Drugs, a section of the journal Frontiers in Pharmacology

Received: 12 August 2018
Accepted: 08 November 2018
Published: 29 November 2018

Citation:
Li Q, Zhang H, Zhu X, Liu C, Wu M, Li C, Li X, Gao L and Ding Y (2018) Tolerance, Variability and Pharmacokinetics of Albumin-Bound Paclitaxel in Chinese Breast Cancer Patients. Front. Pharmacol. 9:1372. doi: 10.3389/fphar.2018.01372

Objective: The aim of this study was to explore the tolerance, variability, and pharmacokinetics (PK) of albumin-bound paclitaxel (QL, HR, ZDTQ) among Chinese breast cancer patients.

Methods: Three randomized, open-label, two-period crossover bioequivalence studies were conducted with albumin-bound paclitaxel. Each subject received a single dose of 260 mg/m^2 albumin-bound paclitaxel [sponsor 1 (QL, light food), sponsor 2 (HR, fasting), sponsor 3 (ZDTQ, light food); test] or Abraxane® (reference) and was monitored for 72 h. Serum concentrations of total paclitaxel and unbound paclitaxel were measured using liquid chromatography/mass spectrometry (LC/MS), and appropriate pharmacokinetic parameters were determined by non-compartmental methods. Safety assessments included adverse events, hematology and biochemistry tests.

Results: The bioequivalence analyses of the QL, HR, and ZDTQ products included 24, 23, and 24 patients, respectively. The mean $t_{1/2}$ was 20.61–27.31 h for total paclitaxel. Food intake did not affect the pharmacokinetics of paclitaxel. From the comparison of total paclitaxel and unbound paclitaxel, the 90% confidence intervals (CIs) for the ratios of C_{max}, AUC_{0-t}, and $AUC_{0-\infty}$ were within 80.00–125.00%. The intra-subject variability ranged from 6.4–11% to 9.85–15.87% for total paclitaxel and unbound paclitaxel, respectively. Almost all subjects in the test and Abraxane® (reference) groups experienced mild or moderate adverse events. No fatal AEs or study drug injection site reactions related to these drugs were observed.

Conclusion: Albumin-bound paclitaxel (QL, HR or ZDTQ; test products) showed bioequivalence to Abraxane® (reference) with lower intra-subject variability, which was less than 16% in all cases, and was well-tolerated in Chinese breast cancer patients. Twenty-two patients are enough for an albumin-bound paclitaxel bioequivalence study.

Keywords: cancer, albumin-bound, paclitaxel, bioequivalence, variability

INTRODUCTION

World over, breast cancer is the most common type of malignancy among women and the second most frequent cause of cancer-related death in women[1] (Dörfel et al., 2018; Locatelli et al., 2018). The standard therapy for patients with early breast cancer includes surgery, radiotherapy and adjuvant systemic therapy, such as anti-microtubule agents and aromatase inhibitors (Dörfel et al., 2018). However, as breast cancer is a highly heterogeneous condition, the selection of adjuvant systemic therapy depends on stage, histology and on molecular subtypes of the tumor (Dörfel et al., 2018; Locatelli et al., 2018). Current adjuvant systemic therapy options include chemotherapy, endocrine therapy for hormone receptor (HR)-positive tumors, and targeted biological agents such as trastuzumab for human epidermal growth factor receptor (HER2)-positive tumors (Dörfel et al., 2018).

Paclitaxel is an anti-microtubule agent that inhibits cell division by promoting the assembly and stabilization of microtubules (Slingerland et al., 2013). It is active against a broad spectrum of malignancies, such as non-small cell lung cancer and breast cancer (Slingerland et al., 2013; Blair and Deeks, 2015). As paclitaxel is extremely insoluble; it is solubilized in polyethoxylated castor oil for injectable preparation. However, serious and even fatal episodes of hypersensitivity with an incidence of approximately 20% have been reported with this oil (Donehower et al., 1987; Singla et al., 2002; Joerger, 2012). The introduction of premedication with corticosteroids, diphenhydramine, and H_2 antagonists, has fortunately reduced this incidence to 2–4% (Alves et al., 2018). Still, such infusion-related hypersensitivity reactions remain a serious matter. Moreover, solubilization in polyethoxylated castor oil enhances the nonlinear pharmacokinetic (PK) activity of increasing doses of paclitaxel (Sparreboom et al., 1999; Joerger, 2012; Slingerland et al., 2013). Along with, the unbound paclitaxel is also associated with clinical toxicities, such as myelosuppression and peripheral neuropathy (Blair and Deeks, 2015).

Different modifications of drug formulations, e.g., liposomal and albumin-bound, have been studied for their ability to improve delivery of therapeutic doses, drug stability, and drug safety (Du et al., 2018). Albumin-bound paclitaxel contains protein-bound particles of paclitaxel for injectable suspension, which, by avoiding the use of polyethoxylated castor oil also eliminates the need for corticosteroid pretreatment[2]. Additionally, an improved safety profile with albumin-bound paclitaxel may facilitate the administration of higher doses[2] (Du et al., 2018).

With the end of the patent protection period for an innovator's product, generic preparations are introduced into the market repeatedly. Thus, it has become necessary to establish the bioequivalence (BE) between two drug products with the same active moiety. Usually, determination of BE relies on comparisons of the rate and extent of absorption of a product under study (test, T) with those of an innovator's product (reference, R) (Karalis et al., 2012).

The study drugs are paclitaxel albumin protein-bound particles available as an injectable suspension (FDA, 2015). However, the production process is different, such as albumin packaging of paclitaxel process by different sponsors. The US FDA Draft Guidance on paclitaxel recommends estimation of serum unbound and total paclitaxel for BE evaluation (FDA, 2015).

As the intra-subject variability for paclitaxel among the Chinese population is unknown, we first analyzed the PK characteristics of unbound paclitaxel and total paclitaxel in Chinese breast cancer patients. Second, the present study compared the BE (rate and extent of absorption and elimination) of two 260 mg/m^2 albumin-bound paclitaxel (test and reference) formulations as provided by the two study sponsors. Third, we analyzed the effects of sample size and intra-subject variability on the BE of unbound and total paclitaxel. Lastly, the tolerability profiles of different formulations of albumin-bound paclitaxel were assessed.

MATERIALS AND METHODS

Patients and Study Design

Three prospective BE studies with albumin-bound paclitaxel (injectable suspension) were conducted, with drugs provided by three different sponsors, i.e., QL ($n = 25$), HR ($n = 25$), or ZDTQ ($n = 24$), and the reference product, Abraxane®. These single-center, randomized two-period crossover, BE studies, were performed between March 2016 and March 2018, according to the US FDA guidance draft on Paclitaxel. The tolerability and PK of the test products (albumin-bound Paclitaxel, QL, HR, and ZDTQ) and Abraxane® (reference) were compared in patients with breast cancer in these three studies respectively. The inclusion criteria were: (1) age $>$ 18 years; (2) histologic diagnosis of advanced breast cancer for which there is no curative therapy and treatment with single-agent paclitaxel has been considered appropriate by the treating physician; (3) Eastern Cooperative Oncology Group (ECOG) performance status of 0/1; (4) life expectancy of $>$12 weeks; and (5) complete recovery from acute toxicities of prior treatment. Subjects were excluded if they did not have adequate hematologic, kidney, and liver function (hemoglobin $\geq$ 90g/L [not having blood transfusion within 14 days], absolute neutrophil count $\geq 1.5 \times 10^9$/L, blood platelet count $\geq 100 \times 10^9$/L, total bilirubin $<$1 upper limit normal [ULN], alanine aminotransferase [ALT], and aspartate aminotransferase [AST] $<2.5\times$ULN [if liver metastasis, then ALT and AST $\leq 5 \times$ ULN], creatinine $\leq 1.5\times$ULN), or had received radiotherapy, chemotherapy, immunotherapy, or endocrine therapy within 4 weeks prior to the use of the study drug and residual effects were still present.

This study was carried out in accordance with the recommendations of the Good Clinical Practice and the Declaration of Helsinki. The protocol was approved by the Ethics Committee of the First Hospital of Jilin University, Changchun, Jilin, China. All subjects gave written informed consent in accordance with the Declaration of Helsinki.

[1] Available online at: www.rebeccafarm.org

[2] TAXOL® (paclitaxel) INJECTION. https://www.accessdata.fda.gov/drugsatfda_docs/label/2011/020262s049lbl.pdf

A screening visit was scheduled within 14 days prior to administration of the study drug. Then the eligible subjects were admitted to the clinical research unit 1 day before dosing. Following an overnight fast of at least 8-h, subjects were randomized to receive a single intravenous dose of 260 mg/m^2 (infusion 30 ± 3 min) of albumin-bound paclitaxel (test product; QL, HR, or ZDTQ) or Abraxane® (reference product, from the US market) in a 1:1 ratio according to a computer-generated randomization schedule for each study in the first period (**Figures 1**, **2**). Then the same dosing method for the reference or test formulation was followed in second period, or vice versa. Each drug had a unique batch number. The washout period was of 3 weeks. Subjects were administered the drug at the same time on first day of first period and day 22 of second period (**Figure 1**). Albumin-bound paclitaxel by sponsor 1 (QL) and sponsor 3 (ZDTQ) was administered after breakfast (light food), whereas the HR product (sponsor 2) was administered after 8 h of fasting. Patients were carefully monitored, particularly during the infusion. Subjects were discharged after 72 h of drug administration. Blood samples for the primary PK analysis were collected prior to treatment and at specified time points during the 72-h follow-up. Subjects were followed up for safety assessment at 7 ± 1 and 21 ± 1 days.

Estimation of Sample Size

According to the current US FDA guidelines, to achieve an 80–90% power (1-β) in BE studies at the 5% nominal level (α = 5%), the geometric mean ratio (GMR) is usually set to be 95–105% (Karalis et al., 2012). The coefficient of variation (CV) is evaluated as the intra-subject variability (intra-cv). The intra-cv for paclitaxel is assumed to be 20–21.3%[2]. According to the initial estimation by R software, sample size should be of 21 patients. Based on the above sample size estimation result and considering a loss to follow-up of 10% and the opinion of sponsor and investigator, the final needed sample size was considered to be 24 (**Table 1**) (Zhang et al., 2018a,b).

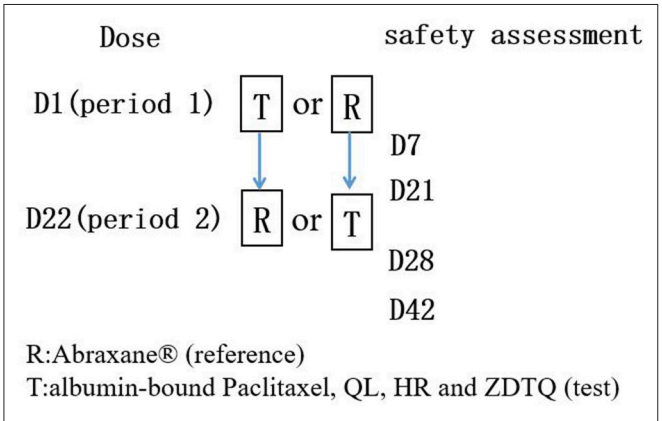

FIGURE 1 | Flow chart of the BE studies. Each subject will had test product (QL, HR, or ZDTQ) and reference product (Abraxane®) at each study.

Pharmacokinetic Analysis

Blood samples (5 ml each time) for PK evaluation were collected into heparin anticoagulant-containing tubes within 0.2 h of initiation of albumin-bound paclitaxel infusion (pre-dose), 0.25 h after the start of infusion, immediately after stopping the infusion, and 0.75, 1, 1.5, 2, 4, 6, 8, 12, 24, 48, and 72 h after the start of infusion. Blood samples were centrifuged at 3,000 rpm for approximately 10 min at 2–8°C in a refrigerated centrifuge. The serum was stored at −70°C until analysis. The serum concentrations of total paclitaxel and unbound paclitaxel were analyzed using a validated, sensitive and specific liquid chromatography tandem mass spectrometry (LC-MS/MS) method at the Shanghai Drug Metabolism Research Center for QL and HR, and Covance for ZDTQ.

The lower limits of quantification (LLOQ) for un-bound paclitaxel and total paclitaxel were 0.2 ng/mL and 5.0 ng/mL, respectively, and the upper limits of quantification (ULOQ) for unbound paclitaxel and total paclitaxel were 2,000 ng/mL and 15,000 ng/mL, respectively for QL and HR.

The LLOQ for un-bound paclitaxel and total paclitaxel were 2 ng/mL and 10.0 ng/mL, respectively, and the ULOQ for unbound paclitaxel and total paclitaxel were 2,000 ng/mL and 10,000 ng/mL, respectively for ZDTQ. The validated concentration ranges were between the LLOQ and ULOQ.

The LC-MS/MS method and rapid equilibrium method have been validated for the determination of paclitaxel concentration in human raw serum and equilibrium serum samples (Ronghao and Jun, 2015). In each analysis batch, the quantity of quality control samples accounted for more than 5% of the unknown samples in the analysis batch. In all quality control samples, the ratio of relative deviation within 15% is more than at least 67% of all quality control samples, and the ratio of relative deviation within 15% is more than at least 50% of each concentration of quality control samples. All analysis batch quality control met the above criteria (**Supplement Table 1**).

Total levels of free and protein-bound paclitaxel were later quantified. Paclitaxel-D5 served as the internal standard. The analytical column was a Eclipse Plus C18 column (100 × 4.6 mm, 3.5 μm, Agilent), and the formula used for calculation of unbound paclitaxel was as follows:

$$\mathbf{C}_{\text{unbound Paclitaxel}} = (\mathbf{C}_{\text{receiver unbound Paclitaxel}}/\mathbf{C}_{\text{donor Paclitaxel}}) \times \mathbf{C}_{\text{total Paclitaxel}}$$

The inter-run assay accuracy, expressed as percent relative error for quality control samples [BIAS(%)]. The assay precision, expressed as the inter-run CV of the measured concentrations of quality control samples [relative standard deviation, RSD(%)].

All analysis batch quality control met the above criteria (**Supplement table 1**).

Tolerability and Safety Assessments

Medical history, physical examination, electrocardiography (ECG), and laboratory test (hematology, biochemistry, and urinalysis, etc.) results were obtained at the time of screening (2–14 days before the first dose of study drug) and at 7 ± 1 and 21 ± 1 days for all subjects in each test period. Vital signs were recorded

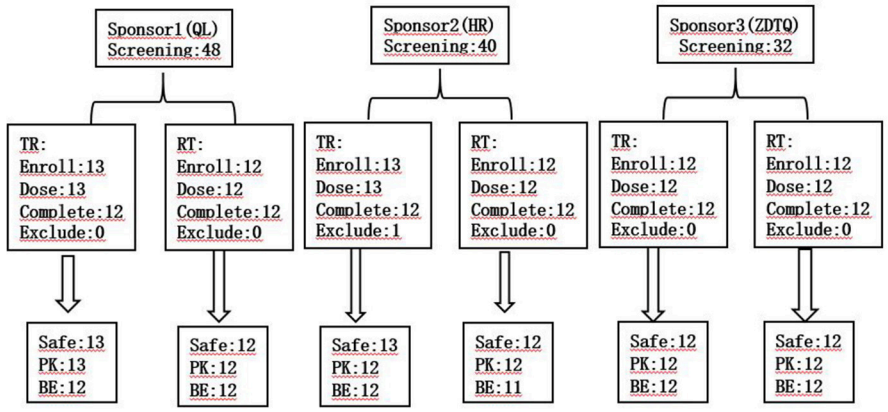

FIGURE 2 | The subject number of the each analysis set. TR, D1 dosing T formulation and D22 dosing R formulation; RT, D1 dosing R formulation and D22 dosing T formulation.

TABLE 1 | Sample size estimation of these studies.

Sponsor	Predicted value of bioavailability	α	1-β	Intra-subject variability	Sample size of estimation	Sample size in the study
Sponsor 1 (QL)	0.95–1.05	0.05	0.8	20.00%	21	24
Sponsor 2 (HR)	0.95–1.05	0.05	0.8	21.30%	21	24
Sponsor 3 (ZDTQ)	0.95–1.05	0.05	0.8	20.00%	21	24

immediately before the first dose and after administration of the drug. Adverse events were recorded daily from the day of administration of the first dose through the end of the study. The National Cancer Institute Common Toxicity Criteria for Adverse Events version 4.03 was used to describe and grade all toxicities and adverse events (AEs).

Statistical Analysis

The serum concentrations vs. time data were analyzed with non-compartmental methods using WinNonlin Professional, Version 6.4 (Pharsight Corporation, NC, USA). The PK analysis used actual sample collection times. Samples below the LLOQ were set to zero before T_{max} and not detectable after T_{max} for the PK analysis. The PK parameters for paclitaxel included C_{max}, area under the curve $(AUC)_{0-t}$, $AUC_{0-\infty}$, T_{max}, and $T_{1/2}$. Descriptive statistics were calculated for PK parameters, demographics, and safety variables and these were analyzed by *t*-test or analysis of variance (ANOVA). ANOVA also was used to compare the AUC and C_{max}, with factors fitted for the effect of sequence, subject within sequence, period, and treatment. The comparisons are presented in terms of the geometric least square means and the 90% confidence interval (CI). BE was established if the 90% CI of the treatment ratio was within the equivalence range of 0.8–1.25. T_{max} and $T_{1/2}$ were analyzed with a Wilcoxon rank test. All statistical tests were performed using SAS 9.1 Statistical Package, and $P < 0.05$ was considered statistically significant.

RESULTS

Subject Screening, Recruitment, and Compliance

A total of 120 Patients with breast cancer were initially screened for these studies. Of these, 74 patients with breast cancer ($n = 25$, 25, 24) were enrolled and received the assigned study drug from sponsor 1-3 (HR, QL, ZDTQ) respectively; these patients also constituted the safety analysis set for each sponsor and 71 patients constituted the BE analysis set (**Figure 2**). The demographics and baseline characteristics of patients treated by the three sponsors were comparable (**Table 2**). Most of the study subjects were Han Chinese. The mean age of the study subjects was 48.8–52 years old.

Albumin-Bound Paclitaxel Serum Concentration–Time Profiles

The total paclitaxel and unbound paclitaxel serum concentrations increased rapidly in all study subjects and reached C_{max} at 0.5 h after the start of infusion. The serum concentrations showed a decline in a biphasic manner, which initially decreased rapidly after the end of infusion and then demonstrated a slight decrease until the lower limit of quantification. The study drugs

TABLE 2 | Demographic characteristics of the subjects.

Sponsor	N	Gender (male/female)	Age [years, mean (SD)]	Ethnicity (han/other)	Body surface area [m^2, mean (SD)]	Body weight [kg, mean (SD)]	ECOG score 0/1
Sponsor 1(QL)	25	1/24	51.4 (8.16)	23/2	1.63 (0.15)	63.52 (9.504)	3/22
Sponsor 2 (HR)	25	2/23	48.8 (9.17)	24/1	1.58 (0.16)	60.0 (10.1)	3/22
Sponsor 3 (ZDTQ)	24	1/23	52 (7.47)	23/1	1.68 (0.16)	60.28 (10.58)	2/22
P		>0.05	>0.05	>0.05	>0.05	>0.05	>0.05

ECOG, Eastern Cooperative Oncology Group.

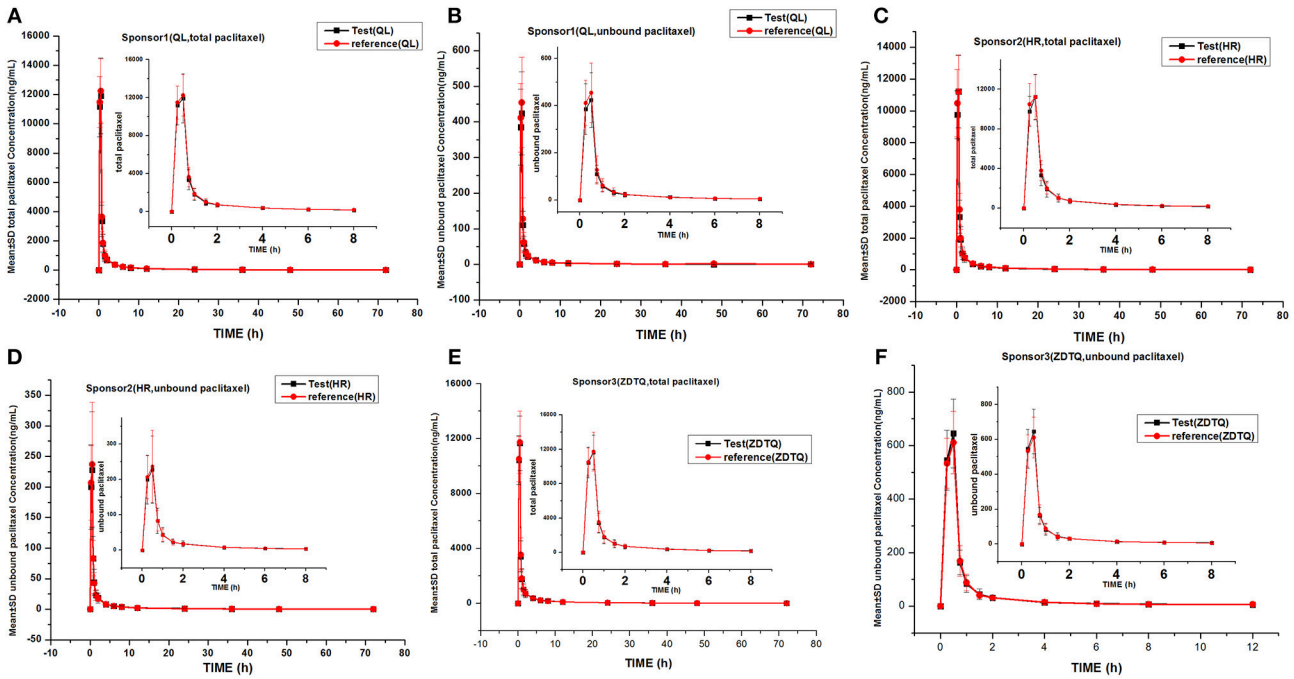

FIGURE 3 | Mean serum concentration–time profiles in the study. **(A)** Sponsor 1 (QL) total paclitaxel; **(B)** Sponsor 1 (QL) unbound paclitaxel; **(C)** Sponsor 1 (HR) total paclitaxel; **(D)** Sponsor 1 (HR) unbound paclitaxel; **(E)** Sponsor 3 (ZDTQ) total paclitaxel; **(F)** Sponsor 3 (ZDTQ) unbound paclitaxel.

exhibited a similar mean serum concentration–time profile in the R and T formulations in studies 1, 2, and 3 (**Figures 3**, **4**).

Pharmacokinetic Parameters of Albumin-Bound Paclitaxel in Studies 1–3

AUC_{0-t} accounted for >90% of the $AUC_{0-\infty}$ in all subjects, which indicated that the plasma concentration vs. time profiles were well characterized. The mean $t_{1/2}$ were 20.61–27.31 and 20.3–26.74 h, and the intra-cv values ranged from 6.4 to 11% and 9.85 to 15.87% for total paclitaxel and unbound paclitaxel, respectively (except the $t_{1/2}$ of 2.53–3 h of unbound paclitaxel of ZDTQ). The Inter-cv values were small, and almost all of these were less than 30%. There were no differences in PK parameters of total paclitaxel among the Sponsor 1 (QL), Sponsor 2 (HR), and Sponsor 3 (ZDTQ) products, which indicate that food did not affect the PK of paclitaxel. However, the unbound paclitaxel exposure was higher and the elimination rate lower with the Sponsor 1 (QL) and Sponsor 3 (ZDTQ) product than with the Sponsor 2 (HR) product (**Table 3**, **Figure 5**). The $t_{1/2}$ of ZDTQ is obviously shorter than those of QL and HR (**Table 3**, **Figure 5**).

Bioavailability and Bioequivalence Analysis

The relative bioavailability of the test products as compared with the reference formulation was 92.16–106.44% for unbound paclitaxel and 93.21–100.8% for total paclitaxel. Both the assessments met the 80–125% BE range recommended by the US FDA (**Table 4**).

Re-Estimation of Sample Size

We re-estimated the sample size for the three studies based on their BE analysis results ($\alpha = 0.05$, power = 0.8, GMR, and intra-cv) and the original hypothesis. The re-estimated sample size was 6–20, which is less than our enrollment size (**Table 4**) (Zhang et al., 2018a,b).

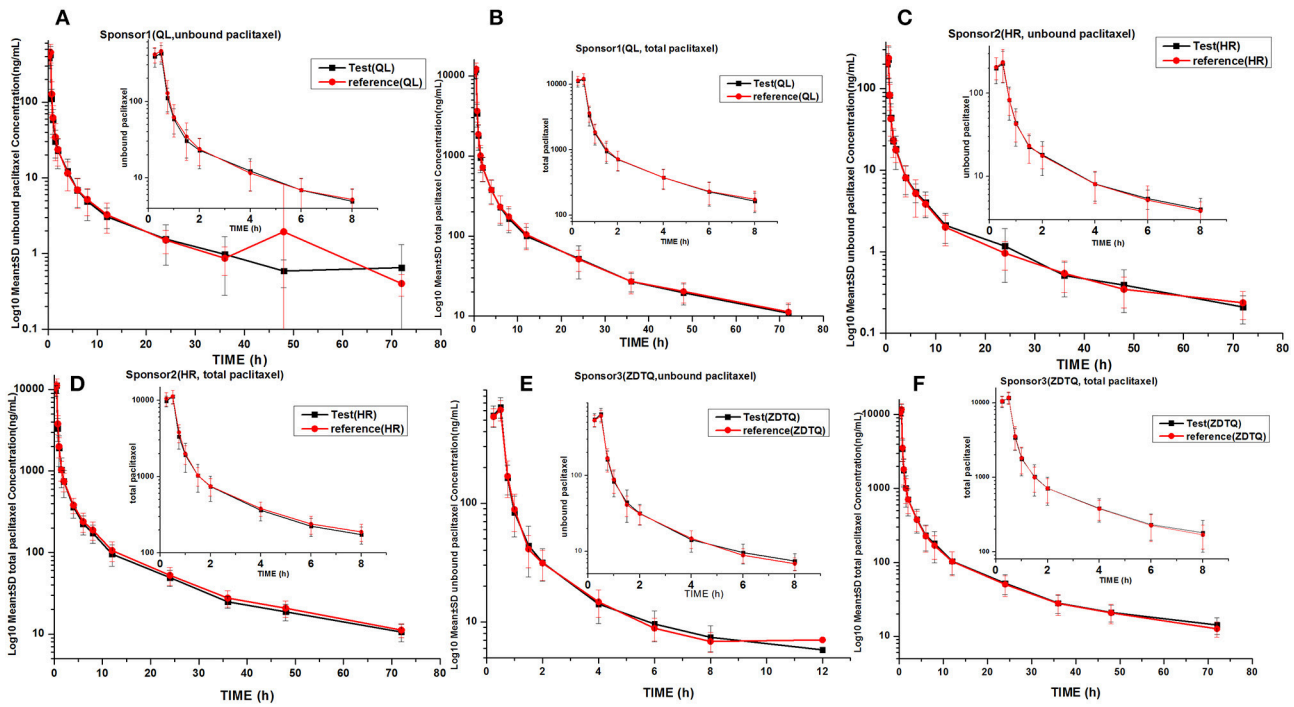

FIGURE 4 | LOG10 Mean serum concentration–time profiles in the study. **(A)** Sponsor 1 (QL) total paclitaxel; **(B)** Sponsor 1 (QL) unbound paclitaxel; **(C)** Sponsor 1 (HR) total paclitaxel; **(D)** Sponsor 1 (HR) unbound paclitaxel; **(E)** Sponsor 3 (ZDTQ) total paclitaxel; **(F)** Sponsor 3 (ZDTQ) unbound paclitaxel.

Safety Evaluations

For QL product, 25 subjects were included in the safety evaluation. The incidence of AEs was 100% with the QL product and reference product. The incidence of AEs of grade II or higher severity was 32.0% (5/25) vs. 41.6% (10/24) in the QL and reference groups, respectively.

For HR product, 25 subjects were included in the safety evaluation. The incidence of AEs was 100% with the HR product and 91.7% with the reference product. The incidence of AEs of grade II or higher severity was 32.0% (8/25) vs. 37.5% (9/24) in the HR and reference groups, respectively.

For ZDTQ product, 24 subjects were included in the safety evaluation. The incidence of AEs was 100% with the ZDTQ product and the reference product. The incidence of AEs of grade II or higher severity was 83.0% (20/24) vs. 87.5% (21/24) in the HR and reference groups, respectively.

There was one SAE (cataract) with ZDTQ; which was found to be unrelated to the drug. No fatal AEs or study drug injection site reactions of the drugs were observed. The test and reference groups had a similar incidence and pattern of AEs. There were no reports of unexpected AEs. The common hematologic adverse reactions included: neutropenia, leucopenia, thrombocytopenia, and anemia. The common non-hematologic adverse reactions included: increased ALT, AST, and fasting serum glucose levels; hyperesthesia; skin rashes; itching; fever; fatigue; nausea; diarrhea; and vomiting. In these studies, 24 (32.4%) and 23 (31%) subjects had concomitant medication use for co-existing diseases and administration of colony-stimulating factors was the most common group. There was no use of metabolic inducers or inhibitors, such as cyclosporine, phenobarbital, and ketoconazole, among the patients.

DISCUSSION

In these BE studies, all formulations of albumin-bound paclitaxel (QL, HR, and ZDTQ) were found to be bioequivalent to the reference formulation (Abraxane®) (Slingerland et al., 2013). The most frequently reported AEs were neutropenia, leucopenia, and thrombocytopenia (Slingerland et al., 2013). Following intravenous administration of the study drug (test or reference), paclitaxel serum concentrations declined in a biphasic manner, with the initial rapid decline representing distribution to the peripheral compartment and the slower second phase representing drug elimination[3] (Slingerland et al., 2013). The terminal half-life of total paclitaxel was about 20.61–27.31 h, which is consistent with the reference product (Abraxane®) label[2]. The large volume of distribution (>1,000 L) of paclitaxel indicates extensive extravascular distribution and/or tissue binding of paclitaxel (Petrelli et al., 2010; Ronghao and Jun, 2015; Hyman et al., 2018; Xiang et al., 2018)[3]. There was higher exposure and lower elimination rate of unbound paclitaxel QL and ZDTQ as compared to HR product.

There are three plausible explanations. First, systematic errors and large standard deviations might have led to this difference.

[3] Available online at www.accessdata.fda.gov

TABLE 3 | Pharmacokinetic parameters of paclitaxel in each study [Geometric Mean (CV%)].

PK parameter	Sponsor 1 (QL, light food condition)		*p**	Sponsor2(HR, fasting condition)		*p**	Sponsor3(ZDTQ, light food condition)		*p**	Literature[label]	*p#*
	T (*N* = 25)	R (Abraxane®, *N* = 24)		T (*N* = 24)	R (Abraxane®, *N* = 24)		T (*N* = 24)	R (Abraxane®, *N* = 24)			
UNBOUND PACLITAXEL											
T_{max} (h)	0.50 (0.25, 0.51)	0.50 (0.25, 0.52)	>0.05	0.5 (0.25, 0.5)	0.5 (0.25, 0.5)	>0.05	0.500 (0.25, 0.50)	0.500 (0.25, 0.50)	>0.05		>0.05
C_{max} (ng/mL)	444.47 (26.37)	476.68 (26.26)	>0.05	234.5 (35.69)	254.5 (36.8)	>0.05	659.95 (17.64)	621.95 (18.30)	>0.05	1284 (41.5)	<0.05
AUC_{0-t} (h*ng/mL)	402.38 (29.11)	440.09 (32.51)	>0.05	252.9 (25.66)	261.8 (25.79)	>0.05	456.54 (21.09)	451.48 (19.54)	>0.05	1159 (29.1)	<0.05
$AUC_{0-\infty}$(h*ng/mL)	418.35 (29.62)	456.42 (31.84)	>0.05	259.1 (24.92)	269.2 (25.57)	>0.05	486.66 (20.88)	482.00 (20.47)	>0.05		<0.05
$t_{1/2}$ (h)	21.60 (43.63)	26.74 (47.09)	>0.05	20.8 (54.27)	20.3 (38.88)	>0.05	2.53 (23.99)	3.00 (69.21)	>0.05		<0.05
CL/F (L/h)	1105.90 (33.37)	1020.30 (33.82)	>0.05	1670.63 (32.17)	1637.55 (28.14)	>0.05	939.25 (26.13)	953.03 (29.43)	>0.05		<0.05
Vd/F (L)	34241.78 (50.70)	38522.03 (51.48)	>0.05	50106.05 (66.99)	48635.48 (55.23)	>0.05	3303.71 (19.74)	3791.99 (51.62)	>0.05		<0.05
TOTAL PACLITAXEL											
T_{max} (h)	0.500 (0.25, 0.52)	0.50 (0.25, 0.52)	>0.05	0.5 (0.25, 0.5)	0.5 (0.25, 0.5)	>0.05	0.500 (0.25, 0.50)	0.500 (0.25, 0.50)	>0.05		
C_{max} (ng/mL)	12294.80 (19.28)	12771.25 (16.17)	>0.05	11301 (19.05)	12030 (17.50)	>0.05	11827.50 (15.60)	11905.41 (18.31)	>0.05	19556 (36.2)	>0.05
AUC_{0-t} (h*ng/mL)	12196.61 (23.30)	12619.40 (21.83)	>0.05	12025 (19.55)	12730 (16.04)	>0.05	11989.89 (25.41)	11978.56 (25.05)	>0.05	20324 (19.5)	>0.05
$AUC_{0-\infty}$ (h*ng/mL)	12587.13 (23.29)	13077.56 (22.02)	>0.05	12451 (19.59)	13132 (16.03)	>0.05	12476.88 (24.90)	12405.71 (24.66)	>0.05		>0.05
$t_{1/2}$ (h)	24.48 (18.27)	27.31 (36.96)	>0.05	26.9 (25.20)	24.7 (24.22)	>0.05	21.87 (48.22)	20.61 (34.10)	>0.05	20 (21.3)	>0.05
CL/F (L/h)	35.53 (26.50)	34.09 (24.82)	>0.05	34.39 (25.92)	32.62 (25.17)	>0.05	37.12 (28.28)	37.39 (28.25)	>0.05		>0.05
Vd/F (L)	1253.78 (32.84)	1314.46 (37.19)	>0.05	1304.86 (33.25)	1145.11 (28.43)	>0.05	1131.92 (52.09)	1065.89 (31.90)	>0.05		>0.05

**paired t test between test (QL and HR) and reference (Abraxane) formation at each sponsor; #, ANOVA test between QL and HR. label: TAXOL® (paclitaxel) Injection.*

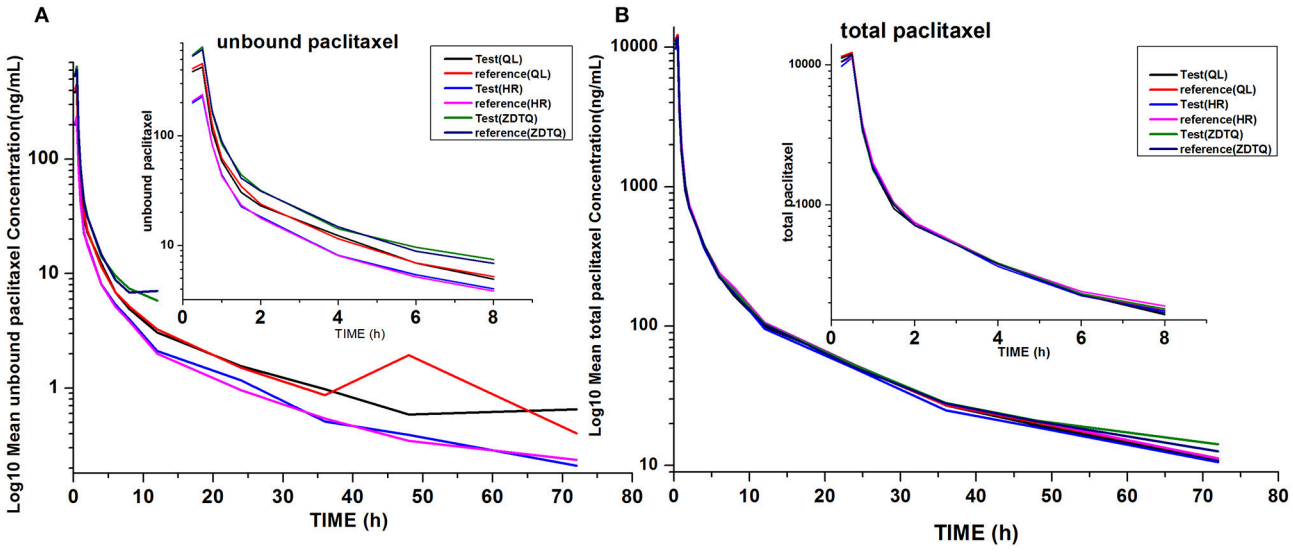

FIGURE 5 | Total LOG10 Mean serum concentration–time profiles in the study. **(A)** total paclitaxel; **(B)** unbound paclitaxel.

The exposure reported by Sponsor 2 (HR) was lower, regardless of the test and reference formulation. The unbound paclitaxel concentration was obtained with the following formula:

$$\mathbf{C}_{\text{unbound paclitaxel}} = (\mathbf{C}_{\text{receiver unbound paclitaxel}}/\mathbf{C}_{\text{donor paclitaxel}}) \times \mathbf{C}_{\text{total paclitaxel}}$$

The rapid equilibrium method may have deviation, which might have contributed to the higher unbound paclitaxel concentration when the total paclitaxel concentration was similar. The second reason could be the small difference in binding or wrapping rates. For example, when the binding or wrapping rates of paclitaxel with albumin are 98.0 and 96.5%, which are within the acceptable range, and the total paclitaxel concentration is 12,000 ng/mL; the unbound paclitaxel concentrations will be 240 ng/mL (12,000 × 98.0%) and 420 ng/mL (12,000 × 96.5%), respectively. The third reason could be differences in the metabolism of paclitaxel. Paclitaxel is metabolized into 6α-hydroxypaclitaxel by cytochrome2C8, and to two minor metabolites, 3-*p*-hydroxypaclitaxel, and 6α, 3′-*p*-dihydroxypaclitaxel, by cytochrome 3A4. *In vitro*, the metabolism of paclitaxel to 6α-hydroxypaclitaxel is inhibited by various agents (e.g., verapamil, ketoconazole, vincristine, etc.)[2]; however, none of the patients was taking any such concomitant drug in these studies. Thus, we speculate that a gene polymorphism of CYP could have affected the metabolic capability, which leads to higher clearance and ultimately lower exposure of unbound paclitaxel (Hendrikx et al., 2013; Frederiks et al., 2015; Xie et al., 2015).

As ZDTQ had higher LLOQ, the lower concentration of unbound paclitaxel was not checked 12 h after dosing. The terminal elimination half-life is the time taken by the drug to decrease its plasma concentration to half. The length can reflect the drug elimination rate *in vivo*. If the terminal concentration is very low (the LLOQ is low), the drug elimination terminal slope is small and the half-life is long; if the terminal concentration is high (the LLOQ is high), the drug elimination terminal slope is large and the half-life is short[4]. Then the $t_{1/2}$ of ZDTQ is obviously shorter than those of QL and HR. It can be found at **Supplement Figure 1**. The two figures of time-concentration PK curve have been drawn from the same subject. We used 0–12 h time-concentration (**Supplement Figure 1A**) and 0–72 h time-concentration (**Supplement Figure 1B**) to calculate the $t_{1/2}$. Then we can see the different $t_{1/2}$ (4.7 vs. 21 h).

Food intake did not affect the PK of paclitaxel, which is supported by the similar exposures of total paclitaxel. The US FDA guidance document suggests that if a patient's health status prevents fasting, the clinic trial site may provide a light diet during the study, when all procedures are need to completed under same condition in the bioequivalence study (Davit et al., 2008; Srinivas, 2009).

The intra-subject variability was small as compared with earlier observations among breast cancer patients, i.e., 6.4–15.9 vs. 21.3% for total paclitaxel and unbound paclitaxel, respectively, which further suggests that paclitaxel is a low variable drug (Karalis et al., 2008). Due to the intravenous administration, paclitaxel entered into blood circulation and gastrointestinal absorption was bypassed. The physiological factors can significantly vary not only between subjects but also within the same subject, e.g., luminal/mucosal enzymes, regional pH, biliary or pancreatic secretions, gastric emptying, intestinal motility, and circadian rhythm etc, (Karalis et al., 2008). These factors can contribute to high intra-subject variability

[4]Pharmacokinetics and Pharmacodynamics Concepts and Applications, Fourth Edition.

TABLE 4 | Bioequivalence assessment summary and re-estimation of sample size.

	Sponsor1 (QL, $N = 24$)			Sponsor 2 (HR, $N = 23$)			Sponsor 3(ZDTQ, $N = 24$)		
PK parameter	**Intra-CV(%)**	**GMR (90%CI) (%)**	**Re-estimated the sample size**	**Intra-CV(%)**	**GMR (90%CI) (%)**	**Re-estimated the sample size**	**Intra-CV(%)**	**GMR (90%CI)(%)**	**Re-estimated the sample size**
UNBOUND PACLITAXEL									
C_{max} (ng/mL)	12.13	93.12 (87.70–98.86)	12	15.87	92.18 (85.04–99.91)	20	9.85	106.44 (101.38–111.75)	9
AUC_{0-t}(h*ng/mL)	12.2	92.16 (86.77–97.88)	14	12.34	97.05 (91.15–103.32)	10	12.56	101.35 (95.26–107.84)	10
$AUC_{0-\infty}$ (h*ng/mL)	12.14	92.18 (86.81–97.88)	14	12.38	96.64 (90.75–102.91)	10	12.83	101.41 (95.18–108.04)	10
TOTAL PACLITAXEL									
C_{max} (ng/mL)	6.4	94.99 (92.03–98.05)	8	9.76	93.21 (88.70–97.95)	10	6.86	100.02 (96.68–103.48)	6
AUC_{0-t}(h*ng/mL)	7.81	95.6 (91.98–99.37)	8	10.1	93.26 (88.59–98.17)	10	11	100.29 (94.99–105.90)	9
$AUC_{0-\infty}$ (h*ng/mL)	8.47	95.28 (91.37–99.36)	8	9.83	93.53 (88.97–98.32)	10	10.96	100.8 (95.49–106.42)	9

*20% lost to follow-up.

of the drug (Shah et al., 1991; Karalis et al., 2008). Then, we re-estimated the sample size of both the studies. We found that these studies did not need a large sample size. In future, we recommend that 22 subjects may be enough, considering the intra-cv measurement (6.4–15.87%) (Shah et al., 1991).

Paclitaxel is known to cause myelosuppression, peripheral neuropathy, myalgia/arthralgia, cardiovascular events, alopecia, and gastrointestinal toxicity (Henderson and Bhatia, 2007; Conlin et al., 2010; Slingerland et al., 2013; Lluch et al., 2014; Li et al., 2015). The severity of neutropenia correlates with the dose of paclitaxel and can be dose-limiting[2]. Dose intensification is not possible in cases of such acute toxicities, and dose reduction may have be necessary to improve a patient's condition, with the possibility of reducing treatment effectiveness. Therefore, albumin-bound paclitaxel was developed with a goal of improving the safety profile of paclitaxel treatment by eliminating the potentially toxic component polyethoxylated castor oil while maintaining or enhancing treatment efficacy (Slingerland et al., 2013). However, if the unbound paclitaxel concentration is associated with these toxicities, it is considered as an indicator to evaluate the technology of the production process (Vishnu and Roy, 2010; Guarneri et al., 2012; Palumbo et al., 2015). When the concentration of unbound paclitaxel is low, it indicates that the paclitaxel is covered by albumin successfully. The incidences of AEs and those of grade II or higher severity were comparable between the test formulation and reference formulation, and both the products were well tolerated by the patients. This shows that the imitation formulation is successful.

CONCLUSIONS

These randomized, two-period, crossover, clinical BE studies show that albumin-bound paclitaxel products (QL, HR, and ZDTQ) are bioequivalent to Abraxane® (reference) with a lower intra-cv and similar safety profiles of among Chinese breast cancer patients.

ETHICS STATEMENT

These studies were conducted in accordance with Good Clinical Practice and the Declaration of Helsinki. An independent Ethics Committee (of The First Hospital of Jilin University, Changchun, Jilin, China) approved the protocol before the start of the study. All patients provided informed consent before the start of any study-related procedure.

AUTHOR CONTRIBUTIONS

XL, QL, HZ, and YD designed the experiment. LG, XL, QL, HZ, MW, XZ and ChL performed the clinic trials. HZ and CuL analyzed the data. QL, HZ and YD wrote and edited the paper, and drew the figures.

ACKNOWLEDGMENTS

This work was supported by the National Science Foundation of China (grant numbers: 81602897, 81300313, 30872174, 2017ZX09304004, and 2017ZX09101001-002-041).

SUPPLEMENTARY MATERIAL

The Supplementary Material for this article can be found online at: https://www.frontiersin.org/articles/10.3389/fphar.2018.01372/full#supplementary-material

REFERENCES

Alves, R. C., Fernandes, R. P., Eloy, J. O., Salgado, H. R. N., and Chorilli, M. (2018). Characteristics, properties and analytical methods of paclitaxel: a review. *Crit. Rev. Anal. Chem*. 8, 110–118. doi: 10.1080/10408347.2017.1416283

Blair, H. A., and Deeks, E. D. (2015). Albumin-bound paclitaxel: a review in non-small cell lung cancer. *Drugs* 75, 2017–2024. doi: 10.1007/s40265-015-0484-9

Conlin, A. K., Seidman, A. D., Bach, A., Lake, D., Dickler, M., D'Andrea, G., et al. (2010). Phase II trial of weekly nanoparticle albumin-bound paclitaxel with carboplatinand trastuzumab as first-line therapy for women with HER2-overexpressingmetastatic breast cancer. *Clin. Breast Cancer* 10, 281–287. doi: 10.3816/CBC.2010.n.036

Davit, B. M., Conner, D. P., Fabian-Fritsch, B., Haidar, S. H., Jiang, X., Patel, D. T., et al. (2008). Highly variable drugs: observations from bioequivalence data submitted to the FDAfor new generic drug applications. *AAPS J*. 10, 148–156. doi: 10.1208/s12248-008-9015-x

Donehower, R. C., Rowinsky, E. K., Grochow, L. B., Longnecker, S. M., and Ettinger, D. S. (1987). Phase I trial of taxol in patients with advanced cancer. *Cancer Treat. Rep*. 71, 1171–1177.

Dörfel, S., Steffens, C. C., Meyer, D., Tesch, H., Kruggel, L., Frank, M., et al. (2018). Adjuvant chemotherapeutic treatment of 1650 patients with early breast cancer in routine care in Germany: data from the prospective TMK cohort study. *Breast Cancer* 25, 275–283. doi: 10.1007/s12282-017-0823-7

Du, X., Khan, A. R., Fu, M., Ji, J., Yu, A., and Zhai, G. (2018). Current development in the formulations of non-injection administration ofpaclitaxel. *Int. J. Pharm*. 542, 242–252. doi: 10.1016/j.ijpharm.2018.03.030

FDA (2015). *Draft Guidance on Paclitaxel*. Available online at https://www.fda.gov/downloads/drugs/guidancecomplianceregulatoryinformation/guidances/ucm320015.pdf

Frederiks, C. N., Lam, S. W., Guchelaar, H. J., and Boven, E. (2015). Genetic polymorphisms and paclitaxel- or docetaxel-induced toxicities: asystematic review. *Cancer Treat. Rev*. 41, 935–950. doi: 10.1016/j.ctrv.2015.10.010

Guarneri, V., Dieci, M. V., and Conte, P. (2012). Enhancing intracellular taxane delivery: current role and perspectives ofnanoparticle albumin-bound paclitaxel in the treatment of advanced breast cancer. *Expert Opin. Pharmacother*. 13, 395–406. doi: 10.1517/14656566.2012.651127

Henderson, I. C., and Bhatia, V. (2007). Nab-paclitaxel for breast cancer: a new formulation with an improved safetyprofile and greater efficacy. *Expert Rev. Anticancer Ther*. 7, 919–943. doi: 10.1586/14737140.7.7.919

Hendrikx, J. J., Lagas, J. S., Rosing, H., Schellens, J. H., Beijnen, J. H., and Schinkel, A. H. (2013). P-glycoprotein and cytochrome P450 3A act together in restricting the oralbioavailability of paclitaxel. *Int. J. Cancer* 132, 2439–2447. doi: 10.1002/ijc.27912

Hyman, D. M., Rizvi, N., Natale, R., Armstrong, D. K., Birrer, M., Recht, L., et al. (2018). Phase I study of MEDI3617, a selective angiopoietin-2 inhibitor alone andcombined with carboplatin/paclitaxel, paclitaxel, or bevacizumab for advancedsolid tumors. *Clin Cancer Res*. 24, 2749–2757. doi: 10.1158/1078-0432.CCR-17-1775

Joerger, M. (2012). Prevention and handling of acute allergic and infusion reactions in oncology. *Ann Oncol.* 23(Suppl. 10), x313–x319. doi: 10.1093/annonc/mds314

Karalis, V., Macheras, P., Van Peer, A., and Shah, V. P. (2008). Bioavailability and bioequivalence: focus on physiological factors andvariability. *Pharm. Res*. 25, 1956–1962. doi: 10.1007/s11095-008-9645-9

Karalis, V., Symillides, M., and Macheras, P. (2012). Bioequivalence of highly variable drugs: a comparison of the newly proposedregulatory approaches by FDA and EMA. *Pharm. Res*. 29, 1066–1077. doi: 10.1007/s11095-011-0651-y

Li, Y., Chen, N., Palmisano, M., and Zhou, S. (2015). Pharmacologic sensitivity of paclitaxel to its delivery vehicles drives distinct clinical outcomes of paclitaxel formulations. *Mol. Pharm*. 12, 1308–1317. doi: 10.1021/acs.molpharmaceut.5b00026

Lluch, A., Alvarez, I., Muñoz, M., Seguí, M. Á., Tusquets, I., and García-Estévez, L. (2014). Treatment innovations for metastatic breast cancer: nanoparticle albumin-bound(NAB) technology targeted to tumors. *Crit. Rev. Oncol. Hematol*. 89, 62–72. doi: 10.1016/j.critrevonc.2013.08.001

Locatelli, M., Tinari, N., Grassadonia, A., Tartaglia, A., Macerola, D., Piccolantonio, S., et al. (2018). FPSE-HPLC-DAD method for the quantification of anticancer drugs in human wholeblood, plasma, and urine. *J. Chromatogr. B Analyt. Technol. Biomed. Life Sci*. 1095, 204–213. doi: 10.1016/j.jchromb.2018.07.042

Palumbo, R., Sottotetti, F., Trifirò, G., Piazza, E., Ferzi, A., Gambaro, A., et al. (2015). Nanoparticle albumin-bound paclitaxel (nab-paclitaxel) as second-linechemotherapy in HER2-negative, taxane-pretreated metastatic breast cancerpatients: prospective evaluation of activity, safety, and quality of life. *Drug Des. Devel. Ther*. 9, 2189–2199. doi: 10.2147/DDDT.S79563

Petrelli, F., Borgonovo, K., and Barni, S. (2010). Targeted delivery for breast cancer therapy: the history ofnanoparticle-albumin-bound paclitaxel. *Expert Opin. Pharmacother*. 11, 1413–1432. doi: 10.1517/14656561003796562

Ronghao, X., and Jun, Z. (2015). *Chinese Pharmacopoeia. Fourth Edition*.

Shah, V. P., Midha, K. K., Dighe, S., McGilveray, I. J., Skelly, J. P., Yacobi, A., et al. (1991). Analytical methods validation: bioavailability, bioequivalence andpharmacokinetic studies. Conference report. *Eur. J. Drug Metab. Pharmacokinet*. 16, 249–255. doi: 10.1007/BF03189968

Singla, A. K., Garg, A., and Aggarwal, D. (2002). Paclitaxel and its formulations. *Int. J. Pharm*. 235, 179–192. doi: 10.1016/S0378-5173(01)00986-3

Slingerland, M., Guchelaar, H. J., Rosing, H., Scheulen, M. E., van Warmerdam, L. J., Beijnen, J. H., et al. (2013). Bioequivalence of Liposome-Entrapped Paclitaxel Easy-To-Use (LEP-ETU) formulationand paclitaxel in polyethoxylated castor oil: a randomized, two-period crossover study in patients with advanced cancer. *Clin Ther*. 35, 1946–1954. doi: 10.1016/j.clinthera.2013.10.009

Sparreboom, A., van Zuylen, L., Brouwer, E., Loos, W. J., de Bruijn, P., Gelderblom, H., et al. (1999). Cremophor EL-mediated alteration of paclitaxel distribution in human blood:clinical pharmacokinetic implications. *Cancer Res*. 59, 1454–1457.

Srinivas, N. R. (2009). Considerations for metabolite pharmacokinetic data inbioavailability/bioequivalence assessments. Overview of the recent trends. *Arzneimittelforschung* 59, 155–165. doi: 10.1055/s-0031-1296380

Vishnu, P., and Roy, V. (2010). Nab-paclitaxel: a novel formulation of taxane for treatment of breast cancer. *Womens Health* 6, 495–506. doi: 10.2217/WHE.10.42

Xiang, J., Wu, B., Zhou, Z., Hu, S., Piao, Y., Zhou, Q., et al. (2018). Synthesis and evaluation of a paclitaxel-binding polymeric micelle for efficient breast cancer therapy. *Sci. China Life Sci*. 61, 436–447. doi: 10.1007/s11427-017-9274-9

Xie, J. D., Huang, Y., Chen, D. T., Pan, J. H., Bi, B. T., Feng, K. Y., et al. (2015). Fentanyl enhances hepatotoxicity of paclitaxel via inhibition of CYP3A4 and ABCB1 transport activity in mice. *PLOS ONE* 10:e0143701. doi: 10.1371/journal.pone.0143701

Zhang, H., Li, Q., Zhu, X., Li, C., Li, X., Liu, C., et al. (2018b). Tolerance, variability, and pharmacokinetics of bevacizumab biosimilars inChinese healthy male subjects. *Cancer Chemother. Pharmacol.* 82, 615–623. doi: 10.1007/s00280-018-3645-1

Zhang, H., Li, Q., Zhu, X., Wu, M., Li, C., Li, X., et al. (2018a). Association of variability and pharmacogenomics with bioequivalence of gefitinib in healthy male subjects. *Front. Pharmacol.* 9:849. doi: 10.3389/fphar.2018.00849

Conflict of Interest Statement: The authors declare that the research was conducted in the absence of any commercial or financial relationships that could be construed as a potential conflict of interest.

frontiers in Pharmacology

ORIGINAL RESEARCH
published: 21 February 2019
doi: 10.3389/fphar.2019.00089

L-4, a Well-Tolerated and Orally Active Inhibitor of Hedgehog Pathway, Exhibited Potent Anti-tumor Effects Against Medulloblastoma *in vitro* and *in vivo*

Mingfei Zhu[1†], Hong Wang[1†], Chenglin Wang[2], Yanfen Fang[1], Tong Zhu[1], Weili Zhao[2], Xiaochun Dong[2] and Xiongwen Zhang[1*]*

[1] Shanghai Engineering Research Center of Molecular Therapeutics and New Drug Development, School of Chemistry and Molecular Engineering, East China Normal University, Shanghai, China, [2] Department of Medicinal Chemistry, School of Pharmacy, Fudan University, Shanghai, China

OPEN ACCESS

Edited by:
Carmen Alvarez-Lorenzo, University of Santiago de Compostela, Spain

Reviewed by:
Violaine See, University of Liverpool, United Kingdom
Eugenio Gaudio, Istituto Oncologico della Svizzera Italiana, Switzerland

***Correspondence:**
Xiongwen Zhang
xwzhang@sat.ecnu.edu.cn
Xiaochun Dong
xcdong@fudan.edu.cn

[†] These authors have contributed equally to this work

Specialty section:
This article was submitted to Pharmacology of Anti-cancer Drugs, a section of the journal Frontiers in Pharmacology

Received: *05 September 2018*
Accepted: *23 January 2019*
Published: *21 February 2019*

Citation:
Zhu M, Wang H, Wang C, Fang Y, Zhu T, Zhao W, Dong X and Zhang X (2019) L-4, a Well-Tolerated and Orally Active Inhibitor of Hedgehog Pathway, Exhibited Potent Anti-tumor Effects Against Medulloblastoma in vitro and in vivo. Front. Pharmacol. 10:89. doi: 10.3389/fphar.2019.00089

Inhibition of aberrant Hedgehog (Hh) pathway had been proved to be a promising therapeutic intervention in cancers like basal cell carcinoma (BCC), medulloblastoma (MB), and so on. Two drugs (Vismodegib, Sonidegib) were approved to treat BCC and more inhibitors are in clinical investigation. However, the adverse effects and drug resistance restricted the use of Hh inhibitors. In the present study, 61 synthesized compounds containing central backbone of phthalazine or dimethylpyridazine were screened as candidates of new Hh signaling inhibitors by performing dual luciferase reporter assay. Among the compounds, L-4 exhibited an IC_{50} value of 2.33 nM in the Shh-Light II assay. L-4 strongly inhibited the Hh pathway *in vitro* and blocked the Hh pathway by antagonizing the smoothened receptor (Smo). Remarkably, L-4 could significantly suppress the Hh pathway activity provoked by Smo mutant (D473H) which showed strong resistant properties to existing drugs such as Vismodegib. Orally administered L-4 exhibited prominent dose-dependent anti-tumor efficacy *in vivo* in Ptch+/−; p53−/− MB allograft model. Furthermore, L-4 showed good tolerance in acute toxicity test using ICR mice. These evidences indicated that L-4 was a potent, well-tolerated, orally active inhibitor of Hedgehog pathway, and might be a promising candidate in development of Hh-targeted anti-cancer drugs.

Keywords: L-4, hedgehog, Smo, medulloblastoma, D473H

INTRODUCTION

The Hedgehog pathway is evolutionarily conserved and plays vital roles in the early development of the mammals by controlling cell proliferation and differentiation (Pomeroy et al., 2002; Jiang and Hui, 2008). It was found in a state of suppression in most adult tissues and only involved in the maintenance and repair of some tissues (Rimkus et al., 2016). The main components of the Hh pathway in mammals include the following parts: three Hh ligands (Sonic hedgehog,

Abbreviations: BCA, bicinchoninic acid; BCC, basal cell carcinoma; CMCNa, carboxymethyl cellulose sodium; GLI, glioma associated oncogene; Hh, hedgehog; ICR mice, institute of cancer research mice; MB, medulloblastoma; PTCH, patched; SHH, sonic hedgehog; Smo, smoothened; SPF, specific pathogen-free; TGI, tumor growth inhibition; WNT, wingless.

Indian hedgehog, Desert hedgehog) which can stimulate the Hh pathway, PTCH which represses the activity of Smo, Smo which acts as a positive regulatory protein, and the GLI family (Ruiz and Altaba, 1997). PTCH and Smo are transmembrane proteins (Roudaut et al., 2011). In the absence of Hh ligands, PTCH inhibits Smo activity by repressing its trafficking and localization to the cilia (Cheng and Bishop, 2002; Goetz and Anderson, 2010). Once the Hh ligands bind to PTCH, PTCH would leave the cilia and Smo would be able to accumulate and activate in the cilia (Sharpe et al., 2015; Zhang et al., 2017). Activated Smo subsequently starts a downstream signaling leading to the activation of transcription factors, GLI. Then, the activated GLIs translocate into the nucleus to induce the expression of various context-specific genes which regulate cellular differentiation, proliferation and survival (Scales and de Sauvage, 2009; Stecca and Ruiz, 2010).

Aberrant activation of Hh pathway signaling leads to abnormal development of the tissues and is linked to many malignant tumors like BCC, MB, and so on (Epstein, 2008; Rimkus et al., 2016; Tan et al., 2018). MB, known as a primitive neuroectodermal tumor, is the most common malignant pediatric brain tumor (Romer et al., 2004). It happens in the cerebellum and accounts for about 20% of all pediatric brain tumors (Ellison et al., 2003). Previous studies had shown that Hh pathway was closely related to MB. Mutant PTCH1 was reported to cause the human developmental disorder Gorlin syndrome which increased a notable risk of advanced BCC and MB. This indicated that Hh pathway contributed to the formation of MB (Hahn et al., 1996). Actually, further researches showed abnormal expression of PTCH1, SMO, and SUFU in a large percentage of spontaneous MB (Epstein, 2008; Kool et al., 2008). Up to now, MB are termed four subgroups: WNT, SHH, group 3, and group 4 (Taylor et al., 2012). Among them, Hh pathway subtype accounts for 30% of MB (Kool et al., 2012; Korshunov et al., 2012). Thus, research and development of inhibitors targeting the Hh pathway might be a promising strategy for MB therapy (Rimkus et al., 2016).

Cyclopamine is the first Hh inhibitor to be found which advances our research of the Hh pathway as a therapeutic target substantially (Incardona et al., 1998; Tremblay et al., 2009). It is an allosteroid alkaloid extracted from the veratrine (Incardona et al., 1998). Cyclopamine could directly combine with the transmembrane domain of Smo proteins and prevent the conformational change and activation of Smo (Chen et al., 2016). However, the poor potency and oral solubility limit its application in clinical therapy (Tremblay et al., 2009). In recent years, great effort has been taken predominantly on targeting Smo. So far, a variety of Smo inhibitors have been reported. Among them, Vismodegib (GDC-0449) (Robarge et al., 2009; Kumar et al., 2017) and Sonidegib (NVP-LDE225) (Pan et al., 2010; Jalili et al., 2013) have been approved by FDA for the treatment of BCC. However, Vismodegib and Sonidegib showed undesirable adverse effect and drug resistance subsequently in clinic therapy (Scales and de Sauvage, 2009). According to the research, there are 15–33% untreated BCC patients harbor Smo mutations and the percentage increases to 69–77% in resistant tumors (Dong et al., 2018). The MB relapsed after a few months of Vismodegib treatment and it was found that the mutation of Smo D473H gave rise to the drug resistance (Yauch et al., 2009). Thus, the binding ability of Hh inhibitors to D473H is important to overcome the drug resistance.

NVP-LEQ506 (Peukert et al., 2013) and Taladegib (LY-2940680) (Bendell et al., 2018) are two representative Hh inhibitors in clinic trial. NVP-LEQ506 was developed by Novartis and LY-2940680 was developed by Lilly United States and Ignyta. LY-2940680 and Anta XV (lead compound of NVP-LEQ506) are both benzylphthalazine derivatives which were reported to be potent Hh pathway inhibitors with low nanomolar affinity for Smo. Based on these previous studies, we designed and synthesized a series of small molecular compounds containing central backbone of phthalazine or dimethylpyridazine as candidates of new Hh signaling inhibitors. The piperazine linker of lead compound Anta XV was replaced by piperidin-4-amine moiety and the benzyl group was optimized with different aromatic rings to generate compounds series A. We applied the similar strategy to replace the 4-methylamino-piperidine linker of LY-2940680 with pyrrolidin-3-amine moiety and the 1-methyl-1H-pyrazol group with benzene ring to generate compounds series L. Furthermore, in some compounds, the bicyclic phthalazine core was replaced with dimethylpyridazine to mimic the pharmacophore of NVP-LEQ506. After screening for inhibitive effects on Hh signaling pathway of these compounds, L-4 was found to be the most potent compound. Herein, evaluation of anti-tumor effects of L-4 *in vitro* and *in vivo* was conducted.

MATERIALS AND METHODS

Reagents

Vismodegib, Taladegib, and SAG were purchased from Selleck (TX, United States). NVP-LEQ506 was bought from MedChemExpress (NJ, United States). L-4 was synthesized in-house. For *in vitro* experiments, compounds were dissolved in DMSO (Beyotime, Shanghai, China) and stock solutions were stored at −20°C. For *in vivo* experiments, Vismodegib, Taladegib and L-4 were formulated in 0.5% methylcellulose (Aladdin, Shanghai, China).

Cell Lines and Cell Culture

Shh-Light II cell line was a gift of Professor. Philip Beachy in Stanford University and cells were maintained in DMEM (Hyclone, UT, United States) containing 10% fetal bovine serum (FBS) (Biological Industries, Israel), zeocin (Invitrogen, CA, United States) 0.15 mg/mL and G418 (Invitrogen) 0.4 mg/mL at 37°C in a 5% CO_2 atmosphere. HEK293 human epithelial kidney cell was purchased from Cell Bank of China Science Academy (Shanghai, China) and cells were maintained in DMEM containing 10% FBS, streptomycin 100 μg/mL and penicillin 100 U/mL as recommended at 37°C in a 5% CO_2 atmosphere.

Animals

All animal (purchased from Shanghai SLAC Laboratory Animal Co., Ltd., Shanghai, China) care and experimental protocols for this study complied with the Chinese regulations and the

Guidelines for the Care and Use of Laboratory Animals drawn up by the National Institutes of Health (USA) and were approved by the Institutional Animal Care and Use Committee of the East China Normal University. ICR mice and BALB/c nude mice (6–8 weeks old) were purchased from the Shanghai SLAC Laboratory Animal CO., LTD., Mice were maintained on a 12:12 light-dark cycle in a temperature-controlled (21∼23°C) and SPF conditional room. Mice were provided with standard rodent chow and water *ad libitum*. All animals were acclimatized for a week before beginning the study.

Gli-Luc Reporter Assay

Shh-Light II cells were seeded in 96-well plants at a density of 4000 cells/200 μL. After 48 h of various compounds treatment as indicated, the luciferase activity was examined with Dual-Luciferase Assay Reporter System (Promega, Madison, WI, United States) following the manufacturer's instructions. The firefly luciferase values were normalized to Renilla values. GraphPad Prism software was used to generate dose–response curves and IC_{50} values with five parameters logarithmic non-linear regression fitting.

Medulloblastoma Primary Cells Culture and Brdu Assay

Ptch+/−; p53−/− mice were gained from hybridization of Ptch+/− mice and p53−/− mice. p53−/− mice were kindly provided by Professor Wei Zhang (East China Normal University, Shanghai, China) and Ptch+/− mice were bought from Model Animal Research Center of Nanjing University (Nanjing, China). The primary spontaneously MB in Ptch+/−; p53−/− mice were collected and allografted into BALB/c nude mice. After development in the nude mice, tumors were harvested. The cells were maintained in Neurobasal A medium (Invitrogen) containing B-27 supplement (Invitrogen), EGF 20 ng/ml (Invitrogen), bFGF 20 ng/ml (Invitrogen), non-essential amino acids (Invitrogen), N-acetylcysteine 60 μg/ml (Sigma-aldrich, St. Louis, MO, United States).

Medulloblastoma cells were seeded in 96-well plates at a density of 20000 cells/200 μL. After treated with various concentrations of L-4 for 36 h, the Brdu assay was conducted using the Brdu Cell Proliferation Kit (Abcam, Cambridge, United Kingdom) according to manufacturer's instructions.

Microscopy Analysis of Fluorescent BODIPY-Cyclopamine Competition Assay

Human wild type Smo (hSmo) expression vector is a gift from Professor Ke Yu (Fudan University, Shanghai, China). Microscopy analysis of fluorescent BODIPY-cyclopamine competition assay was performed as following. In brief, the HEK293 cells were seeded in 6-well plates and transfected with wild type hSmo expression vector. Two days after transfection, the cells were seeded in 24-well plates and incubated with compounds. After incubation for 10 h, the cells were washed with PBS twice, fixed with 4% paraformaldehyde in dark for 10 min, washed with PBS again and incubated with Triton X-100 solution for 10 min. The cells were then stained with DAPI (Sigma-aldrich) and photographed using a fluorescence microscope.

Flow Cytometry Analysis of Fluorescent BODIPY-Cyclopamine Competition Assay

Fluorescent BODIPY-cyclopamine competition assay was adopted as following. In brief, HEK293 cells were seeded in 6-well plates and transfected with wild type hSmo expression vector. Two days later, cells were seeded in 24-well plates and treated with the compounds. After incubation for 10 h, the cells were harvest and tested by flow cytometry. The green fluorescence of BODIPY-cyclopamine bound to Smo was examined by a flow cytometer (Guava EasyCyte 6HT-2 L, Merck Millipore, Billerica, MA, United States). At least 5000 cells were analyzed for each data point. FACS data were analyzed with InCyte software.

Antagonizing Drug-Resistant Assay

Drug-resistant D473H Smo expression vector is a gift from Professor Ke Yu (Fudan University, Shanghai, China). Shh-Light II cells were transfected with wild type and mutant D473H Smo expression vectors. Then the cells were seeded in 96-well plates and treated with Vismodegib and L-4 at various concentrations. After incubation for 48h, a dual luciferase reporter assay (Promega, Madison, WI, United States) was performed following the manufacturer's instructions. 293T cells transfected with mutant Smo D473H were treated with Vismodegib and L-4 for 48 h, then cells were harvested and subjected to WB analysis.

Molecular Modeling

Molecular docking was carried out by using Glide module in Schrödinger 2013 software package. The crystallographic structure of the human Smo 7TM receptor was retrieved from the RCSB protein data bank (ID: 4JKV). The SWISS-MODEL online server was employed to construct the mutant D473H by replace the specific residue Asp473. The WT and D473H structures were minimized by using AMBER16 software and then were prepared by using the Protein Preparation Wizard module. Two ligands were selected in the docking study: L4 and Vismodegib. Before docking, they have been processed by using the Ligprep module in Schrödinger 2013. These two molecules were docked into the binding pocket of the WT and D473H protein structure. The best docked poses were select for further analysis.

Western Blot Analysis

The proteins of whole cell lysates were prepared in RIPA buffer containing protease and phosphatase inhibitors (Thermo Fisher Scientific, Waltham, MA, United States), and quantified by the BCA method. Immunoblotting analysis of Gli1 and Ptch1 were performed as previously described (Dorward et al., 2016). The expression of β-actin was used as loading control. Antibodies against Smo and β-actin were purchased from Santa Cruz Biotechnology (CA, United States). Antibody against Ptch1

was purchased from Abcam. Antibody against Histone H3 was purchased from CST (Danvers, MA, United States).

Cell fractionation was performed as following. The collected cells were lysed by cytoplasmic lysis buffer [50 mM Tris-HCl (PH 7.4), 140 mM NaCl, 1.5 mM $MgCl_2$, and 0.5% NP-40 (1.06 g/ml)] for 20 min. Then the lysate was centrifuged for 10 min at 3000 rpm at 4°C and the supernatant was collected as cytoplasmic lysate. The pellet was washed once by cytoplasmic lysis buffer and dissolved by RIPR buffer (Thermo Fisher Scientific, Waltham, MA, United States) for 20 min. Then the lysate was centrifuged for 10 min at 12000 rpm at 4°C and the supernatant was collected as nuclear lysate.

Medulloblastoma Allograft Model

The primary intracranial MB spontaneously developed in Ptch+/−; p53−/− mice were harvested and subcutaneously allografted into athymic nude mice. The tumors in nude mice were further collected and cut into 1 mm^3 fragments. Then the fragments were inoculated subcutaneously into the right flank of other nude mice. When the tumor volume reached 150–200 mm^3, the mice were randomized grouped into control and treatment groups to receive treatment accordingly. L-4 was orally administered at 5, 10, and 20 mg/kg once a day for 13 days. Taladegib was used as a positive control and orally administered at 20 mg/kg once a day. The tumor growth was recorded with the measurement of length (L) and width (W) by caliper every other day and calculated as tumor volume (V) = $L \times W^2/2$. Meanwhile, the body weights of mice were recorded. The TGI was calculated as TGI% = [1-(mean tumor volume of the treated group on the last day-mean tumor volume of the treated group on day 0)/(mean tumor volume of the control group on the last day-mean tumor volume of the control group on day 0)] × 100%. The tumor regression of individual mouse was defined as the tumor volume at the end was less than the tumor volume when treatment was initiated.

Acute Toxicity Test

According to guideline 425 Organisation for Economic Co-operation Development [OECD], 2008, L-4 was administered in a single dose of 2000 mg/kg by oral in five female ICR mice ($n = 5$). A negative control was established by administering a 0.5% CMCNa solution to a female mouse ($n = 1$). Body weight of the animals were recorded shortly before the administration of the L-4 and then daily, during the treatment period. After administration, animals were observed individually during the first 30 min and then daily for 14 days. Observations included mortality and changes in skin and fur, eyes and mucous membranes, and also respiratory, circulatory, autonomic and central nervous systems, and somatomotor activity and behavior pattern. Attention should be directed to observations of tremors, convulsions, salivation, diarrhea, lethargy, sleep, and coma.

Statistical Analysis

The statistical significance of differences between groups was evaluated by the unpaired Student's t test and indicated with $^{**}P < 0.01$, $^{*}P < 0.05$. All statistical tests were two sided.

RESULTS

Screening Hh Signaling Inhibitory Activities of the Synthesized Compounds

To evaluate the inhibitory effects of all the compounds, dual luciferase reporter assays were conducted using Shh-Light II cells, which were NIH-3T3 cells stably fused with a Gli-responsive firefly luciferase and Renilla-luciferase (Xin et al., 2014). As shown in **Table 1**, 61 compounds were screened and 14 compounds showed good inhibitory potency. Then, we selected 5 representative compounds to further check the *in vitro* concentration-inhibition IC_{50} values. NVP-LEQ506 and LY-2940680 were used as positive controls. The IC_{50} values ranged from 1 to 50 nM (**Table 2**). L-4 (**Figure 1**) showed the best inhibitory potency with an IC_{50} of 2.33 nM.

L-4 Inhibits the Proliferation of Medulloblastoma Cells With Activation of Hh Pathway Signaling

The potency of L-4 in inhibiting the proliferation of cancer cells related to activation of Hh pathway was tested. The Ptch+/−; p53−/− MB mouse model, a generally accepted Hh-driven mouse MB model which had been used to evaluate the anti-cancer effect of Smo inhibitors (Wetmore et al., 2001), was established. Spontaneous MB cells were then isolated from nude mice for testing the antiproliferative effect of compound L-4 using Brdu assay. Vismodegib and LY2940680 were used as positive controls. The results showed that L-4 dose-dependently inhibited the proliferation of MB cells in a similarity to that of Vismodegib and LY2940680 (**Figure 2A**). The IC_{50} of L-4 was 31.36 nM and the IC_{50} of Vismodegib and LY2940680 were 37.65 and 35.5 nM, respectively. Also, Western bolt results showed that L-4 dose-dependently inhibited the expression of Gli1 and Ptch1 in MB cells (**Figure 2B**).

L-4 Binds With Smo and Restrains the Expression of Gli1 and Ptch1

To check whether the inhibitory potency of L-4 against the Hh pathway is due to targeting Smo, direct interaction of L-4 with Smo was analyzed by using BODIPY-cyclopamine, a kind of cyclopamine derivative with fluorescent label (Solinas et al., 2012; Sharpe et al., 2015). Firstly, HEK293 cells were transfected with the wild type Smo expression vector and the effect of transfection was examined by western blot (**Figure 3A**). Then, fluorescent BODIPY-cyclopamine competition assay was performed. In the presence of 10 μM L-4, cellular fluorescence of BODIPY-cyclopamine was not observed by the fluorescence microscopy analysis (**Figure 3B**). It was similar to the positive control, cyclopamine (Schaefer et al., 2013). As shown in **Figures 3C,D**, results of quantitative analysis using flow cytometry suggested that there was a dose-dependent replacement of BODIPY-cyclopamine by L-4. Taken together, our data demonstrated that L-4 was able to displace the BODIPY-cyclopamine from Smo and

TABLE 1 | Inhibitory rate of compounds to the Hh pathway tested by dual luciferase reporter assays in Shh-Light II cells.

Compound (30 nM)	First screening inhibitory rate (%)	Second screening inhibitory rate (%)	Compound (30 nM)	First screening inhibitory rate (%)	Second screening inhibitory rate (%)
A-1	−7.04	20.15	L-7	61.61	61.17
A-2	30.32	34.48	L-8	46.78	27.97
A-3	25.85	47.63	L-9	106.47	95.84
A-4	18.11	17.66	L-10	81.75	63.77
A-5	30.52	37.46	L-11	77.72	88.68
A-6	9.27	−23.23	L-12	45.68	52.01
A-7	32.16	17.73	L-13	60.13	83.02
A-8	64.04	60.00	L-14	42.59	50.88
A-9	52.99	35.33	L-15	50.17	67.34
A-10	52.09	40.40	L-16	54.76	71.98
A-11	57.83	50.82	L-17	34.08	64.95
A-12	68.36	41.20	L-18	−15.90	37.28
A-13	21.12	29.80	L-19	13.64	52.67
A-14	17.34	47.50	L-20	14.84	36.03
A-15	−14.65	36.85	L-21	−5.37	39.89
A-16	58.48	54.85	L-22	69.50	59.59
A-17	−13.85	0.34	L-23	71.19	68.26
A-18	31.45	27.03	L-24	−9.40	−2.67
A-19	11.29	19.64	L-25	45.58	55.74
A-20	62.98	67.09	L-26	14.60	30.87
A-21	33.79	62.53	L-27	42.37	52.25
A-22	43.88	32.58	L-28	−12.71	26.22
A-23	–	73.58	L-29	−9.52	44.36
A-24	–	46.92	L-30	13.40	−1.34
A-25	–	21.82	L-31	13.93	3.76
A-26	–	20.51	L-32	15.10	38.84
L-1	−18.49	−16.43	L-33	35.28	71.25
L-2	20.99	33.38	L-34	66.91	81.92
L-3	26.88	−17.38	L-35	–	43.60
L-4	109.69	104.42	LY-2940680	–	94.99
L-5	15.07	43.32	GDC-0449	108.02	95.33
L-6	27.29	32.60	NVP-LEQ506	96.24	–

TABLE 2 | IC_{50} value of compounds to the Hh pathway tested by dual-luciferase reporter assays in Shh-Light II cells.

Compounds	Hedgehog inhibitory IC_{50} (nM, mean ± SEM)
LY-2940680	2.26 ± 0.23
NVP-LEQ506	1.23 ± 0.13
A-8	21.22 ± 3.78
L-7	48.66 ± 2.97
A-11	38.38 ± 4.10
L-4	2.33± 0.18
A-20	39.83 ± 4.35

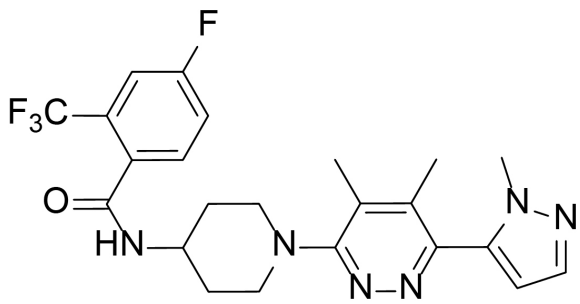

FIGURE 1 | Structure of L-4.

inhibited the Hh signaling pathway by targeting Smo. Moreover, results of western blot (**Figure 3E**) suggested that L-4 dose-dependently reduced the expression of Gli1 and Ptch1 in Shh-Light II cells.

It had been shown that Gli1 translocated from the cytoplasm to the nucleus to induce a series of downstream genes expression (Sharpe et al., 2015). Thus, the shuttle of Gli1 in intercellular compartments after treated with L-4 was observed. As showed in **Figure 3F**, SAG induced the shuttle of Gli1 to the nucleus in Shh-Light II cells. While, after treatment with different concentrations of L-4 for 48 h, a strong decrease of Gli1 both in the cytoplasm and the nucleus could be observed. The results indicated that

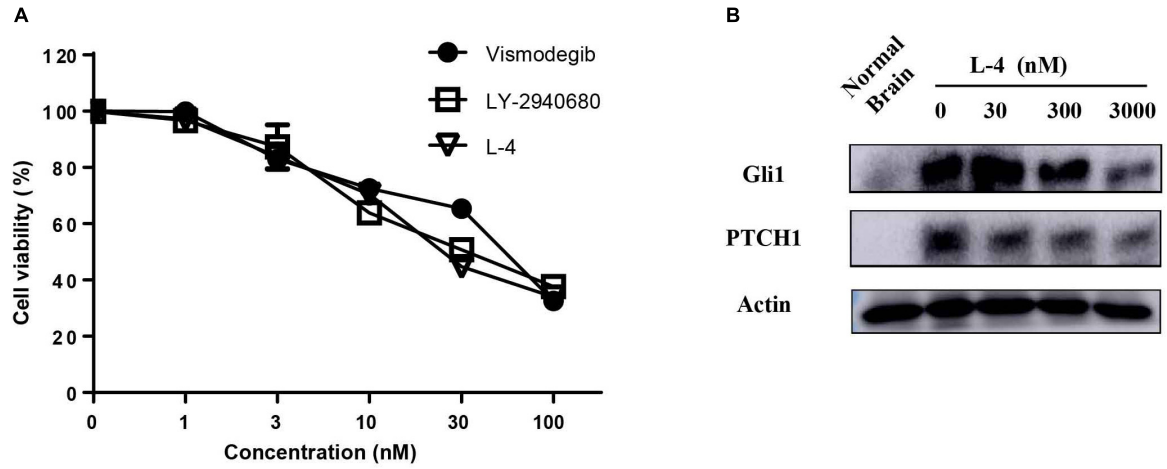

FIGURE 2 | L-4 suppressed the proliferation and Hh pathway of Ptch+/−; p53−/− medulloblastoma (MB) cells *in vitro*. **(A)** L-4 inhibited the proliferation of Ptch+/−; p53−/− MB cells assessed by Brdu analysis. MB cells were exposed to various concentrations of L-4 for 36 h. Vismodegib and LY-2940680 were used as positive controls. **(B)** L-4 inhibited the expression of Gli1 and Ptch1 in primary Ptch+/−; p53−/− MB cells. MB cells were treated with various concentration of L-4 after 48 h and collected for lysis. Protein extracts were probed with specific antibodies against Gli1, Ptch1, and Actin (as a loading control). Cells isolated from normal mouse brain was marked as "Normal Brain."

the inhibition of Smo by L-4 not only had a negative effect on translocation of Gli1, but also inhibited the Gli1 expression.

L-4 Inhibits Drug-Resistant Mutant Smo

Whether L-4 could inhibit the aberrant Hh pathway provoked by mutant Smo D473H was checked. Mutant Smo D473H is an important reason for giving rise to the resistance to the current existing drugs (Dijkgraaf et al., 2011; Infante et al., 2016). Compared to the conspicuous inhibitory effect on the Shh-Light II cells stimulated by Smo wild type expression vectors, L-4 showed similar inhibitory effects on the Shh-light II cells with overexpression of mutant Smo D473H (**Figure 4A**). The IC_{50} values of L-4 in inhibiting wild type and D473H were 23.46 and 24.55 nM, respectively. On the contrary, the inhibiting effects of Vismodegib on Hh pathway provoked by overexpression of D473H were reduced (**Figure 4B**). In the present study, the IC_{50} values of Vismodegib in inhibiting wild type and D473H were 21.63 and 326.8 nM, respectively. To further confirm these results, we transfected mutant Smo D473H into 293T cells and there was a corresponding activation in Gli1 and PTCH1. Although these proteins were largely resistant to Vismodegib, they were dose dependently inhibited by L-4 (**Figure 4C**). To sum up, we indicate that L-4 could effectively target the mutant Smo D473H.

The Binding Mode of L-4 With Wild Type and Mutant Smo

The molecular docking simulation was used to study the binding modes of L-4 and Vismodegib with wild type and mutated D473H Smo. The predicted binding mode showed that the interaction between L-4 and wt-Smo was much stronger. As shown in **Figure 5A**, the inhibitor L-4 forms three critical hydrogen bonds with Smo protein: one hydrogen bond from the amide oxygen atom to Asn219 residue, two hydrogen bonds between the dimethylpyridazine core and Arg400. Furthermore, the phenyl ring and pyridazine ring also interacted with the benzene ring of Phe484 and Tyr394 via π-π stacking. It suggested the interaction between L4 and wt-Smo was much stronger. These interactions have hardly changed after the D473H mutation (**Figure 5B**), the distance of Hydrogen bond is changed from 2.9, 3.4, and 3.3 Å to 3.0, 3.1, and 3.4 Å, respectively. The amide oxygen atom of Vismodegib also formed one hydrogen bond with Arg400 (2.9 Å) in wt-Smo, which disappeared after D473H mutation (5.2 Å). In fact, the D473H mutation (relatively larger side chain) could change the structure of the binding pocket, especially the position of Arg400. There is only one hydrogen bond between Vismodegib and the wt-Smo, which could be easily disrupted by D473H mutation and leaded to drug resistance (**Figures 5C,D**). The Computational predicted binding modes were in good agreement with the experiment results.

L-4 Inhibits the Hh Signaling Pathway Activity *in vivo*

Subcutaneous Ptch+/−; p53−/− MB allograft model was used to assess the *in vivo* anti-tumor efficacy of L-4. L-4 was orally administered at a dose of 5, 10, or 20 mg/kg once a day. As showed in **Figures 6A,C,D**, L-4 showed dose-dependent anti-tumor activity after 13 days of oral administration. Even at the lowest dose level of 5 mg/kg, tumor growth was significantly inhibited by L-4 compared to the vehicle control. TGI were 53.3, 84.3, and 93.3% under the dose of 5, 10, and 20 mg/kg, respectively. Body weights did not change significantly in mice treated with L4 at all doses (**Figure 6B**). Four hours after the last dose of vehicle, L-4 and LY-2940680 treatment, tumors were harvested and Gli1 and Pthc1 expression levels were checked as pharmacodynamic markers of Hh pathway. The results showed that L-4 could dose-dependently decrease the expression of Gli1 and Ptch1 in tumors (**Figure 6E**). Herein, these studies suggested

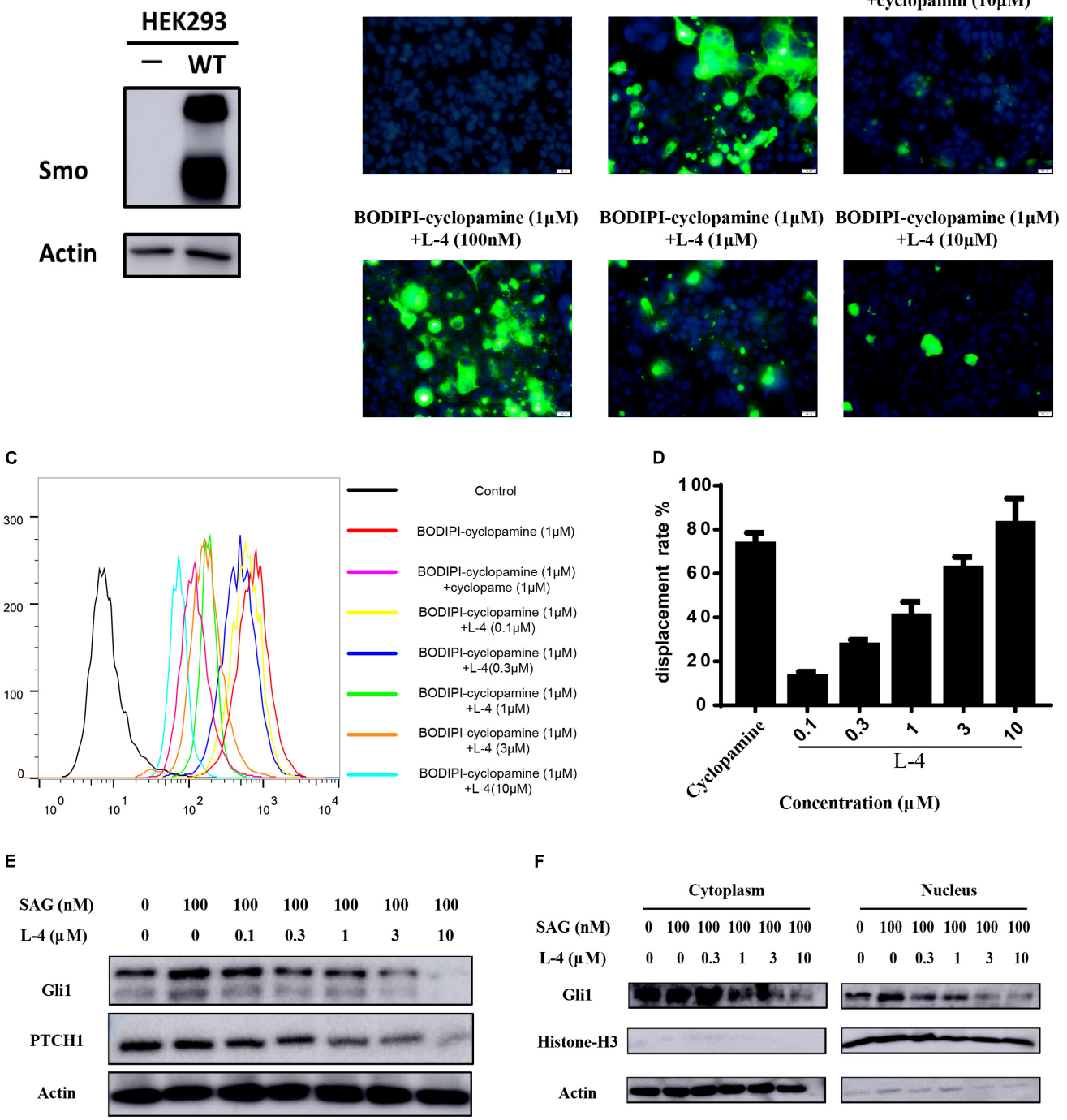

FIGURE 3 | L-4 inhibited the Hh pathway by binding to Smo. **(A)** Western blot analysis of Smo expression in HEK293 cells. HEK293 cells were transfected with wild type hSmo expression vector and the Smo protein expression level was examined by western blot. Actin was used as a loading control. **(B)** BODIPI-cyclopamine competition analysis was examined by fluorescent microscope. Photographs were representatives from three independent experiments. **(C,D)** BODIPI-cyclopamine competition analysis was examined by flow cytometry. The results were expressed as mean ± SEM of three independent experiments (n = 3). **(E)** L-4 inhibited the expression of Gli1 and Ptch1 in Shh-Light II cells. Shh-Light II cells were treated with 100 nM SAG and various concentrations of L-4 for 48 h were harvested and subjected to WB analysis. **(F)** L-4 decreased the Gli1 expression both in the cytoplasm and the nucleus in Shh-Light II cells. The cells were treated with 100 nM SAG and various concentrations of L-4 for 48 h. After treatment, cell fractionation was performed and lysates were subjected to WB analysis.

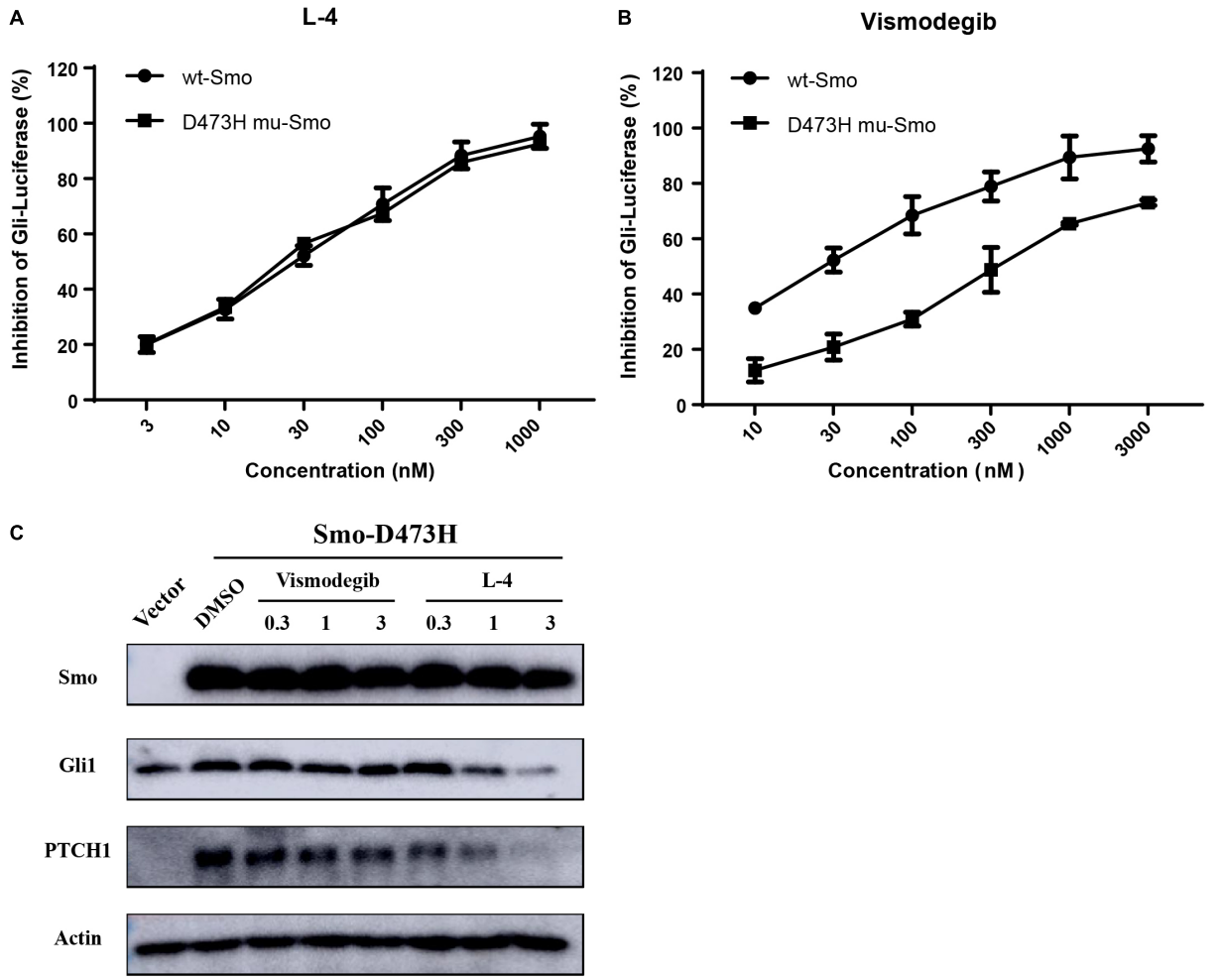

FIGURE 4 | L-4 inhibited the Gli-luciferase activity stimulated by wild type Smo and mutant Smo D473H. Light II cells transfected with wild type Smo or Smo D473H plasmids were exposed to L-4 for 48 h and then were harvested for dual luciferase reporter assays. The results were expressed as the mean ± SEM. **(A)** L-4 dose-dependently inhibited the Gli luciferase activity proved by wild type Smo and mutant Smo D473H. **(B)** Vismodegib failed to inhibited the Gli luciferase activity initiated by mutant Smo D473H. **(C)** L-4 dose-dependently inhibited the expression of Gli1 and Ptch1 in 293T cells transfected with mutant Smo D473H. Transfected cells were treated with Vismodegib and L-4 for 48 h. Cells were harvested and subjected to WB analysis.

that L-4 successfully induced TGI *in vivo* as it worked *in vitro* by inhibiting Hh pathway.

L-4 Shows No Toxicity in 14-Day Test of ICR Mice

L-4 was run through acute toxicity test as part of the preclinical safety assay. In 14-day test using ICR mice, mice receiving a single dose of 2000 mg/kg L-4 did not exhibit any toxic symptom (**Figure 6F**). Briefly, it could be predicted that the LD_{50} of the L-4 might be higher than 2000 mg/kg.

DISCUSSION

The abnormal expression of Hh pathway, which has a key role in the development and maintenance of many organs and tissues, has been linked to tumorigenesis. It had been proved that aberrant in this pathway can lead to BCC and MB. Recent researches demonstrated that Hh pathway could also be linked to many other cancers, including pancreatic (Rajurkar et al., 2012; Miyazaki et al., 2016; Kumar et al., 2017), colon (Park et al., 2011), gastric (Tang et al., 2018), lung (Zhu et al., 2017), breast (Song et al., 2016), and prostate cancers (Chen et al., 2011), leukemias and multiple myeloma (Blotta et al., 2012). As a result, development of novel Hh inhibitors is of great meaning and urgency. Here, we designed and synthesized a series of small molecular compounds containing central backbone of phthalazine or dimethylpyridazine as candidates of new Hh signaling inhibitors. After evaluation with dual luciferase reporter assays using Shh-Light II cells, among the all compounds, L-4 showed the best inhibitory potency with an IC_{50} of 2.33 nM.

In vitro, evaluating by Brdu assay, L-4 showed obvious inhibitory effect on the proliferation of primary MB cells with nanomolar IC_{50} just as Vismodegib and Taladegib. In addition,

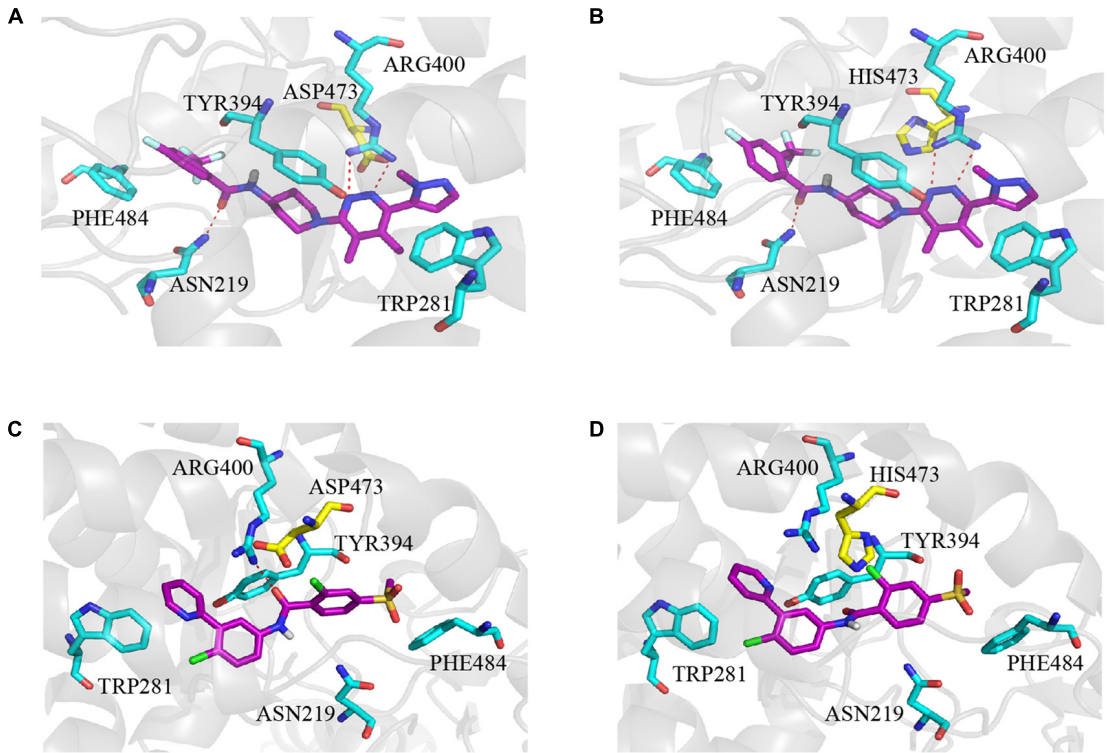

FIGURE 5 | Computational predicted binding mode of L-4 and Vismodegib with wild type and mutated D473H Smo. **(A)** L-4-Smo (WT), **(B)** L-4-SMO (D473H), **(C)** Vismodegib -Smo (WT), and **(D)** Vismodegib-Smo (D473H). All pictures were generated by using Pymol.

western blot analysis of primary MB cells treated with L-4 revealed that the expression of Hh pathway were repressed. These results confirmed that L-4 had inhibition effects on proliferation of MB cells by targeting Hh pathway.

BODIPI-cyclopamine is the derivative of cyclopamine with a fluorescent tag. Those inhibitors which share the same binding domain with cyclopamine can competitively prevent BODIPI-cyclopamine from binding to Smo protein. Correspondingly, the reduce of fluorescence signal of BODIPI-cyclopamine would be detected in the microscopy and flow cytometry analysis. In this occasion, we are able to confirm the binding domain between the inhibitor and Smo. To check whether L-4 could directly bind to Smo and to find the domain of binding between L-4 and Smo, BODIPI-cyclopamine competition assay was conducted in the present study. Both the results of fluorescence microscope analysis and the results of flow cytometry analysis showed the concentration-dependent competitive relationship between L-4 and BODIPI-cyclopamine. The results suggested that L-4 could directly bind to the transmembrane domain of Smo and occupied the same pocket as cyclopamine. As previous reported, in activating Hh pathway, Gli1 shuttles from the cell cytoplasm to nucleus to start the downstream signal in nucleus (Scales and de Sauvage, 2009). Under the treatment of L-4, there was an obvious decrease of Gli1 in both cytoplasm and nucleus. The reduce of Gli1 in the nucleus might be resulted from block of the Hh pathway by L-4. Under blocking of the Hh pathway, more Gli1 protein was restrained by the SuFu, and thus few Gli1 could go through the nucleus. Since Gli1 is also a Hh target gene and significantly influenced by activation of Hh pathway, there might be a negative feedback after L-4 binds to the Smo. Less Gli1 shuttles into nucleus might lead to reduction in the gene expression of Gli1 which resulted in the decrease of expression of Gli1 protein. Therefore, the level of Gli1 in cytoplasm also decreased.

We further checked the ability of L-4 in binding with mutant Smo D473H. In the antagonizing drug-resistant assay, L-4 exhibited equivalent potency in inhibiting the Gli-luciferase activity, and downstream biomarkers provoked by Smo wild type and Smo D473H. On the contrary, Vismodegib showed ameliorated ability in inhibiting the Gli-luciferase activity provoked by Smo D473H. In 293T cells, L-4 blocked the downstream Hh pathway biomarkers driven by mutant Smo D473H while Vismodegib failed. The results suggested possible better therapeutic effects of L-4 than Vismodegib in clinic because many patients suffered from drug resistance after treated by Vismodegib. Take molecular modeling into consideration, strong hydrogen bonds between L-4 and Smo protein suggested that the binding between L-4 and Smo might be stable. Particularly, results of calculational chemistry also showed that L-4 could equally bind to the wild type and mutant Smo, which supported results of our drug-resistant study. Vismodegib showed much weaker binding ability to mutant Smo. The docking scores of Vismodegib to wild type Smo and mutant Smo were −8.62 and −7.39, respectively. The

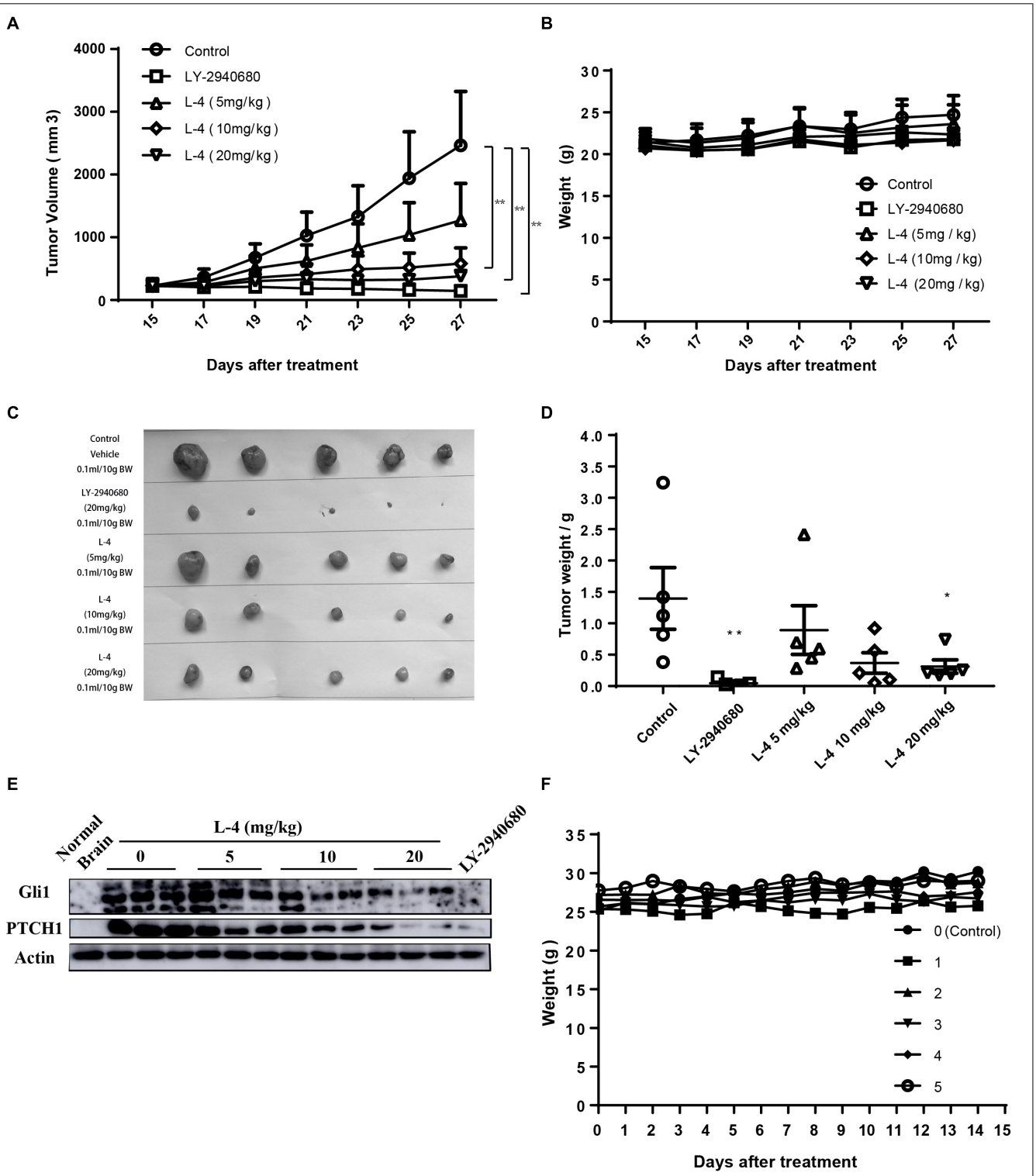

FIGURE 6 | Anti-tumor activity of L-4 in Ptch+/−; p53−/− MB allograft model. Mice bearing in MB were orally administered with LY-2940680 and L-4 once a day for 13 days. **(A)** Tumor volume for indicated days was showed as mean ± SEM ($n = 5$). **(B)** Mean body weights were presented as mean ± SEM ($n = 5$). **(C)** The pictures of tumors. **(D)** Tumor weight. **(E)** L-4 inhibited the Gli1 and PTCH1 expression in the tumors. After 4 h of last dosage, tumor samples were collected for examining the expression of Gli1 and PTCH1 protein expression. **(F)** Body weight for the ICR mice in the acute toxicity test. Number 0 was the negative control mouse orally administered with 0.5% CMCNa solution. Number 1–5 were the mice orally administered with a single dose of 2000 mg/kg L-4, separately. $^{*}p < 0.05$, $^{**}p < 0.01$ vs. control.

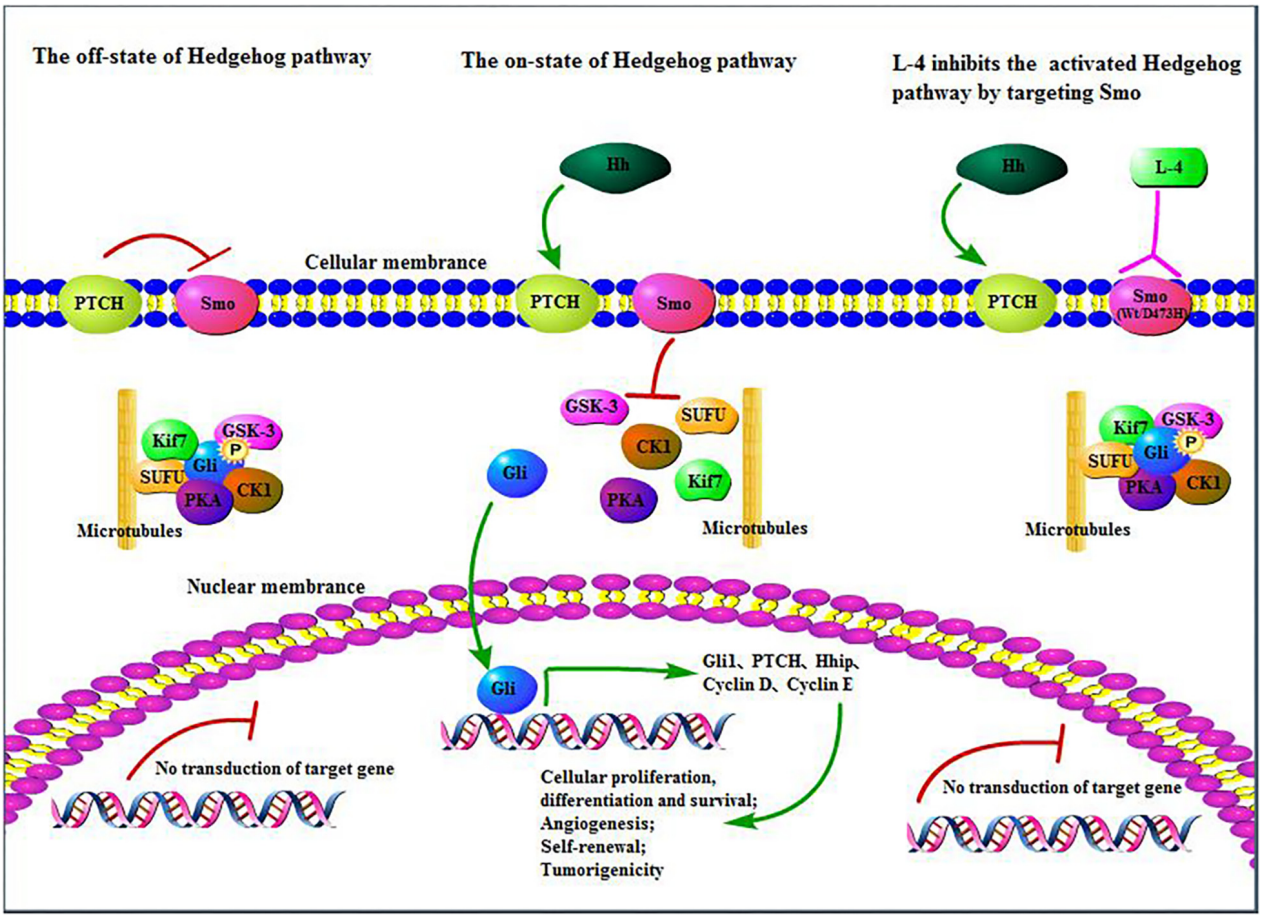

FIGURE 7 | L-4 inhibited the Hedgehog pathway by targeting Smo. L-4 bound with wild type and mutant D473H Smo to prevent Gli from being released from SUFU protein complex and then inhibited the translocation of Gli into the nucleus to induce the expression of various context-specific genes which regulate cellular differentiation, proliferation, and survival.

inhibition ability of Vismodegib in antagonizing mutant D473H is more than ten folds weaker than that of wild type. The results were consistent with the IC_{50} values of Vismodegib in inhibiting wild type and mutant D473H transfected in the Shh-Light II cells, which were 21.6 and 326.8 nM, respectively. The mutation (relatively larger side chain) of Smo can change the structure of the binding pocket, especially the position of Arg400. There is only one hydrogen bond between Vismodegib and the Smo which can be easily disrupted by the mutation, while the interaction between L-4 and Smo is much stronger, thus their binding is not greatly affected by the mutation.

Of note, our tumor profiling data indicated that orally administration of L-4 showed remarkable dose-dependent anti-cancer effects in the Ptch+/−; p53−/− MB allograft model without inducing loss of body weight. At the dose of 20 mg/kg, tumors in all five mice almost stopped growing in the 13-day treatment. The expression levels of Gli1 and Ptch1 in tumors reduced along with augment of the dose of L-4. It suggested that L-4 inhibited MB tumor growth by inhibiting Hh pathway and Gli1 and Ptch1 might be important pharmacodynamic markers. Besides, according to the results of acute toxicity test, L-4 was well tolerated in adult mice and no obvious side effects were observed.

In all, L-4 exhibited excellent drug-like properties. L-4 could bind to both wild type and mutant D473H Smo and then inhibited the escapement of Gli from SUFU protein complex and translocation of Gli into the nucleus which would induce the expression of various context-specific genes related to regulation of cellular differentiation, proliferation, and survival (**Figure 7**). It had considerable anti-tumor efficacy *in vitro* and *in vivo*. It was highly soluble and with limited toxicity. Nowadays, many preclinical and clinical studies are conducted to develop novel Hh inhibitors or combine Hh inhibitors with other clinical medicine in hope to cure cancers with overexpressed Hh pathway (Riobo et al., 2006; Wang et al., 2012; Amakye et al., 2013). Although previous studied Hh inhibitors failed in clinical trials in all other tumors except BCC and MB, more effort should be taken to research and develop new Hh inhibitors. Since L-4 could bind with wild type and mutant Smo in the aberrant Hh pathway, it is reasonable that L-4 could be a promising candidate as new anti-cancer agent and create more opportunities in cancer therapy.

AUTHOR CONTRIBUTIONS

XZ, YF, WZ, and XD conceived and designed the study. MZ, HW, and CW performed the experiments. TZ performed the molecular docking analysis. MZ wrote the manuscript. XZ, WZ, and XD supervised the whole experimental work and revised the manuscript. All authors read and approved the final manuscript.

FUNDING

This work was supported by National Natural Science Foundation of China (81872496, 21572037, 21572263, and 21572067), the Science and Technology Commission of Shanghai Municipality (16DZ2280100), and pilot project of the Chinese Academy of Sciences (XDA12020356).

REFERENCES

Amakye, D., Jagani, Z., and Dorsch, M. (2013). Unraveling the therapeutic potential of the Hedgehog pathway in cancer. *Nat. Med.* 19, 1410–1422. doi: 10.1038/nm.3389

Bendell, J., Andre, V., Ho, A., Kudchadkar, R., Migden, M., Infante, J., et al. (2018). Phase I Study of LY2940680, a Smo antagonist, in patients with advanced cancer including treatment-naive and previously treated basal cell carcinoma. *Clin. Cancer Res.* 24, 2082–2091. doi: 10.1158/1078-0432.CCR-17-0723

Blotta, S., Jakubikova, J., Calimeri, T., Roccaro, A. M., Amodio, N., Azab, A. K., et al. (2012). Canonical and noncanonical Hedgehog pathway in the pathogenesis of multiple myeloma. *Blood* 120, 5002–5013. doi: 10.1182/blood-2011-07-368142

Chen, B., Trang, V., Lee, A., Williams, N. S., Wilson, A. N., Epstein, E. H., et al. (2016). Posaconazole, a second-generation triazole antifungal drug, inhibits the hedgehog signaling pathway and progression of basal cell carcinoma. *Mol. Cancer Ther.* 15, 866–876. doi: 10.1158/1535-7163.MCT-15-0729-T

Chen, M., Carkner, R., and Buttyan, R. (2011). The hedgehog/Gli signaling paradigm in prostate cancer. *Expert Rev. Endocrinol. Metab.* 6, 453–467. doi: 10.1586/EEM.11.2

Cheng, S. Y., and Bishop, J. M. (2002). Suppressor of Fused represses Gli-mediated transcription by recruiting the SAP18-mSin3 corepressor complex. *Proc. Natl. Acad. Sci. U.S.A.* 99, 5442–5447. doi: 10.1073/pnas.082096999

Dijkgraaf, G. J., Alicke, B., Weinmann, L., Januario, T., West, K., Modrusan, Z., et al. (2011). Small molecule inhibition of GDC-0449 refractory smoothened mutants and downstream mechanisms of drug resistance. *Cancer Res.* 71, 435–444. doi: 10.1158/0008-5472.CAN-10-2876

Dong, X., Wang, C., Chen, Z., and Zhao, W. (2018). Overcoming the resistance mechanisms of Smoothened inhibitors. *Drug Discov. Today* 23, 704–710. doi: 10.1016/j.drudis.2018.01.012

Dorward, H. S., Du, A., Bruhn, M. A., Wrin, J., Pei, J. V., Evdokiou, A., et al. (2016). Pharmacological blockade of aquaporin-1 water channel by AqB013 restricts migration and invasiveness of colon cancer cells and prevents endothelial tube formation in vitro. *J. Exp. Clin. Cancer Res.* 35:36. doi: 10.1186/s13046-016-0310-6

Ellison, D. W., Clifford, S. C., Gajjar, A., and Gilbertson, R. J. (2003). What's new in neuro-oncology? Recent advances in medulloblastoma. *Eur. J. Paediatr. Neurol.* 7, 53–66. doi: 10.1016/s1090-3798(03)00014-x

Epstein, E. H. (2008). Basal cell carcinomas: attack of the hedgehog. *Nat. Rev. Cancer* 8, 743–754. doi: 10.1038/nrc2503

Goetz, S. C., and Anderson, K. V. (2010). The primary cilium: a signalling centre during vertebrate development. *Nat. Rev. Genet.* 11, 331–344. doi: 10.1038/nrg2774

Hahn, H., Wicking, C., Zaphiropoulous, P. G., Gailani, M. R., Shanley, S., Chidambaram, A., et al. (1996). Mutations of the human homolog of Drosophila patched in the nevoid basal cell carcinoma syndrome. *Cell* 85, 841–851. doi: 10.1016/S0092-8674(00)81268-4

Incardona, J. P., Gaffield, W., Kapur, R. P., and Roelink, H. (1998). The teratogenic veratrum alkaloid cyclopamine inhibits Sonic hedgehog signal transduction. *Development* 125, 3553–3562.

Infante, P., Alfonsi, R., Ingallina, C., Quaglio, D., Ghirga, F., D'Acquarica, I., et al. (2016). Inhibition of Hedgehog-dependent tumors and cancer stem cells by a newly identified naturally occurring chemotype. *Cell Death Dis.* 7:e2376. doi: 10.1038/cddis.2016.195

Jalili, A., Mertz, K. D., Romanov, J., Wagner, C., Kalthoff, F., Stuetz, A., et al. (2013). NVP-LDE225, a potent and selective SMOOTHENED antagonist reduces melanoma growth in vitro and in vivo. *PLoS One* 8:e69064. doi: 10.1371/journal.pone.0069064

Jiang, J., and Hui, C. C. (2008). Hedgehog signaling in development and cancer. *Dev. Cell* 15, 801–812. doi: 10.1016/j.devcel.2008.11.010

Kool, M., Korshunov, A., Remke, M., Jones, D. T., Schlanstein, M., Northcott, P. A., et al. (2012). Molecular subgroups of medulloblastoma: an international meta-analysis of transcriptome, genetic aberrations, and clinical data of WNT, SHH, Group 3, and Group 4 medulloblastomas. *Acta Neuropathol.* 123, 473–484. doi: 10.1007/s00401-012-0958-8

Kool, M., Koster, J., Bunt, J., Hasselt, N. E., Lakeman, A., van Sluis, P., et al. (2008). Integrated genomics identifies five medulloblastoma subtypes with distinct genetic profiles, pathway signatures and clinicopathological features. *PLoS One* 3:e3088. doi: 10.1371/journal.pone.0003088

Korshunov, A., Remke, M., Kool, M., Hielscher, T., Northcott, P. A., Williamson, D., et al. (2012). Biological and clinical heterogeneity of MYCN-amplified medulloblastoma. *Acta Neuropathol.* 123, 515–527. doi: 10.1007/s00401-011-0918-8

Kumar, V., Chaudhary, A. K., Dong, Y., Zhong, H. A., Mondal, G., Lin, F., et al. (2017). Design, synthesis and biological evaluation of novel hedgehog inhibitors for treating pancreatic cancer. *Sci. Rep.* 7:1665. doi: 10.1038/s41598-017-01942-7

Miyazaki, Y., Matsubara, S., Ding, Q., Tsukasa, K., Yoshimitsu, M., Kosai, K., et al. (2016). Efficient elimination of pancreatic cancer stem cells by hedgehog/GLI inhibitor GANT61 in combination with mTOR inhibition. *Mol. Cancer* 15:49. doi: 10.1186/s12943-016-0534-2

Organisation for Economic Co-operation Development [OECD] (2008). *Guideline 425: Acute Oral Toxicity-Up and Down Procedure*. Available at: https://www.oecd-ilibrary.org/environment/test-no-425-acute-oral-toxicity-up-and-down-procedure_9789264071049-en

Pan, S., Wu, X., Jiang, J., Gao, W., Wan, Y., Cheng, D., et al. (2010). Discovery of NVP-LDE225, a potent and selective smoothened antagonist. *ACS Med. Chem. Lett.* 1, 130–134. doi: 10.1021/ml1000307

Park, K. S., Martelotto, L. G., Peifer, M., Sos, M. L., Karnezis, A. N., Mahjoub, M. R., et al. (2011). A crucial requirement for Hedgehog signaling in small cell lung cancer. *Nat. Med.* 17, 1504–1508. doi: 10.1038/nm.2473

Peukert, S., He, F., Dai, M., Zhang, R., Sun, Y., Miller-Moslin, K., et al. (2013). Discovery of NVP-LEQ506, a second-generation inhibitor of smoothened. *ChemMedChem.* 8, 1261–1265. doi: 10.1002/cmdc.201300217

Pomeroy, S. L., Tamayo, P., Gaasenbeek, M., Sturla, L. M., Angelo, M., McLaughlin, M. E., et al. (2002). Prediction of central nervous system embryonal tumour outcome based on gene expression. *Nature* 415, 436–442. doi: 10.1038/415436a

Rajurkar, M., De Jesus-Monge, W. E., Driscoll, D. R., Appleman, V. A., Huang, H., Cotton, J. L., et al. (2012). The activity of Gli transcription factors is essential for Kras-induced pancreatic tumorigenesis. *Proc. Natl. Acad. Sci. U.S.A.* 109, E1038–E1047. doi: 10.1073/pnas.1114168109

Rimkus, T. K., Carpenter, R. L., Qasem, S., Chan, M., and Lo, H. W. (2016). Targeting the sonic hedgehog signaling pathway: review of smoothened and GLI inhibitors. *Cancers* 8:E22. doi: 10.3390/cancers8020022

Riobo, N. A., Lu, K., Ai, X. B., Haines, G. M., and Emerson, C. P. (2006). Phosphoinositide 3-kinase and Akt are essential for Sonic Hedgehog signaling. *Proc. Natl. Acad. Sci. U.S.A.* 103, 4505–4510. doi: 10.1073/pnas.0504337103

Robarge, K. D., Brunton, S. A., Castanedo, G. M., Cui, Y., Dina, M. S., Goldsmith, R., et al. (2009). GDC-0449-a potent inhibitor of the hedgehog pathway. *Bioorg. Med. Chem. Lett.* 19, 5576–5581. doi: 10.1016/j.bmcl.2009.08.049

Romer, J. T., Kimura, H., Magdaleno, S., Sasai, K., Fuller, C., Baines, H., et al. (2004). Suppression of the Shh pathway using a small molecule inhibitor eliminates medulloblastoma in Ptc1(+/−)p53(−/−) mice. *Cancer Cell* 6, 229–240. doi: 10.1016/j.ccr.2004.08.019

Roudaut, H., Traiffort, E., Gorojankina, T., Vincent, L., Faure, H., Schoenfelder, A., et al. (2011). Identification and mechanism of action of the acylguanidine MRT-83, a novel potent Smoothened antagonist. *Mol. Pharmacol.* 79, 453–460. doi: 10.1124/mol.110.069708

Ruiz, I., and Altaba, A. (1997). Catching a Gli-mpse of Hedgehog. *Cell* 90, 193–196. doi: 10.1016/S0092-8674(00)80325-6

Scales, S. J., and de Sauvage, F. J. (2009). Mechanisms of Hedgehog pathway activation in cancer and implications for therapy. *Trends Pharmacol. Sci.* 30, 303–312. doi: 10.1016/j.tips.2009.03.007

Schaefer, G. I., Perez, J. R., Duvall, J. R., Stanton, B. Z., Shamji, A. F., and Schreiber, S. L. (2013). Discovery of small-molecule modulators of the sonic hedgehog pathway. *J. Am. Chem. Soc.* 135, 9675–9680. doi: 10.1021/ja400034k

Sharpe, H. J., Wang, W., Hannoush, R. N., and de Sauvage, F. J. (2015). Regulation of the oncoprotein Smoothened by small molecules. *Nat. Chem. Biol.* 11, 246–255. doi: 10.1038/nchembio.1776

Solinas, A., Faure, H., Roudaut, H., Traiffort, E., Schoenfelder, A., Mann, A., et al. (2012). Acylthiourea, acylurea, and acylguanidine derivatives with potent hedgehog inhibiting activity. *J. Med. Chem.* 55, 1559–1571. doi: 10.1021/jm2013369

Song, L., Wang, W., Liu, D., Zhao, Y., He, J., Wang, X., et al. (2016). Targeting of sonic hedgehog-Gli signaling: a potential therapeutic target for patients with breast cancer. *Oncol. Lett.* 12, 1027–1033. doi: 10.3892/ol.2016.4722

Stecca, B., and Ruiz, I. A. A. (2010). Context-dependent regulation of the GLI code in cancer by Hedgehog and non-Hedgehog signals. *J. Mol. Cell Biol.* 2, 84–95. doi: 10.1093/jmcb/mjp052

Tan, I. L., Wojcinski, A., Rallapalli, H., Lao, Z., Sanghrajka, R. M., Stephen, D., et al. (2018). Lateral cerebellum is preferentially sensitive to high sonic hedgehog signaling and medulloblastoma formation. *Proc. Natl. Acad. Sci. U.S.A* 115, 3392–3397. doi: 10.1073/pnas.1717815115

Tang, C. T., Lin, X. L., Wu, S., Liang, Q., Yang, L., Gao, Y. J., et al. (2018). NOX4-driven ROS formation regulates proliferation and apoptosis of gastric cancer cells through the GLI1 pathway. *Cell Signal.* 46, 52–63. doi: 10.1016/j.cellsig.2018.02.007

Taylor, M. D., Northcott, P. A., Korshunov, A., Remke, M., Cho, Y. J., Clifford, S. C., et al. (2012). Molecular subgroups of medulloblastoma: the current consensus. *Acta Neuropathol.* 123, 465–472. doi: 10.1007/s00401-011-0922-z

Tremblay, M. R., Lescarbeau, A., Grogan, M. J., Tan, E., Lin, G., Austad, B. C., et al. (2009). Discovery of a potent and orally active hedgehog pathway antagonist (IPI-926). *J. Med. Chem.* 52, 4400–4418. doi: 10.1021/jm900305z

Wang, Y., Ding, Q., Yen, C. J., Xia, W., Izzo, J. G., Lang, J. Y., et al. (2012). The crosstalk of mTOR/S6K1 and Hedgehog pathways. *Cancer Cell* 21, 374–387. doi: 10.1016/j.ccr.2011.12.028

Wetmore, C., Eberhart, D. E., and Curran, T. (2001). Loss of p53 but not ARF accelerates medulloblastoma in mice heterozygous for patched. *Cancer Res.* 61, 513–516.

Xin, M., Zhang, L., Tang, F., Tu, C., Wen, J., Zhao, X., et al. (2014). Design, synthesis, and evaluation of pyrrolo[2,1-f][1,2,4]triazine derivatives as novel hedgehog signaling pathway inhibitors. *Bioorg. Med. Chem.* 22, 1429–1440. doi: 10.1016/j.bmc.2013.12.055

Yauch, R. L., Dijkgraaf, G. J., Alicke, B., Januario, T., Ahn, C. P., Holcomb, T., et al. (2009). Smoothened mutation confers resistance to a Hedgehog pathway inhibitor in medulloblastoma. *Science* 326, 572–574. doi: 10.1126/science.1179386

Zhang, X., Zhao, F., Wu, Y., Yang, J., Han, G. W., Zhao, S., et al. (2017). Crystal structure of a multi-domain human smoothened receptor in complex with a super stabilizing ligand. *Nat. Commun.* 8:15383. doi: 10.1038/ncomms15383

Zhu, J. Y., Yang, X., Chen, Y., Jiang, Y., Wang, S. J., Li, Y., et al. (2017). Curcumin suppresses lung cancer stem cells via inhibiting wnt/beta-catenin and sonic hedgehog pathways. *Phytother. Res.* 31, 680–688. doi: 10.1002/ptr.5791

Conflict of Interest Statement: The authors declare that the research was conducted in the absence of any commercial or financial relationships that could be construed as a potential conflict of interest.

frontiers in Pharmacology

ORIGINAL RESEARCH
published: 02 April 2019
doi: 10.3389/fphar.2019.00330

Alkylaminophenol Induces G1/S Phase Cell Cycle Arrest in Glioblastoma Cells Through p53 and Cyclin-Dependent Kinase Signaling Pathway

*Phuong Doan[1,2], Aliyu Musa[2,3], Nuno R. Candeias[4], Frank Emmert-Streib[2,3], Olli Yli-Harja[2,5,6] and Meenakshisundaram Kandhavelu[1,2]**

[1] Molecular Signaling Lab, Faculty of Medicine and Health Technology, Tampere University and BioMediTech, Tampere, Finland, [2] Institute of Biosciences and Medical Technology, Tampere, Finland, [3] Predictive Medicine and Data Analytics Lab, Faculty of Medicine and Health Technology, Tampere University and BioMediTech, Tampere, Finland, [4] Faculty of Engineering and Natural Sciences, Tampere University, Tampere, Finland, [5] Computaional Systems Biology Group, Faculty of Medicine and Health Technology, Tampere University and BioMediTech, Tampere, Finland, [6] Institute for Systems Biology, Seattle, WA, United States

OPEN ACCESS

Edited by:
Carmen Alvarez-Lorenzo, University of Santiago de Compostela, Spain

Reviewed by:
Wei-jiang Zhao, Shantou University Medical College, China
Joseph Louis Lasky, Cure 4 The Kids, United States

***Correspondence:**
Meenakshisundaram Kandhavelu
meenakshisundaram.kandhavelu@tuni.fi

Specialty section:
This article was submitted to Pharmacology of Anti-Cancer Drugs, a section of the journal Frontiers in Pharmacology

Received: 19 August 2018
Accepted: 19 March 2019
Published: 02 April 2019

Citation:
Doan P, Musa A, Candeias NR, Emmert-Streib F, Yli-Harja O and Kandhavelu M (2019) Alkylaminophenol Induces G1/S Phase Cell Cycle Arrest in Glioblastoma Cells Through p53 and Cyclin-Dependent Kinase Signaling Pathway. Front. Pharmacol. 10:330. doi: 10.3389/fphar.2019.00330

Glioblastoma (GBM) is the most common type of malignant brain tumor in adults. We show here that small molecule 2-[(3,4-dihydroquinolin-1(2H)-yl)(p-tolyl)methyl]phenol (THTMP), a potential anticancer agent, increases the human glioblastoma cell death. Its mechanism of action and the interaction of selective signaling pathways remain elusive. Three structurally related phenolic compounds were tested in multiple glioma cell lines in which the potential activity of the compound, THTMP, was further validated and characterized. Upon prolonged exposer to THTMP, all glioma cell lines undergo p53 and cyclin-dependent kinase mediated cell death with the IC_{50} concentration of 26.5 and 75.4 μM in LN229 and Snb19, respectively. We found that THTMP strongly inhibited cell growth in a dose and in time dependent manner. THTMP treatment led to G1/S cell cycle arrest and apoptosis induction of glioma cell lines. Furthermore, we identified 3,714 genes with significant changes at the transcriptional level in response to THTMP. Further, a transcriptional analysis (RNA-seq) revealed that THTMP targeted the p53 signaling pathway specific genes causing DNA damage and cell cycle arrest at G1/S phase explained by the decrease of cyclin-dependent kinase 1, cyclin A2, cyclin E1 and E2 in glioma cells. Consistently, THTMP induced the apoptosis by regulating the expression of Bcl-2 family genes and reactive oxygen species while it also changed the expression of several anti-apoptotic genes. These observations suggest that THTMP exerts proliferation activity inhibition and pro-apoptosis effects in glioma through affecting cell cycle arrest and intrinsic apoptosis signaling. Importantly, THTMP has more potential at inhibiting GBM cell proliferation compared to TMZ, the current chemotherapy treatment administered to GBM patients; thus, we propose that THTMP may be an alternative therapeutic option for glioblastoma.

Keywords: phenol, anticancer, cytotoxicity, apoptosis induction, gene expression, cell cycle

INTRODUCTION

Glioblastoma (GBM) is known as the most aggressive primary brain tumor. Although different treatments have been combined such as surgical operation, chemotherapy, or radiotherapy, no standard treatment has been proven to be effective for treating brain tumor. It is noted that patients with glioblastoma have an average survival of 12–15 months. For chemotherapy, temozolomide (TMZ) is one of the drugs accepted to be used in combination with radiotherapy to treat brain tumor (Stupp et al., 2005). However, some limitations related to use of TMZ such as the over expression of O6-methylguanine-DNA methyltransferase (MGMT) and/or lacking of a DNA repair pathway in GBM cells (Hegi et al., 2005) still need to be addressed; therefore, effective recurrence needs to be explored further.

A comprehensive understanding of the response of glioblastomas to chemotherapy and detailed chemotherapy resistance analysis of gliomas may help to identify effective agents for the treatment of this disease. Currently, many chemical compounds including sorafenib (Yang et al., 2010), bevacizumab (Friedman et al., 2009), and kaempferol (Sharma et al., 2007) have been studied for anti-glioma ability, especially for inducing GBM growth arrest and apoptosis. In the past few decades, many efforts have been made in understanding chemotherapy-induced DNA damage response (DDR) such as activation of checkpoint, repair and cell death pathways. It is reported that GBM responds to DNA damage induced by genotoxic drugs by activating DNA repair machinery (Erasimus et al., 2016). Thereby, improving chemotherapy response should be made to address this issue. Beside the DNA damage, targeting cell cycle arrest and apoptosis also grasped the attention for GBM treatment. In glioma cells, several key regulatory elements of cell cycle and apoptosis alter the expression of cyclin-dependent kinases such as Bcl-2 protein family, p53 protein, inhibitor of apoptosis proteins (IAPs) or receptor tyrosine kinases like the epidermal growth factor receptor (EGFR) and their down-stream signaling cascade. Among these signaling pathways, p53 plays an essential role in cellular responses to DNA damage and regulation of cell cycle and apoptosis. It is well known that p53 functions as a transcription factor for genes relevant for the regulation of the cell cycle (e.g., p21) or apoptosis (e.g., BAX, BAK, PUMA, Bcl-2). Furthermore, p53 may also promote apoptosis through transcription-independent mechanisms and direct interactions with members of the Bcl-2 family of proteins in the cytosol or mitochondria.

In the past decades, many advances have been made in understanding the ability of phenolic compounds in acting as effective chemopreventive agents especially throughout the properties of inducing cell cycle arrest and apoptosis in tumor cells (Wu et al., 2009). Several mechanisms were studied explaining the effectiveness of these compounds as chemopreventive agents for cancer treatment. These compounds can suppress the overexpression of pro-oxidant enzymes implicated in the development of cancer. They are also able to inhibit the transcriptional factor activation, thus regulating target genes correlated with cell survival, apoptosis and proliferation (Wcislo et al., 2013). For instance, polyphenols have the ability to modulate various targets of apoptosis pathways including the expression of regulatory proteins, cytochrome *c,* activation of caspase 9 and caspase 3 (Selvendiran et al., 2006), increase of caspases-8 and t-Bid levels (Selvendiran et al., 2006), increase of Bax and Bak expression (Selvendiran et al., 2006), down-regulation of Bcl-2 and Bcl-XL expression, and modulation of transcription factor NF-κB (Gong et al., 2003). In addition, a study of resveratrol, a natural phenol, revealed the ability to prevent or delay the onset of several types of cancers because they can regulate multiple cellular processes associated with carcinogenesis. In detail, this compound can inhibit cell proliferation and induce apoptosis by dysregulating cell cycle (Gali-Muhtasib et al., 2015), increasing caspase activity (Kim et al., 2003), and decreasing Bcl-2 and Bcl-XL levels.

Alkylaminophenols, being Mannich bases, are a particular kind of phenols (Roman, 2015). Although reported as precursors of quinone methides (Weinert et al., 2006), which can react with biomacromolecules (Thompson et al., 1993), alkylaminophenol moiety is also found in some FDA-approved drugs namely, amodiaquine, used for malaria treatment (Olliaro et al., 1996) and in topotecan, a topoisomerase inhibitor chemotherapeutic agent (Pommier, 2006). Previously, we reported the potential anticancer activity as apoptosis inducer of several alkylaminophenols on osteosarcoma cells, namely: *N*-[2-hydroxy-5-nitrophenyl(4′-methylphenyl)methyl]indoline (HNPMI) (Doan et al., 2016), 2-[(1,2,3,4-tetrahydroquinolin-1-yl)(4-methoxyphenyl)methyl]phenol (THMPP) (Karjalainen et al., 2017) and 2-[(3,4-dihydroquinolin-1(2H)-yl)(p-tolyl)methyl]phenol (THTMP) (Neto et al., 2016). To our knowledge, the anticancer activity of various phenolic derivatives have been evaluated on several human cancer cell lines but the effect as well as the in depth mechanism of phenols on brain cancer are not well investigated. Motivated by the numerous reports on the anticancer properties of phenolic compounds and our previous studies on alkylaminophenols, we recently examine the effect of HNPMI, THMPP, and THTMP on multiple glioblastoma cell lines (1321N1, LN229, and Snb19). Several *in vitro* preclinical assays were performed to indicate the cytotoxicity of this derivative on GBM. Specifically, the ability to kill GBM cells.

In spite of the multiple mechanisms have been proposed for chemotherapeutic resistance in glioblastoma cells, the analysis of molecular signaling events is still not comprehensive. To date, advances in high-throughput sequencing methodology have provided a large amount of information regarding gene expression at the transcriptome level, as well as the underlying molecular events in response to chemotherapeutic drugs. Hence, the RNA-seq technique was used in this work to investigate alkylaminophenol -responsive genes in GBM cells. Here, we compared the gene expression profile of GMB cells between an alkylaminophenol and temozolomide. After determining the gene expression profile, we focused on the cell cycle arrest and the apoptosis pathway activated by our alkylaminophenol and investigated the significant of cell cycle genes as well as pro-apoptosis and anti-apoptosis genes in gliomas chemotherapeutic resistance. The cell cycle arrest was then validated by FUCCI biosensor and the apoptosis induction validation was performed

using Annexin V and PI double staining. Moreover, ROS production and caspase 3/7 activation measurements were conducted to reconfirm the involvement of apoptosis pathway when the GBM cells were treated with phenolic derivatives.

MATERIALS AND METHODS

GBM Cell Lines and Chemical Preparation

1321N1 is a human astrocytoma cell line isolated as a sub clone of the cell line 1181N1 which in turn was isolated from the parent line U-118 MG (one of a number of cell lines derived from malignant gliomas). LN229 cell line was taken from a patient with right frontal parieto-occipital glioblastoma. The cells exhibit mutated p53 (TP53) and possible homozygous deletions in the p16 and p14ARF tumor suppressor genes. Snb19 is a malignant glioblastoma cell line initiated from the surgical resection of a left parietooccipital glioblastoma multiforme tumor. This line has been shown by DNA profiling studies to be a derivative of the U-373 cell line.

Synthesis and spectral characterization of compounds HNPMI (18), THMPP (19), and THTMP (20) were previously reported. These compounds and TMZ (Sigma-Aldrich, United States) were dissolved in dimethyl sulphoxide (DMSO, Sigma-Aldrich, St. Louis, MO, United States) to obtain a stock of 100 mM, from which, intermediate dilutions were prepared. The final concentrations used were 100, 75, 50, 25, and 10 μM, in the culture medium.

Cell Culture

The human glioma cell lines Snb19, LN229, and mouse embryonal fibroblast (MEF) cell lines were cultured in Dulbecco's Modified Eagle Medium (DMEM) supplemented with 10% FBS, 0.1 mg/ml Streptomycin, 100 U/ml Penicillin, and 0.025 mg/ml Amphotericin B. For 1321N1 cell line, the culture medium was prepared as previously but it was supplemented with 2 mM sodium pyruvate. HEK293T cells were cultured in DMEM supplemented with 10% FBS, 0.1 mg/ml Streptomycin, 100 U/ml Penicillin, 2 mM sodium pyruvate, and 0.025 mg/ml Amphotericin B. The culture was maintained at 37°C in a humidified atmosphere containing 5% CO2. All of the components for cell culture were purchased from Sigma-Aldrich, St. Louis, MO, United States.

In vitro Cytotoxicity Assay

Cytotoxicity assay was performed to evaluate cell growth inhibition of the three compounds HNPMI, THMPP, and THTMP at 100 μM concentration on three glioblastoma cell lines (1321N1, Snb19, and LN229). Cells were seeded with an initial density of 1×10^5 cells/well in 12-well plates containing appropriate medium for each cell line. When the cells reach 60–70% of confluence, the cells were then treated with the three compounds at 100 μM and incubated for 24 h at culture conditions. Treated cells were collected using centrifugation at 3000 rpm for 10 min. Number of live and dead cells were determined using trypan blue solution and Countess II FL Automated Cell Counter (Thermo Fisher Scientific). Inhibition percentage was calculated using the formula (1). In this experiment, biological and technical replicates were conducted for each condition. Temozolomide (TMZ, Sigma-Aldrich, St. Louis, MO, United States) and DMSO 2% were used as positive and negative control, respectively.

$$\text{Inhibition (\%)} = \frac{\text{Mean No. of untreated cells (DMSO control)} - \text{Mean No. of treated cells}}{\text{Mean No. of untreated cells (DMSO control)}} \times 100 \quad (1)$$

The cytotoxicity of the top compound was evaluated on multiple GBM cell lines, 1321N1, LN229, Snb19, and HEK293T (immortal cells) human embryonic kidney and normal brain cells MEF. Ten micromolar concentration of the top compound was used to treat the cells followed by trypan blue exclusion assay to quantify the percentage of live and dead cells. The inhibition percentage was calculated as described above.

Inhibitory Kinetic Study

The inhibitory kinetic study was performed for 24 h exposure time using different concentrations 100, 75, 50, 25, 10 μM of the top compound on 1321N1, Snb19, and LN229 cells. After treatment, the cells were collected as described in the cytotoxicity assay. The positive control TMZ was also utilized. After that the dose-response curves were plotted. Half maximal inhibitory concentration (IC_{50}) was calculated based on the curves fit. The two cell lines with best IC_{50} were selected for further time-dependent study. In this study, the cells were treated with IC_{50} concentration of the top compound and incubated for 48 and 72 h. The time-dependent graph was plotted.

Illumina Sequencing and Bioinformatics Analysis

To perform the RNA-seq, RNA of samples had to be isolated. LN229 and Snb19 cells were seeded into 6 well-plate and incubated overnight. The cells were treated with THTMP and TMZ for 24 h at IC_{50} concentration. The total RNA of the cells were isolated using GeneJET RNA Purification Kit (Thermo Fisher Scientific) following the manufacture's instructions. Then, the total RNA of 18 samples of LN229 and Snb19 cells (including triplicates of THTMP treated, TMZ treated and untreated samples) were sent to whole transcriptome sequencing by Biomedicum Functional Genomics Unit (FuGU, University of Helsinki, Finland) using Illumina NextSeq 500. The sequencing produced data in bcl format which was converted into FASTQ file format.

RNASeq Data Analysis Pipeline

FastQC (Andrews, 2010) (version 0.11.2) was used for quality control to ensure that the quality value was above Q30. The Human (homo sapiens) genome FASTA file[1] and gene annotation

[1] ftp://ftp.ensembl.org/pub/release-92/fasta/homo_sapiens/dna/

GTF file (Homo sapiens human release 92[2]) were obtained from Ensembl. Although RNA-seq is a popular research tool, there is no gold standard for analyzing RNA-seq data. Among the available tools, we chose up-to-date open source tools for mapping, retrieving read counts, and differential expression analysis. We used STAR (Dobin et al., 2013) (version 2.6) to generate indexes and to map reads to the human genome. For assembly, we chose SAMtools (Li et al., 2009) (version 1.2) and the "union" mode of HTSeq (Anders et al., 2014) (version 0.9.1), as the gene-level read counts could provide more flexibility in the differential expression analysis. Both STAR and HTSeq analyses were conducted using the high-performance research computing resources provided by TUT TCSC Merope computing cluster[3] in the Linux operating system (version 2.6.32). Differential expression (DE) and statistical analysis were performed using DESeq2 (Love et al., 2014) (release 3.3) in R (version 3.2.4). DESeq2 was chosen as a leading statistical method[4]. DESeq2 internally corrects for library size, so it is important to provide un-normalized raw read counts as input. We used variance stabilizing transformation to account for differences in sequencing depth. *P*-values were adjusted for multiple testing using the Benjamini-Hochberg procedure (Benjamini and Hochberg, 1995). A false discovery rate adjusted *p*-value (i.e., *q*-value) <0.05 was set for the selection of DE genes.

Gene Ontology (GO) and Pathway Analysis

Gene ontology (Ashburner et al., 2000) and KEGG pathway (Kanehisa and Goto, 2000) analyses were performed with the PANTHER over-representation Test (released on Feb 03, 2018) in PANTHER version 13.1[5] (Mi et al., 2009; Emmert-Streib and Glazko, 2011). This program supports the human genome. PANTHER uses a binomial test and a Bonferroni correction for multiple testing and displayes *z*-scores to indicate whether a potential regulator is activated or inhibited. We used the default settings for statistical analysis in both the PANTHER pathway and GO terms. In the analyses, only pathways and GO terms with *p*-value <0.05 and fold change of 1.5 were set as cutoff values.

Analysis of Cell Cycle Progression

The Snb19 and LN229 cells were cultured in 96-well plates with the initial density of 1×10^5 cells/well. Cells were incubated overnight with appropriate culture conditions. When the cell confluence reached 60%, they were treated with the IC_{50} concentration of the top compound for 8 h. Then Premo FUCCI Cell Cycle Sensor *BacMam 2.0* (Thermo Fisher Scientific) was added into each well and incubated for 16 h following the manufacture's protocol. The cells were then captured using confocal microscope. The analysis of images was done based on different fluorescent colors of the cells in which red fluorescent cells were the cells in G1 phase, green fluorescent cells means the cells in S, G2, M phase and the overlaid red and green fluorescent cells are the cells in G1/S phase (Zielke and Edgar, 2015).

Annexin V-FITC/PI Apoptotic Assay

To determine the apoptosis and/or necrosis of the top compound on Snb19 and LN229 cell lines, the Dead Cell Apoptosis Kit with Annexin V FITC and PI (Thermo Fisher Scientific) was used. The apoptosis determination was performed followed by the standard protocol from the manufacture. Briefly, the cells were cultured in 6 well-plate with the initial density of 5×10^5 cells/well. The cells were treated with IC_{50} concentration of the top compound, TMZ and negative control (DMSO) were harvested and washed in cold PBS. The cell pellets were then resuspended in 1× annexin-binding buffer provided in the kit. Then, 5 μL of FITC conjugated Annexin V and 1 μL of the 100 μg/mL PI working solutions were added to the 100 μL of cell suspension. The cells were incubated at room temperature for 15 min prior to the fluorescence measurements. The image acquisition was done by using EVOS imaging system (Thermo Fisher Scientific) with 20 × objective magnification.

Detection of Intracellular Reactive Oxygen Species

The Snb19 and LN229 cells were cultured in 12-well plates with the initial density of 1×10^5 cells/well. Cells were incubated overnight with appropriate culture conditions then treated with the IC_{50} concentration of the top compound and TMZ for 5 h. After that, cells were harvested by centrifugation at 3000 rpm for 10 min and transferred into 96-well plate. Cells were incubated with 2 μM 2′,7′-dichlorodihydrofluorescein diacetate (H2DCFDA), known as dichlorofluorescin diacetate (Sigma-Aldrich, St. Louis, MO, United States), for 30 min at cell culture conditions. The cells were then washed with pre-warm PBS and recovered in pre-warmed completed medium for 20 min prior the fluorescence measurement. Fluorescence intensity was measured using plate reader (Fluoroskan Ascent FL, Thermo Labsystems) at excitation 485 nm and emission 538 nm. DMSO and hydrogen peroxide 200 μM were used as the negative and positive controls. The fold increase in ROS production was calculated using the following formula (2).

$$\text{Fold increase} = \frac{F_{\text{test}} - F_{\text{blank}}}{F_{\text{control}} - F_{\text{blank}}} \quad (2)$$

Where: F_{test} is the fluorescence readings from the treated wells, $F_{control}$ is the fluorescence readings from the untreated wells, and F_{blank} is the fluorescence readings from the unstained wells.

Caspases 3/7 Activities Assay

Snb19 and LN229 cells were seeded on 96 well-plates at the initial density of 1×10^4 cells/well with appropriate medium. After culturing for 24 h, cells were treated with TMZ and the top compound at IC_{50} concentration for 5 h. Determination of caspase activity was performed using Caspase-Glo 3/7 Assay kit (Promega, Madison United States) followed by the standard protocol from the manufacture. Briefly, the plate containing cells were removed from incubator and allowed to equilibrate to room

[2] ftp://ftp.ensembl.org/pub/release-92/gtf/homo_sapiens

[3] https://wiki.eduuni.fi/display/tutsgn/TUT+Narvi+Cluster

[4] https://bioconductor.org/packages/release/bioc/vignettes/DESeq2/inst/doc/DESeq2.html

[5] http://www.pantherdb.org/, released on October 24, 2016

temperature for 30 min. An amount of 100 μl of Caspase-Glo reagent was added to the plate containing 100 μl of treated cell, untreated cell, blank or TMZ. After that, content of wells was gently mixed using a plate shaker at 300–500 rpm for 30 s. The plate was incubated for further 1 h before measuring the luminescence using a plate-reading luminometer (Fluoroskan Ascent FL, Thermo Labsystems). The fold increase in caspase 3/7 was calculated using formula (2) as described in ROS assay.

Statistical Analysis

All of the experiments were conducted with three biological repeats and technical repeats. The data was analyzed using SPSS 20.0. For comparison between the tested groups, statistical significant differences were evaluated with the *t*-test using a threshold of $P < 0.001$ and $P < 0.05$. For comparison of more than two groups, statistical significance was determined with a one-way ANOVA test with the level of significance at $p < 0.05$.

RESULTS

Characterization of Human Glioma Cells Treated With Alkylaminophenols

Three GBM cell lines were treated with 100 μM HNPMI, THMPP, and THTMP (**Figure 1A**). After 24 h of treatment, the cells lost the proliferative activity with dramatic changes in morphology, losing attachment property and incrementing granularity (**Figure 1B**). Delightfully, THTMP strongly inhibited the growth of GBM cells 1321N1, LN229, and Snb19 (**Figure 1C**). At 100 μM, THTMP was responsible for almost 100% cell death of 1321N1 and LN229 and approximately 80% cell death of Snb19. HNPMI also showed high cytotoxicity on LN229 and Snb19 with more than 80% cell death while it had little effect on 1321N1 with only 23% cell death. THMPP has the least cytotoxicity effect compared to THTMP and HNPMI (**Figure 1C**).

From the above results, it is concluded that THTMP is a potent inhibitor of GBM cell growth. Here, we also used an immortal cell line, HEK293T and a non-tumorous cell line, MEF to examine the effect of THTMP. In general, THTMP has higher cytotoxicity effect on GBM cells compared with immortal and non-tumorous cells. In which, approximately 3 to 12% cell death were found in different GBM cell lines whilst only 2 and 1% growth inhibition were observed in HEK293T and MEF cells, respectively (**Figure 1D**). Thus, this result suggests that THTMP has the selectivity on GBM cells and was hence selected for further studies.

The dose-dependent inhibitory effect of THTMP against GBM cells was studied at 10, 25, 50, 75 and 100 μM concentrations (**Figure 1E**). Among three cell lines, LN229 was the most affected by THTMP with an IC_{50} concentration of 26.5 ± 0.03 μM, followed by 1321N1 with an IC_{50} of 61.9 ± 0.65 μM and least inhibited cell line was Snb19 with an IC_{50} of 75.5 ± 2.18. Besides, TMZ showed better effect on Snb19 than LN229 while seemly no effect was observed in 1321N1. This is in an agreement with the previous findings (Lee, 2016).

Based on the results obtained for THTMP and TMZ in dose response curve, further studies were performed on LN229 and Snb19 to understand the compound action mode as anticancer drug. To observe the effect of THTMP over the hours on cell viability, LN229 and Snb19 cells were treated for 24, 48, and 72 h with IC_{50} concentration (**Figure 1F**). The result showed that there was a time-dependent effect on Snb19 from 24 to 72 h and on LN229 from 24 to 48 h. In details, the growth inhibition of Snb19 was increased from 32.2 to 36.5% and to 43.1% at 24, 48, and 72 h post-treatment, respectively. The growth inhibition of LN229 was increased from 29.4% at 24 h treatment to 33.4% at 48 h treatment and was decreased to 13.7% at 72 h treatment.

Global Change in Gene Expression in Response to Top Compound

Principal Component Analysis (PCA) and Hierarchical Clustering Analysis

We performed PCA at each sample to determine whether samples in each cell line group clustered with each other or other groups. First, we used HTSeq to count reads that uniquely aligned to one gene, and these data were then imported into DESeq2 to generate PCA plots (**Figure 2A**). Furthermore, PCA scree plots confirmed that principal components 1 (PC1) and 2 (PC2) accounted for 70–80% of the total variation in gene expression at each time point (**Figure 2B**). To further investigate the cell-type dependent nature of the DEGs, we performed hierarchical clustering of the top 100 DEGs (i.e., those with the smallest *q*-values identified in the cell line analysis in DESeq2). In agreement with the PCA plots, this analysis demonstrated clustering of almost all sample groups from each cell line forming two clusters (**Figure 2D**).

Differentially Expressed Genes (DEGs)

In average, 20,090 genes were mapped by at least one read in each of the two cell line samples. Overall, 7,299 DEGs with a *q*-value <0.05 and fold change >1.5 (LN229 1,550; Snb19 5,749) were detected over the two comparisons (C1: THTMP vs. Untreated; C2: THTMP vs. TMZ) in the cell type analysis of DESeq2 (**Supplementary Tables S1–S4**). The results of plot analysis of gene expression in two cell lines of the GBM after treatment are shown in **Figure 2C**. The numbers of differentially expressed genes with more than 1.5-fold change were higher in Snb19 than in LN229 (**Figure 3D**). Indeed, there were higher number of differentially expressed genes in these Snb19 cell line when compared with LN229 cell line as shown in **Figure 2C**. We applied the MA plot function in DESeq2 to visualize the top genes with the smallest *q*-values (**Figure 3A**). We investigated the similarity in differential gene expression profiles regulated LN229 and Snb19. The fold-changes in overlapped genes filtered by the *q*-value <0.05 were plotted for LN229 and Snb19 cell lines. Comparison of gene expression profiles showed correlations between LN229 and Snb19 cell lines ($R^2 > 0.10$, **Figure 3C** left in C1; $R^2 > 0.12$, **Figure 3C** right in C2). Venn diagrams indicated overlap in genes whose expression was regulated in the same direction (**Figure 3B**). We identified 3,714 DEGs between THTMP and untreated (negative control) samples among the cell lines (*q*-value <0.05) (**Supplementary Tables S1–S4** and **Figure 3B** top). In this comparison, Snb19 demonstrated the

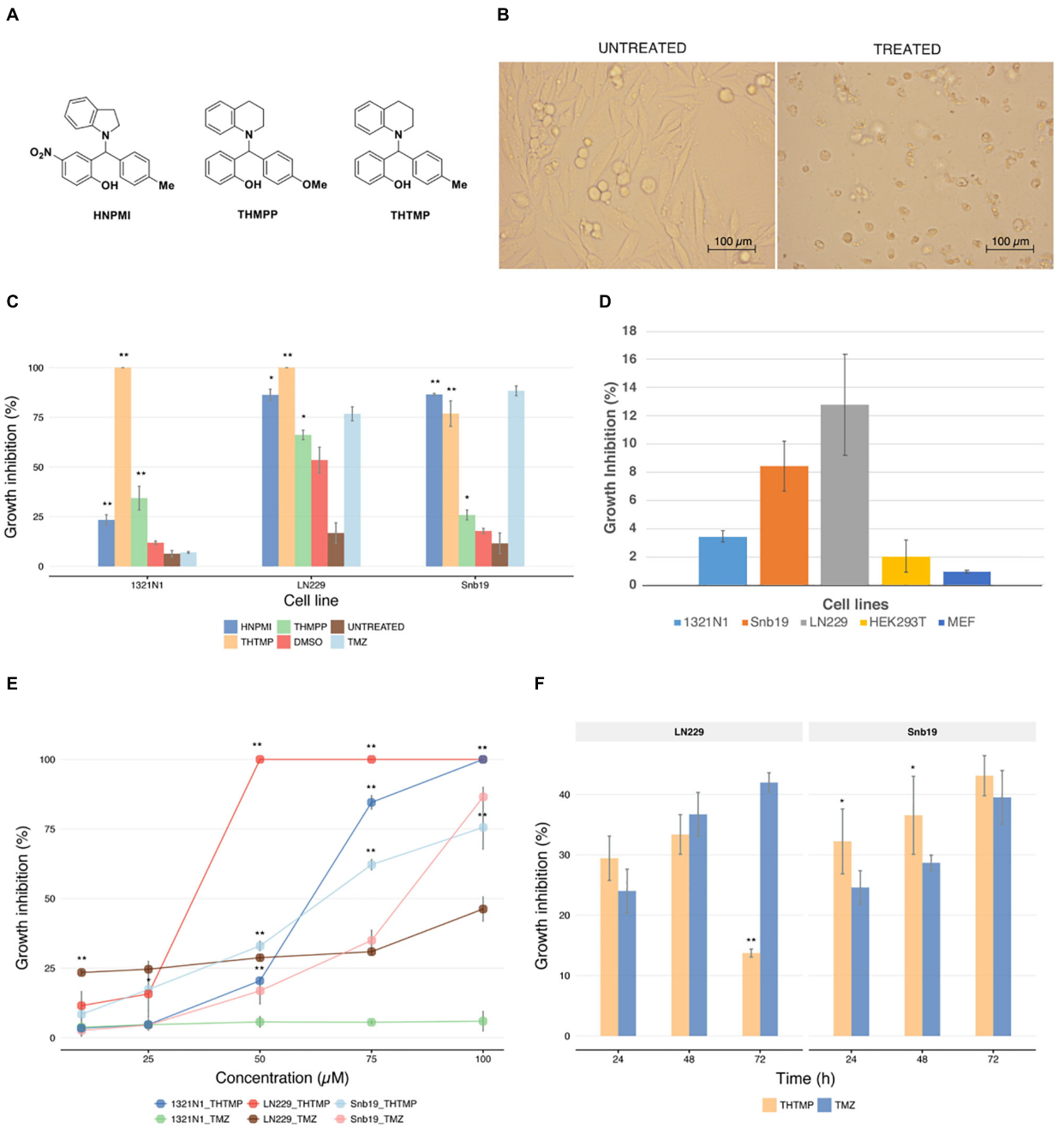

FIGURE 1 | Effect of alkylaminophenols characterized by cell growth arrest. **(A)** Molecular structure of three tested phenolic compounds (HNPMI, THMPP, and THTMP). **(B)** Demonstrated images of morphological changes in GBM cells at 24 h after treatment. **(C)** Cell growth inhibition was determined with trypan blue solution for compounds HNPMI, THMPP, THTMP, and TMZ against GBM cells (1321N1, LN229, and Snb19) at 100 μM concentration. **(D)** Growth inhibitory effect of THTMP on different cell lines 1321N1, LN229, and Snb19 and HEK293T cells at 10 and 100 μM at 24 h post-treatment. **(E)** Effect of THTMP and TMZ on GBM cell growth. Different concentrations including 10, 25, 50, 75, and 100 μM were utilized and incubated for 24 h. **(F)** Time-dependent effect of THTMP and TMZ on LN229 and Snb19 at 24, 48, and 72 h post-treatment at IC50 concentrations. All experiments were performed with three biological repeats and two technical repeats. $^{**}P < 0.001$, $^{*}P < 0.05$ compared to the TMZ.

most DEGs, with 321 of the 3,714 DEGs common to both LN229 and Snb19. We also compared the THTMP and TMZ samples as a positive control group, both individually and combined as a single "affected" group. In these comparisons, 3,585 number of DEGs were identified, with the largest number of DEGs identified in Snb19 cell line, and 289 out of 3,585 DEGs common in both cell lines (**Supplementary Tables S1–S4** and **Figure 3B** down).

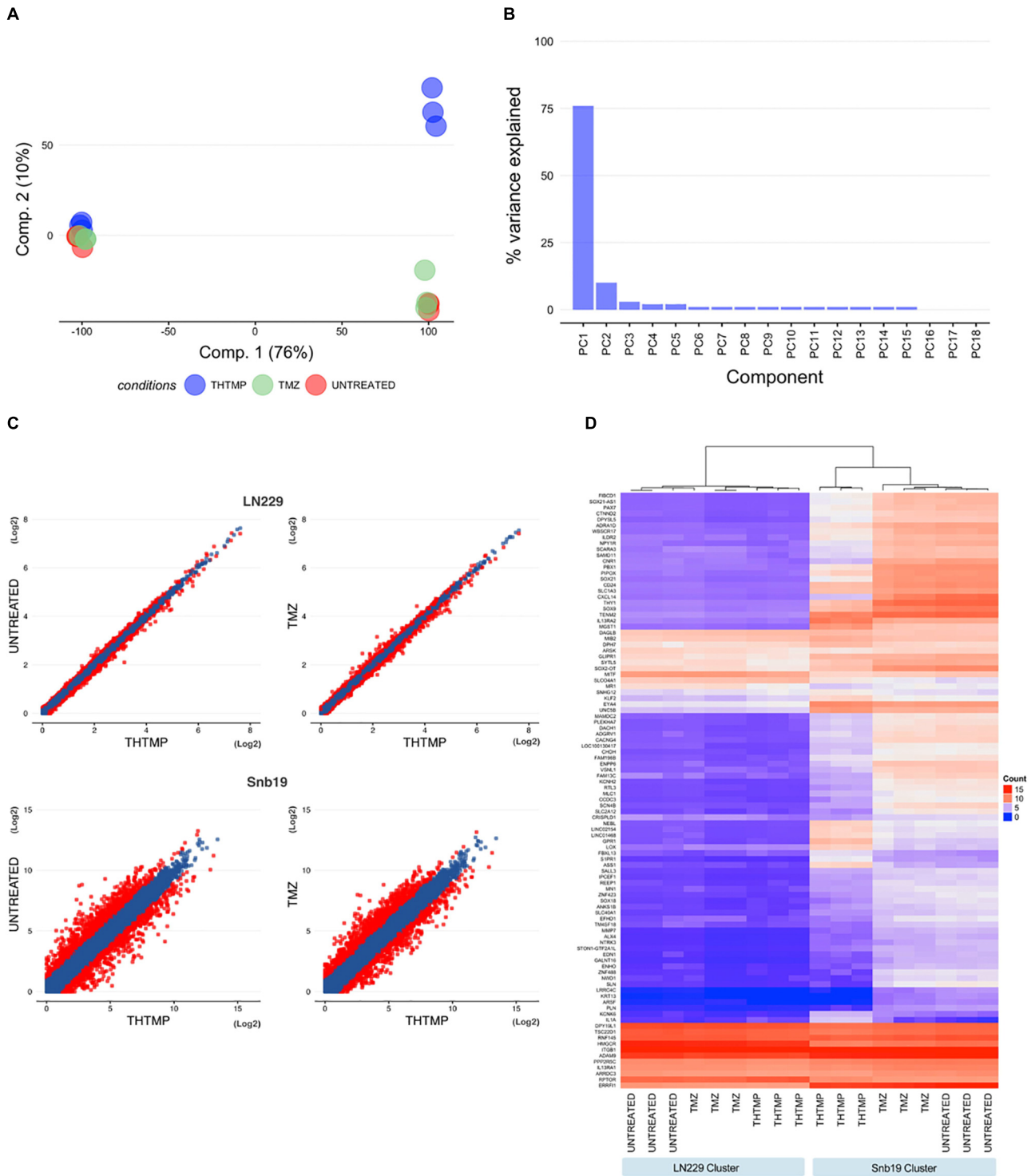

FIGURE 2 | Hierarchical clustering analysis, heatmap, and principal component analysis. **(A)** Principal component analysis (PCA) for all samples measured from LN229 and Snb19 cell lines. Principal component 1 (PC1) and principal component 2 (PC2) were identified by variance stabilizing transformation in DESeq2 on cell line samples. (Red, Untreated samples; Green, Temozolomide samples; Blue, THTMP samples). **(B)** The figure shows the percentage of variance that indicates how much variance was explained by PC1 and PC2. **(C)** Scatter plot analysis of gene expression using comparisons (THTMP vs. Untreated and THTMP vs. TMZ) in LN229 and Snb19 cell lines from the GMB. Genes whose expression levels changed by more than 1.5-fold after treatment are indicated in red. **(D)** Hierarchical clustering analysis and heatmap of the 100 genes with the smallest q-values in the time course analysis in DESeq2 (for Untreated, Temozolomide, and THTMP designate three replicate samples; negative, positive, and compound are individual cell lines in each group).

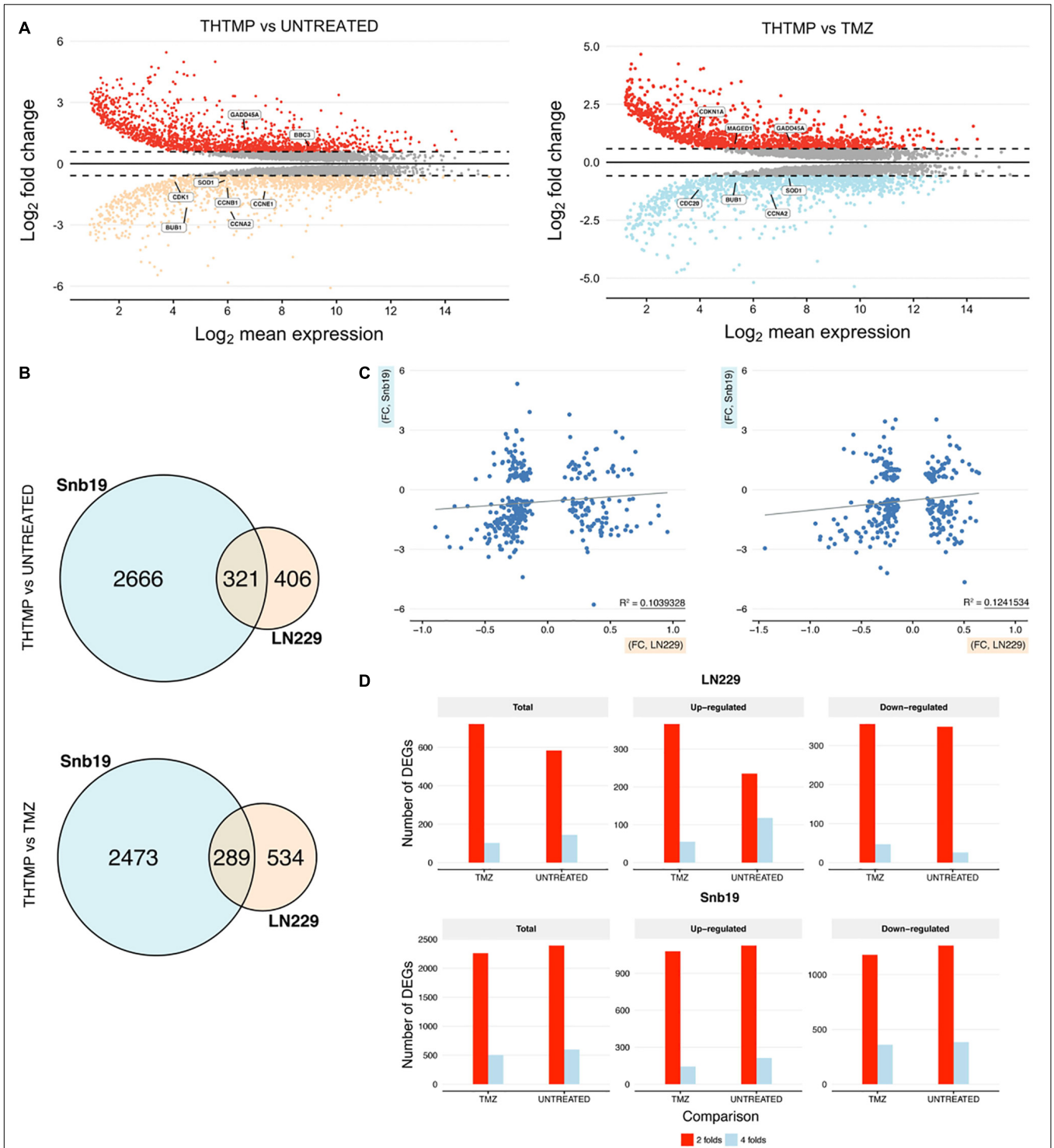

FIGURE 3 | DEGs comparisons on LN229 and Snb19 samples. **(A)** MA-plot from means and log fold changes. The figure shows differential gene expression from the two inter-group comparisons (THTMP vs. Untreated; THTMP vs. Temozolomide). For MA-plot construction, a gene was considered to be differentially expressed between groups at an absolute log2 fold change >1.5 or<-1.5 and a *q*-value of 0.05 (moderated *t*-test; Benjamini-Hochberg procedure). **(B)** Overlapping DEGs in LN229 and Snb19 samples compared with positive and negative control at C1 and C2. For each comparison, only genes with a *q*-value <0.05 were considered as DEGs. The number of DEGs found at each comparison are indicated. **(C)** Scatter plots of fold-changes in gene expression levels after treatment of C1 and C2. The R^2 value was calculated for genes with *t*-test *p*-values <0.1. **(D)** The total number and upregulated/downregulated number of DEGs of both cell lines after treatment.

A substantial overlap of DEGs was present when comparing LN229 and Snb19 samples with the control group at C1 and C2. The overlapping DEGs between the cell line were higher at C1 (3,714 DEGs) than at C2 (3,585 DEGs), supporting the two groups behave similarly at the end-stage of the treatment, as expected based on **Figure 3B**. Both cell lines shared appreciable proportions of gene expression profiles (21.23% of genes in LN229; 78.76% of genes in Snb19). The complete lists of DEGs from the cell line analysis and all pairs of comparisons appear in **Supplementary Tables S1–S4**.

Dynamic Cellular Damage Responses Induced by THTMP

The gene ontology was conducted to analyze up and down regulated genes regarded to DNA damage. GO analysis identified the list of genes that were enriched in DNA replication, sister chromatid segregation, DNA-dependent DNA replication, chromosome segregation, sister chromatid cohesion, and nuclear chromosome segregation process. These biological processes are involved in the DNA replication pathway in both cell lines when they were treated with THTMP and TMZ (**Figure 4A**). Enrichment analysis for GO molecular function and pathways clearly demonstrated related phenotypes associated with GBM (**Figures 4B,C**). GO terms cadherin binding, damaged DNA binding for molecular function appeared to be significantly overrepresented, and none significantly underrepresented. Cadherin binding, a type I membrane protein involved in cell adhesion and damaged DNA binding, interacting selectively and non-covalently with damaged DNA have coordinated effect on regulation and function in DNA damage (Daido et al., 2005). Previous studies have shown that GBMs are highly resistant to single inhibitor, suggesting that combinational strategies involving standard chemotherapies like TMZ and pathway inhibitors might be a possible future direction for treating GBM (Jacinto and Esteller, 2007).

Genes associated with the DNA damage were listed in the **Figure 4D**. In general, more DEGs were observed in Snb19 when they were treated with THTMP and TMZ. Here, the top 20 DEGs were listed in **Figure 4D**. In LN229, eight DEGs were expressed when they were treated with THTMP and six DEGs were found in TMZ treatment. CDK1 gene is downregulated when the cells were treated with THTMP and TMZ in both cell types. It is reported that CDK1 was observed to be enriched in the p53 signaling pathway, which is induced by a number of stress signals, including DNA damage, oxidative stress and activated oncogenes. It is noted that p53 signaling network is an integral tumor suppressor pathway in GBM pathogenesis that affects cellular processes, including cell cycle control and cell death execution (Stegh et al., 2010). Moreover, CDKN1A was found to be upregulated in Snb19 when they were treated with THTMP (**Figure 4D**). It is noted that CDKN1A is a gene encoding for p21 protein which contributes to the cell response to DNA damage not only by inactivating G1-phase cyclins/CDKs complexes, but also through other processes, which possibly include direct interaction with PCNA to inhibit DNA replication, and indirect effects mediated by interaction with other cell cycle regulators.

Thereby, our result suggests that DNA damage has been confirmed by the downregulation of CDK1 as well as upregulation of CDKN1A leading to activation of p53 and p21 signaling; thus, inhibiting the growth of glioblastoma. Moreover, CDK1 also plays an important role in cell cycle control (Santamaría et al., 2007). Here, the downregulation of CDK1 expression was identified in THTMP treated conditions confirming cyclin-dependent kinase mediated cell cycle arrest. Detailed investigation of cell cycle arrest was performed using biosensor and gene expression profiling.

THTMP Induces G1/S DNA Damage Checkpoint

It has been demonstrated that DNA damage induced the cell cycle arrest in proliferating mammalian cells (Erasimus et al., 2016). At first, cell cycle progression was imaged using FUCCI fluorescent biosensor and microscopy. Different phases of the cell cycle were determined based on different fluorescence signals, red signal corresponding to G1 phase, yellow signal corresponding to G1/S phase and green signal corresponding to S/G2/M phase (**Figure 5A**). In this study, similar results were observed in both cell lines after the treatment. In DMSO condition, the highest number of cells were present in S/G2/M phase, moderate number of the cells were present in G1 phase, and least number of the cells were present in G1/S phase. Upon THTMP treatment, the majority of the cells were presence in G1 phase, following is the G1/S phase and small number of cells were in S/G2/M phase. In TMZ condition, the percentage of cells in different phases varied between G1/S and S/G2/M phase. According to these results, it is to conclude that GBM cells were arrested at G1/S phase when they were treated with THTMP and were arrested at S/G2/M phase when they were under TMZ treatment (**Figure 5B**).

Here, we show that THTMP induced the downregulation of many genes related to DNA replication, thereby, inhibiting the process of DNA replication and cell cycle progression. Next, genes associated with cell cycle progression were selectively analyzed (**Figure 5C**). There are several biological processes involved in cell cycle pathway that have been activated by the treatment. It includes cell cycle G1/S phase, G1/S transition of mitotic cell cycle, G2/M transition of mitotic cell cycle, cell cycle G2/M phase transition, cell cycle checkpoint and positive regulation of cell cycle (**Figure 4A**). Regarding the expression of various genes involved in cell cycle, genes in Snb19 have higher fold change compared to those in LN229 (**Figure 5C**). For example, the fold change of CCNA2 gene is −0.4 and −2.5 in LN229 and Snb19, respectively, when they were treated with THTMP. The fold change of CCNB2 gene is −0.3 and −2.1 in LN229 and Snb19, respectively, when they were treated with TMZ.

Here, the genes associated with G1 phase and G1/S checkpoint were first selectively analyzed (**Figure 5C**). CCNA2 gene coding to cyclin A2 protein was found to be downregulated in both cell lines when they were treated with THTMP. In Snb19, genes CCNE1 and CCNE2 coding to Cyclin E1 and E2 proteins were found to be decreased in THTMP treatment. It is noted that overexpression of Cyclin A and Cyclin E has the function to

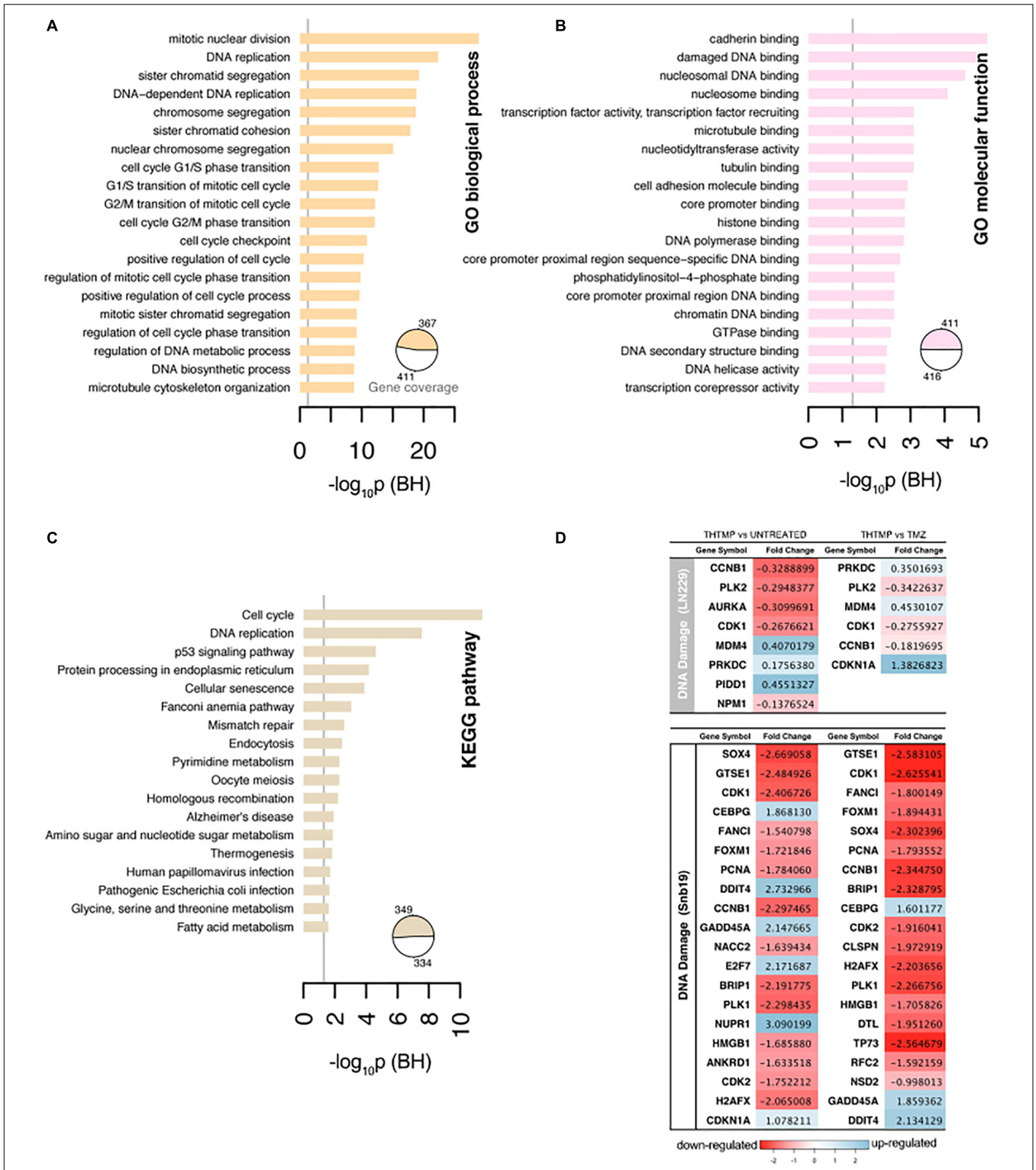

FIGURE 4 | Selected results of Gene Ontology terms and pathways over-representation analysis (FDR < 0.01) on the top 20 terms. **(A)** Overrepresented Gene Ontology (GO) Biological process terms. **(B)** Overrepresented GO Molecular function terms. **(C)** Overrepresented KEGG pathway terms. The x-axis contains the number of genes involved in a particular pathway that were found differentially expressed in our study. The pie charts indicate the fraction of the signature genes associated with significantly enriched terms. The number of genes were normalized to allow comparisons between groups within the same cell line, and the vertical line on the pathways corresponds to the significant *p*-values. **(D)** The top 20 DEGs which are involved in the DNA damage on LN229 and Snb19. The DEGs were color coded, with the colors corresponding to the up- and down- expressed.

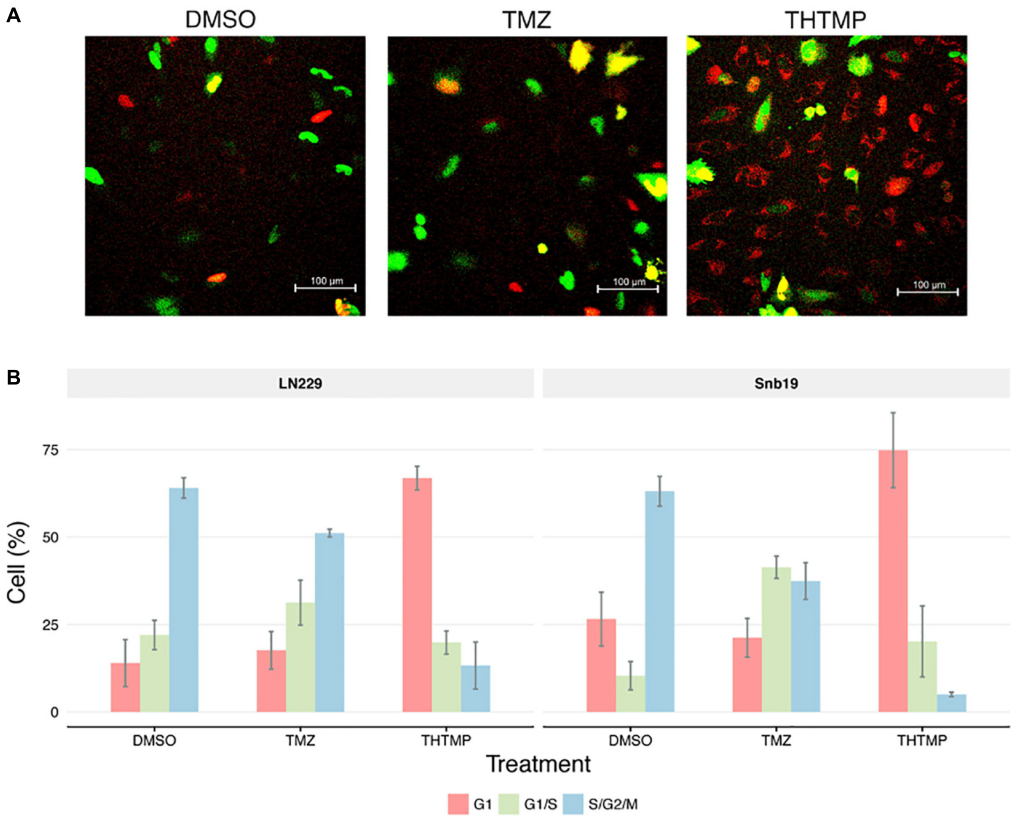

C

Cell Cycle (LN229)	THTMP vs UNTREATED		THTMP vs TMZ	
	Gene Symbol	Fold Change	Gene Symbol	Fold Change
	GPNMB	0.4275336	TGFA	−0.8198255
	TGFA	−0.4802352	GPNMB	0.4286971
	TPX2	−0.3663348	RPTOR	0.5010283
	RPTOR	0.4319812	PRKDC	0.3501693
	TOP2A	−0.2915763	DYNC1H1	0.4522853
	RACGAP1	−0.3829775	PLK2	−0.3422637
	ANXA1	−0.3380360	PTTG1	−0.3895131
	CCNA2	−0.4173247	PPP1R15A	0.4068579
	CCNB1	−0.3288899	ARPP19	−0.2919227
	DLGAP5	−0.4681369	TOP2A	−0.1928397
	BUB1	−0.3852701	DDX39B	0.5631880
	DDX39B	0.7523769	CIT	0.2868897
	NUSAP1	−0.2900128	MDM4	0.4530107
	CENPE	−0.3671398	NUSAP1	−0.2182103
	CEP131	0.4754550	CCNB2	−0.2991284
	SGO2	−0.4134285	DDX11	0.5265886
	ANLN	−0.2413095	HMMR	−0.3823959
	UBE2C	−0.2975740	CDK1	−0.2755927
	DUSP1	0.6165863	DHCR24	−0.2013785
	CDC20	−0.2700165	CDKN1A	1.3826823

Cell Cycle (Snb19)	THTMP vs UNTREATED		THTMP vs TMZ	
	Gene Symbol	Fold Change	Gene Symbol	Fold Change
	THBS1	−2.855987	ANLN	−2.409892
	ANLN	−2.367344	THBS1	−2.606246
	DLGAP5	−2.702034	TOP2A	−2.895878
	PBX1	−3.037413	DLGAP5	−2.647333
	TOP2A	−2.669321	NUSAP1	−2.739889
	NUSAP1	−2.593800	CENPF	−2.573051
	SMC2	−1.890055	SMC2	−1.928556
	CENPF	−2.479174	PBX1	−2.819423
	MKI67	−2.700883	NCAPD2	−2.102092
	KIF23	−1.818429	MKI67	−2.733082
	NCAPD2	−2.014852	KIF23	−1.885570
	CCNA2	−2.547481	CCNA2	−2.555355
	BUB1	−2.115452	CDK1	−2.625541
	CCNB2	−2.056732	BUB1	−2.163774
	CDC20	−1.995207	CCNB2	−2.140393
	CCNB1	−2.297465	CDC20	−2.081145
	GADD45A	2.147665	CCNB1	−2.344750
	CDKN1A	1.078211	GADD45A	1.859362
	CCNE2	−2.259402	CCNE2	−2.551983
	CCNE1	−1.014676	CCNE1	−1.196947

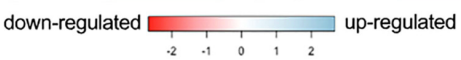

FIGURE 5 | Cell cycle analysis using FUCCI and RNA-seq. **(A)** Demonstrated images of cell which were dyed with FUCCI in different conditions (DMSO, TMZ, and THTMP). Red cells corresponding to the cells in G1, yellow cells corresponding to the cells in G1/S phase and the green cells corresponding to the cells in S/G2/M phase **(B)** Percentage of total cell in different phases when they were treated with THTMP and TMZ. **(C)** The top 20 DEGs which are involved in the cell cycle on LN229 and Snb19. The DEGs were color coded, with the colors corresponding to the up- and down- expressed.

regulate G1/S transition when they complex with CDK2; thus, decreased expression level of CCNA2, CCNE1, and CCNE2 could lead to mediate the G1/S arrest. Moreover, BUB1 was identified to be downregulated in this study and was enriched in biological processes associated with the mitotic cell cycle, including cell cycle chromatid segregation, G1/S transition of mitotic cells and DNA replication. CDC20 appears to act as a regulator protein interacting with several other proteins at multiple points in the cell cycle. We found that CDC20 gene was downregulated and enriched in cell cycle and oocyte meiosis pathways.

In case of TMZ treatment, FUCCI analysis shows that both Snb19 and LN229 cells were arrested at S/G2/M phase. It is in accordance with our gene expression analysis. Genes CCNB1, CCNB2, CCNA2, which relate to Cyclin B1 and Cyclin A2, were found to be decreased. These two cyclins have the function to regulate G2/M transition when they complex with CDK1. Moreover, CDKN1A (p21) and GADD45A, two downstream target genes of p53 in the G2 checkpoint, were found to be increased in LN229 and Snb19, respectively, at the transcriptional level. Previous studies have reported that increased p21 expression led to the repression of cyclin B1 and Cdc2 promoters and that increased GADD45A expression inhibits Cdc2 activity, thereby mediating G2/M arrest (Jin et al., 2000; Yang et al., 2000).

The results show that THTMP induced cell cycle arrest at G1/S phase while TMZ induced cell cycle arrest at G2/M phase in both cell lines. This result implies that THTMP has inhibited synthesis of GBM cells before they can entry to replication and division periods; therefore, strongly preventing cell proliferation. Moreover, G1/S phase arrest of cell cycle progression provides an opportunity for cells to either undergo repair mechanisms or follow the apoptotic pathway (Bartek and Lukas, 2001).

THTMP Increases ROS Production and Induces Pro-apoptotic and Anti-apoptotic Genes

Apoptosis induction assay was performed using Annexin V/PI double staining. Here, the percentage of apoptosis was calculated based on the cells with Annexin V-FITC positive and PI negative and both Annexin V-FITC and PI positive. The percentage of necrosis was defined based on the cells with Annexin V-FITC negative and PI positive (Chen et al., 2008). **Figure 6A** shows the live, apoptosis and necrosis of LN229 and Snb19 when they were treated with THTMP and TMZ. Generally, apoptosis induction was observed in both cell lines compared with positive control and untreated conditions. The apoptosis percentage of LN229 cells treated with THTMP is 45.8% while only 21.9 and 11.2% were obtained when they were treated with TMZ and DMSO, respectively. In case of Snb19 cells, 56.4% of apoptotic cells were found in THTMP treated condition whilst TMZ and untreated conditions exhibit only 36.2 and 11.5% apoptotic cells. Beside the apoptotic cells, necrotic cells were also observed in both cell lines. However, necrosis percentage is less than 10% in case of Snb19 while in LN229, 27.0 and 7.6% were found to be necrotic cells when they were treated with TMZ and THTMP, respectively.

The results above are in accordance with the gene expression profile showing the enrichment of apoptosis pathways including neuron apoptotic process, positive regulation of neuron apoptotic process, regulation of apoptotic signaling pathway, regulation of neuron apoptotic process, intrinsic apoptotic signaling pathway and extrinsic apoptotic signaling pathway. Genes involved in regulation of apoptotic process were presented in **Figure 6B**. Moreover, the gene expression profile indicates lower number of the DEGs related to apoptosis process in TMZ treatment compared to THTMP treatment (**Figure 6B**). The expression changes showing in **Figure 6B** revealed that THTMP tended to induce pro-apoptotic genes, reduce anti-apoptotic genes and also induce some anti-apoptotic genes.

Among pro-apoptotic genes, CTNNB1 gene coding for β-catenin protein was downregulated in LN229 cells when they were treated with THTMP. It is reported that abnormal accumulation of β-catenin contributes to most cancers and repressed CTNNB1 also leads to inducing apoptosis in some tumor cells (Yang et al., 2017). Interestingly, the pro-apoptotic Bcl-2 family gene MAGED1 was also found to be upregulated in LN229 whereas BBC3 (PUMA) gene was upregulated in Snb19 when they were treated with THTMP. Moreover, BCL2L12, an anti-apoptotic gene, was found to be downregulated in Snb19 cells. It is noted that BCL2L12 expression is upregulated in most human glioblastomas. Expression of Bcl2L12 results in resistance to apoptosis (Yang et al., 2015). Our findings demonstrated that THTMP has shown the ability to induce apoptosis of Snb19 and LN229 via mitochondrial pathway throughout the upregulation of pro-apoptotic and downregulation of anti-apoptotic Bcl-2 family genes.

Although the altered expression of genes described above could confirm apoptosis, genes involved in anti-apoptosis were expressed when the cells were treated with THTMP. The anti-apoptotic characteristics of Snb19 cells were identified by the downregulation of several genes from the membrane stress receptors, such as TNFSF10, TNFSF12, and TNFRSF2. Moreover, the upregulation of RELA, a member of NFkB family, suggested a decline in inflammatory processes and strong anti-apoptotic properties for this cell line. In LN229 cells, the regulation of the TNF receptor pathway as well as NFkB signaling pathway was not significantly affected, but there was a modest upregulation of BIRC6 encoded for BIRC protein, a member of the inhibitor of apoptosis (IAP) gene family preventing apoptotic cell death. Interestingly, the BIRC5 was suppressed in Snb19.

In addition to the activation of apoptotic pathways in the treated cells, reactive oxygen species (ROS) could lead to cell cycle arrest and induces apoptosis in anticancer treatment (Circu and Aw, 2010). It is well known that ROS is produced in both normal and abnormal cells especially in cancer cells. ROS plays an important role in proliferation, survival, metastasis and angiogenesis (Clerkin et al., 2008). In this study, the effects of THTMP, TMZ and H_2O_2, a positive control in the levels of ROS on GBM cells, was assessed using ROS production assay. **Figure 6C** shows an increase of ROS level when the cells were treated with THTMP and TMZ. Interestingly, the fold increase of ROS of Snb19 and LN229 cells treated with THTMP were higher than H_2O_2. As seen in **Figure 6C**, Snb19 cells have higher level of

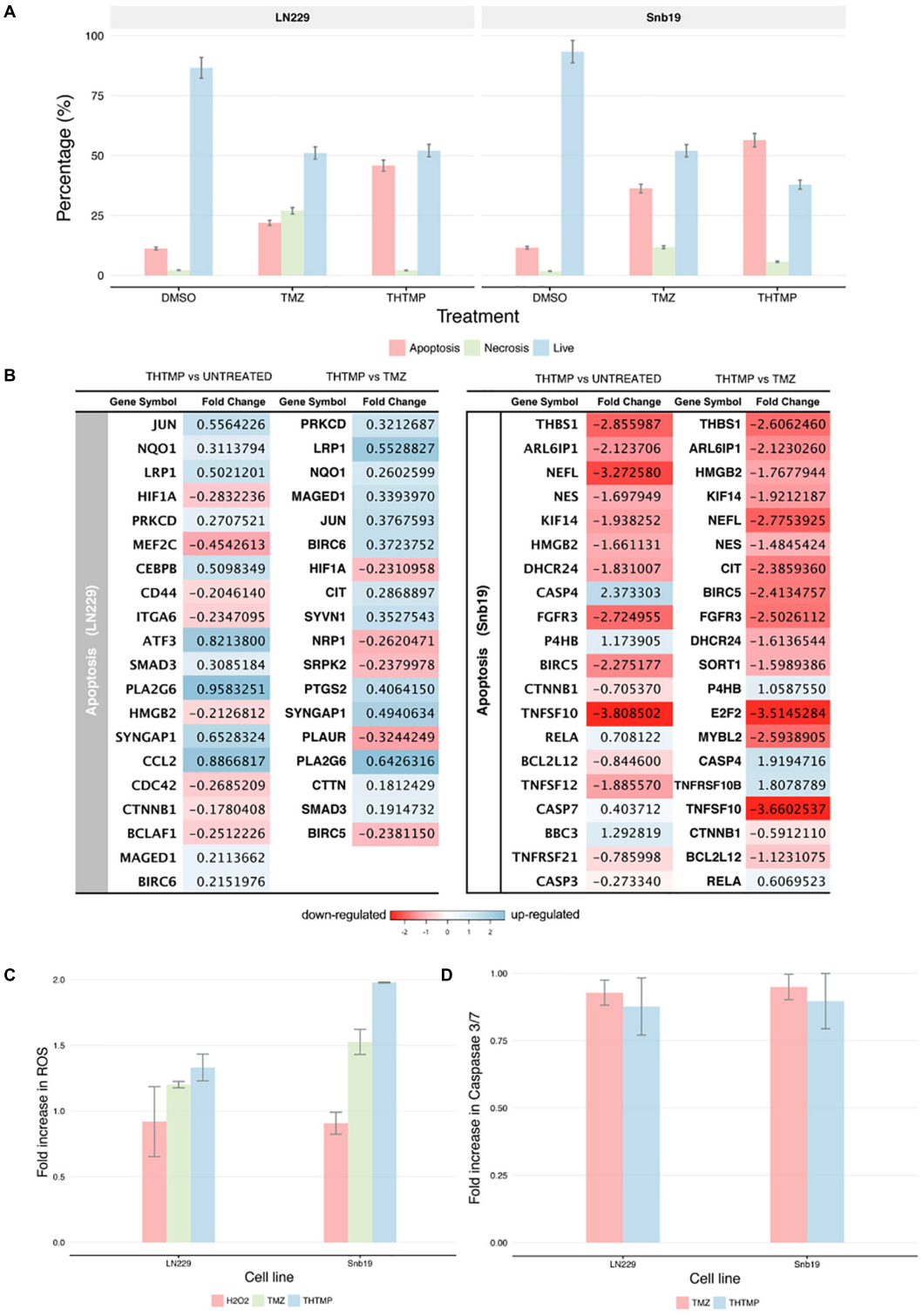

FIGURE 6 | Apoptosis induction determination using double stains Annexin V and Propidium iodide and RNA-seq. **(A)** Percentage of apoptosis, necrosis and live cell using Dead Cell Apoptosis Kit with Annexin V-FITC and PI of untreated cell (DMSO control TMZ and compound THTMP at 24 h post-treatment on Snb19 and LN229. **(B)** The top 20 DEGs which are involved in apoptosis of LN229 and Snb19. The DEGs were color coded, with the colors corresponding to the up- and down- expressed. **(C)** Effect of THTMP and TMZ in intracellular ROS production. Fluorescence intensity of ROS was determined by activity of 2 μM H2DCFDA (30 min), fluorescent probe. H_2O_2 was used as the positive control. **(D)** Activity of caspases 3/7 in LN229 and Snb19. Caspase 3/7 was determined using luminescence plate reader. Fold increase in ROS and caspases 3 and 7 activity of LN229 and Snb19 cell lines was calculated when they were treated with THTMP and PC at IC_{50} concentration. Triplicates were performed for each condition.

ROS compared to LN229 in all of the conditions. In which, up to 2 fold increase was found in THTMP treatment of Snb19 while only 1.3 fold increase was observed in LN229. The same trend was observed for the TMZ treatment in which 1.5 fold and 1.2 fold were obtained in Snb19 and LN229, respectively. Thus, ROS were significantly produced when GBM cells were affected with THTMP. This suggests that higher ROS level could be interlinked with the observed apoptotic cell death of cancer cells upon treatment with compound THTMP. Moreover, in mammalian cells, ROS are produced by normal oxidative metabolism and cellular antioxidants such as superoxide dismutase (SOD1) and thioredoxin (TRX1) detoxify these species (Covarrubias et al., 2008). A study indicated that decreasing SOD1 and TRX1 could lead to apoptosis induction in glioma cells when they were treated with kaempferol, a natural phenolic compound, via elevation of ROS (Sharma et al., 2007). In agreement, we also found out that while THTMP treatment had no effect on TRX1, a decrease in SOD1 was observed in Snb19 cells (**Supplementary Table S3**). Thus, THTMP induced ROS-mediated apoptosis.

According to **Figure 6D**, caspase 3/7 was not significantly increased in both cell lines when they were treated with THTMP and TMZ. This is also in agreement with the gene expression profile where we could not find the significant expression of CASP3 and CASP7 in LN229 cells (**Figure 6B**). In case of Snb19 cells, although the CASP3 and CASP7 were expressed, the CASP3 was downregulated and CASP7 was upregulated when they were treated with THTMP (**Figure 6B**). This result interprets the no change in caspase 3/7 activation assay results (**Figure 6C**). The repression of caspase genes might be caused from the activation of anti-apoptotic genes (Stegh et al., 2008). Thus, apoptosis inductions of GBM cells by THTMP and TMZ were not via caspase 3/7. Instead of CASP3 and CASP7, CASP4 was found to be upregulated in Snb19 when they were treated with both THTMP and TMZ. Therefore, the result implies the involvement of caspase 4 in Snb19 when they were treated with THTMP and TMZ.

DISCUSSION

DNA damage response induced by THTMP was validated and shown to be dose-and time-dependent. A detailed analysis of global molecular expression profiling is required in order to understand the complex cellular responses. Here, by combining biochemical studies with high-throughput RNA sequencing, the changes in gene expression in glioma cells induced by THTMP was explored. Our results show that genes involves in DNA damage, DNA replication, cell cycle arrest and apoptosis induction were transcriptionally modulated and highly enriched when GBM cells were treated with THTMP.

Firstly, our study demonstrated a THTMP induced activation of various genes associated with DNA damage and cell cycle arrest. The cell cycle arrest in GBM when they were treated with THTMP and TMZ may be explained by transcriptional expression change of some crucial genes that are listed in **Figure 5B**. CCNA2 gene was found in both Snb19 and LN229 when they were treated with THTMP compound. This gene belongs to a highly conserved cyclin family and the encoded protein of this gene is crucial in the control of the cell cycle at G1/S and G2/M transition points. Here, several important genes in control cell cycle at G1/2 and G2/M such as CCNA2, BUB1, CDC20 are selected for further discussion in order to understand their mechanism in controlling cell cycle of GBM.

In previous studies, it is reported that overexpression of CCNA2 is involved in tumor transformation and progression in numerous types of cancer (Uhlen et al., 2010). As expected, our results show that CCNA2 was downregulated, which is in accordance with the function of cyclin A2 protein in cell cycle indicating that CCNA2 inhibits the growth of GBM. BUB1 was also found to be downregulated that can explain the G1/S transition arrest since the BUB family of genes encode proteins that are involved in large multi-protein kinetochore complex, and are reported to be key component of the checkpoint regulator pathway. BUB1 encodes a serine/threonine protein kinase which plays an important role in mitosis (Tang et al., 2006), and BUB1 accumulates at unattached kinetochores where it mediates the recruitment of mitotic arrest deficient (Mad) dimers. Combination of Mad and BUB1 leads to prevention of premature separation of sister chromatids until all chromosomes are correctly attached to kinetochores; thus, correctly chromosome segregation achieved (Ricke et al., 2011). This suggests that GBM cell growth may be inhibited by regulating the mitotic cell cycle in THTMP treated conditions (Grabsch et al., 2003). In addition, previous reports indicate that CDC20 is highly expressed in various type of human tumors including breast, cervical and glioblastoma cancer (Marucci et al., 2008; Jiang et al., 2011; Rajkumar et al., 2011). It is also reported that expression level of CDC20 is correlated with the grade of glioblastoma and it is expressed at different levels in patients at different ages (Bie et al., 2011). In the study CDC20 was downregulated, which leads to conclude that CDC20 may inhibit GBM growth. According to the biological process enrichment results, CCNA2 was enriched in cell cycle and oocyte meiosis pathways, in which CDK1, BUB1 and CDC20 were also involved. These genes are also known as key genes playing a crucial role in promoting GBM growth (Chen et al., 2016). Repression of these genes when the cells were treated with THTMP indicates that this compound strongly inhibits the growth of GBM throughout cell cycle arrest.

Secondly, we detected apoptotic effects induced by THTMP. Analysis of apoptosis genes subsequently revealed that the progress of apoptosis was accompanied by changes in both pro-apoptotic and anti-apoptotic gene expression, consistent with the observation in other chemotherapeutic therapies in cancer cells (Kim et al., 2003). It is noted that BCL2L12 is overexpressed in primary GBM and functions to inhibit post-mitochondrial apoptosis signaling (Stegh et al., 2007). This study shows that THTMP has induced apoptosis via mitochondrial pathway in both LN229 and Snb19 cell lines due to the suppression of Bcl-2 family, BCL2L12. The study also shows that a large number of genes of Snb19 was expressed compared to LN229 when they were treated with THTMP. The anti-apoptotic genes expressed in LN229 and Snb19 are different. This result implies that apoptosis pathways of GBM cells will be executed in different mechanisms when they were treated with THTMP. This study

shows that TMZ also induced apoptosis in GBM cells as explored by Annexin V/PI double staining; however, the gene profile of this condition is still limited. Here, the absence of caspase 3/7 activation indicates that THTMP has not induced apoptosis via caspase 3 and 7 of LN229 and Snb19, but the caspase 4 might be involved in the apoptosis pathway of Snb19 cells.

CONCLUSION

Overall, the effect of THTMP on GBM cells is relatively much stronger than TMZ in all aspects. This study provides experimental evidence that THTMP is capable of inhibiting the growth of GBM cells. THTMP has the ability to induce DNA damage through the p53 signaling pathway leading to cell cycle arrest. The G1/S checkpoint arrest depends on the decrease of cyclin A2 in both Snb19 and LN229 cells-treated with THTMP. Moreover, the decrease of cyclin E1 and E2 in Snb19 in THTMP treatment also contributes to the G1/S checkpoint arrest. This result suggests that THTMP facilitates cancer cells to undergo programmed cell death pathways, apoptosis in glioblastoma cells. The induction of apoptosis of GBM in THTMP treated conditions is associated with increasing pro-apoptotic factor of Bcl-2. In addition, it is indicated that caspase 4 may play a role in this apoptosis induction instead of caspase 3/7.

The findings on inhibition of GBM proliferation and downregulation of cell cycle genes in the G1/S phase not only provide a better understanding of the mechanisms of THTMP, a phenolic compound, as anticancer agent, but also open an avenue for investigating the role of oxidative stress in GBM involving cell cycle and apoptosis regulation. However, testing THTMP on glioma animal model and computational pharmacogenomics approaches (Musa et al., 2018) will allow this compound to be used as a potential chemotherapeutic drug for glioma treatment.

AUTHOR CONTRIBUTIONS

PD executed experiments and data analysis. AM analyzed the RNAseq data. NC prepared and characterized the compounds. FE-S contributed in development of the project. OY-H contributed in development of the project, conceived and managed the project. MK designed and supervised the experiments of the biological assays, data analysis, conceived and managed the project. All authors involved in the manuscript write up and approved the final version of the manuscript.

FUNDING

This study was supported by Academy of Finland (Nr.297200) and TUT presidents grant.

ACKNOWLEDGMENTS

We thank Biomedicum Functional Genomics Unit (FuGU, University of Helsinki, Finland) for helping us to perform RNA-seq. We also thank Prof. Ville Santala for providing access to the plate reader instrument for reactive oxygen species and Caspase measurements at TUT.

SUPPLEMENTARY MATERIAL

The Supplementary Material for this article can be found online at: https://www.frontiersin.org/articles/10.3389/fphar.2019.00330/full#supplementary-material

REFERENCES

Anders, S., Pyl, P. T., and Huber, W. (2014). HTSeq – a python framework to work with high-throughput sequencing data HTSeq – a python framework to work with high-throughput sequencing data. *Bioinformatics* 31, 166–169. doi: 10.1093/bioinformatics/btu638

Andrews, S. (2010). *FastQC*: *A Quality Control Tool for High Throughput Sequence Data.* Available at: http://www.bioinformatics.babraham.ac.uk/projects/fastqc/ (Retrieved October 21, 2018).

Ashburner, M., Ball, C. A., Blake, J. A., Botstein, D., Butler, H., Cherry, J. M., et al. (2000). Gene ontology: tool for the unification of biology. *Nat. Genet.* 25, 25–29. doi: 10.1038/75556

Bartek, J., and Lukas, J. (2001). Pathways governing G1/S transition and their response to DNA damage. *FEBS Lett.* 490, 117–122. doi: 10.1016/S0014-5793(01)02114-7

Benjamini, Y., and Hochberg, Y. (1995). Controlling the false discovery rate: a practical and powerful approach to multiple testing. *J. R. Stat. Soc. Ser. B* 57, 289–300. doi: 10.2307/2346101

Bie, L., Zhao, G., Cheng, P., Rondeau, G., Porwollik, S., Ju, Y., et al. (2011). The accuracy of survival time prediction for patients with glioma is improved by measuring mitotic spindle checkpoint gene expression. *PLoS One* 6:e25631. doi: 10.1371/journal.pone.0025631

Chen, C., Sun, C., Tang, D., Yang, G., Zhou, X., and Wang, D. (2016). Identification of key genes in glioblastoma-associated stromal cells using bioinformatics analysis. *Oncol. Lett.* 11, 3999–4007. doi: 10.3892/ol.2016.4526

Chen, S., Cheng, A. C., Wang, M. S., and Peng, X. (2008). Detection of apoptosis induced by new type gosling viral enteritis virus in vitro through fluorescein annexin V-FITC/PI double labeling. *World J. Gastroenterol.* 14, 2174–2178. doi: 10.3748/wjg.14.2174

Circu, M. L., and Aw, T. Y. (2010). Reactive oxygen species, cellular redox systems, and apoptosis. *Free Radic. Biol. Med.* 48, 749–762. doi: 10.1016/j.freeradbiomed.2009.12.022

Clerkin, J. S., Naughton, R., Quiney, C., and Cotter, T. G. (2008). Mechanisms of ROS modulated cell survival during carcinogenesis. *Cancer Lett.* 266, 30–36. doi: 10.1016/j.canlet.2008.02.029

Covarrubias, L., Hernández-García, D., Schnabel, D., Salas-Vidal, E., and Castro-Obregón, S. (2008). Function of reactive oxygen species during animal development: passive or active? *Dev. Biol.* 320, 1–11. doi: 10.1016/j.ydbio.2008.04.041

Daido, S., Yamamoto, A., Fujiwara, K., Sawaya, R., Kondo, S., and Kondo, Y. (2005). Inhibition of the DNA-dependent protein kinase catalytic subunit radiosensitizes malignant glioma cells by inducing autophagy. *Cancer Res.* 65, 4368–4375. doi: 10.1158/0008-5472.CAN-04-4202

Doan, P., Karjalainen, A., Chandraseelan, J., Sandberg, O., Yli-Harja, O., Rosholm, T., et al. (2016). Synthesis and biological screening for cytotoxic activity of N- substituted indolines and morpholines. *Eur. J. Med. Chem.* 120, 296–303. doi: 10.1017/CBO9781107415324.004

Dobin, A., Davis, C. A., Schlesinger, F., Drenkow, J., Zaleski, C., Jha, S., et al. (2013). STAR: ultrafast universal RNA-seq aligner. *Bioinformatics* 29, 15–21. doi: 10.1093/bioinformatics/bts635

Emmert-Streib, F., and Glazko, G. V. (2011). Pathway analysis of expression data: deciphering functional building blocks of complex diseases. *PLoS Comput. Biol.* 7:e1002053. doi: 10.1371/journal.pcbi.1002053

Erasimus, H., Gobin, M., Niclou, S., and Van Dyck, E. (2016). DNA repair mechanisms and their clinical impact in glioblastoma. *Mutat. Res. Mutat. Res.* 769, 19–35. doi: 10.1016/j.mrrev.2016.05.005

Friedman, H. S., Prados, M. D., Wen, P. Y., Mikkelsen, T., Schiff, D., Abrey, L. E., et al. (2009). Bevacizumab alone and in combination with irinotecan in recurrent glioblastoma. *J. Clin. Oncol.* 27, 4733–4740. doi: 10.1200/JCO.2008.19.8721

Gali-Muhtasib, H., Hmadi, R., Kareh, M., Tohme, R., and Darwiche, N. (2015). Cell death mechanisms of plant-derived anticancer drugs: beyond apoptosis. *Apoptosis* 20, 1531–1562. doi: 10.1007/s10495-015-1169-2

Gong, L., Li, Y., Nedeljkovic-Kurepa, A., and Sarkar, F. H. (2003). Inactivation of NF-kappaB by genistein is mediated via Akt signaling pathway in breast cancer cells. *Oncogene* 22, 4702–4709. doi: 10.1038/sj.onc.1206583

Grabsch, H., Takeno, S., Parsons, W. J., Pomjanski, N., Boecking, A., Gabbert, H. E., et al. (2003). Overexpression of the mitotic checkpoint genes BUB1, BUBR1, and BUB3 in gastric cancer-association with tumour cell proliferation. *J. Pathol.* 200, 16–22. doi: 10.1002/path.1324

Hegi, M. E., Diserens, A.-C., Gorlia, T., Hamou, M.-F., de Tribolet, N., Weller, M., et al. (2005). MGMT gene silencing and benefit from temozolomide in glioblastoma. *N. Engl. J. Med.* 352, 997–1003. doi: 10.1056/NEJMoa043331

Jacinto, F. V., and Esteller, M. (2007). MGMT hypermethylation: a prognostic foe, a predictive friend. *DNA Repair* 6, 1155–1160. doi: 10.1016/j.dnarep.2007.03.013

Jiang, J., Jedinak, A., and Sliva, D. (2011). Ganodermanontriol (GDNT) exerts its effect on growth and invasiveness of breast cancer cells through the down-regulation of CDC20 and uPA. *Biochem. Biophys. Res. Commun.* 415, 325–329. doi: 10.1016/j.bbrc.2011.10.055

Jin, S., Antinore, M. J., Lung, F. D. T., Dong, X., Zhao, H., Fan, F., et al. (2000). The GADD45 inhibition of Cdc2 kinase correlates with GADD45-mediated growth suppression. *J. Biol. Chem.* 275, 16602–16608. doi: 10.1074/jbc.M000284200

Kanehisa, M., and Goto, S. (2000). KEGG: keyoto encyclopedia of genes and geneomes. *Nucleic Acids Res.* 28, 27–30. doi: 10.1093/nar/28.1.27

Karjalainen, A., Doan, P., Sandberg, O., Chandraseelan, J., Yli-Harja, O., Candeias, N., et al. (2017). Synthesis of phenol-derivatives and biological screening for anticancer activity. *Anticancer Agents Med. Chem.* 17, 1710–1720. doi: 10.2174/1871520617666170327142027

Kim, Y. A., Lee, W. H., Choi, T. H., Rhee, S. H., Park, K. Y., and Choi, Y. H. (2003). Involvement of p21WAF1/CIP1, pRB, Bax and NF-kappaB in induction of growth arrest and apoptosis by resveratrol in human lung carcinoma A549 cells. *Int. J. Oncol.* 23, 1143–1149.

Lee, S. Y. (2016). Temozolomide resistance in glioblastoma multiforme. *Genes Dis.* 3, 198–210. doi: 10.1016/j.gendis.2016.04.007

Li, H., Handsaker, B., Wysoker, A., Fennell, T., Ruan, J., Homer, N., et al. (2009). The sequence alignment/map format and sAMtools. *Bioinformatics* 25, 2078–2079. doi: 10.1093/bioinformatics/btp352

Love, M. I., Huber, W., and Anders, S. (2014). Moderated estimation of fold change and dispersion for RNA-seq data with DESeq2. *Genome Biol.* 15:550. doi: 10.1186/s13059-014-0550-8

Marucci, G., Morandi, L., Magrini, E., Farnedi, A., Franceschi, E., Miglio, R., et al. (2008). Gene expression profiling in glioblastoma and immunohistochemical evaluation of IGFBP-2 and CDC20. *Virchows Arch.* 453, 599–609. doi: 10.1007/s00428-008-0685-7

Mi, H., Dong, Q., Muruganujan, A., Gaudet, P., Lewis, S., and Thomas, P. D. (2009). PANTHER version 7: improved phylogenetic trees, orthologs and collaboration with the gene ontology consortium. *Nucleic Acids Res.* 38, D204–D210. doi: 10.1093/nar/gkp1019

Musa, A., Ghoraie, L. S., Zhang, S. D., Glazko, G., Yli-Harja, O., Dehmer, M., et al. (2018). A review of connectivity map and computational approaches in pharmacogenomics. *Brief. Bioinform.* 19, 506–523. doi: 10.1093/bib/bbw112

Neto, Í, Andrade, J., Fernandes, A. S., Pinto Reis, C., Salunke, J. K., Priimagi, A., et al. (2016). Multicomponent petasis-borono mannich preparation of alkylaminophenols and antimicrobial activity studies. *ChemMedChem* 11, 2015–2023. doi: 10.1002/cmdc.201600244

Olliaro, P., Nevill, C., LeBras, J., Ringwald, P., Mussano, P., Garner, P., et al. (1996). Systematic review of amodiaquine treatment in uncomplicated malaria. *Lancet* 348, 1196–1201. doi: 10.1016/S0140-6736(96)06217-4

Pommier, Y. (2006). Topoisomerase I inhibitors: camptothecins and beyond. *Nat. Rev. Cancer* 6, 789–802. doi: 10.1038/nrc1977

Rajkumar, T., Sabitha, K., Vijayalakshmi, N., Shirley, S., Bose, M. V., Gopal, G., et al. (2011). Identification and validation of genes involved in cervical tumourigenesis. *BMC Cancer* 11:80. doi: 10.1186/1471-2407-11-80

Ricke, R. M., Jeganathan, K. B., and van Deursen, J. M. (2011). Bub1 overexpression induces aneuploidy and tumor formation through Aurora B kinase hyperactivation. *J. Cell Biol.* 193, 1049–1064. doi: 10.1083/jcb.201012035

Roman, G. (2015). Mannich bases in medicinal chemistry and drug design. *Eur. J. Med. Chem.* 89, 743–816. doi: 10.1016/j.ejmech.2014.10.076

Santamaría, D., Barrière, C., Cerqueira, A., Hunt, S., Tardy, C., Newton, K., et al. (2007). Cdk1 is sufficient to drive the mammalian cell cycle. *Nature* 448, 811–815. doi: 10.1038/nature06046

Selvendiran, K., Koga, H., Ueno, T., Yoshida, T., Maeyama, M., Torimura, T., et al. (2006). Luteolin promotes degradation in signal transducer and activator of transcription 3 in human hepatoma cells: An implication for the antitumor potential of flavonoids. *Cancer Res.* 66, 4826–4834. doi: 10.1158/0008-5472.CAN-05-4062

Sharma, V., Joseph, C., Ghosh, S., Agarwal, A., Mishra, M. K., and Sen, E. (2007). Kaempferol induces apoptosis in glioblastoma cells through oxidative stress. *Mol. Cancer Ther.* 6, 2544–2553. doi: 10.1158/1535-7163.MCT-06-0788

Stegh, A. H., Brennan, C., Mahoney, J. A., Forloney, K. L., Jenq, H. T., Luciano, J. P., et al. (2010). Glioma oncoprotein Bcl2L12 inhibits the p53 tumor suppressor. *Genes Dev.* 24, 2194–2204. doi: 10.1101/gad.1924710

Stegh, A. H., Kesari, S., Mahoney, J. E., Jenq, H. T., Forloney, K. L., Protopopov, A., et al. (2008). Bcl2L12-mediated inhibition of effector caspase-3 and caspase-7 via distinct mechanisms in glioblastoma. *Proc. Natl. Acad. Sci.* 105, 10703–10708. doi: 10.1073/pnas.0712034105

Stegh, A. H., Kim, H., Bachoo, R. M., Forloney, K. L., Zhang, J., Schulze, H., et al. (2007). Bcl2L12 inhibits post-mitochondrial apoptosis signaling in glioblastoma. *Genes Dev.* 21, 98–111. doi: 10.1101/gad.1480007

Stupp, R., Mason, W., van den Bent, M. J., Weller, M., Fisher, B. M., Taphoorn, M. J. B., et al. (2005). Radiotherapy plus concomitant\nand adjuvant temozolomide for glioblastoma. *N. Engl. J. Med.* 352, 987–996. doi: 10.1056/NEJMoa043330

Tang, Z., Shu, H., Qi, W., Mahmood, N. A., Mumby, M. C., and Yu, H. (2006). PP2A is required for centromeric localization of sgo1 and proper chromosome segregation. *Dev. Cell* 10, 575–585. doi: 10.1016/j.devcel.2006.03.010

Thompson, D. C., Thompson, J. A., Sugumaran, M., and Moldéus, P. (1993). Biological and toxicological consequences of quinone methide formation. *Chem. Biol. Interact.* 86, 129–162. doi: 10.1016/0009-2797(93)90117-H

Uhlen, M., Oksvold, P., Fagerberg, L., Lundberg, E., Jonasson, K., Forsberg, M., et al. (2010). Towards a knowledge-based human protein atlas. *Nat. Biotechnol.* 28, 1248–1250. doi: 10.1038/nbt1210-1248

Wcislo, G., Korniluk, J., and Szarlej-Wcislo, K. (2013). Cancer chemoprevention by resveratrol treatment. *Polyphenols Hum. Health Dis.* 2, 1323–1330. doi: 10.1016/B978-0-12-398456-2.00099-2

Weinert, E. E., Dondi, R., Colloredo-Melz, S., Frankenfield, K. N., Mitchell, C. H., Freccero, M., et al. (2006). Substituents on quinone methides strongly modulate formation and stability of their nucleophilic adducts. *J. Am. Chem. Soc.* 128, 11940–11947. doi: 10.1021/ja062948k

Wu, Y.-S., Coumar, M. S., Chang, J.-Y., Sun, H.-Y., Kuo, F.-M., Kuo, C.-C., et al. (2009). Synthesis and evaluation of 3-aroylindoles as anticancer agents: metabolite approach. *J. Med. Chem.* 52, 4941–4945. doi: 10.1021/jm900060s

Yang, C.-M., Ji, S., Li, Y., Fu, L.-Y., Jiang, T., and Meng, F.-D. (2017). β-Catenin promotes cell proliferation, migration, and invasion but induces apoptosis in renal cell carcinoma. *Onco. Targets Ther.* 10, 711–724. doi: 10.2147/OTT.S117933

Yang, F., Brown, C., Buettner, R., Hedvat, M., Starr, R., Scuto, A., et al. (2010). Sorafenib induces growth arrest and apoptosis of human glioblastoma cells through the dephosphorylation of signal transducers and activators of transcription 3. *Mol. Cancer Ther.* 9, 953–962. doi: 10.1158/1535-7163.MCT-09-0947

Yang, M. C., Loh, J. K., Li, Y. Y., Huang, W. S., Chou, C. H., Cheng, J. T., et al. (2015). Bcl2L12 with a BH3-like domain in regulating apoptosis and TMZ-induced autophagy: a prospective combination of ABT-737 and TMZ for treating glioma. *Int. J. Oncol.* 46, 1304–1316. doi: 10.3892/ijo.2015.2838

Yang, Q., Manicone, A., Coursen, J. D., Linke, S. P., Nagashima, M., Forgues, M., et al. (2000). Identification of a functional domain in a GADD45-mediated G2/M checkpoint. *J. Biol. Chem.* 275, 36892–36898. doi: 10.1074/jbc.M005319200

Zielke, N., and Edgar, B. A. (2015). FUCCI sensors: Powerful new tools for analysis of cell proliferation. *Wiley Interdiscip. Rev. Dev. Biol.* 4, 469–487. doi: 10.1002/wdev.189

Conflict of Interest Statement: The authors declare that the research was conducted in the absence of any commercial or financial relationships that could be construed as a potential conflict of interest.

frontiers in Oncology

ORIGINAL RESEARCH
published: 13 June 2019
doi: 10.3389/fonc.2019.00499

Catechins-Modified Selenium-Doped Hydroxyapatite Nanomaterials for Improved Osteosarcoma Therapy Through Generation of Reactive Oxygen Species

Suliman Khan[1,2,3], *Muhammad Wajid Ullah*[4], *Rabeea Siddique*[1,4], *Yang Liu*[1,5], *Ismat Ullah*[6], *Mengzhou Xue*[1,5]*, *Guang Yang*[4]* and *Hongwei Hou*[2,3]*

[1] The Department of Cerebrovascular Diseases, The Second Affiliated Hospital of Zhengzhou University, Zhengzhou, China, [2] The Key Laboratory of Aquatic Biodiversity and Conservation of Institute of Hydrobiology, Chinese Academy of Sciences, Wuhan, China, [3] University of Chinese Academy of Sciences, Beijing, China, [4] Department of Biomedical Engineering, Huazhong University of Science and Technology, Wuhan, China, [5] Henan Medical Key Laboratory of Translational Cerebrovascular Diseases, Zhengzhou, China, [6] State Key Laboratory of Materials Processing and Die/Mold Technology, School of Materials Science and Engineering, Huazhong University of Science and Technology, Wuhan, China

OPEN ACCESS

Edited by:
Fabrizio Marcucci,
University of Milan, Italy

Reviewed by:
Sreeparna Banerjee,
Middle East Technical University, Turkey
Carmen Alvarez-Lorenzo,
University of Santiago de Compostela, Spain

***Correspondence:**
Mengzhou Xue
xumengzhou@zzu.edu.cn
Guang Yang
yang_sunny@yahoo.com
Hongwei Hou
houhw@ihb.ac.cn

Specialty section:
This article was submitted to Pharmacology of Anti-Cancer Drugs, a section of the journal Frontiers in Oncology

Received: 04 January 2019
Accepted: 24 May 2019
Published: 13 June 2019

Citation:
Khan S, Ullah MW, Siddique R, Liu Y, Ullah I, Xue M, Yang G and Hou H (2019) Catechins-Modified Selenium-Doped Hydroxyapatite Nanomaterials for Improved Osteosarcoma Therapy Through Generation of Reactive Oxygen Species. Front. Oncol. 9:499. doi: 10.3389/fonc.2019.00499

Osteosarcoma is the most common bone cancer with limited therapeutic options. It can be treated by selenium-doped hydroxyapatite owing to its known antitumor potential. However, a high concentration of Se is toxic toward normal and stem cells whereas its low concentration cannot effectively remove cancer cells. Therefore, the current study was aimed to improve the anticancer activity of Se-HAp nanoparticles through catechins (CC) modification owing to their high cancer therapeutic value. The sequentially developed catechins modified Se-HAp nanocomposites (CC/Se-HAp) were characterized for various physico-chemical properties and antitumor activity. Structural analysis showed the synthesis of small rod-like single phase HAp nanoparticles (60 ± 15 nm), which effectively interacted with Se and catechins and formed agglomerated structures. TEM analysis showed the internalization and degradation of CC/Se-HAp nanomaterials within MNNG/HOS cells through a non-specific endocytosis process. Cell toxicity analysis showed that catechins modification improved the antitumor activity of Se-HAp nanocomposites by inducing apoptosis of human osteosarcoma MNNG/HOS cell lines, through generation of reactive oxygen species (ROS) which in turn activated the caspase-3 pathway, without significantly affecting the growth of human normal bone marrow stem cells (hBMSCs). qPCR and western blot analyses revealed that casp3, p53, and bax genes were significantly upregulated while cox-2 and PTK-2 were slightly downregulated as compared to control in CC/Se-HAp-treated MNNG/HOS cell lines. The current study of combining natural biomaterial (i.e., catechins) with Se and HAp, can prove to be an effective therapeutic approach for bone cancer therapy.

Keywords: osteosarcoma, catechins, selenium, hydroxyapatite, ROS, cancer therapy

INTRODUCTION

Cancer is the major health concerns and the second leading cause of death all over the world (1). Osteosarcoma, a commonly known bone cancer, cause malignant primary bone tumor with a high mortality rate, both in children and adolescents (2). It can easily metastasize to lungs after its germination in the distal femur and proximal tibia (3–8). In addition, the difficulty in cleaning up after the treatment increases the probability of recurrent osteosarcoma. Furthermore, the defects caused by surgery need to be filled for bone repair to relieve the physical limitations to patients. Therefore, extensive efforts have been devoted to the development of advanced targeted drug delivery systems and heat mediators to regulate oncogenes and tumorigenesis in treating osteosarcoma (9, 10).

The bone strength mainly relies on selenium (Se), calcium (Ca), and vitamins (K and D) contents. It is further enhanced by the addition of several other trace elements, such as manganese (Mn), zinc (Zn), fluorine (F), copper (Cu), magnesium (Mg), strontium (Sr), boron (B), and iron (Fe), etc. (11–15). Se deficiency is associated with the risk of developing multiple cancers; such as in bone, breast, ovary, prostate, gastrointestinal tract, and lungs (16, 17). To minimize the risk associated with the Se deficiency, its doping with hydroxyapatite (HAp) can be an effective approach which may potentially reduce the growth of osteosarcoma cells. Currently, HAp has received immense consideration in reconstructive surgeries, orthodontic, orthopedic substances, and three-dimensional printing of scaffolds owing to its high bioactive and osteoconductive properties (18–20). Its large surface area allows it to strongly interact with the neighboring bone and connective tissues *in vivo*. Se prevents the cancer development through generation of reactive oxygen species (ROS) (16); however, it possesses low anticancer activity when used at low concentrations, while its higher concentration can potentially inhibit the growth of normal cells leading toward osteosarcoma (21). This necessitates the improvement of its anticancer activity while still retaining its low or no toxicity toward the normal cells. To this end, its modification with another anticancer reagent to improve its antitumor activity can have the additive effect toward the osteosarcoma cells.

Green tea contains several important chemical reagents, among which 30% are catechins including epigallocatechin gallate (EGCG), epigallocatechin (EGC), epicatechin gallate (ECG), and epicatechin (EC). These play a preventive role against the development of different types of cancers (22–25). A recent study by Stadlbauer et al. suggested that epicatechin-3-O-gallate and 5,7-difluoro-epicatechin-3-O-gallate can potentially prevent the tumorigenesis during the initiation, promotion, and progression of cancer by diminishing the inflammation level through reduction of inflammatory lymphocytes (26). Similarly, EGCG affects several signal transduction pathways related to cancer development and exhibits strong anticancer activity by targeting several cell signaling pathways causing tumor growth suppression, induction of apoptosis through generation of reactive oxygen species, and inhibition of metastasis and angiogenesis (25, 27–30). In addition, it also exerts anticancer activity by acting as a chemo/radio-sensitizer when combined with conventional therapies (31). *In vitro* and *in vivo* studies have demonstrated that catechins control the cancer development by different mechanisms, such as through induction of apoptosis to control the cell growth arrest, through altered expression of cell-cycle regulatory proteins, by activating killer caspases, and through suppression of nuclear factor kappa-B activation (23). Catechins also act as carcinoma blockers by modulating the signal transduction pathways, involved in cell proliferation, transformation, inflammation, and metastasis (29, 32–37).

Owing to the known antitumor properties of catechins, the current study was aimed to develop catechins-modified Se-doped HAp nanocomposites (CC/Se-HAp) for potential application in osteosarcoma therapy. The developed nanocomposites were characterized by various physico-chemical and biological properties. The sequential self-assembly of green tea-derived catechins with Se-doped HAp resulted in formation of stable nanocomplexes which showed improved anticancer activity *in vitro* as compared to Se-doped HAp nanocomposite. These nanocomposites enhanced the ROS-mediated apoptosis through activation of caspase-3 pathway. These findings demonstrate the antitumor potential of the developed catechin-modified Se-doped HAp nanocomposites with the improved outcome to prevent the adverse and toxic effects of high concentration of Se toward the normal cells for cancer therapy.

MATERIALS AND METHODS

Materials

The chemical reagents, including calcium nitrate tetrahydrate ($Ca(NO_3)_2.4H_2O$) and sodium selenite (Na_2SiO_3), were purchased from National Medicine Chemical Reagent Company (China). Ammonium hydrogen phosphate ($(NH_4)_2HPO_4$) was purchased from Regal Biotech Technology, Inc. (Shanghai, China), whereas sodium polyacrylate [[[Inline Image]]$CH_{2[[InlineImage]]}CH(CO_2Na)$[[Inline Image]]]$_n$ (PPAS) (MW: 5100) from Sigma-Aldrich (St. Louis, MO, USA). Commercial Brazilian green tea was purchased from a tea center (Peshawar, Pakistan). In all experiments, ultrapure deionized (DI) distilled water was used. Dulbecco's Modified Eagle Medium (DMEM), fetal bovine serum (FBS), eagle's modified minimum essential medium (MEM), streptomycin, and penicillin were obtained from Hyclone (USA). The cell counting kit-8 (CCK-8) was purchased from Sigma Aldrich (St. Louis, USA).

Cell Culturing

Human osteosarcoma cell lines (MNNG/HOS) were kindly provided by Tongji Medical College of Huazhong University of Science and Technology, Wuhan, China. The human bone marrow stem cells (hBMSCs) were purchased from Chinese Center of Type Culture Collection of Wuhan University, Wuhan, China. The MNNG/HOS and hBMSCs cells were cultured in MEM and DMEM media, respectively. Both culture media were supplemented with 10% fetal bovine serum, 100 mg/mL streptomycin, and 100 unit/mL penicillin, and kept in an incubator at 37°C (5% CO_2, 95% relative humidity). The culture media for both cell lines were refreshed after 24 h.

Synthesis of HAp Nanoparticles

The pristine HAp nanoparticles were synthesized *via* aqueous precipitation method followed by sonication technique using calcium nitrate tetrahydrate ($Ca(NO_3)_2{\cdot}4H_2O$), ammonium hydrogen phosphate ($(NH_4)_2HPO_4$), and ammonium hydroxide (HN_4OH) solution as reported previously (15). A schematic representation of preparation of HAp nanoparticles is shown in **Supplementary Figure S1**. Briefly, 1.0 M calcium nitrate tetrahydrate solution was prepared in DI water with the desired concentrations of sodium selenite. The pH was adjusted to 10.5 with 25% (v/v) ammonium hydroxide solution. Thereafter, 0.6 M ammonium hydrogen phosphate solution (pH $\geq$ 9) was added dropwise (2.0–2.5 mL/min) into the cationic mixture to form a white precipitated mixture. The precipitated mixture was stirred for 4 h at 70°C, using sodium polyacrylate (PPAS, MW 5100) as a dispersant, followed by sonication for 20 min and allowed to settle down at room temperature for 24 h, until the formation of gel. The gel was collected *via* centrifugation, washed three-times with DI water, and dried at 60°C in a hot air oven.

Synthesis of Se-Doped HAp and CC/Se-HAp Nanocomposites

The stoichiometric Se-doped HAp and CC/Se-HAp nanocomposites were prepared by a modified aqueous co-precipitation method (16), using ammonium hydrogen phosphate, calcium nitrate tetrahydrate, and sodium selenite were used as sources of phosphorous (P), calcium (Ca), and selenium (Se), respectively (**Table S1**). Briefly, Se-HAp nanomaterial was prepared through dropwise and simultaneous addition of aqueous solutions of 5.45 mM $(NH4)_2HPO_4$ and 0.55 mM Na_2SeO_3 into the aqueous solution of $Ca(NO_3)_2{\cdot}4H_2O$, under vigorous stirring at 70°C. The pH was adjusted to 10.5 with 25% (v/v) ammonium hydroxide solution (**Supplementary Figure S1**, middle). The precipitate was stirred continuously for 24 h at 70°C, using PAAS as a dispersant, until the formation of a semitransparent and well-dispersed gel. This gel was then collected *via* centrifugation, washed three-times with DI water, and dried at 60°C in a hot air oven. For preparation of CC/Se-HAp nanocomposites, different catechins solutions (CC-1, CC-2, and CC-3) were prepared from green tea (**Supplementary Material**), and subsequently used to prepare CC/Se-HAp-1, CC/Se-HAp-2, and CC/Se-HAp-3 nanocomposites, respectively (**Supplementary Figure S1**).

Characterization

The synthesized pristine HAp nanoparticles, and Se-HAp and CC/Se-HAp nanocomposites were characterized for various structural and chemical properties. The phase composition of synthesized HAp, Se-HAp, and CC/Se-HAp was investigated by using XRD (PANalytical B.V., Netherlands). The morphology of synthesized nanomaterials was examined by transmission electron microscopy (TEM, Tecnai G2 20, FEI, Holland), while structural analysis was carried out using Gemini scanning electron microscope, SEM 300 (Zeiss Germany). FTIR (Vertex 70, Bruker, German) analysis was carried out to investigate the functional groups present in the pristine nanoparticles, using the classical KBr pellet system technique in transmission mode (See **Supplementary Material** for detailed information).

Cellular Uptake Analysis

The cellular uptake of CC/Se-HAp nanomaterials was determined through TEM analysis (38). Briefly, the synthesized nanomaterials were directly added to the culture dishes, separately containing human osteosarcoma cell line (MNNG/HOS), at a concentration of 50 μg/mL and cultured in MEM medium for 12 h. The medium was changed after every 2 days. For TEM analysis, the cell sections were immediately prepared and observed with a specific cell TEM (H-7000FA, HITACHI, Japan) by following a previously published protocol (39). Briefly, the overnight cultured seeded cells (1×10^6 cells per well) were treated with nanomaterials in reduced serum (MEM) and cell monolayers were rinsed with D-PBS and fixed in a mixture of 2% paraformaldehyde, 2.5% glutaraldehyde, and 0.15 M sodium phosphate at pH 7.4, and incubated overnight at 37°C. The monolayers were fixed in a mixture of 1% osmium tetroxide, 1.25% potassium ferrocyanide, and 0.15 M sodium phosphate buffer and rinsed in DI water. Cells were embedded in polybed epoxy resin after dehydrating them using acetone. Finally, the ultrathin sections were stained with 4% aqueous uranyl acetate and Reynolds' lead citrate and observed under TEM.

In vitro Cytotoxicity Assay

The cytotoxic effects of Se-HAp, CC/Se-HAp, and $NaSeO_3$ (control) against human bone marrow stem cells (hBMSCs) and human osteosarcoma cell line (MNNG/HOS) were measured using a CCK-8 assay kit. Briefly, the cells were seeded at a density of 1×10^4 cells per well in a 96-well plate followed by adding 100 μg/mL of each nanomaterial to respective well. The plates were incubated for 6, 12, 18, 24, 36, 42, and 48 h. After incubation, the portion of viable cells was determined using CCK-8 assay according to the manufacturer's protocol (**Supplementary Material**). Optical density (OD) values were measured for all samples at 450 nm using a microplate reader (Eon, BioTek, USA). The viability of cells was expressed as a percentage of untreated control cells.

Caspase-3 Activity Assay

Caspase-3 activity was assessed calorimetrically using the CaspACE Assay System (Promega, Madison, WI, USA), following the manufacturer's instructions. The MNNG/HOS cells at a density of 1×10^6 cells per well were treated with caspase inhibitor Ac-DEVD-CHO (or antioxidant N-acetyl-cysteine). Cells were then treated with CC/Se-HAp nanomaterials and incubated for 18 h prior to lysis. Cell lysates were incubated with the caspase-3 substrate for 4 h. Free Ac-DEVD-p-nitroaniline was monitored by a spectrophotometer at 405 nm.

Determination of Intracellular ROS Level

ROS generation was measured by a previously reported method using a non-fluorescent probe, 2,7-diacetyl dichlorofluorescein (H_2DCFDA) (16, 40). Briefly, the MNNG/HOS cells were cultured in 6 and 24-well plates at a density of 1×10^6 cells

per well, for 16 h and incubated with CC/Se-HAp (100 μg/mL), HAp (100 μg/mL), and sodium selenite (2 μM) for 6, 8, 10, and 24 h. The cells were then incubated with 1 μM of DFCH/DA for 30 min at 37°C and washed three times with phosphate buffer saline (PBS) and resuspended in PBS. ROS generation was measured by flow cytometry (Cytomics FC500, Beckman Coulter, U.S.A.) at 485 nm excitation and 538 nm emission wavelengths. To investigate the inhibition effect of ROS generation in the presence of CC/Se-Hap, N-acetylcysteine (NAC) was added to each well and cultured for 1 h before incubation with materials under investigation. The inhibition effect of ROS generation was also confirmed by adding MnTMPyP (10 μM) to each well and cultured for 1 h before incubation with the nanomaterials.

Western Blot Analysis

Cells were cultured and treated with Na_2SeO_3, Se-HAp, and CC/Se-HAp. The cells were then lysed using lysis buffer on ice for 20 min and centrifuged at 12,500 rpm for 10 min at 4°C. The protein concentration was determined by BCA assay (Thermo-Fisher Scientific) according to the manufacturer's instructions. Loading of 60 μg protein onto SDS-polyacrylamide gel was followed by electrophoresis and transferred to polyvinylidene fluoride (PVDF) membrane. The membrane was blocked with blocking buffer containing TBS [Tween-20 (0.1%), tri-sec-buffer saline (10%), DI water (89.9%)], and 5% skimmed milk for 2 h and incubated overnight at 4°C with monoclonal antibodies against gapdh, p53, bcl-2, caspase3, caspase9, cox-2, nf-kb, and bax. The membranes were then soaked with horseradish peroxidase (HPR)-conjugated secondary antibodies for 1 h at room temperature. The immunoblots were observed using chemiluminescence system (Bio-Rad, Hungary Ltd) according to the manufacturer's instructions.

Apoptosis Analysis

The qualitative apoptosis of MNNG/HOS cells was determined by treating comparable number of cells (1×10^6 cells per well) with both Na_2SeO_3 and CC/Se-HAp nanomaterials in a 12-well plate. The cells were washed with PBS and fixed in cold methanol: acetone solution for 5 min. The cells were then treated with DAPI (4 μg/ml 4,6-diamidine-2-phenylindole dihydrochloride) at room temperature for 10 min. The cells were examined by fluorescence microscopy (Olympus) at 200× magnification. For quantitative apoptosis study, MNNG/HOS cells were seeded onto 12-well plates (10^6 cells/well). After incubation, the cells were treated with Na_2SeO_3 and CC/Se-HAp, keeping untreated cells as a control. The cells were trypsinized after incubation for 24 h, collected, and resuspended in 350 μL binding buffer. Then 4 μL annexin V-FITC and 8 μL PI were added to the cell suspension and mixed in dark for 15 min prior to flow cytometry analysis.

Quantitative Real-Time Polymerase Chain Reaction

The apoptosis-related gene expression levels were analyzed using real-time PCR. The total RNA of cells, both treated with the nanomaterials under investigation and control, was extracted by using Trizol reagent according to the manufacturer's instructions (Thermo-Fisher, Applied Biosystems). The RNA concentration was measured using a spectrophotometer. cDNA was synthesized using a high capacity RNA to cDNA kit (Thermo-Fisher, Applied Biosystems). qPCR analysis was performed according to the standard protocol (Applied Biosystems). The forward and reverse primers were generated through Primer-BLAST (NCBI) and/or primer-3.0 (**Table S2**). Relative gene expression was quantified by the ΔΔCT method using ACTIN as a reference gene.

Statistical Analysis

Results were expressed as means ± SD for each group. The analyses were performed using the two-tailed student's *t*-test. Statistically significant differences between the control and CC/Se-HAp nanomaterials were considered at $^*p < 0.05$. All statistical analyses were performed in Prism Software (Graph Pad Prism 7, La Jolla, CA, USA) and MS Excel 2016 (Microsoft).

RESULTS

Synthesis of CC/Se-HAp Nanomaterials

The catechins-modified selenium-doped hydroxyapatite nanoparticles (CC/Se-HAp) were synthesized through the aqueous precipitation method (**Figure S1**). According to the previous reports, selenium replaces phosphate during the synthesis of HAp nanoparticles (16, 19, 21, 41). The synthesized Se-HAp nanoparticles were modified with catechin contents through vigorous mixing in a sonicator. It was hypothesized that catechins modification of Se-HAp nanoparticle will enhance their anticancer activity owing to the known anticancer activities of individual catechins and Se-HAp nanoparticles. The prepared nanomaterials were characterized for various physico-chemical properties such as size, chemical structure, structural morphology, and colloidal stability, which are important factors in the designing of nanoparticles (39).

Structural Analysis of CC/Se-HAp Nanomaterials

XRD analysis of the as-prepared nanomaterials was carried out to investigate the basic polymorphic structure of HAp and any structural variations during the Se-doping and catechins modification (**Figure 1**). The XRD spectrum of the extended linear scanning (10–70°) of HAp showed characteristic peaks confirming its successful synthesis, where the peaks were comparable with the standard HAp (JCPDS card no. 24-0033). Further, the intense and sharp peaks indicate the crystalline nature of synthesized HAp nanoparticles. The Se-doping of HAp slightly altered its crystallinity as indicated by the less intense crystallinity peaks. The Se-HAp and CC/Se-HAp samples showed a single phase (solid solution) with a hexagonal structure [space group, p63/m (176)]. The XRD spectra of CC/Se-HAp-1, CC/Se-HAp-2, and CC/Se-HAp-3 further indicated the synthesis of crystalline nanoparticles with crystallinity scope inferior to pristine HAp and Se-HAp. This crystallinity scope was further decreased with the increased concentration of catechins. Additionally, the peak intensities were slightly shifted toward higher 2θ value and three major differential peaks (211), (112), and (300) were merged into single peak, which indirectly indicates the substitution effect with nanosized

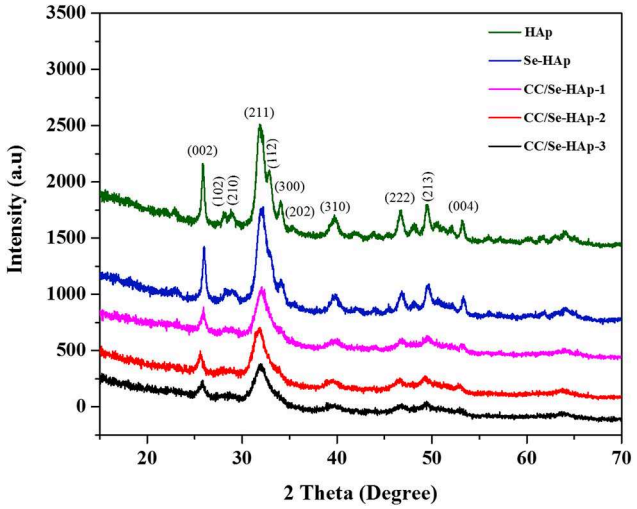

FIGURE 1 | X-ray diffraction spectra of pristine HAp nanoparticles, and selenium-doped hydroxyapatite (Se-HAp), and modification of Se-HAp composites with different concentrations of catechins, i.e., 5% (CC/Se-HAp1), 7% (CC/Se-HAp2), and 10% (CC/Se-HAp3). The patterns of XRD depicted that both HAp and Se-HAp presented the typical HAp peaks, with the no significant differences. The peak (211) associated CC/Se-HAp showed a reduction in crystallinity which determines the association of catechin contents.

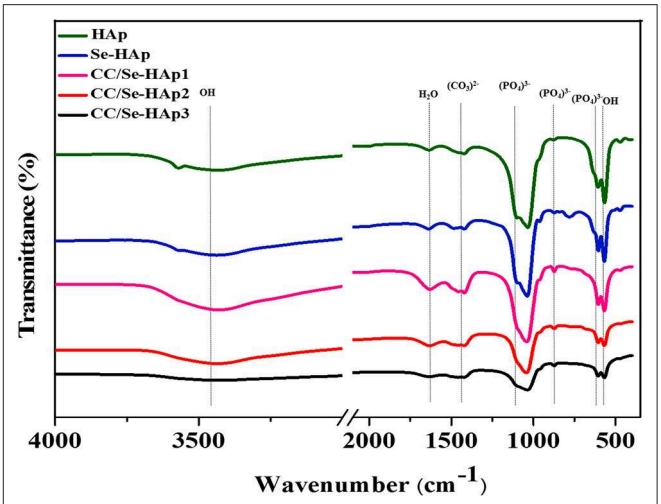

FIGURE 2 | Fourier transform infrared spectra of pristine HAp, Se-HAp, and its modification with different concentrations of catechins, i.e., 5% (CC/Se-HAp1), 7% (CC/Se-HAp2), and 10% (CC/Se-HAp3). The peaks show that both HAp and Se-HAp presented the typical HAp functional groups, with a decrease in intensity (1,000 cm^{-1}) upon catechins modification.

TABLE 1 | Summary of effect of selenium and catechins contents on the lattice parameters (a and c), unit cell volume, crystal size, and crystallinity of pristine HAp and catechins-modified selenium-doped HAp nanocomposites.

Sample	Lattice parameters (Å)		Unit cell volume $(Å)^3$	Crystallinity (X_C)	Crystal size (D_{002}) nm
	a	c			
HAp	9.4482	6.883	532.10	1.612	29.78
Se-HAp	9.3804	6.8547	522.33	1.13	25.45
CC/Se-HAp1	9.3546	6.8499	519.18	0.22	21.58
CC/Se-HAp2	9.3215	6.8676	516.76	0.20	18.91
CC/Se-HAp3	9.2989	6.8442	512.51	0.13	15.89

features. The effect of Se-doping and catechins modification on lattice parameters (a and c), unit cell volume $(Å)^3$, crystal size (D), and crystallinity (X_c) are summarized in **Table 1**.

Chemical Structure Analysis of CC/Se-HAp Nanomaterials

FTIR spectroscopy was used to investigate the presence of specific functional groups (**Figure 2**) (42). The peaks for O-H vibrations were observed at 633 cm^{-1} and 3,500–3,000 cm^{-1}. The peak at 1,640 cm^{-1} was assigned to the bending mode of H_2O molecule present in the HAp lattice, which are in agreement with previous reports (41, 43). The peaks observed at 1,486, 1,459, 1,420, 1,424, and 872 cm^{-1} correspond to the carbonate (CO_3^{2-}) groups, which indicated its substitution at PO_4^{-3} (B-site) and OH positions (A-site) in the HAp lattice. The substitution of CO_3^{2-} in the OH group might result in an increased length of the unit cell toward the a-axis and a decline toward c-axis, as reported previously (44). Similarly, the peaks for stretching vibrations due to OH group were present at 3,570 cm^{-1} and 630 cm^{-1} (45, 46) in all spectra of HAp, Se-HAp, and CC/Se-HAp samples while its intensity was relatively low in the spectrum for Se-HAp nanocomposite.

Structural Morphology of CC/Se-HAp Nanomaterials

From **Figure 3**, TEM analysis showed the formation of small rod-like structure of various HAp samples under investigation. The modified aqueous precipitation method effectively maintained the rod-like morphology of HAp upon doping with Se and catechins modification, and were well-dispersed in PBS and formed a stable colloidal suspension even when stored for over a month.

According to SEM micrographs (**Figures 4A–E**), the size of different HAp samples was estimated to be 60 ± 15 nm as determined *via* "Fiji v2" software, indicating their nano-crystalline features. The micrographs of pristine HAp and Se-HAp showed that the nanoparticles were nearly uniformly distributed and formed a moderately rough surface with slight pores, and particles were observed with dominant small rod-like morphology (**Figure 4**). In contrast, the Se-HAp samples with catechins content were highly agglomerated and exhibited dense rough surface with small rod-like morphology (**Figures 4B–E**). These results indicate that incorporation of Se and catechins content into HAp structure resulted in the synthesis of highly-agglomerated material and the particles exhibited small rod-like morphology. The strong agglomeration among the particles was due to the presence of catechins content which could be defined by the decreased particle size as confirmed *via* XRD analysis (**Figure 1**). XRF analysis was carried out to confirm the formation of HAp, Se-HAp, and CC/Se-HAp nanomaterials and to measure

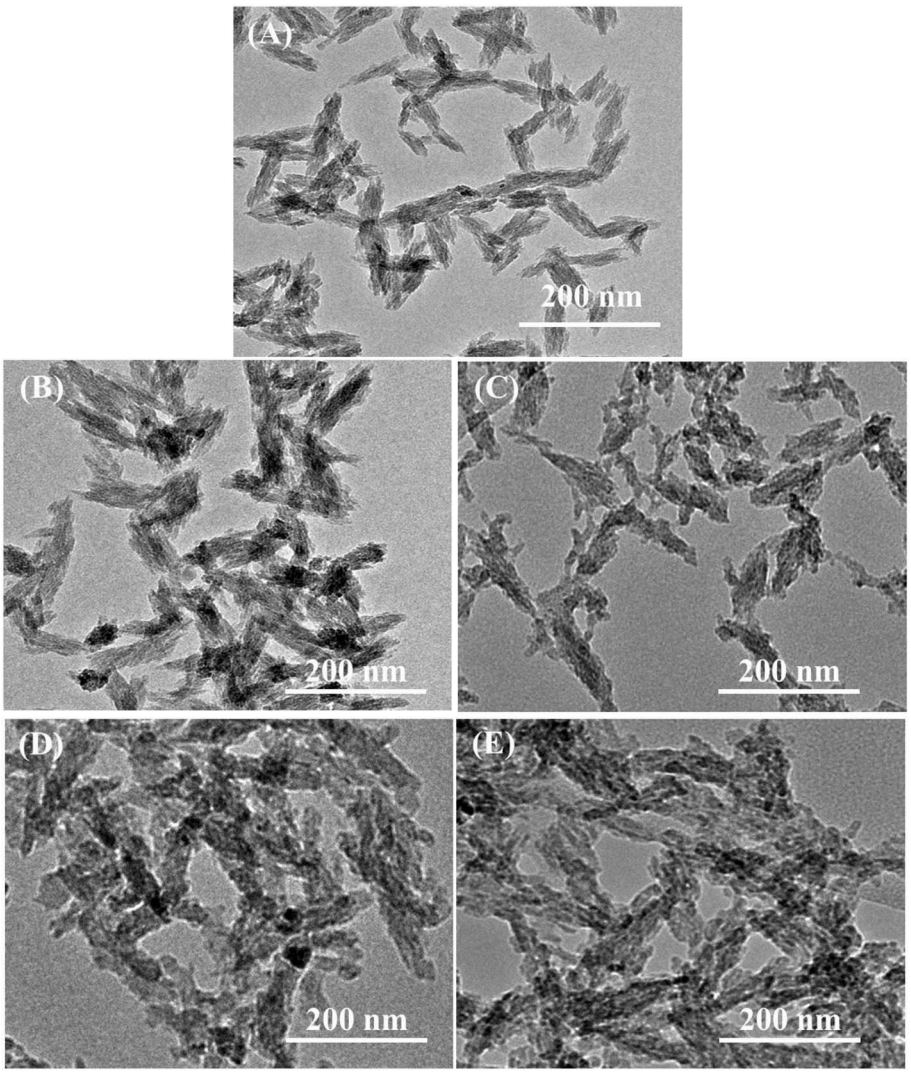

FIGURE 3 | Transmission electron micrographs of **(A)** pristine HAp nanoparticles and **(B)** Se-HAp, **(C)** CC/Se-HAp1, **(D)** CC/Se-HAp2, and **(E)** CC/Se-HAp3 nanocomposites.

the degree of atomic percentage of Se substituted/doped during the synthesis of nanocomposites. The elemental mapping *via* XRF showed that Se distribution in CC/Se-HAp was reduced in comparison with HAp and Se-HAp where it was evenly distributed in the entire nanocomposite and was comparable to Ca and phosphate ions (**Figures 3**, **4**). Overall, these findings imply that the incorporation of Se and catechins into HAp lattices did not alter the primary features of HAp nanoparticles including the physical dimension, geometrical shape, and crystal lattice. The integrated Se have the potential to be delivered *via* a degradation-mediated sustained release.

In vitro Cytotoxicity of CC/Se-HAp Nanomaterials

The *in vitro* anticancer activity of CC/Se-HAp nanomaterials was investigated against MNNG/HOS cells, using CCK-8 assay kit. The principle of this assay is that the color of developing substrate WST-8 is reduced by the intracellular dehydrogenase in live cells to water-soluble orange colored formazan, which is directly quantified photo-metrically and its absorbance reflects the number of viable cells in the culture medium (47). As shown in **Figure 5A**, the Se-HAp is much less toxic to MNNG/HOS cells as compared to CC/Se-HAp, confirming the improved activity of CC/Se-HAp against MNNG/HOS cells upon catechins modification. Further, CC/Se-HAp-3 showed high toxicity toward the cells as compared to CC/Se-HAp-1 and CC/Se-HAp-2 nanocomposites. In contrast, the Se-HAp nanoparticles showed toxicity toward MNNG/HOS; however, it was much lower than CC/Se-HAp nanocomposites. To investigate the safety of the developed CC/Se-HAp nanocomposites toward the normal cells, their toxicity effect was determined toward the stem cells (hBMSCs) and the results are shown in **Figure 5B**. The results showed significantly higher toxicity of Se-HAp toward hBMSCs as compared to CC/Se-HAp. Furthermore, the response

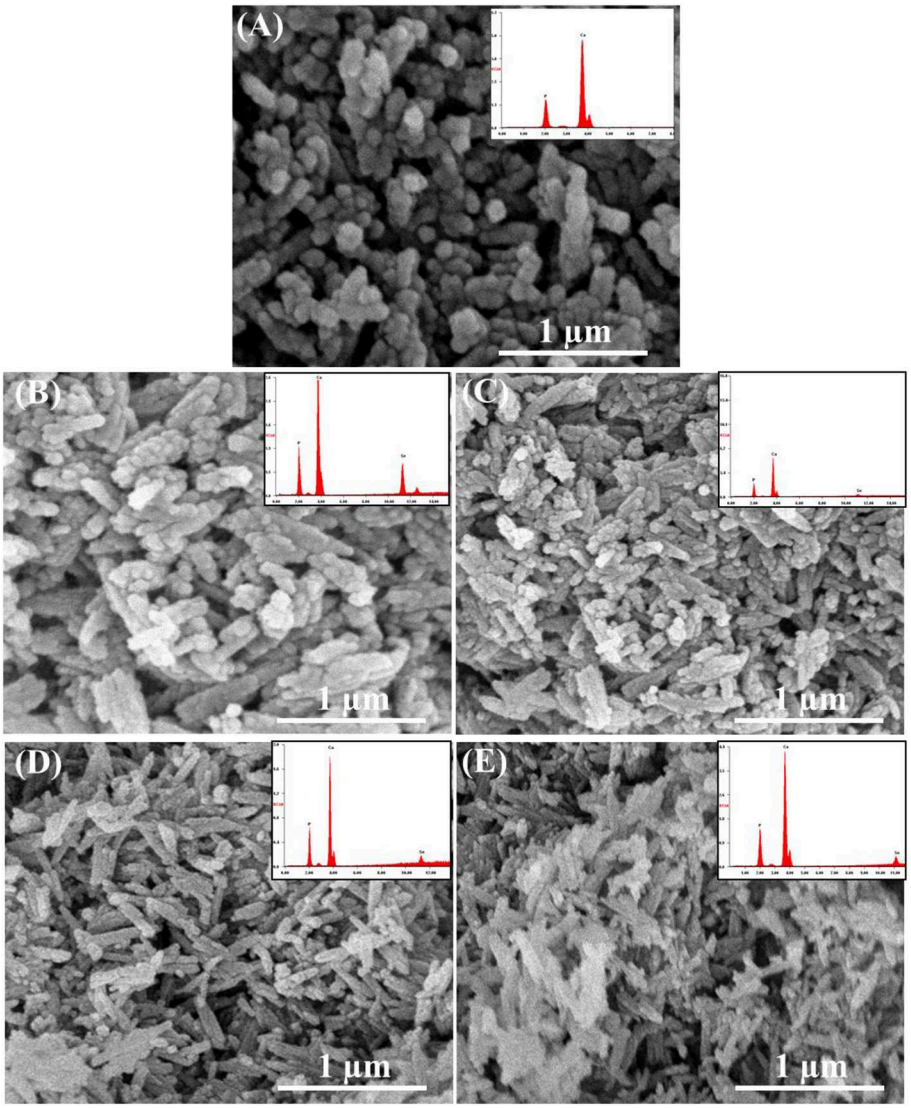

FIGURE 4 | Field-emission scanning electron micrographs and XRF spectra (inset) of **(A)** pristine HAp nanoparticles, and **(B)** Se-HAp, **(C)** CC/Se-HAp1, **(D)** CC/Se-HAp2, and **(E)** CC/Se-HAp3 nanocomposites.

of CC/Se-HAp to MNNG/HOS and its degradation behavior was also confirmed by cytotoxicity evaluation. It indicated that incubation time was directly associated with the cytotoxicity of nanoparticles (**Figure 5C**). For instance, the cell viability was mainly associated with the degradation of nanoparticles. Cell viabilities of CC/Se-HAp-3, CC/Se-HAp-2, CC/Se-HAp-1, Se-HAp, Se, and HAp were 98, 91, 98, 81, 76, and 100%, respectively, after the interaction of cells and nanoparticle for 6 h. Moreover, these viability values were 5, 14, 28, 37, 29, and 100%, respectively, after cell-nanoparticles interaction for 48 h. Se (representation for Na_2SeO_3) was used as a positive inhibition control, which showed prominent inhibition effect. Surprisingly, the inhibition effect of Se-HAp was superior to CC/Se-HAp up to 18 h; however, the cytotoxicity of CC/Se-HAp nanoparticles increased continuously until the maximum incubation period of 48 h. These results indicate that catechins and selenium contents of CC/Se-HAp affect the cell viability and lysosomal permeability. Higher catechin contents along with selenium in CC/Se-HAp nanomaterials result in lower cell viability due to faster degradation rate. The apoptosis during earlier incubation (0–24 h) might be attributed to the phase of burst release, whereas the high cytotoxic effect could be due to the sustained release during the extended incubation (24–48 h). These results demonstrate that catechins modification of Se-HAp increased its toxicity toward the cancer cell lines (MNNG/HOS) due to their degradation within the cell.

Internalization and ROS Generation

TEM micrographs indicated the internalization of CC/Se-HAp nanomaterials into MNNG/HOS cells *via* endocytosis. After encapsulated in the endosomes, the nanomaterials were transported to lysosome for intracellular degradation (**Figure 6C**,

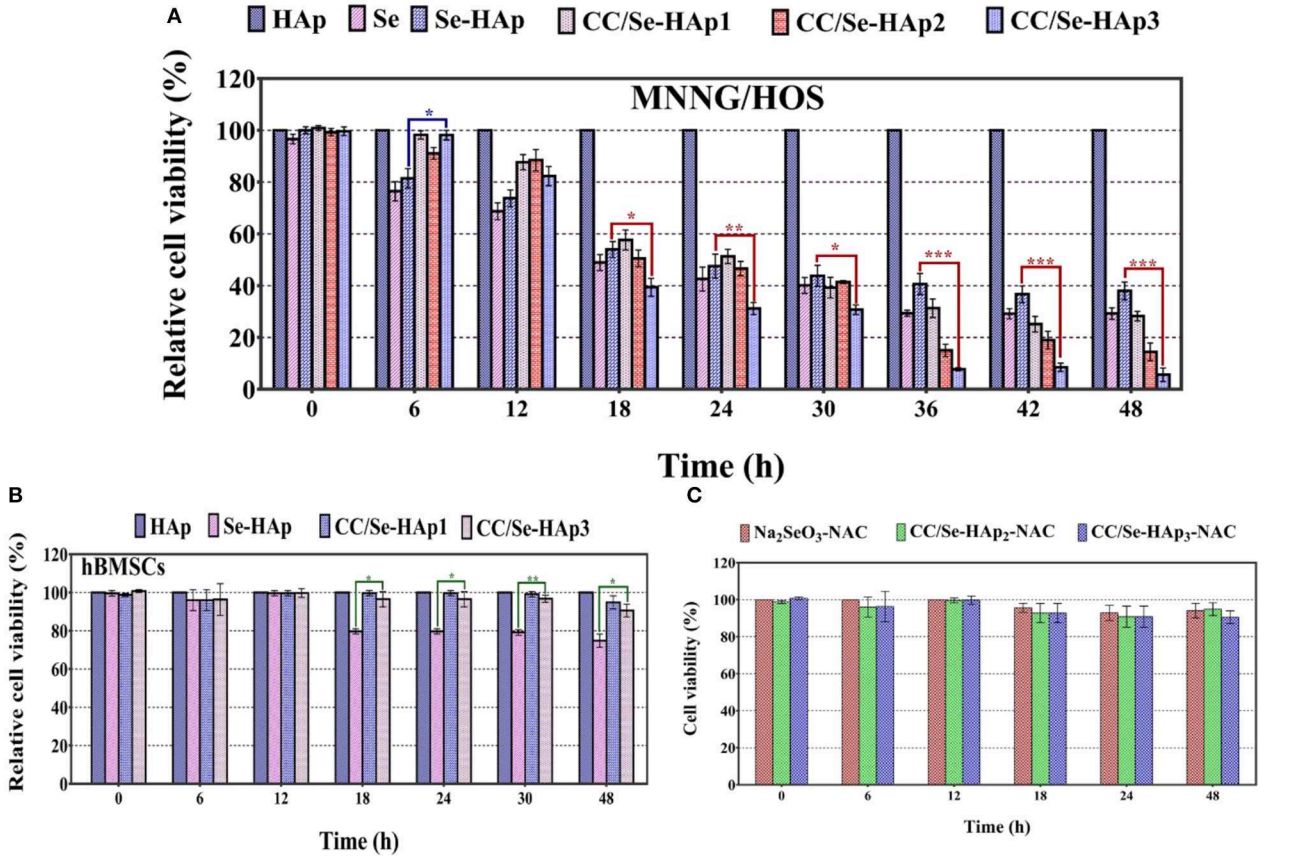

FIGURE 5 | (A) Cytotoxicity analysis of human osteosarcoma cell line (MNNG/HOS) against Se-HAp and its modification with different concentrations of catechins, i.e., 5% (CC/Se-HAp1), 7% (CC/Se-HAp2), and 10% (CC/Se-HAp3) relative to control. **(B)** Viability analysis of human bone marrow stem cells (hBMSCs) on Se-HAp and its modification with 5% catechins (i.e., CC/Se-HAp1) and 10% catechins (i.e., CC/Se-HAp3) relative to control. **(C)** ROS inhibitor attenuated the cytotoxic effect of nanoparticles, which resulted in higher cell viability. $^{*}p < 0.01$, $^{**}p < 0.001$, $^{***}p < 0.0001$ indicate significant differences of CC/Se-HAp-3 in comparison with Se-HAp.

Figure S3) and increasing lysosomal permeability. The gradual degradation of internalized nanomaterials in the lysosomes was confirmed by their gradually increased activity with the incubation time. The anticancer drugs have been extensively reported to kill the cancer cells through ROS generation (16, 25, 48). Therefore, we investigated the underlying mechanism of CC/Se-HAp mediated apoptosis of cancer cells through ROS generation by hypothesizing that CC/Se-HAp nanomaterials can induce ROS production in mitochondria. To verify the proposed hypothesis, we detected the ROS generation at specific time intervals (0, 6, 8, 12, 18, and 24 h) by monitoring the "fluorescent product of DCF." This unique ROS indicator was generated during the processes of ROS production (**Figure 6A**). The results showed the highest level of DCF in response to the treatment of cancer cells with CC/Se-HAp-3. This analysis further indicated that CC/Se-HAp-3 nanoparticles induced highest ROS production after cell-nanomaterials interaction for 18 h. This ROS produced level was significantly higher than that of Se-HAp and Se (Na_2SeO_3). These results depicted that such a low cell viability caused by CC/Se-HAp was induced by ROS generation that caused cell apoptosis. To further confirm these results, we inhibited the ROS generation by treating the cancer cells with *N-acetylcysteine* (NAC) prior to nanoparticles treatment. With this treatment, the CC/Se-HAp-3 treatment indicated almost 100% cell viability of cancer cells, as the nanoparticles could not induce the apoptosis after the inhibition of intracellular ROS generation (**Figure 6B**). The inhibition of ROS generation also inhibited the cytotoxic effect of nanoparticles (**Figure 6C**). Therefore, these results depicted that ROS generation is a key player in the process of CC/Se-HAp mediated cancer cells apoptosis.

Regulation of Apoptosis-Associated Genes

The expression ratios of CASP-3, CASP-9, TP-53, COX-2, BCL-2, BAX, NF-kB, and FAK (PTK-2) in MNNG/HOS cells treated with nanomaterials for 24 h in comparison with non-treated cells, using qPCR are shown in **Figure 7A**. These findings demonstrate that the relative expressions of P-53, CASP-3, and BAX genes were significantly upregulated, while that of BCL-2 and COX-2 were slightly reduced. To further confirm the qPCR results of the ROS and apoptosis-related genes, their expression levels were measured using western blot technique. According to the western

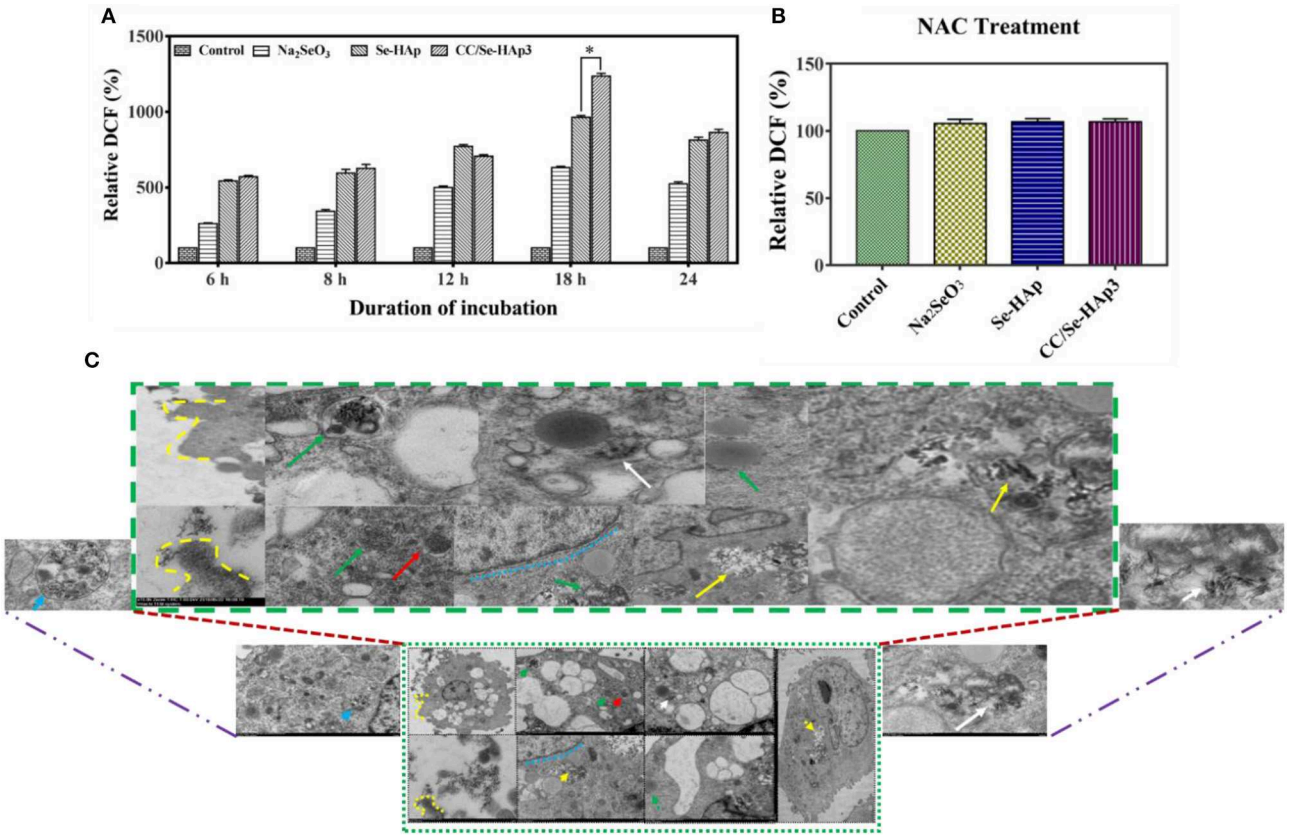

FIGURE 6 | ROS generation and internalization of nanoparticles. **(A)** Relative fluorescence intensity of DCF (percent) generated during the process of ROS formation demonstrated that CC/Se-HAp exhibited a remarkable increase in DCF, as compared to Se-HAp or Na_2SeO_3. **(B)** Relative fluorescence intensity of DCF (percent) in presence of ROS inhibitor was non-detectable in presence of both catechin and selenium. **(C)** TEM micrographs illustrating the internalization of CC/Se-HAp nanomaterials into the human osteosarcoma cell through a typical endocytosis process. TEM images show that the nanoparticles were internalized by human osteosarcoma cells through a typical endocytosis process. Yellow dotted lines describe cell membrane invagination that is followed by endosome formation. Red arrows specifying region indicates newly generated endosomes loaded with nanoparticles. Green arrows determine the primary lysosome combined with the endosome. White arrows denote the degradation and release of active agents. Blue arrows represent the noticeable degradation of nanoparticles within the lysosome (secondary). Yellow arrows represent the nanoparticles in the vicinity of the nucleus (probably lysosomal disruption). *$p < 0.01$ indicates significant differences of ROS generation in response to CC/Se-HAp treatment in comparison with Se-HAp treatment.

blot results, bcl-2, cox-2, and fak were down-regulated whereas caspase-3, caspase-9, p-53, nf-kb, and bax were upregulated in osteosarcoma cells in response to CC/Se-HAp nanoparticles treatment as compared to control (**Figure 7C**). These results are consistent with the qPCR results, which in turn are consistent with ROS generation and apoptosis.

It is well-documented that ROS generation induces caspase activation (17). Therefore, activation of caspase-3 was confirmed using CaspACE Assay System. The results showed that CC/Se-HAp induced caspase-3 activation in osteosarcoma cells (**Figure 7B**). The quantitative analysis showed that CC/Se-HAp activated higher levels of caspase-3 as compared to Se-HAp. These results strengthen the ROS-mediated apoptosis in CC/Se-HAP treated cancer cells. To further confirm the caspase-3 activation, the CC/Se-HAp-induced caspase-3 activity was determined by treating the osteosarcoma cells with caspase inhibitor using NAC. This treatment indicated similar caspase-3 levels in cancer cells treated with CC/Se-HAp-3, Se-HAp, and control. To further analyze the apoptotic effect of CC/Se-HAp nanoparticles, the osteosarcoma cells were treated with nanomaterials and analyzed through flow DAPI staining. The results demonstrated that nuclei of cells treated with nanomaterials were smaller and brighter stained with the crescent shape as compared to that of control cells which possessed intact and rounded nuclei with diffuse DAPI staining (**Figure 7D**). Furthermore, the cells showed separate globular structures (apoptotic bodies) around the periphery. The DAPI staining showed a dramatic increase in the number of apoptotic cells treated with CC/Se-HAp nanoparticles. DAPI staining revealed that exposure of cells to nanoparticles markedly increased the apoptosis, coincidently with the cytotoxicity test. In contrast, annexin V-FITC staining showed the notable percentage of early and late apoptotic cells in response to CC/Se-HAp treatment as compared to cells treated with Na_2SeO_3 (**Figures S2, S3**). These results demonstrate that CC/-Se-HAp nanomaterials enhanced the cellular apoptosis.

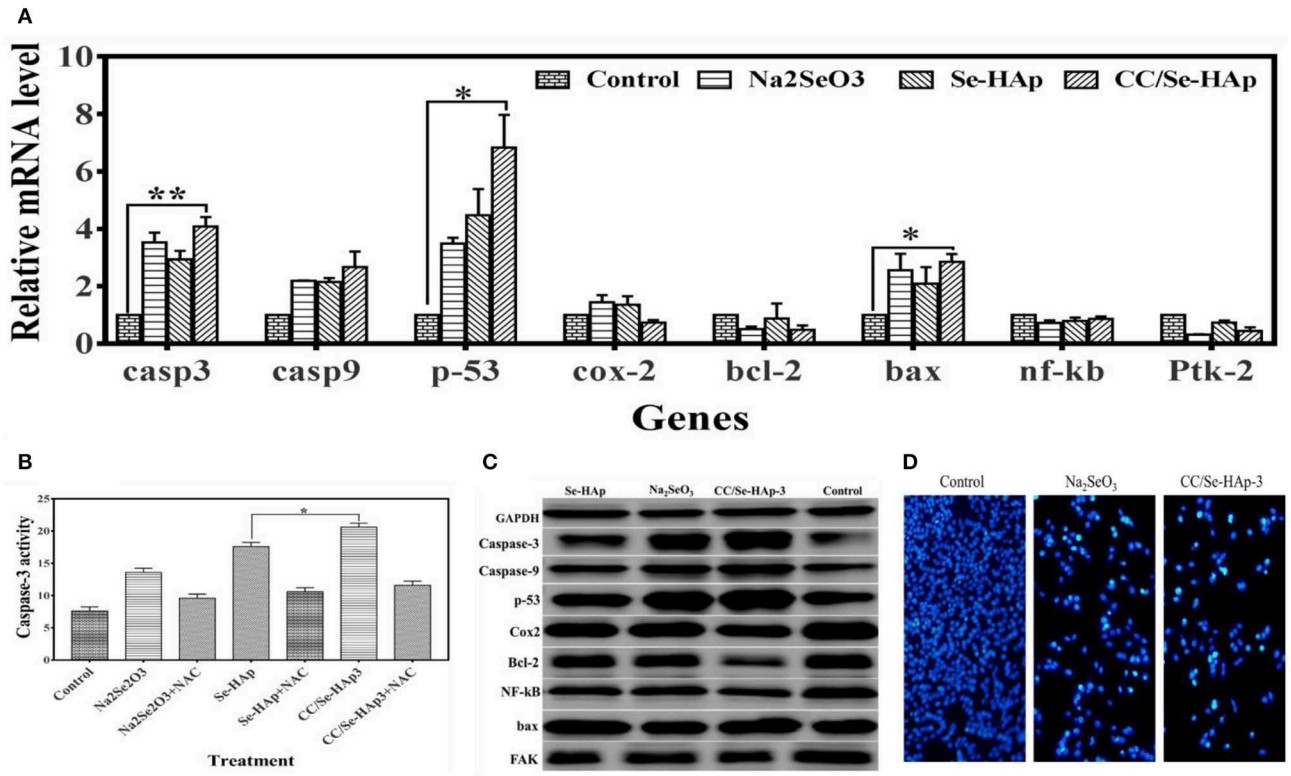

FIGURE 7 | Molecular analysis associated with apoptosis of MNNG/HOS cells treated with nanoparticles. **(A)** Expression levels of genes (analyzed through qPCR) associated with cancer and/or apoptosis were altered, which indicate their association with nanoparticles treatment. **(B)** The caspase-3 activity assay was evaluated by using the CaspACE Assay System. The increase in caspase-3 determines that CC/Se-HAp-mediated apoptosis is involved caspase-3 pathway. **(C)** Key proteins involved in apoptosis and cancer were analyzed using western blot in order to confirm the qPCR results. Western blot indicates the alteration in protein levels in response to treatment of nanoparticles. **(D)** The qualitative analysis of apoptosis using fluorescence cytometry confirms the effectiveness of nanoparticles. $^{*}p < 0.05$ and $^{**}p < 0.01$ indicate significant differences in comparison with control.

Overall, these results indicate that two agents (i.e., catechins and selenium) simultaneously induced ROS generation for subsequent activation of caspase-3 and upregulation of P53, which led to higher apoptosis of cancer cells.

DISCUSSION

Natural bone is a hierarchically structured material assembled from basic building blocks of mineral nanoparticles in the frame of bone tissues and collagen protein, which become weak as a result of osteosarcoma (49). To treat osteosarcoma, different strategies including tissues cleaning and bone surgery are currently in practice; however, such strategies are not as accurate and lead to physical disability and recurrence of osteosarcoma. Therefore, targeted and specific therapeutic agents are required to completely kill the cancer cells. Hydroxyapatite is the main inorganic mineral in vertebrate bones and tooth enamels that has been extensively studied as excellent bone substitutes. Its doping with selenium has been reported previously as a potential anticancer agent (16, 17); however, it is toxic toward the normal cells when used at higher concentrations. Therefore, modification of Se-HAp nanoparticles with other anticancer agents, such as catechins, could be used to protect bone cancer metastasis and potentiate cancer cells removal. In the current study, a series of catechins-modified Se-doped HAp (CC/Se-HAp) nanocomposites were prepared and characterized for various physico-chemical and biological properties. In addition, the nanomaterials were evaluated for their size, morphology, and colloidal stability which are important factors in the designing of nanoparticles (39). Further, the developed nanomaterials showed a higher anticancer activity as compared to Se-HAp nanoparticles *in vitro*.

As reported previously, the nanoparticles having a size <100 nm possess better cell endocytosis (50–53) and mechanical compatibility with natural bone can effectively promote osteogenesis (54, 55). To this end, the developed nanoscale HAp nanoparticles (60 ± 15) can serve as ideal template for the development of new bone and effective nanocarrier in anticancer drug delivery system. TEM micrographs (**Figure 3**), showed that the developed nanomaterials possessed nano-dimensional size and single crystalline structure. Moreover, the CC/Se-HAp nanomaterials existed in a uniaxial-like form, i.e., larger dimensions in length (axial) and smaller dimensions in width (equatorial). Further, FTIR spectrum of pristine HAp showed the distinctive peaks for the triply degenerate υ_3 asymmetric and

non-degenerate υ_1 symmetric of P-O stretching vibrations were present between 1,200 and 900 cm^{-1}, which are in agreement with a previous report (46). Similarly, the double degenerate υ_2 and triple degenerate υ_4 bending of O-P-O were present between 600 and 400 cm^{-1} for all samples which is in accordance with the typical FTIR pattern of HAp (15, 41, 56).

Both selenium and catechin doses separately have been reported to have direct cytotoxic effects on malignant tumors *in vitro* and *in vivo* (16, 29, 31, 48). However, these particles are far behind the clinical studies due to their toxicity toward the normal cells and show low activity against cancer cells. Therefore, combining catechins with Se-HAp is expected to minimize the toxic effects of selenium toward the normal cells. Our data showed that CC/Se-HAp nanoparticles caused tumor growth inhibition through ROS generation in P53 mediated pathway, as indicated by the higher ROS generation and increased P53 levels (**Figures 7A,D**). Previous *in vitro* studies showed that Se-HAp nanoparticles induce ROS generation that leads to apoptosis (16). Comparatively, our data showed that CC/Se-HAp can induce higher cancer cell apoptosis (**Figure 7A**). In addition, the cytotoxicity results of CC/Se-HAp nanomaterials are comparable with a study which showed that nanoparticles with a size <100 nm possess better cell endocytosis efficiency as compared to those with a larger size (16). Therefore, the needle-like HAp nanoparticles prepared in the present study were expected to induce cytotoxicity and can effectively promote osteogenesis, as reported previously (16).

Generally, the cell viability is associated with the degradation of nanoparticles; therefore, the cell apoptosis was sufficiently higher after the cell-nanoparticles interactions for 24 h. These findings imply that Se and catechin contents in CC/Se-HAp nanoparticles after degradation in lysosome led to cell apoptosis. Researchers have explored the antitumor potential of different nanoparticles through ROS induction. For instance, Zn^{2+} could trigger ROS generation, thereby activates a p53-mediated apoptotic pathway (16, 57). Furthermore, catechins selectively induce ROS generation only in cancer cells (25). In current study, the higher levels of P53 and caspase-3 indicate the antitumor activities of selenium ions and catechin contents due to ROS generation. These findings are consistent with the earlier studies which showed that ROS generation could induce cancer cells apoptosis in P53 dependent pathway with the involvement of caspase-3 (16, 25). Studies have also shown that P53 activation in cancer cells induces the expression of P53 target genes which further leads to cell growth inhibition and apoptosis. Catechins also induce the activation of P53 in cancer cells (25, 58). Therefore, it is anticipated that CC/Se-HAp could affect the P53 mediated apoptosis pathway in a similar fashion. Furthermore, the internalization of nanoparticles on the surface is associated with the actin rearrangement near the plasma membrane and extension into the extracellular space (38). Similarly, the TEM micrographs (**Figure 6C**) revealed that most of the nanoparticles were rapidly internalized into the MNNG/HOS cells. This observation confirms the internalization and translocation of CC/Se-HAp nanoparticles. These observations are also in agreement with a previous report (16). Finally, the degradation of internalized CC/Se-HAp nanomaterials restrains the viability of cells as indicated by the reduced cell viability (**Figure 6A**). Furthermore, the internalization indicates that the nanomaterials were gradually degraded within the lysosomes with the increased incubation time, which is in agreement with a previously reported study of Se-doped HAp nanoparticles (16).

Overall, the results of present study indicate that CC/Se-HAp nanoparticles have the greater potency for the targeted treatment of the osteosarcoma with least side effects toward the normal stem cells. However, further analysis like release mechanism, release kinetics, action mechanism, and fate of the released particles from nanomaterials at different pH and with different concentrations of catechins and selenium, would provide the base for clinical trials of the developed therapeutic drug in the osteosarcoma therapy.

AUTHOR CONTRIBUTIONS

All authors contributed directly in the designing, experimentation, and write up of manuscript under the supervision of MX, GY, and HH.

FUNDING

The project was supported by the National Science Foundation of China (grant number 31870917, 81471174, 81520108011, and 81870942), National Key Research and Development Program of China (grant no: 2018YFC1312200), Innovation Scientists and Technicians Troop Constructions Projects of Henan Province of China for MX, and China Postdoctoral Science Foundation (2016M602291).

ACKNOWLEDGMENTS

The authors are thankful for the Chinese Academy of Science and The World Academy of Science (CAS-TWAS) scholarship program.

SUPPLEMENTARY MATERIAL

The Supplementary Material for this article can be found online at: https://www.frontiersin.org/articles/10.3389/fonc.2019.00499/full#supplementary-material

REFERENCES

1. Siegel RL, Miller KD, Jemal A. Cancer statistics, 2017. *CA Cancer J Clin.* (2017) 67:7–30. doi: 10.3322/caac.21387

2. Hao S, Shen Y, Wu H, Meng J, Xie L, Wen T, et al. Modulatory effects of the composition and structure on the osteogenic enhancement for superparamagnetic scaffolds. *Eng Sci.* (2018) 4:100–10. doi: 10.30919/es8d782

3. Khanna C, Wan X, Bose S, Cassaday R, Olomu O, Mendoza A, et al. The membrane-cytoskeleton linker ezrin is necessary for osteosarcoma metastasis. *Nat Med*. (2004) 10:182–6. doi: 10.1038/nm982
4. Koshkina NV, Kleinerman ES, Waldrep C, Jia S-F, Worth LL, Gilbert BE, et al. 9-Nitrocamptothecin liposome aerosol treatment of melanoma and osteosarcoma lung metastases in mice. *Clin Cancer Res*. (2000) 6:2876–80. doi: 10.1111/j.1749-6632.2000.tb07033.x
5. Luu HH, Kang Q, Park JK, Si W, Luo Q, Jiang W, et al. An orthotopic model of human osteosarcoma growth and spontaneous pulmonary metastasis. *Clin Exp Metastasis*. (2005) 22:319–29. doi: 10.1007/s10585-005-0365-9
6. Bacci G, Rocca M, Salone M, Balladelli A, Ferrari S, Palmerini E, et al. High grade osteosarcoma of the extremities with lung metastases at presentation: treatment with neoadjuvant chemotherapy and simultaneous resection of primary and metastatic lesions. *J Surg Oncol*. (2008) 98:415–20. doi: 10.1002/jso.21140
7. Ory B, Heymann M, Kamijo A, Gouin F, Heymann D, Redini F. Zoledronic acid suppresses lung metastases and prolongs overall survival of osteosarcoma-bearing mice. *Cancer Interdiscip Int J Am Cancer Soc*. (2005) 104:2522–9. doi: 10.1002/cncr.21530
8. Koshkina NV, Kleinerman ES. Aerosol gemcitabine inhibits the growth of primary osteosarcoma and osteosarcoma lung metastases. *Int J Cancer*. (2005) 116:458–63. doi: 10.1002/ijc.21011
9. Sarath Chandra V, Baskar G, Suganthi RV, Elayaraja K, Ahymah Joshy MI, Sofi Beaula W, et al. Blood compatibility of iron-doped nanosize hydroxyapatite and its drug release. *ACS Appl Mater Interfaces*. (2012) 4:1200–10. doi: 10.1021/am300140q
10. Willis RE. Targeted cancer therapy: vital oncogenes and a new molecular genetic paradigm for cancer initiation progression and treatment. *Int J Mol Sci*. (2016) 17:E1552. doi: 10.3390/ijms17091552
11. Shepherd JH, Shepherd DV, Best SM. Substituted hydroxyapatites for bone repair. *J Mater Sci Mater Med*. (2012) 23:2335–47. doi: 10.1007/s10856-012-4598-2
12. Ji Y, Wang A, Wu G, Yin H, Liu S, Chen B, et al. Synthesis of different sized and porous hydroxyapatite nanorods without organic modifiers and their 5-fluorouracil release performance. *Mater Sci Eng C*. (2015) 57:14–23. doi: 10.1016/j.msec.2015.07.008
13. Khan FU, Asimullah, Khan SB, Kamal T, Asiri AM, Khan IU, et al. Novel combination of zero-valent Cu and Ag nanoparticles @ cellulose acetate nanocomposite for the reduction of 4-nitro phenol. *Int J Biol Macromol*. (2017) 102:868–77. doi: 10.1016/j.ijbiomac.2017.04.062
14. Ahmad I, Khan SB, Kamal T, Asiri AM. Visible light activated degradation of organic pollutants using zinc–iron selenide. *J Mol Liq*. (2017) 229:429–35. doi: 10.1016/j.molliq.2016.12.061
15. Ullah I, Li W, Lei S, Zhang Y, Zhang W, Farooq U, et al. Simultaneous co-substitution of Sr2+/Fe3+ in hydroxyapatite nanoparticles for potential biomedical applications. *Ceram Int*. (2018) 44:21338–48. doi: 10.1016/j.ceramint.2018.08.187
16. Wang Y, Wang J, Hao H, Cai M, Wang S, Ma J, et al. *In vitro* and *in vivo* mechanism of bone tumor inhibition by selenium-doped bone mineral nanoparticles. *ACS Nano*. (2016) 10:9927–37. doi: 10.1021/acsnano.6b03835
17. Wang Y, Ma J, Zhou L, Chen J, Liu Y, Qiu Z, et al. Dual functional selenium-substituted hydroxyapatite. *Interface Focus*. (2012) 2:378–86. doi: 10.1098/rsfs.2012.0002
18. Aljohani W, Ullah MW, Zhang X, Yang G. Bioprinting and its applications in tissue engineering and regenerative medicine. *Int J Biol Macromol*. (2018) 107:261–75. doi: 10.1016/j.ijbiomac.2017.08.171
19. Fox K, Tran PA, Tran N. Recent advances in research applications of nanophase hydroxyapatite. *Chem Phys Chem*. (2012) 13:2495–506. doi: 10.1002/cphc.201200080
20. Gabriel LP, Santos ME, Jardini AL, Bastos GN, Dias CG, Webster TJ, et al. Bio-based polyurethane for tissue engineering applications: how hydroxyapatite nanoparticles influence the structure, thermal and biological behavior of polyurethane composites. *Nanomedicine*. (2017) 13:201–8. doi: 10.1016/j.nano.2016.09.008
21. Ma J, Wang Y, Zhou L, Zhang S. Preparation and characterization of selenite substituted hydroxyapatite. *Mater Sci Eng C*. (2013) 33:440–5. doi: 10.1016/j.msec.2012.09.011
22. Robb CS, Geldart SE, Seelenbinder JA, Brown PR. Analysis of green tea constituents by HPLC-FTIR. *J Liq Chromatogr Relat Technol*. (2002) 25:787–801. doi: 10.1081/JLC-120003036
23. Butt MS, Ahmad RS, Sultan MT, Qayyum MMN, Naz A. Green tea and anticancer perspectives: updates from last decade. *Crit Rev Food Sci Nutr*. (2015) 55:792–805. doi: 10.1080/10408398.2012.680205
24. Zhang W, Liu K, Liu S, Ji B, Wang Y, Liu Y. MicroRNA-133a functions as a tumor suppressor by targeting IGF-1R in hepatocellular carcinoma. *Tumor Biol*. (2015) 36:9779–88. doi: 10.1007/s13277-015-3749-8
25. Tsai CY, Chen CY, Chiou YH, Shyu HW, Lin KH, Chou MC, et al. Epigallocatechin-3-gallate suppresses human herpesvirus 8 replication and induces ROS leading to apoptosis and autophagy in primary effusion lymphoma cells. *Int J Mol Sci*. (2018) 19:E16. doi: 10.3390/ijms19010016
26. Stadlbauer S, Steinborn C, Klemd A, Hattori F, Ohmori K, Suzuki K, et al. Impact of green tea catechin ECG and its synthesized fluorinated analogue on prostate cancer cells and stimulated immunocompetent cells. *Planta Med*. (2018) 84:813–19. doi: 10.1055/s-0044-102099
27. Tohyama Y, Takano T, Tanaka C, He J, Tohyama K, Yamamura H, et al. Induction of apoptosis by epigallocatechin-3-gallate in human lymphoblastoid B cells. *Biochem Biophys Res Commun*. (2007) 362:951–7. doi: 10.1016/j.bbrc.2007.08.079
28. Nakazato T, Ito K, Ikeda Y, Kizaki M. Green tea component, catechin, induces apoptosis of human malignant B cells via production of reactive oxygen species. *Clin Cancer Res*. (2005) 11:6040–9. doi: 10.1158/1078-0432.CCR-04-2273
29. Yu Y, Deng Y, Lu BM, Liu YX, Li J, Bao JK. Green tea catechins: a fresh flavor to anticancer therapy. *Apoptosis*. (2014) 19:1–18. doi: 10.1007/s10495-013-0908-5
30. Oh S, Gwak J, Park S, Yang CS. Green tea polyphenol EGCG suppresses Wnt/β-catenin signaling by promoting GSK-3β- and PP2A-independent β-catenin phosphorylation/degradation. *BioFactors*. (2014) 40:586–95. doi: 10.1002/biof.1185
31. Lecumberri E, Dupertuis YM, Miralbell R, Pichard C. Green tea polyphenol epigallocatechin-3-gallate (EGCG) as adjuvant in cancer therapy. *Clin Nutr*. (2013) 32:894–903. doi: 10.1016/j.clnu.2013.03.008
32. Farhan M, Khan HY, Oves M, Al-Harrasi A, Rehmani N, Arif H, et al. Cancer therapy by catechins involves redox cycling of copper ions and generation of reactive oxygen species. *Toxins*. (2016) 8:37. doi: 10.3390/toxins8020037
33. Haratifar S, Meckling KA, Corredig M. Antiproliferative activity of tea catechins associated with casein micelles , using HT29 colon cancer cells. *J Dairy Sci*. (2014) 97:672–8. doi: 10.3168/jds.2013-7263
34. Quesada IM, Bustos M, Blay M, Pujadas G, Ardèvol A, Salvadó MJ, et al. Dietary catechins and procyanidins modulate zinc homeostasis in. *J Nutr Biochem*. (2011) 22:153–63. doi: 10.1016/j.jnutbio.2009.12.009
35. Shan H, Shi Y, Quan J. Identification of green tea catechins as potent inhibitors of the polo-box domain of Polo-like kinase 1. *ChemMedChem*. (2015) 10:158–63. doi: 10.1002/cmdc.201402284
36. Jiang P, Wu X, Wang X, Huang W, Feng Q. NEAT1 upregulates EGCG-induced CTR1 to enhance cisplatin sensitivity in lung cancer cells. *Oncotarget*. (2016) 7:43337–51. doi: 10.18632/oncotarget.9712
37. Fujiki H, Sueoka E, Rawangkan A, Suganuma M. Human cancer stem cells are a target for cancer prevention using (–)- epigallocatechin gallate. *J Cancer Res Clin Oncol*. (2017) 143:2401–12. doi: 10.1007/s00432-017-2515-2
38. Gratton SEA, Ropp PA, Pohlhaus PD, Luft JC, Madden VJ, Napier ME, et al. The effect of particle design on cellular internalization pathways. *Proc Natl Acad Sci USA*. (2008) 105:11613–18. doi: 10.1073/pnas.0801763105
39. Yuan Y, Liu C, Qian J, Wang J, Zhang Y. Size-mediated cytotoxicity and apoptosis of hydroxyapatite nanoparticles in human hepatoma HepG2 cells. *Biomaterials*. (2010) 31:730–40. doi: 10.1016/j.biomaterials.2009.09.088
40. Tsai YJ, Chen BH. Preparation of catechin extracts and nanoemulsions from green tea leaf waste and their inhibition effect on prostate cancer cell PC-3. *Int J Nanomed*. (2016) 11:1907–26. doi: 10.2147/IJN.S103759
41. Kolmas J, Groszyk E, Piotrowska U. Nanocrystalline hydroxyapatite enriched in selenite and manganese ions: physicochemical and antibacterial properties. *Nanoscale Res Lett*. (2015) 10:278. doi: 10.1186/s11671-015-0989-x
42. Ullah MW, Ul-Islam M, Khan S, Kim Y, Park JK. Structural and physico-mechanical characterization of bio-cellulose produced by a cell-free system. *Carbohydr Polym*. (2016) 136:908–16. doi: 10.1016/j.carbpol.2015.10.010

43. Tkachenko MV, Kamzin AS. Synthesis and properties of hybrid hydroxyapatite–ferrite (Fe3O4) particles for hyperthermia applications. *Phys Solid State*. (2016) 58:763–70. doi: 10.1134/S1063783416040260
44. Ereiba KMT, Mostafa AG, Gamal GA, Said AH. *In vitro* study of iron doped hydroxyapatite. *J Biophys Chem*. (2013) 04:122–30. doi: 10.4236/jbpc.2013.44017
45. Rossi AL, Longuinho MM, Tanaka MN, Farina M, Borojevic R, Rossi AM. Intracellular pathway and subsequent transformation of hydroxyapatite nanoparticles in the SAOS-2 osteoblast cell line. *J Biomed Mater Res Part A*. (2018) 106:428–39. doi: 10.1002/jbm.a.36256
46. Zhang W, Chai Y, Cao N, Wang Y. Synthesis and characterization of selenium substituted hydroxyapatite via a hydrothermal procedure. *Mater Lett*. (2014) 134:123–5. doi: 10.1016/j.matlet.2014.07.072
47. Di Z, Shi Z, Ullah MW, Li S, Yang G. A transparent wound dressing based on bacterial cellulose whisker and poly(2-hydroxyethyl methacrylate). *Int J Biol Macromol*. (2017) 105(Pt 1):638–44. doi: 10.1016/j.ijbiomac.2017.07.075
48. Luo H, Yang Y, Huang F, Li F, Jiang Q, Shi K, et al. Selenite induces apoptosis in colorectal cancer cells via AKT-mediated inhibition of β-catenin survival axis. *Cancer Lett*. (2012) 315:78–85. doi: 10.1016/j.canlet.2011.10.014
49. Isakoff MS, Bielack SS, Meltzer P, Gorlick R. Osteosarcoma: current treatment and a collaborative pathway to success. *J Clin Oncol*. (2015) 33:3029–35. doi: 10.1200/JCO.2014.59.4895
50. Saw WS, Ujihara M, Chong WY, Voon SH, Imae T, Kiew LV, et al. Size-dependent effect of cystine/citric acid-capped confeito-like gold nanoparticles on cellular uptake and photothermal cancer therapy. *Colloids Surfaces B Biointerfaces*. (2018) 161:365–74. doi: 10.1016/j.colsurfb.2017.10.064
51. Chithrani BD, Ghazani AA, Chan WCW. Determining the size and shape dependence of gold nanoparticle uptake into mammalian cells. *Nano Lett*. (2006) 6:662–8. doi: 10.1021/nl052396o
52. Lu F, Wu S, Hung Y, Mou C. Size effect on cell uptake in well-suspended, uniform mesoporous silica nanoparticles. *Small*. (2009) 5:1408–13. doi: 10.1002/smll.200900005
53. Shang L, Nienhaus K, Nienhaus GU. Engineered nanoparticles interacting with cells: size matters. *J Nanobiotechnol*. (2014) 12:1–11. doi: 10.1186/1477-3155-12-5
54. Wang X, Xu S, Zhou S, Xu W, Leary M, Choong P, et al. Topological design and additive manufacturing of porous metals for bone scaffolds and orthopaedic implants: a review. *Biomaterials*. (2016) 83:127–41. doi: 10.1016/j.biomaterials.2016.01.012
55. Murugan R, Ramakrishna S. Development of nanocomposites for bone grafting. *Compos Sci Technol*. (2005) 65:2385–406. doi: 10.1016/j.compscitech.2005.07.022
56. Lowry N, Brolly M, Han Y, McKillop S, Meenan BJ, Boyd AR. Synthesis and characterisation of nanophase hydroxyapatite co-substituted with strontium and zinc. *Ceram Int*. (2018) 44:7761–70. doi: 10.1016/j.ceramint.2018.01.206
57. Kiełbowicz-Matuk A, Rey P, Rorat T. Interplay between circadian rhythm, time of the day and osmotic stress constraints in the regulation of the expression of a Solanum Double B-box gene. *Ann Bot*. (2014) 113:831–42. doi: 10.1093/aob/mct303
58. Petre CE, Sin S-H, Dittmer DP. Functional p53 signaling in Kaposi's sarcoma-associated herpesvirus lymphomas: implications for therapy. *J Virol*. (2007) 81:1912–22. doi: 10.1128/JVI.01757-06

Conflict of Interest Statement: The authors declare that the research was conducted in the absence of any commercial or financial relationships that could be construed as a potential conflict of interest.

frontiers in Pharmacology

REVIEW
published: 10 July 2019
doi: 10.3389/fphar.2019.00772

Potential for Nuclear Medicine Therapy for Glioblastoma Treatment

*Clément Bailly[1,2], Aurelien Vidal[3], Coralie Bonnemaire[3], Françoise Kraeber-Bodéré[2,4], Michel Chérel[2,5], Amandine Pallardy[1], Caroline Rousseau[5], Emmanuel Garcion[6], Franck Lacoeuille[6,7], François Hindré[6], Samuel Valable[8], Myriam Bernaudin[8], Caroline Bodet-Milin[1,2] and Mickaël Bourgeois[1,2,3]**

[1] Nuclear Medicine, Centre Hospitalier Universitaire (CHU) de Nantes, Nantes, France, [2] CRCINA, INSERM, CNRS, Université d'Angers, Université de Nantes, Nantes, France, [3] Arronax, Saint-Herblain, France, [4] Nuclear Medecine, Centre Hospitalier Universitaire (CHU) de Nantes, Nantes, France, [5] Institut de Cancérologie de l'Ouest (ICO), Angers, France, [6] Team 17—Design and Application of Innovative Local Treatments in Glioblastoma, INSERM U1232 Centre de Recherche en Cancérologie et Immunologie Nantes Angers (CRCINA), Nantes, France, [7] Nuclear Medicine, Centre Hospitalier Universitaire d'Angers, Angers, France, [8] Normandie Université, Caen, France

OPEN ACCESS

Edited by:
Christian Celia, Università degli Studi G. d'Annunzio Chieti e Pescara, Italy

Reviewed by:
Abraham Kuten, Rambam Health Care Campus, Israel
Ekaterina Dadachova, University of Saskatchewan, Canada

***Correspondence:**
Mickaël Bourgeois
bourgeois@arronax-nantes.fr

Specialty section:
This article was submitted to Pharmacology of Anti-Cancer Drugs, a section of the journal Frontiers in Pharmacology

Received: *18 January 2019*
Accepted: *14 June 2019*
Published: *10 July 2019*

Citation:
Bailly C, Vidal A, Bonnemaire C, Kraeber-Bodéré F, Chérel M, Pallardy A, Rousseau C, Garcion E, Lacoeuille F, Hindré F, Valable S, Bernaudin M, Bodet-Milin C and Bourgeois M (2019) Potential for Nuclear Medicine Therapy for Glioblastoma Treatment. Front. Pharmacol. 10:772. doi: 10.3389/fphar.2019.00772

Glioblastoma is the most common malignant adult brain tumor and has a very poor patient prognosis. The mean survival for highly proliferative glioblastoma is only 10 to 14 months despite an aggressive current therapeutic approach known as Stupp's protocol, which consists of debulking surgery followed by radiotherapy and chemotherapy. Despite several clinical trials using anti-angiogenic targeted therapies, glioblastoma medical care remains without major progress in the last decade. Recent progress in nuclear medicine, has been mainly driven by advances in biotechnologies such as radioimmunotherapy, radiopeptide therapy, and radionanoparticles, and these bring a new promising arsenal for glioblastoma therapy. For therapeutic purposes, nuclear medicine practitioners classically use β^- particle emitters like ^{131}I, ^{90}Y, $^{186/188}Re$, or ^{177}Lu. In the glioblastoma field, these radioisotopes are coupled with nanoparticles, monoclonal antibodies, or peptides. These radiopharmaceutical compounds have resulted in a stabilization and/or improvement of the neurological status with only transient side effects. In nuclear medicine, the glioblastoma-localized and targeted internal radiotherapy proof-of-concept stage has been successfully demonstrated using β^- emitting isotopes. Similarly, α particle emitters like ^{213}Bi, ^{211}At, or ^{225}Ac appear to be an innovative and interesting alternative. Indeed, α particles deliver a high proportion of their energy inside or at close proximity to the targeted cells (within a few micrometers from the emission point versus several millimeters for β^- particles). This physical property is based on particle–matter interaction differences and results in α particles being highly efficient in killing tumor cells with minimal irradiation of healthy tissues and permits targeting of isolated tumor cells. The first clinical trials confirmed this idea and showed good therapeutic efficacy and less side effects, thus opening a new and promising era for glioblastoma medical care using α therapy. The objective of this literature review is focused on the developing field of nuclear medicine and aims to describe the various parameters such as targets, vectors, isotopes, or injection route (systemic and local) in relation to the clinical and preclinical results in glioblastoma pathology.

Keywords: glioblastoma, nuclear medicine, cancer, radioimmunotherapy (RIT), peptide receptor radiotherapy (PRRT), radionanoparticles

INTRODUCTION

Glioblastoma is a neoplasm derived from astrocytes, a subtype of brain macroglial cells. Historically, astrocytomas from the most benign to the most aggressive tumors have been classified using four grades (Louis et al., 2016): pilocytic astrocytoma (grade I tumors), diffuse astrocytoma (grade II tumors), anaplastic astrocytoma (grade III tumors), and glioblastoma (grade IV tumors). Glioblastoma appears to be the most aggressive and also, unfortunately, the most frequent primary brain tumor. The worldwide incidence of glioblastoma is less than 10 per 100,000 people (Hanif et al., 2017; Tamimi and Juweid, 2017) and represents approximately 50–60% of gliomas and 15% of all primary brain tumors in adults (Ostrom et al., 2016; Tamimi and Juweid, 2017; Li et al., 2018). Currently, glioblastoma can be divided into different subtypes based on molecular classification, which includes an isocitrate dehydrogenase-1 (IDH) mutation described in the 2016 WHO classification (Louis et al., 2016), or the more recently described 1p/19q codeletion and TERT promoter mutation (Eckel-Passow et al., 2015; Karsy et al., 2017; van den Bent et al., 2017). The current standardized therapeutic protocol known as Stupp's protocol consists of a debulking surgery followed by radiotherapy and chemotherapy (Stupp et al., 2005). Despite the increase in the molecular knowledge of the pathology and the emergence of targeted therapies with some clinical trials based on this molecular stratification (Chen et al., 2017), patient outcomes remain poor with a survival rate of 14–15 months after diagnosis (Thakkar et al., 2014; Kaley et al., 2018), and there has been no significant progress made in the last decade.

The recent progress in nuclear medicine development has generated a new promising arsenal for glioblastoma therapy. This has been mainly driven by biotechnologies such as radioimmunotherapy, radiopeptide therapy, and radionanoparticles. The four main parameters required for successful radionuclide targeted therapies for glioblastoma are the selection of an appropriate target, the size of the targeting vector, the physical properties of the radionuclide, and the physicochemical properties of the vector (Cordier et al., 2016). The objective of this literature review is focused on the improving field of nuclear medicine and describes the various parameters such as targets, vectors, isotopes, or injection route (systemic and local) in relation to clinical and preclinical results in glioblastoma pathology.

NUCLEAR MEDICINE AND RADIOPHARMACEUTICALS

Nuclear medicine is the medical specialty that uses radioactive atoms for diagnosis and/or therapy. In the therapeutic case, to obtain specific irradiation of tumor cells, the radioactivity could be attached to a pharmaceutical molecule that binds to specific molecules expressed on the target tumor cells. This specific radioactive molecule is called a radiopharmaceutical, and currently, we have many possible combinations. The pharmacological specific component of a radiopharmaceutical in glioblastoma therapy can be based on the target protein structure and includes peptides or monoclonal antibodies, or molecular structures like nanoparticles. For the radioactive side of therapeutic radiopharmaceuticals, nuclear medicine practitioners can use massive particle emitters, which deliver their ionizing energy locally like Auger electrons, or β^- or α particles. Auger electrons are low-energy electrons that emit a very localized irradiation (several nanometers around the emission point) with high biological effects. Beta-negative particles have a relatively (compared with alpha particles) low linear energy transfer (LET) and emit their energy over a few millimeters. Radionuclide choice is based on the tumor size. For example, yttrium-90 emits a long-range beta emission and could be used for larger masses, while lutetium-177 has a short range, favoring treatment of minimal residual disease.

Alpha particles deliver a high fraction of their energy inside the targeted cells, leading to highly efficient killing. This makes them suitable for targeting isolated tumor cells and minimal residual disease. The physical properties of radionuclides used for glioblastoma are summarized in **Table 1**.

Radioimmunotherapy Approach

Radioimmunotherapy (RIT) is a nuclear medicine modality that uses a monoclonal antibody (mAb) to achieve targeted vectorization of a radionuclide. The monoclonal antibody binds to specific antigens expressed or overexpressed on the tumor cells. For certain antigen targets, like epidermal growth factor receptor (EGFR), tenascin, or DNA histone H1 complex, clinical trials are underway; and the initial results show promise. Additional targets such as CA XII or cadherin 5 are also showing encouraging results at the preclinical stage.

TABLE 1 | Physical properties of radioisotopes used in glioblastoma therapy.

Radionuclide	Emission type	Half-life (h)	E_{max} (keV) of main emission	Maximum range in soft tissues (mm)
Iodine-125	Auger	1426	3.19	Nanometer scale
Iodine-131	β^-	193	606.3	2.9
Yttrium-90	β^-	64	2,280.1	12.0
Lutetium-177	β^-	162	498.3	2.0
Rhenium-186	β^-	89.2	1,069.5	5.0
Rhenium-188	β^-	17	2,120.4	10.8
Astatine-211	α	7.2	5.870 to 7.45	0.055 to 0.080
Bismuth-213	α	0.76	8.4	0.1
Actinium-225	α	240	8.4	0.1

GFR Targeting

EGFR is a cell-surface receptor involved in regulation of cell proliferation, angiogenesis, and tumor metastases. EGFR is particularly overexpressed in over 90% of glioblastomas and constitutes an interesting target for glioblastoma RIT (Frederick et al., 2000). One of the first glioblastoma RIT clinical trials using a mAb directed against the EGFR antigen and radiolabeled with iodine-125 showed a significant and promising increase in median survival. In this phase II clinical study, 180 patients, of which 118 had a glioblastoma diagnosis, received intravenous or intra-arterial RIT as an adjuvant therapy after surgery, radiotherapy, and with or without chemotherapy. The mean total administered dose was 5.2 GBq (one injection per week for 3 weeks). The overall median survival for the glioblastoma group was 13.4 months, demonstrating a significant outcome improvement. Furthermore, a subgroup of patients less than 40 years old showed a median survival of 25.4 months (Emrich et al., 2002). This first RIT application was confirmed by a second phase II clinical trial, which involved 192 patients with glioblastoma. Patients received 1.8 GBq each week for 3 weeks (total of 4.44 to 5.55 GBq) of RIT after debulking surgery and radiation therapy. The results showed no grade 3/4 toxicological events and an overall median survival of 15.7 months with an increment to 20.2 months for the arm with temozolomide and RIT-associated therapy (Li et al., 2010).

Another EGFR RIT targeting modality was tested by Casacó et al. in 2008 using a single-dose intracavitary injection of anti-EGFR (nimotuzumab) radiolabeled with rhenium-188. This phase I clinical trial included eight patients with glioblastoma multiform. The maximal tolerated dose was determined at 370 MBq for 3 mg of mAb. In the 370 MBq group, two patients presented a complete response after 3 years of monitoring, and one patient presented a partial response for more than 1 year. However, no improvement in median survival was reported due to the large variability (from 6.1 to 18.7 months), and a transient to very severe neurotoxicity was also observed (Casacó et al., 2008).

Tenascin Targeting

The extracellular matrix protein tenascin-C is another target of interest for glioblastoma RIT. Tenascin-C is overexpressed in more than 90% of all glioblastoma cases, and this protein is involved in adhesion, migration, and proliferation with increased proliferation with higher grades of tumor malignancy (Zagzag et al., 1996; Midwood et al., 2016).

The iodine-131-radiolabeled anti-tenascin mAb BC2 was the first used in this indication for 10 patients with recurring glioblastoma after surgery, radiotherapy, and chemotherapy. The mean dose of 551.3 MBq for 1.93 mg of mAb was injected directly into the tumor by the stereotaxic method. Both systemic and neurologic toxicities were negligible, and RIT failed to show any favorable results in four patients. Nevertheless, for three patients, the pathology appeared to be stabilized; for two patients, the results revealed a partial remission; and one patient showed complete remission (Riva et al., 1992). This approach was confirmed using other anti-tenascin mAb. BC4 was injected intratumorally in 30 patients with recurrent glioblastoma at a higher dose (1,100 MBq of iodine-131 repeated two, three, or four times) without adverse systemic effects and comparable results (Riva et al., 1994). A major phase I/II clinical trial using iodine-131-labeled mAb BC2 and BC4 enrolled 111 patients who suffered diverse malignant gliomas (20 patients for phase I and 91 for phase II). Like the previous proof-of-concept trial, the radioactive mAb was injected directly into the tumor, and the results for the phase I patients revealed a maximal tolerated dose of 2,590 MBq with serious brain edema for larger doses. For the phase II component, patients received a mean dose of 2,035 MBq with minimal toxicity. Among the patients with glioblastoma, the response rate was 47.2%, and the clinical objective responses were as follows: partial response 12.8%, complete response 1.4%, and no evidence of disease 32.8%. The overall survival median was 19.0 months (Riva et al., 1999).

Yttrium-90, an alternative to iodine-131, has also been trialed with an anti-tenascin BC4 mAb. For 26 patients with recurrent glioblastoma, an amelioration of median survival from 20 months for RIT only to 22 months when RIT was associated with mitoxantrone chemotherapy was demonstrated (Boiardi et al., 2005). These results obtained after an intracranial injection of 185 to 925 MBq of BC-4 mAb was confirmed when RIT was associated with temozolomide chemotherapy (Bartolomei et al., 2004).

Tenascin targeting appears to be one of the most promising RITs for glioblastoma, and many recent clinical trials using anti-tenascin 81C6 mAb showed similar results to the BC-2 and BC-4 mAbs. The radioisotope mainly used in these clinical trials is the β^-/γ emitter iodine-131. This RIT protocol consists of an intracranial injection of 370 to 6,660 MBq and increased the median survival to 20.6 months for newly diagnosed glioblastomas and 14.5 months for recurrent disease (**Figure 1**) (Reardon et al., 2006b). This clinical progress was accompanied by reversible grade 3/4 hematologic toxicity and grade 3 neurologic toxicity, which could limit the therapeutic dose in certain cases (Bigner et al., 1995; Akabani et al., 1999; Cokgor et al., 2000; Reardon et al., 2002; Akabani et al., 2005; Reardon et al., 2006a; Reardon et al., 2008).

81C6 mAb is also used with astatine-211, an innovative radioactive alpha emitter. In this clinical trial, which involved 18 patients, 81C6 was radiolabeled with 71–347 MBq of astatine-211 and was injected in the surgically created resection cavity. No patient experienced dose-limiting toxicity (six patients experienced a reversible grade 2 neurotoxicity), and the median survival time for glioblastoma patients was 54 weeks compared with 23–31 weeks observed for patients receiving conventional therapies (Zalutsky et al., 2008).

DNA Histone H1 Complex

DNA histone H1 complex is a ubiquitous intracellular antigen exposed in the necrotic core of solid tumors. This targeting is designated as tumor necrosis treatment (TNT) and could be used with a ^{131}I iodinated radiolabeled mAb (Shapiro et al., 2006) under the commercial name Cotara®. The first-phase I/II RIT clinical trial based on TNT targeting enrolled 51 patients and defined the optimal functional dose for a clinical target volume. The dosing regimen was determined to be 37 to 55.5 MBq/cm^3 without toxicity (Hdeib and Sloan, 2012). The most frequent

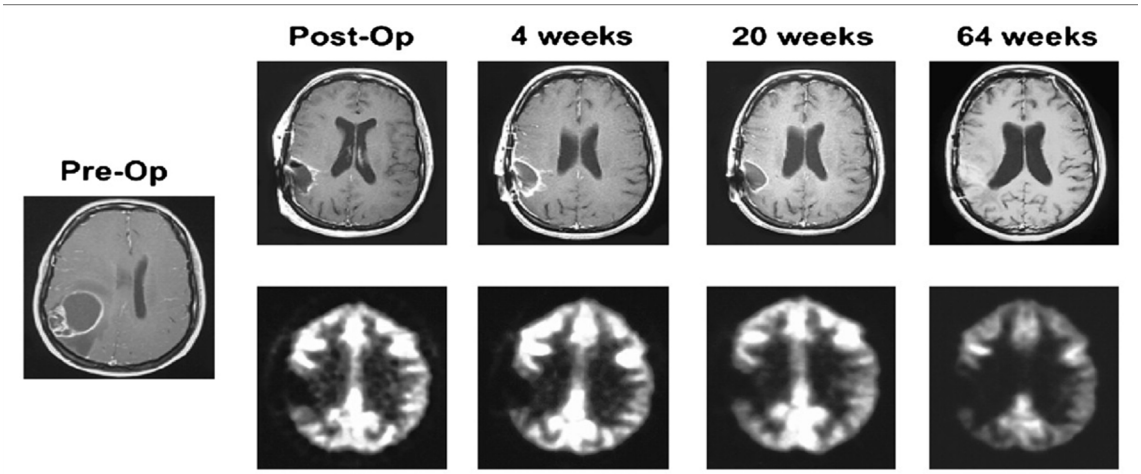

FIGURE 1 | Serial MRI (top and middle) and ^{18}F-FDG PET scan results of representative patient after ^{131}I-ch81C6 therapy. Corresponding ^{18}F-FDG PET scan images (bottom) demonstrate a lack of increased metabolic activity in region of surgically created resection cavity. *This research was originally published in JNM* (Reardon et al., 2006b).

adverse events included nervous system disorders such as brain edema (16%), hemiparesis (14%), or headache (14%) (Patel et al., 2005), but a median survival time of 37.9 weeks was reported. In addition, 7 of the 28 recurrent glioblastoma patients survived for more than 1 year.

Carbonic Anhydrase

To allow survival within a hypoxic tumor microenvironment, glioblastoma cells overexpress certain enzymes such carbonic anhydrase XII (CA XII) or carbonic anhydrase IX (CA IX) (Mboge et al., 2015; Cetin et al., 2018). CA is a membrane-bound protein overexpressed in glioma but absent from healthy brain tissue and appears to be a potential RIT target. In a preclinical study in mice, a human glioblastoma was xenografted, and the animals were treated by intravenous tail vein injection of a lutetium-177-labeled mAb Fab fragment directed against CA XII. Biodistribution analysis showed a significant (tumor xenograft-specific) accumulation in the brain tumor (3.1% of injected dose 3 h after injection) (Fiedler et al., 2018).

To our knowledge, CA IX is not currently used for therapy in nuclear medicine but was used for molecular imaging of glioblastoma and could be used in the near future for phenotypic imaging and theranostic approach (Li et al., 2015).

Cadherin 5

Glioblastoma like many solid tumors is associated with an aggressive and aberrant neovasculature and, in recent years, has become an important target using mAb drugs such as bevacizumab, which targets Vascular endothelial growth factor A (VEGF-A). E4G10 is an mAb targeting vascular endothelial cadherin (e.g., cadherin 5), a molecule specifically expressed at vascular cell–cell junctions in newly forming blood vessels. When labeled with the multiple alpha emitter actinium-225 and intravenously injected into transgenic glioblastoma mice, the E4G10 mAb showed therapeutic efficacy with a significant increase in survival (Behling et al., 2016) and remodeling of the vascular blood–brain-barrier microenvironment, which increased the penetration of chemotherapy drugs like dasatinib (Behling et al., 2016).

Integrin $\alpha_V\beta3$

Integrin $\alpha_V\beta3$ is involved in tumor neoangiogenesis and appears to be an oncologic target in various diseases including glioblastoma. Abegrin® is an mAb directed against $\alpha_V\beta3$ and can be used in RIT after radiolabeling with yttrium-90. A proof of concept in a mouse glioblastoma xenograft model showed a partial tumor regression as assessed by image monitoring compared with control groups (Liu et al., 2011).

Radiopeptide Approach

Peptide receptor radionuclide therapy (PRRT) is an emerging nuclear medicine approach that vectorizes a radionuclide to a specific receptor overexpressed on a tumor using a labeled agonist or antagonist peptide. Various target receptors suitable for PRRT of glioblastoma are being examined in clinical trials with early promising results.

Somatostatin Receptors

Somatostatin is a well-known cyclic neuropeptide in nuclear medicine for both diagnosis and therapy of neuro-endocrine tumors. Octreotide derivatives, which mimic somatostatin, present different binding profiles for each somatostatin receptor isotype ($SSTR_{1-5}$). In glioblastoma therapy, a first clinical trial of 43 patients treated with 400 to 3,700 MBq of ^{90}Y-DOTA-lanreotide was conducted using a fractionated one-to-six therapy cycle. This proof-of-concept study showed five cases (11.6%) of regressive disease (reduction of more than 25% of the tumor size), 14 cases (32.6%) of stable disease, and 24 patients (55.8%) with progressive disease (increase of more than 25% of tumor size). Furthermore, five patients reported a subjective improvement in

quality of life measures (Virgolini et al., 2002). In another trial evaluating the clinical impact of PRRT, an octreotide analog (^{90}Y-DOTATOC) was used to treat recurrent high-grade glioma. Three patients with glioblastoma multiform (WHO grade IV) were locally injected *via* a subcutaneous reservoir system implanted into the resection cavity. Patients received 1,660 to 2,200 MBq of ^{90}Y-DOTATOC in three or four fractions at an interval of 3 to 4 months. The only adverse effects observed were a reoccurrence of an epileptic seizure for one patient and a mild and transient headache for another. There was a complete remission for one patient and partial remission in the other two patients. The Karnofsky performance score increased by 10% to 40% for the three patients, and they reported an improved quality of life. While two patients died 10 to 13 months after admission in the clinical trial (Heute et al., 2010), the third was alive 4 years after admission.

Neurokinin Receptor

Neurokinin type 1 receptors (NK1Rs) appear to be exclusively expressed on the cell surface of gliomas and have been shown to be overexpressed in primary malignant gliomas like glioblastoma (Hennig et al., 1995; Kneifel et al., 2006). The major and physiologic ligand for NK1R is a tachykinin neurotransmitter family member known as substance P.

A pilot study included 20 patients (4 with glioblastoma and 16 with other astrocytoma grade) who received ^{90}Y-, ^{177}Lu-, or ^{213}Bi-radiolabeled substance P into the tumor or into the resected cavity. There was an absence of PRRT drug-related toxicity and 11 months of median survival (range 6–24 months) after therapy initiation. Furthermore, the capacity to modify the radioactive metal in order to optimize tumor growth inhibition and the radionecrotic transformation show promising results for substance P PRRT (Kneifel et al., 2006).

A phase I study whereby 17 patients suffering glioblastoma multiform received repetitive intratumoral injection of ^{90}Y-substance P also showed promising results. Fifteen patients stabilized or improved their functional status when PRRT was used as a neoadjuvant therapy with a mean achieved extent of 96% in subsequent resection surgery (due to an improvement of tumor demarcation by radionecrosis) (Cordier et al., 2010). The radiobiologic mechanisms and therapeutic effects of PRRT are directly dependent on the physical properties of the radioactive sources used. As a consequence, it has become potentially appealing to use short-range alpha-particle-emitting radionuclides in glioblastoma PRRT. A pilot alpha PRRT study using ^{213}Bi-substance P included five patients and provided a proof of concept for this innovative approach, with no safety concerns and a transformation of primarily non-operable gliomas into resectable gliomas after treatment (Cordier et al., 2010).

A clinical trial of nine patients suffering recurrent glioblastoma were injected with 1.4 to 9.7 GBq of ^{213}Bi-substance P into a resected cavity using a fractionated therapy cycle (one to six). The results supported the pilot study, with a median progression free-survival time of 5.8 months and overall survival time of 16.4 months (**Figure 2**). The median overall survival time from the first diagnostic was 52.3 months, and two of the nine patients (22.2%) are still alive 39 and 51 months after the PRRT initiation (Krolicki et al., 2018). A more recent clinical trial of 20 patients confirms the initial results with only mild and transient adverse reactions, demonstrating that PRRT with ^{213}Bi-substance P is safe and well tolerated (Krolicki et al., 2018). The main limitation of ^{213}Bi is the short half-life of the isotope (only 45.6 min), which places limits in terms of radiopharmaceutical preparation time, supply chain between preparation and injection, and dosimetric cumulative dose. To resolve this issue, other alpha-emitting isotopes with longer half-lives such as ^{225}Ac or ^{211}At have been used to label substance P, and preclinical studies are underway (Lyczko et al., 2017; Majkowska-Pilip et al., 2018).

Matrix Metalloproteinase

Chlorotoxin is a 36-amino-acid neurotoxin present in the highly toxic venom of the giant yellow Israeli scorpion (*Leiurus*

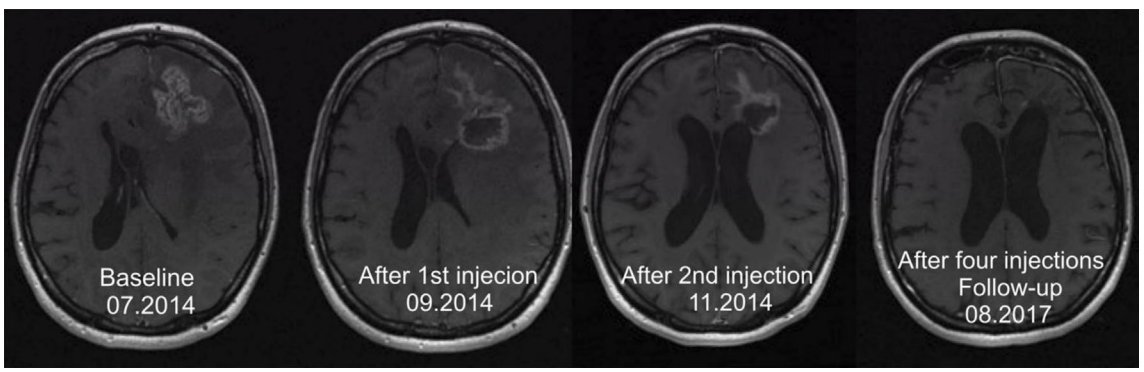

FIGURE 2 | In a 32-year-old woman suffering from an astrocytoma WHO grade II, conversion into a secondary Glioblastoma multiforme (GBM) manifested 10.6 months after initial diagnosis. Following standard treatment consisting of surgery, radiotherapy, and chemotherapy with temozolomide, four cycles of ^{213}Bi-DOTA-substance P were applied. The total activity injected amounted to 8.0 GBq of the therapeutic isotope. The T1-weighted enhanced MRI examination revealed shrinkage of the tumor by 32% (Krolicki et al., 2018).

quinquestriatus). It binds to chloride channels (DeBin et al., 1993) and to matrix metalloproteinase-2 with a preference for malignant cells of neuroectodermal origin like gliomas (Cohen-Inbar and Zaaroor, 2016). TM-601 is a recombinant version of chlorotoxin that was radiolabeled with iodine-131 to treat glioblastoma. A phase I single-dose study with 370 MBq of ^{131}I-TM-601 administered intracavitarially in 18 high-grade gliomas showed a well-tolerated therapy with no dose-limiting toxicities and promising results (four patients with stable disease at day 180 and two patients without evidence of disease for more than 30 months) (Mamelak et al., 2006).

Chemokine Receptor-4

Chemokine receptor-4 (CXCR4) is overexpressed in glioblastoma and is associated with a poor patient outcome (Bian et al., 2007; Tabouret et al., 2015). A first clinical trial of the chemokine receptor ligand Pentixafor® radiolabeled with the positron emitter gallium-68 showed high fixation and provided a nuclear medicine image of glioblastoma (Lapa et al., 2016). An alternative to the diagnostic Pentixafor® is Pentixather®, where the radionuclide is a beta-negative emitter (^{177}Lu). This radiobiological model is currently in development (Buck et al., 2017) and in the near future could be used for glioblastoma PRRT.

Radionanoparticle Approach

The use of nanotechnologies in oncology is booming, and glioblastoma nuclear medicine therapy with the use of radionanoparticles appears to be an emerging field. These radioactive nanocarriers can be passive and act as a simple tumor brachytherapy approach or can be active with a specific targeting to vectorize a large amount of radioactivity. In the active case, the targeting is directed against a glioblastoma-specific antigen or receptor as described above for RIT or PRRT.

Passive Approach

The passive approach of radionanoparticle delivery has been used with different nano-objects such as metallofullerenes, liposomes, or lipid nanocapsules (LNC).

The use of metallofullerene (^{177}Lu-DOTA-f-$Gd_3N@C_{80}$) in an orthotopic xenograft brain tumor model demonstrated its efficacy when the radionanoparticles were delivered by intratumoral convection-enhanced delivery (CED), and it showed an extended survival time of more than 2.5 times that of the untreated group (Shultz et al., 2011).

Liposomes can be loaded with beta-negative emitters such rhenium-186 and provide promising results when administered by CED in an orthotopic glioblastoma rat model (126 days' median survival compared with 49 days for the control group) (Phillips et al., 2012).

The use of colloidal drugs like LNC loaded with rhenium-188 in a rat orthotopic model induced a remarkable survival benefit (increased median survival time of 257%) after intratumoral stereotactic injection at day 6 and CED injection at day 12 (Vanpouille-Box et al., 2011).

Active Targeting Approach

A recent approach using radionanoparticles consists of an active targeting approach where the nanoparticles are functionalized and directed against a tumor target. The aim of this active targeting is to optimize the confinement of the radioactivity near to the tumor cells. As an example, LNC can be loaded with rhenium-188 and coupled to a monoclonal antibody directed against the CXCR4 antigen. These CXCR4-recognizing immune-nanoparticles can then irradiate the tumor cells and have been shown to improve the preclinical efficacy in an orthotopic mouse model. Recurrence for the passive protocol was observed at 65 versus 100 days for the active targeting approach, and this appears to be the most effective therapy with the longest measured time to progression (Séhédic et al., 2017).

DISCUSSION

During the last decade, the knowledge about the phenotypic signature of glioblastoma has increased markedly and resulted in therapeutic progress stemming from improved targeted therapies. Nuclear medicine therapies for glioblastoma have typically used specific vectors to deliver radioactivity to the tumor site. While the initial proof-of-concept studies and human clinical trials have shown encouraging results, some parameters remain to be improved. These include improved efficacy and safety, more localized irradiation of tumor cells, and reduction in bystander irradiation.

These parameters are mostly dependent on the radionuclide and vector choice. Classically, electrons (beta negative and Auger electrons) present an energy-dependent irradiation range. Auger electron emitters (e.g., ^{125}I) need an intracellular vectorization close to the tumor cell nucleus to be effective, while beta-negative emitters (e.g., ^{131}I, ^{90}Y, or ^{177}Lu) present a wider irradiation range from several millimeters to centimeters. These physical properties can present advantages, such as large irradiation of tumor margins and "cross fire" effects, which can compensate for the pharmacological heterogeneous distribution of the radiopharmaceutical compound, as well as disadvantages such as incremental local toxicity due to irradiation of healthy tissue. Alpha emitters (e.g., ^{213}Bi, ^{211}At, or ^{225}Ac) deposit a very high energy over a very short range, in the order of 100 μm and can provide a very local irradiation with very low toxicity. The selection of the most appropriate and effective radionuclide in relation to the pathology status (size, dissemination, tumor margin status, etc.) appears to be one of the key factors for successful therapy.

The biodistribution and homogeneous repartition of the vector in the tumor mass are also a requirement for successful treatment. Tumor neoangiogenesis is known to result in morphologically abnormal and highly disorganized structures at the origin of rheologic dysfunction such as arteriovenous shunts or blood flow inversion. As a consequence of this phenomenon, the biodistribution of pharmaceutical compounds (radiopharmaceutical or chemotherapy) is altered

inside the tumor, especially for high-molecular-weight drugs like monoclonal antibodies. From a pharmacological point of view, peptide vectorization appears to be more effective in allowing infiltration into the extracellular space of a tumor cell mass. However, clinical studies have shown mAb or high-molecular-weight compounds like radionanoparticles to be effective, and the theoretical "biodistribution barrier" can be bypassed after resection surgery or with co-administration of osmotic drugs like mannitol. For these vectorized approaches (e.g., RIT and PRRT), the key of success is mainly driven on pharmacologic-phenotypic based triad: specific presence of the target, expression level of the target, and pharmacological access to the target. Today, the rising of glioblastoma phenotypic knowledge has permitted to identify various interesting targets such as antigens for RIT and receptors for PRRT. The feasibility of RIT and PRRT in glioblastoma therapy is well established, and the first clinical trial results appear to be promising with well-known targets (e.g., tenascin, EGFR, or neurokinin receptors). Emerging targets such as cadherin, integrin, or chemokine receptors seem to give good results in preclinical and early-phase clinical trials. PRRT is a growing approach, particularly through the easiness where the vector is produced [Good Manufacturing Practice (GMP) compliance automatic synthesis], but presents a risk of direct pharmacological adverse event with the peptide dose used. From a general point of view, it still seems to be early to extrapolate these preliminary but very promising results that need to be clinically confirmed to evaluate the relevance of these approaches and if one (or several) target stands out in terms of therapy benefits.

The surgical administration pathway is also a key factor to optimize in glioblastoma management. If the classical intravenous injection route is used, access to the tumor for the radiotherapeutic drug is *via* the blood–brain barrier; however, other administration pathways are possible. The intratumoral or intra-resected tumoral cavity injection (by port-a-cath system, Rickham, or Ommaya reservoir) is classically used in glioblastoma therapy and shows some benefits in terms of patient outcomes. This intratumoral administration modality can be also modulated in terms of the volume injected, infusion rate, or positive back-pressure. The positive back-pressure used during the injection is known as convection enhanced delivery (CED) and is a promising methodology that ensures an increased interstitial diffusion of the radiopharmaceutical compound around the catheter implantation and a *de facto* increase in the diffusion and homogeneity of the irradiation features (Ung et al., 2015; Vogelbaum and Aghi, 2015). For the unvectorized approaches (e.g., naked nanoparticles in passive approach), the limitation concerns the feasibility of local injection that requires a surgical access. When the neurosurgical procedure allows the injection and if there is no leakage in systemic circulation and a limited diffusion in the extra-cellular matrix, the irradiation could be considered as "classical" brachytherapy. To circumvent the leakage and diffusion risks of passive approach, functionalized nanoparticle (e.g., active approach) presents the advantages of greater confinement of radioactivity inside the tumor or intra-resected tumoral cavity.

One of the limitations of nuclear medicine is the potential for adverse events due to the irradiation of healthy tissues. Increased knowledge of the radiobiological differential mechanisms between healthy and tumoral tissues is associated with recent progress in nuclear medicine therapy and demonstrates the effectiveness of the fractionation approach to increase the tumor irradiation total doses with reduced side effects (Reulen et al., 2015).

CONCLUSION

Glioblastoma is the most common primary brain tumor in adults and is typically associated with fatal outcome. Despite recent progress, the survival rate for patients remains poor, and the standard treatment is based on debulking surgery, radiotherapy, and chemotherapy. The current advances in nuclear medicine provide many powerful tools for glioblastoma therapy, and the evolution of biotechnological technologies linked to the molecular knowledge of the pathology and the development of innovative radionuclides has opened the field to new clinical opportunities. Since the first therapeutic injection of a radioactive compound, nuclear medicine applications have been constantly evolving, and new targets like tumoral microenvironment immune checkpoint inhibitors (e.g., CTLA4 or PD1/PDL1 targets) still need to be explored in the field of glioblastoma treatment (Reardon et al., 2016; Huang et al., 2017). In many clinical and preclinical trials, the combination of chemotherapy and nuclear medicine therapy shows an improvement in clinical outcomes by an additive effect of both modalities or by a synergistic effect with a radiosensitization by chemotherapeutic administration (Bartolomei et al., 2004; Milanović et al., 2014).

Many clinical trials demonstrate the efficacy and safety of nuclear medicine approaches, but these have only been assessed in phase I or II clinical trials. These results need to be strengthened, and phase III are trials are necessary to confirm the emerging place of nuclear medicine in the therapeutic arsenal against glioblastoma.

AUTHOR CONTRIBUTIONS

All authors listed have made substantial, direct, and intellectual contribution to the work and approved it for publication.

FUNDING

This work has been supported by the French National Agency for Research called Investissements d'Avenir *via* grants Labex IRON n°ANR-11-LABX-0018-01 and Equipex Arronax plus n°ANR-11-EQPX-0004.

REFERENCES

Akabani, G., Reardon, D. A., Coleman, R. E., Wong, T. Z., Metzler, S. D., Bowsher, J. E., et al. (2005). Dosimetry and radiographic analysis of 131I-labeled anti-tenascin 81C6 murine monoclonal antibody in newly diagnosed patients with malignant gliomas: a phase II study. *J. Nucl. Med.* 46 (6), 1042–1051.

Akabani, G., Reist, C. J., Cokgor, I., Friedman, A. H., Friedman, H. S., Coleman, R. E., et al. (1999). Dosimetry of 131I-labeled 81C6 monoclonal antibody administered into surgically created resection cavities in patients with malignant brain tumors. *J. Nucl. Med.* 40 (4), 631–638.

Bartolomei, M., Mazzetta, C., Handkiewicz-Junak, D., Bodei, L., Rocca, P., Grana, C., et al. (2004). Combined treatment of glioblastoma patients with locoregional pre-targeted 90Y-biotin radioimmunotherapy and temozolomide. *Q. J. Nucl. Med. Mol. Imaging.* 48 (3), 220–228.

Behling, K., Maguire, W. F., Di Gialleonardo, V., Heeb, L. E. M., Hassan, I. F., Veach, D. R., et al. (2016). Remodeling the vascular microenvironment of glioblastoma with α-particles. *J. Nucl. Med.* 57 (11), 1771–1777. doi: 10.2967/jnumed.116.173559

Behling, K., Maguire, W. F., López Puebla, J. C., Sprinkle, S. R., Ruggiero, A., O'Donoghue, J., et al. (2016). Vascular targeted radioimmunotherapy for the treatment of glioblastoma. *J. Nucl. Med.* 57 (10), 1576–1582. doi: 10.2967/jnumed.115.171371

Bian, X.-W., Yang, S.-X., Chen, J.-H., Ping, Y.-F., Zhou, X.-D., Wang, Q.-L., et al. (2007). Preferential expression of chemokine receptor CXCR4 by highly malignant human gliomas and its association with poor patient survival. *Neurosurgery* 61 (3), 570–578, discussion 578–9. doi: 10.1227/01.NEU.0000290905.53685.A2

Bigner, D. D., Brown, M., Coleman, R. E., Friedman, A. H., Friedman, H. S., McLendon, R. E., et al. (1995). Phase I studies of treatment of malignant gliomas and neoplastic meningitis with 131I-radiolabeled monoclonal antibodies anti-tenascin 81C6 and anti-chondroitin proteoglycan sulfate Me1-14 F (ab′)2—a preliminary report. *J. Neurooncol.* 24 (1), 109–122. doi: 10.1007/BF01052668

Boiardi, A., Eoli, M., Salmaggi, A., Lamperti, E., Botturi, A., Broggi, G., et al. (2005). Systemic temozolomide combined with loco-regional mitoxantrone in treating recurrent glioblastoma. *J. Neurooncol.* 75 (2), 215–220. doi: 10.1007/s11060-005-3030-x

Buck, A. K., Stolzenburg, A., Hänscheid, H., Schirbel, A., Lückerath, K., Schottelius, M., et al. (2017). Chemokine receptor—directed imaging and therapy. *Methods* 130, 63–71. doi: 10.1016/j.ymeth.2017.09.002

Casacó, A., López, G., García, I., Rodríguez, J. A., Fernández, R., Figueredo, J., et al. (2008). Phase I single-dose study of intracavitary-administered nimotuzumab labeled with 188Re in adult recurrent high-grade glioma. *Cancer Biol. Ther.* 7 (3), 333–339. doi: 10.4161/cbt.7.3.5414

Cetin, B., Gonul, I. I., Gumusay, O., Bilgetekin, I., Algin, E., Ozet, A., et al. (2018). Carbonic anhydrase IX is a prognostic biomarker in glioblastoma multiforme. *Neuropathology* 38 (5), 457–462. doi: 10.1111/neup.12485

Chen, R., Smith-Cohn, M., Cohen, A. L., and Colman, H. (2017). Glioma subclassifications and their clinical significance. *Neurotherapeutics* (US) 14 (2), 284–297. doi: 10.1007/s13311-017-0519-x

Cohen-Inbar, O., and Zaaroor, M. (2016). Glioblastoma multiforme targeted therapy: the chlorotoxin story. *J. Clin. Neurosci.* 33, 52–58. doi: 10.1016/j.jocn.2016.04.012

Cokgor, I., Akabani, G., Kuan, C. T., Friedman, H. S., Friedman, A. H., Coleman, R. E., et al. (2000). Phase I trial results of iodine-131-labeled antitenascin monoclonal antibody 81C6 treatment of patients with newly diagnosed malignant gliomas. *J. Clin. Oncol.* 18 (22), 3862–3872. doi: 10.1200/JCO.2000.18.22.3862

Cordier, D., Krolicki, L., Morgenstern, A., and Merlo, A. (2016). Targeted radiolabeled compounds in glioma therapy. *Semin. Nucl. Med.* 46 (3), 243–249. doi: 10.1053/j.semnuclmed.2016.01.009

Cordier, D., Forrer, F., Bruchertseifer, F., Morgenstern, A., Apostolidis, C., Good, S., et al. (2010). Targeted alpha-radionuclide therapy of functionally critically located gliomas with 213Bi-DOTA-[Thi8,Met(O2)11]-substance P: a pilot trial. *Eur. J. Nucl. Med. Mol. Imaging* 37 (7), 1335–1344. doi: 10.1007/s00259-010-1385-5

Cordier, D., Forrer, F., Kneifel, S., Sailer, M., Mariani, L., Mäcke, H., et al. (2010). Neoadjuvant targeting of glioblastoma multiforme with radiolabeled DOTAGA-substance P—results from a phase I study. *J. Neurooncol.* 100 (1), 129–136. doi: 10.1007/s11060-010-0153-5

DeBin, J. A., Maggio, J. E., and Strichartz, G. R. (1993). Purification and characterization of chlorotoxin, a chloride channel ligand from the venom of the scorpion. *Am. J. Physiol.* 264 (2 Pt 1), C361–369. doi: 10.1152/ajpcell.1993.264.2.C361

Eckel-Passow, J. E., Lachance, D. H., Molinaro, A. M., Walsh, K. M., Decker, P. A., Sicotte, H., et al. (2015). Glioma groups based on 1p/19q, IDH, and TERT promoter mutations in tumors. *N. Engl. J. Med.* 372 (26), 2499–2508. doi: 10.1056/NEJMoa1407279

Emrich, J. G., Brady, L. W., Quang, T. S., Class, R., Miyamoto, C., Black, P., et al. (2002). Radioiodinated (I-125) monoclonal antibody 425 in the treatment of high grade glioma patients: ten-year synopsis of a novel treatment. *Am. J. Clin. Oncol.* 25 (6), 541–546. doi: 10.1097/01.COC.0000041009.06780.E5

Fiedler, L., Kellner, M., Gosewisch, A., Oos, R., Böning, G., Lindner, S., et al. (2018). Evaluation of 177Lu[Lu]-CHX-A″-DTPA-6A10 Fab as a radioimmunotherapy agent targeting carbonic anhydrase XII. *Nuclear Med. Biol.* 60, 55–62. doi: 10.1016/j.nucmedbio.2018.02.004

Frederick, L., Wang, X. Y., Eley, G., and James, C. D. (2000). Diversity and frequency of epidermal growth factor receptor mutations in human glioblastomas. *Cancer Res.* 60 (5), 1383–1387.

Hanif, F., Muzaffar, K., Perveen, K., Malhi, S. M., and Simjee, S. U. (2017). Glioblastoma multiforme: a review of its epidemiology and pathogenesis through clinical presentation and treatment. *Asian Pac. J. Cancer Prev.* 18 (1), 3–9. doi: 10.22034/APJCP.2017.18.1.3

Hdeib, A., and Sloan, A. (2012). Targeted radioimmunotherapy: the role of 131I-chTNT-1/B mAb (Cotara) for treatment of high-grade gliomas. *Future Oncol.* 8 (6), 659–669. doi: 10.2217/fon.12.58

Hennig, I. M., Laissue, J. A., Horisberger, U., and Reubi, J. C. (1995). Substance-P receptors in human primary neoplasms: tumoral and vascular localization. *Int. J. Cancer* 61 (6), 786–792. doi: 10.1002/ijc.2910610608

Heute, D., Kostron, H., Guggenberg von, E., Ingorokva, S., Gabriel, M., Dobrozemsky, G., et al. (2010). Response of recurrent high-grade glioma to treatment with (90)Y-DOTATOC. *J. Nucl. Med.* 51 (3), 397–400. doi: 10.2967/jnumed.109.072819

Huang, J., Liu, F., Liu, Z., Tang, H., Wu, H., Gong, Q., et al. (2017). Immune checkpoint in glioblastoma: promising and challenging. *Front. Pharmacol.* 8, 242. doi: 10.3389/fphar.2017.00242

Kaley, T., Touat, M., Subbiah, V., Hollebecque, A., Rodon, J., Lockhart, A. C., et al. (2018). BRAF inhibition in BRAFV600-mutant gliomas: results from the VE-BASKET study. *J. Clin. Oncol.* 36 (35), 3477–3484. doi: 10.1200/JCO.2018.78.9990

Karsy, M., Guan, J., Cohen, A. L., Jensen, R. L., and Colman, H. (2017). New molecular considerations for glioma: IDH, ATRX, BRAF, TERT, H3 K27M. *Curr. Neurol. Neurosci. Rep.* 17 (2), 19. doi: 10.1007/s11910-017-0722-5

Kneifel, S., Cordier, D., Good, S., Ionescu, M. C. S., Ghaffari, A., Hofer, S., et al. (2006). Local targeting of malignant gliomas by the diffusible peptidic vector 1,4,7,10-tetraazacyclododecane-1-glutaric acid-4,7,10-triacetic acid-substance p. *Clin. Cancer Res.* 12 (12), 3843–3850. doi: 10.1158/1078-0432.CCR-05-2820

Krolicki, L., Bruchertseifer, F., Kunikowska, J., Koziara, H., Królicki, B., Jakuciński, M., et al. (2018). Prolonged survival in secondary glioblastoma following local injection of targeted alpha therapy with 213Bi-substance P analogue. *Eur. J. Nucl. Med. Mol. Imaging* 45 (9), 1636–1644. doi: 10.1007/s00259-018-4015-2

Krolicki, L., Bruchertseifer, F., Kunikowska, J., Koziara, H., Królicki, B., Jakuciński, M., et al. (2018). Safety and efficacy of targeted alpha therapy with 213Bi-DOTA-substance P in recurrent glioblastoma. *Eur. J. Nucl. Med. Mol. Imaging* 83, 588. doi: 10.1007/s00259-018-4225-7

Lapa, C., Lückerath, K., Kleinlein, I., Monoranu, C. M., Linsenmann, T., Kessler, A. F., et al. (2016). (68)Ga-Pentixafor-PET/CT for imaging of chemokine receptor 4 expression in glioblastoma. *Theranostics* 6 (3), 428–434. doi: 10.7150/thno.13986

Li, J., Zhang, G., Wang, X., and Li, X.-F. (2015). Is carbonic anhydrase IX a validated target for molecular imaging of cancer and hypoxia? *Future Oncol.* (London, UK) 11 (10), 1531–1541. doi: 10.2217/fon.15.11

Li, L., Quang, T. S., Gracely, E. J., Kim, J. H., Emrich, J. G., Yaeger, T. E., et al. (2010). A phase II study of anti-epidermal growth factor receptor radioimmunotherapy in the treatment of glioblastoma multiforme. *J. Neurosurg.* 113 (2), 192–198. doi: 10.3171/2010.2.JNS091211

Li, K., Lu, D., Guo, Y., Wang, C., Liu, X., Liu, Y., et al. (2018). Trends and patterns of incidence of diffuse glioma in adults in the United States, 1973–2014. *Cancer Med.* 7 (10), 5281–5290. doi: 10.1002/cam4.1757

Liu, Z., Wang, F., and Chen, X. (2011). Integrin targeted delivery of radiotherapeutics. *Theranostics* 1, 201–210. doi: 10.7150/thno/v01p0201

Louis, D. N., Perry, A., Reifenberger, G., Deimling von, A., Figarella-Branger, D., Cavenee, W. K., et al. (2016). The 2016 World Health Organization Classification of Tumors of the Central Nervous System: a summary. *Acta Neuropathol.* 131 (6), 803–820. doi: 10.1007/s00401-016-1545-1

Lyczko, M., Pruszynski, M., Majkowska-Pilip, A., Lyczko, K., Was, B., Meczynska-Wielgosz, S., et al. (2017). (5-11) as potential radiopharmaceutical for glioma treatment. *Nuclear Med. Biol.* 53, 1–8. doi: 10.1016/j.nucmedbio.2017.05.008

Majkowska-Pilip, A., Rius, M., Bruchertseifer, F., Apostolidis, C., Weis, M., Bonelli, M., et al. (2018). In vitro evaluation of 225Ac-DOTA-substance P for targeted alpha therapy of glioblastoma multiforme. *Chem. Biol. Drug Des.* 92 (1), 1344–1356. doi: 10.1111/cbdd.13199

Mamelak, A. N., Rosenfeld, S., Bucholz, R., Raubitschek, A., Nabors, L. B., Fiveash, J. B., et al. (2006). Phase I single-dose study of intracavitary-administered iodine-131-TM-601 in adults with recurrent high-grade glioma. *J. Clin. Oncol.* 24 (22), 3644–3650. doi: 10.1200/JCO.2005.05.4569

Mboge, M. Y., McKenna, R., and Frost, S. C. (2015). Advances in anti-cancer drug development targeting carbonic anhydrase IX and XII. *Top Anticancer Res.* 5 (4), 3–42. doi: 10.2174/9781681083339116050004

Midwood, K. S., Chiquet, M., Tucker, R. P., and Orend, G. (2016). Tenascin-C at a glance. *J. Cell Sci.* 129 (23), 4321–4327. doi: 10.1242/jcs.190546

Milanović, D., Maier, P., Schanne, D. H., Wenz, F., and Herskind, C. (2014). The influence of retinoic acid and thalidomide on the radio sensitivity of U343 glioblastoma cells. *Anticancer Res.* 34 (4), 1885–1891.

Ostrom, Q. T., Liao, P., Stetson, L. C., and Barnholtz-Sloan, J. S. (2016). "Epidemiology of glioblastoma and trends in glioblastoma survivorship," in *Glioblastoma*. (Philadelphia, USA): Elsevier, 11–19. doi: 10.1016/B978-0-323-47660-7.00002-1

Patel, S. J., Shapiro, W. R., Laske, D. W., Jensen, R. L., Asher, A. L., Wessels, B. W., et al. (2005). Safety and feasibility of convection-enhanced delivery of Cotara for the treatment of malignant glioma: initial experience in 51 patients. *Neurosurgery* 56 (6), 1243–1252, discussion 1252–3. doi: 10.1227/01.NEU.0000159649.71890.30

Phillips, W. T., Goins, B., Bao, A., Vargas, D., Guttierez, J. E., Trevino, A., et al. (2012). Rhenium-186 liposomes as convection-enhanced nanoparticle brachytherapy for treatment of glioblastoma. *Neuro-oncology* 14 (4), 416–425. doi: 10.1093/neuonc/nos060

Reardon, D. A., Akabani, G., Coleman, R. E., Friedman, A. H., Friedman, H. S., Herndon, J. E., et al. (2002). Phase II trial of murine (131)I-labeled antitenascin monoclonal antibody 81C6 administered into surgically created resection cavities of patients with newly diagnosed malignant gliomas. *J. Clin. Oncol.* 20 (5), 1389–1397. doi: 10.1200/JCO.2002.20.5.1389

Reardon, D. A., Akabani, G., Coleman, R. E., Friedman, A. H., Friedman, H. S., Herndon, J. E., et al. (2006a). Salvage radioimmunotherapy with murine iodine-131-labeled antitenascin monoclonal antibody 81C6 for patients with recurrent primary and metastatic malignant brain tumors: phase II study results. *J. Clin. Oncol.* 24 (1), 115–122. doi: 10.1200/JCO.2005.03.4082

Reardon, D. A., Gokhale, P. C., Klein, S. R., Ligon, K. L., Rodig, S. J., Ramkissoon, S. H., et al. (2016). Glioblastoma eradication following immune checkpoint blockade in an orthotopic, immunocompetent model. *Cancer Immunol. Res.* 4 (2), 124–35. doi: 10.1158/2326-6066.CIR-15-0151

Reardon, D. A., Quinn, J. A., Akabani, G., Coleman, R. E., Friedman, A. H., Friedman, H. S., et al. (2006b). Novel human IgG2b/murine chimeric antitenascin monoclonal antibody construct radiolabeled with 131I and administered into the surgically created resection cavity of patients with malignant glioma: phase I trial results. *J. Nucl. Med.* 47 (6), 912–918.

Reardon, D. A., Zalutsky, M. R., Akabani, G., Coleman, R. E., Friedman, A. H., Herndon, J. E., et al. (2008). A pilot study: 131I-antitenascin monoclonal antibody 81c6 to deliver a 44-Gy resection cavity boost. *Neuro-oncology* 10 (2), 182–189. doi: 10.1215/15228517-2007-053

Reulen, H.-J., Poepperl, G., Goetz, C., Gildehaus, F. J., Schmidt, M., Tatsch, K., et al. (2015). Long-term outcome of patients with WHO grade III and IV gliomas treated by fractionated intracavitary radioimmunotherapy. *J. Neurosurg.* 123 (3), 760–770. doi: 10.3171/2014.12.JNS142168

Riva, P., Arista, A., Sturiale, C., Moscatelli, G., Tison, V., Mariani, M., et al. (1992). Treatment of intracranial human glioblastoma by direct intratumoral administration of 131I-labelled anti-tenascin monoclonal antibody BC-2. *Int. J. Cancer* 51 (1), 7–13. doi: 10.1002/ijc.2910510103

Riva, P., Arista, A., Sturiale, C., Tison, V., Lazzari, S., Franceschi, G., et al. (1994). Glioblastoma therapy by direct intralesional administration of I-131 radioiodine labeled antitenascin antibodies. *Cell Biophys.* 24-25, 37–43. doi: 10.1007/BF02789213

Riva, P., Franceschi, G., Frattarelli, M., Riva, N., Guiducci, G., Cremonini, A. M., et al. (1999). 131I radioconjugated antibodies for the locoregional radioimmunotherapy of high-grade malignant glioma—phase I and II study. *Acta Oncol.* 38 (3), 351–359. doi: 10.1080/028418699431438

Séhédic, D., Chourpa, I., Tétaud, C., Griveau, A., Loussouarn, C., Avril, S., et al. (2017). Locoregional confinement and major clinical benefit of 188Re-loaded CXCR4-targeted nanocarriers in an orthotopic human to mouse model of glioblastoma. *Theranostics* 7 (18), 4517–4536. doi: 10.7150/thno.19403

Shapiro, W. R., Carpenter, S. P., Roberts, K., and Shan, J. S. (2006). 131I-chTNT-1/B mAb: tumour necrosis therapy for malignant astrocytic glioma. *Expert Opin. Biol. Ther.* 6 (5), 539–545. doi: 10.1517/14712598.6.5.539

Shultz, M. D., Wilson, J. D., Fuller, C. E., Zhang, J., Dorn, H. C., and Fatouros, P. P. (2011). Metallofullerene-based nanoplatform for brain tumor brachytherapy and longitudinal imaging in a murine orthotopic xenograft model. *Radiology* 261 (1), 136–143. doi: 10.1148/radiol.11102569

Stupp, R., Mason, W. P., van den Bent, M. J., Weller, M., Fisher, B., Taphoorn, M. J. B., et al. (2005). Radiotherapy plus concomitant and adjuvant temozolomide for glioblastoma. *N. Engl. J. Med.* 352 (10), 987–996. doi: 10.1056/NEJMoa043330

Tabouret, E., Tchoghandjian, A., Denicolai, E., Delfino, C., Metellus, P., Graillon, T., et al. (2015). Recurrence of glioblastoma after radio-chemotherapy is associated with an angiogenic switch to the CXCL12-CXCR4 pathway. *Oncotarget* 6 (13), 11664–11675. doi: 10.18632/oncotarget.3256

Tamimi, A. F., and Juweid, M. (2017). "Epidemiology and outcome of glioblastoma," in *Glioblastoma* (Brisbane, AU), 143–153. doi: 10.15586/codon.glioblastoma.2017.ch8

Thakkar, J. P., Dolecek, T. A., Horbinski, C., Ostrom, Q. T., Lightner, D. D., Barnholtz-Sloan, J. S., et al. (2014). Epidemiologic and molecular prognostic review of glioblastoma. *Cancer Epidemiol. Biomarkers Prev.* 23 (10), 1985–1996. doi: 10.1158/1055-9965.EPI-14-0275

Ung, T. H., Malone, H., Canoll, P., and Bruce, J. N. (2015). Convection-enhanced delivery for glioblastoma: targeted delivery of antitumor therapeutics. *CNS Oncol.* 4 (4), 225–234. doi: 10.2217/cns.15.12

van den Bent, M. J., Weller, M., Wen, P. Y., Kros, J. M., Aldape, K., and Chang, S. (2017). A clinical perspective on the 2016 WHO brain tumor classification and routine molecular diagnostics. *Neuro-oncology* 19 (5), 614–624. doi: 10.1093/neuonc/now277

Vanpouille-Box, C., Lacoeuille, F., Belloche, C., Lepareur, N., Lemaire, L., LeJeune, J.-J., et al. (2011). Tumor eradication in rat glioma and bypass of immunosuppressive barriers using internal radiation with (188)Re-lipid nanocapsules. *Biomaterials* 32 (28), 6781–6790. doi: 10.1016/j.biomaterials.2011.05.067

Virgolini, I., Britton, K., Buscombe, J., Moncayo, R., Paganelli, G., and Riva, P. (2002). In- and Y-DOTA-lanreotide: results and implications of the MAURITIUS trial. *Semin. Nucl. Med.* 32 (2), 148–155. doi: 10.1053/snuc.2002.31565

Vogelbaum, M. A., and Aghi, M. K. (2015). Convection-enhanced delivery for the treatment of glioblastoma. *Neuro-oncology* 17 (suppl 2), ii3–ii8. doi: 10.1093/neuonc/nou354

Zagzag, D., Friedlander, D. R., Dosik, J., Chikramane, S., Chan, W., Greco, M. A., et al. (1996). Tenascin-C expression by angiogenic vessels in human astrocytomas and by human brain endothelial cells in vitro. *Cancer Res.* 56 (1), 182–189.

Zalutsky, M. R., Reardon, D. A., Akabani, G., Coleman, R. E., Friedman, A. H., Friedman, H. S., et al. (2008). Clinical experience with alpha-particle emitting 211At: treatment of recurrent brain tumor patients with 211At-labeled chimeric antitenascin monoclonal antibody 81C6. *J. Nucl. Med.* 49 (1), 30–38. doi: 10.2967/jnumed.107.046938

Conflict of Interest Statement: The authors declare that the research was conducted in the absence of any commercial or financial relationships that could be construed as a potential conflict of interest.

frontiers in Pharmacology

REVIEW
published: 12 August 2019
doi: 10.3389/fphar.2019.00887

Reversing the Tumor Target: Establishment of a Tumor Trap

Mathie Najberg[1,2], Muhammad Haji Mansor[1,3], Frank Boury[1], Carmen Alvarez-Lorenzo[2†] and Emmanuel Garcion[1†]

[1] CRCINA, INSERM, Université de Nantes, Université d'Angers, Angers, France, [2] Departamento de Farmacología, Farmacia y Tecnología Farmacéutica, R + D Pharma Group (GI-1645), Facultad de Farmacia, Universidade de Santiago de Compostela, Santiago de Compostela, Spain, [3] Center for Education and Research on Macromolecules (CERM), Université de Liège, Liège, Belgium

Despite the tremendous progress made in the field of cancer therapy in recent years, certain solid tumors still cannot be successfully treated. Alongside classical treatments in the form of chemotherapy and/or radiotherapy, targeted treatments such as immunotherapy that cause fewer side effects emerge as new options in the clinics. However, these alternative treatments may not be useful for treating all types of cancers, especially for killing infiltrative and circulating tumor cells (CTCs). Recent advances pursue the trapping of these cancer cells within a confined area to facilitate their removal for therapeutic and diagnostic purposes. A good understanding of the mechanisms behind tumor cell migration may drive the design of traps that mimic natural tumor niches and guide the movement of the cancer cells. To bring this trapping idea into reality, strong efforts are being made to create structured materials that imitate myelinated fibers, blood vessels, or pre-metastatic niches and incorporate chemical cues such as chemoattractants or adhesive proteins. In this review, the different strategies used (or could be used) to trap tumor cells are described, and relevant examples of their performance are analyzed.

Keywords: tumor cell migration, tumor trap, biomimetic trap, cancer therapy, premetastatic niche recruitment

OPEN ACCESS

Edited by:
David A. Gewirtz, Virginia Commonwealth University, United States

Reviewed by:
Olivier Feron, Catholic University of Louvain, Belgium
Gaelle Vandermeulen, Catholic University of Louvain, Belgium

***Correspondence:**
Emmanuel Garcion
emmanuel.garcion@univ-angers.fr

†These authors have contributed equally to this work

Specialty section:
This article was submitted to Pharmacology of Anti-Cancer Drugs, a section of the journal Frontiers in Pharmacology

Received: *06 March 2019*
Accepted: *15 July 2019*
Published: *12 August 2019*

Citation:
Najberg M, Haji Mansor M, Boury F, Alvarez-Lorenzo C and Garcion E (2019) Reversing the Tumor Target: Establishment of a Tumor Trap. Front. Pharmacol. 10:887. doi: 10.3389/fphar.2019.00887

INTRODUCTION

For many decades, surgery, radiotherapy, and chemotherapy have served as the mainstay trident in the fight against cancer (**Figure 1** Scheme I). During this period, the prognosis of many types of cancer has been significantly improved (Brustugun et al., 2018; Zeng et al., 2018; Iacobucci, 2019; Trama et al., 2019). However, the widespread use of these treatments has also uncovered several major limitations. For example, the feasibility of surgery is very much dependent on the localization and the size of the tumor. The procedure is also contraindicated in patients with poor clinical performance. As for radiotherapy and chemotherapy, these treatments are often implicated with serious side effects that, in some cases, may outweigh their potential therapeutic benefits. Moreover, these treatments lack the capacity to prevent metastases, which are responsible for roughly 90% of cancer-associated deaths (Rankin and Giaccia, 2016).

Numerous studies in the quest of improving cancer treatments are driven by the concept of "magic bullet" (**Figure 1** Scheme II-2) put forward by the German scientist Paul Ehrlich (Strebhardt and Ullrich, 2008). If radio- and chemotherapy are considered as weapons of mass destruction, Ehrlich's strategy can be regarded as the sniper of cancer therapy. This concept is mainly based on the idea of increasing the bioavailability and specificity of vector-associated active agents in the body while limiting their premature degradation and toxicity. In the context of anticancer

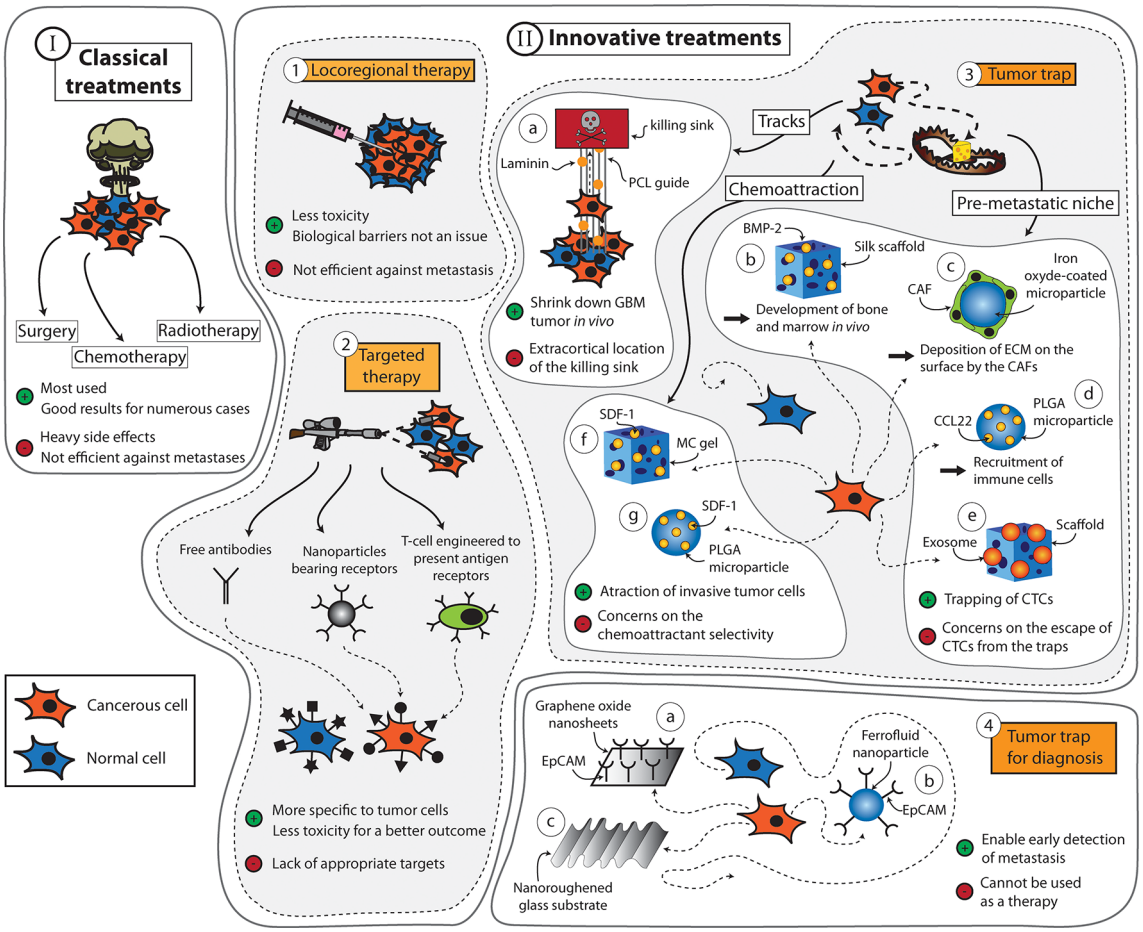

FIGURE 1 | Summary of the strategies that can be applied to fight cancers. (Scheme I) The classic treatments used for cancers are surgery, chemotherapy, and radiotherapy. (Scheme II) Innovative treatments include (1) locoregional therapy, (2) targeted therapy, and (3) tumor traps, among others. Tumor traps can be designed to take advantage of the migration pathways used by the tumor cells. It includes the use of tracks [(a) system developed by Jain et al. (2014) using aligned PCL fibers coated with laminin]. Tumor traps can be designed as synthetic pre-metastatic niches [(b) system developed by Seib et al. (2015) using a silk scaffold loaded with bone morphogenic protein 2 (BMP-2) capable of developing bone and marrow *in vivo*, (c) system developed by De Vlieghere et al. (2015) using iron oxide-coated microparticles encapsulating cancer-associative fibroblasts (CAFs) that continuously deposit ECM on the surface, (d) system developed by Azarin et al. (2015) using poly(lactide-co-glycolic acid) (PLGA) through the induction of the immune system by the CCL22 chemokine, and (e) system developed by De La Fuente et al. (2015) using a three-dimensional scaffold loaded with exosomes]. Finally, tumor traps can use chemoattractive molecules [(f) system developed by Giarra et al. (2018) using a methylcellulose (MC) thermo-responsive hydrogel loaded with stromal derived factor-1 (SDF-1) and (g) the system developed by Haji Mansor et al. (2018) using SDF-1 encapsulated in PLGA nanoparticles]. (4) Tumor traps can also be used for the early detection of metastasis [(a) system developed by Yoon et al. (2013) using graphene oxide nanosheets, (b) CELLSEARCH® CTC test (CELLSEARCH Circulating Tumor Cell, 2019) is a device using ferrofluid nanoparticles with EpCAM antibodies, and (c) system developed by Chen et al. (2016) using a nanoroughened glass substrate].

approaches, the success of selective therapies depends on the discovery of targeting elements that, when coupled with active ingredients and/or diagnostic cues, enable the recognition of well-characterized molecules, cells, or tissues. For example, Adcetris® targets the antigen CD30 in the treatment of Hodgkin's lymphoma, and Kadcyla® targets HER2, which is present in about 20% of breast cancer patients (Kim and Kim, 2015). Nevertheless, the discovery of appropriate targets that are specific to tumor cells remains a challenging task, despite the significant advancements made in the field of genomics and proteomics in recent decades.

Fortunately, a plethora of new therapies are being approved regularly for the treatment of cancer. Among them is the use of locoregional therapies (**Figure 1** Scheme II-1) that includes Nanotherm® (MagForce) that involves injection of magnetic nanoparticles inside the tumor or into the resection cavity. A magnetic field is then applied to generate heat *via* the nanoparticles and kill the cancerous cells locally (Maier-Hauff et al., 2011). It is currently licensed in Europe for the treatment of brain tumors and has received FDA approval in February 2018 to be used in clinical trials involving prostate cancer patients (MagForce, 2018). Another example is Optune® (Novocure Ltd), a tumor-treating field (TTF) device composed of electrodes that can be placed on the patients' scalp and connected to a generator to deliver a low-intensity electric field of 200 kHz (Taphoorn et al., 2018). It is believed to exert anticancer effects by disrupting the division of tumor cells (Giladi et al., 2015). The device has

been approved for the treatment of glioblastoma and shown to increase the median survival from 15 to 21 months when used on top of the standard treatments for this cancer (Stupp et al., 2017). However, many countries and insurance companies do not cover the cost of this treatment, and the clinical adoption of this technology remains limited due to concerns regarding the lack of understanding of the device's exact mechanism of action. Moreover, some skepticism exists toward the legitimacy of the device approval process due to the poor consideration of any placebo effect during the clinical trial phase (Fabian et al., 2019).

Among the numerous classes of novel anticancer treatments entering the market, cancer immunotherapy is arguably the one that is currently attracting the highest level of attention (**Figure 1** Scheme II-2). This class of treatment aims to treat cancer through artificial stimulation of the patient's immune system (Zhang and Chen, 2018). The most cutting-edge subset of this type of treatment is the chimeric antigen receptor (CAR) T-cell immunotherapy, which involves harvesting T cells from a patient and genetically modifying these cells to express a receptor that can bind to a tumor antigen before injecting them back into the patient (Feins et al., 2019). CAR-T cell immunotherapy made its debut in the clinic in August 2017 when Kymriah® (Novartis) was approved by the FDA for the treatment of B-cell acute lymphoblastic leukemia (BCALL) (FDA, 2017a). This was followed by the approval of Yescarta® (Gilead Sciences) in October of the same year for the treatment of diffuse large B-cell lymphoma (FDA, 2017b). Both Kymriah® and Yescarta® exert their effects by targeting CD19 antigen (Zheng et al., 2018). However, there are numerous ongoing clinical studies that explore the feasibility of targeting other antigens including PD-L1 (ClinicalTrials.gov Identifier NCT03672305, NCT03198052, NCT03330834), EpCAM (ClinicalTrials.gov Identifier NCT03013712, NCT03563326, NCT02729493), and CD123 (ClinicalTrials.gov Identifier NCT03796390, NCT02937103, NCT03672851). Many of these trials also attempt to evaluate the efficacy of CAR-T cell immunotherapy against solid tumors to expand its indication beyond certain blood cancers. More comprehensive reviews on the current status and future directions of CAR T-cell immunotherapy as well as other subsets of cancer immunotherapy such as immune checkpoint inhibitors and cancer vaccines can be found elsewhere (Dougan et al., 2018; Li et al., 2018; Sambi et al., 2019).

Despite the continuous increase in the number of novel anticancer treatments entering the clinic, local recurrence in previously healthy tissues seen in many cases of solid tumors remains an unsolved conundrum among clinicians and researchers alike. Development of new therapies for *in situ* control of the disease, while avoiding the problems of biological barriers and systemic toxicity, still proves to be a formidable task. Thus, in parallel to the innovative approaches mentioned previously, the idea of trapping infiltrative or circulating tumor cells (CTCs) within a confined area to facilitate their removal for therapeutic or diagnostic purposes has risen (**Figure 1** Scheme II-3,4). Over the last years, this concept has developed progressively. The aim is twofold: a) to avoid the uncontrolled dissemination of tumor cells and b) to efficiently prevent the phenomenon of epithelial–mesenchymal transition (EMT) or development of metastases. The concept is largely inspired by the "ecological trap" theory (van der Sanden et al., 2013). By considering cancers as ecosystems, it is possible to develop tumor traps not only for the infiltrative tumor cells, but also for the CTCs that are responsible for metastasis. However, imitating the traditional features of a natural habitat or niche for tumor cells and directing their migration pathways present numerous physical and biological challenges. The focus of this review will be on understanding the mechanisms of tumor cell migration and how this knowledge can be used to capture them, keeping in mind that different tumors are likely to utilize different mechanisms.

MIGRATION OF TUMOR CELLS

Tumor cells must cover a great distance on their journey to form metastases (**Figure 2**). The first step of the process is to

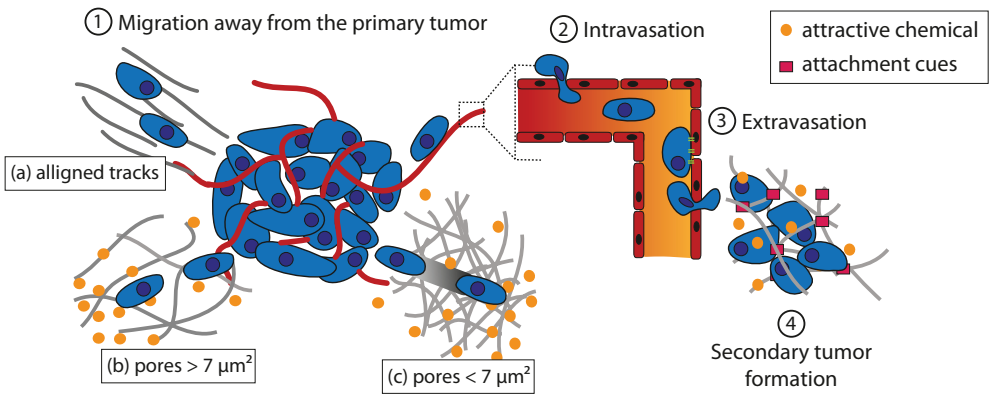

FIGURE 2 | Schematic representation of theorized paths of cancer cell migration away from the primary tumor. (1) Migration away from the primary tumor. Tumor cells can follow aligned tracks (a), or gradients of chemoattractant in solution (chemotaxis) or fixed on a substrate (haptotaxis) through the ECM. If the cross-sectional area of the interfibrillar pore is more than 7 μm², degradation of the matrix is not needed (b); otherwise, a leader cell creates a path for the following cells thanks to MMPs (c). (2) Tumor cells adhere to a vessel and intravasate to reach the blood or lymphatic stream in which they circulate. (3) Once they reach a location where they can adhere to the vessel wall, the cells extravasate. (4) If the environment is favorable, a secondary tumor grows.

migrate away from the primary tumor. Tumor cells can follow aligned tracks a), or gradients of chemoattractant in solution (chemotaxis) or fixed on a substrate (haptotaxis) through the extracellular matrix (ECM) b). If the cross-sectional area of interfibrillar pores is more than 7 μm^2, degradation of the matrix is not needed for cell movement. Alternatively, a leader cell can open a path for the following cells by virtue of the matrix metalloproteinase (MMP) activity c). The second step is to intravasate into the bloodstream or the lymphatic system in which the tumor cells will transit through the circulation. Third, cells extravasate to secondary tissues once they reach a location where they can adhere to the walls of the vessel. The fourth and final step deals with the formation of a secondary tumor. This only occurs if the environment is favorable to tumor growth.

The different strategies implemented to mislead these cells into a trap are described in next sections. These strategies exploit the current knowledge on cancer cell migration and metastasis and the specificities of each type of tumor.

Migration Away From the Primary Tumor

The physical interactions between the ECM and cancer cells play a key role in allowing the cells to start migrating. Cancer cells may undergo an EMT to acquire a motile phenotype (Polyak and Weinberg, 2009). This translates into the loss of intracellular adhesion molecules such as E-cadherin and cytokeratins, resulting in detachment of the cells from the primary tumor, and an overexpression of MMP on their surface that allows the cells to digest laminin and collagen IV to progress in the dense ECM (Polyak and Weinberg, 2009). These changes are thought to be related to the stiffness of the matrix around the tumor, which is of higher values than that of normal tissues (Wozniak et al., 2003; Paszek et al., 2005; Kumar and Weaver, 2009; Levental et al., 2009). For example, the stiffness of GBM tissues is of ~25 kPa. while normal brain tissues have a stiffness of 0.1 to 1 kPa (Wang et al., 2014). Wang et al. investigated the effect of matrix stiffness on GBM cells and found that an increase in matrix rigidity could induce an upregulation of MMP-1, Hras, RhoA, and ROCK1 (Wang et al., 2014), which are involved in increasing cell motility (Pulukuri and Rao, 2008; Liu et al., 2014; Wu et al., 2016; Li et al., 2017). Another physical factor that governs the dissemination of cancer cells is the architecture of the extracellular environment, which includes pores of a diameter ranging from less than 1 to 20 μm (Wolf et al., 2009). Matrix degradation is usually required for cancer cell migration to occur when the cross-sectional area of the interfibrillar pore is less than 7 μm^2, which corresponds to about 10% of the nuclear cross-section of cancer cells (Wolf et al., 2013). Above this value, cells can undergo deformation to migrate through the ECM.

Apart from the porosity of the ECM, the spatial arrangement of the matrix fibers near the primary tumor sites can also influence the motility of tumor cells; aligned fibers offer tracks that are more conducive to migration (Provenzano et al., 2008; Paul et al., 2017). These tracks are found along the ECM fibers in the interstitial space, between the muscle and nerve fibers, and along or within the vasculature of organs, among others (Gritsenko et al., 2012). Moreover, it has been observed that leader tumor cells are able to align collagen fibers to assist the migration of the following cells (Provenzano et al., 2006). In addition to creating the required physical space, these tracks also facilitate cancer cell migration by providing relevant molecular guidance. For example, cancer cells can be guided toward laminin and hyaluronan molecules in the ECM by their integrins and CD44 receptors, respectively, and also *via* haptotaxis by chemokines and growth factors immobilized along the tracks (Aznavoorian et al., 1990; Gritsenko et al., 2012). Jain et al. took inspirations from these biological phenomena and designed a scaffold to guide GBM cells toward a killing sink in an extracortical location (**Figure 1** Scheme II-3-a) (Jain et al., 2014). They utilized aligned poly-L-lysine and laminin-coated polycaprolactone (PCL) nanofibers (10 μm thick) encased in a PCL/polyurethane support (2.4 mm diameter) to imitate the white matter tracts (Bernstein and Woodard, 1995; Giese et al., 2003). The killing sink was composed of a collagen-based hydrogel conjugated to the chemotherapeutic agent cyclopamine. With this approach, the tumor mass of induced GBM in mice could be reduced. However, despite the positive results, this strategy as itself has limited clinical appeals, as the establishment of an extracortical sink in human patients may invite numerous technical difficulties. Instead, exploiting the local (intracortical) migration of the cancer cells may be a more translatable strategy to develop an efficient tumor trap for this cancer.

Intravasation and Tumor Cell Circulation

Tumor cells can circulate through the blood and lymphatic vessels on their journey to form a secondary tumor distant from the primary site (Chiang et al., 2016). This requires the cells to intravasate by passing through the endothelial cell junctions. Intravasation into the blood vessels occurs frequently due to the leaky nature of tumor vasculature. In addition, it has been observed *in vivo* that metastatic cells are able to polarize toward blood vessels. A possible explanation to this phenomenon is that these cells have an increased expression of epidermal growth factor (EGF) and/or colony-stimulating factor 1 (CSF-1) receptors. Thus, they migrate toward a gradient of EGF or CSF-1 released by the macrophages lining the blood vessels (Wyckoff et al., 2000; Wyckoff et al., 2004). However, it is still easier for tumor cells to enter the lymphatic system, as the surrounding ECM network is easier to penetrate and that the endothelial junctions are looser (Wong and Hynes, 2006). Either route can lead to blood vessel dissemination since the lymphatic circulation drains into the blood. As the lymphatic fluid is filtered by the lymph nodes, tumor cells are invariably invading them, starting with the nearest (Nathanson, 2003).

Once in the blood circulation, the trajectory of the tumor cells is influenced by the blood flow, the diameter of the blood vessels, and the intercellular adhesion (Wirtz et al., 2011). Two mechanisms can lead to the arrest of a CTC: physical occlusion and cell adhesion (**Figure 3**). Physical occlusion occurs when the diameter of the blood vessel is smaller or equal to the one of the CTC (usually around 10 μm). This has been observed in the brain by real-time imaging in a mouse model (Kienast et al., 2010). Adhesion of CTCs to the vessel walls occurs when there is a balance between the adhesion force and the shear force

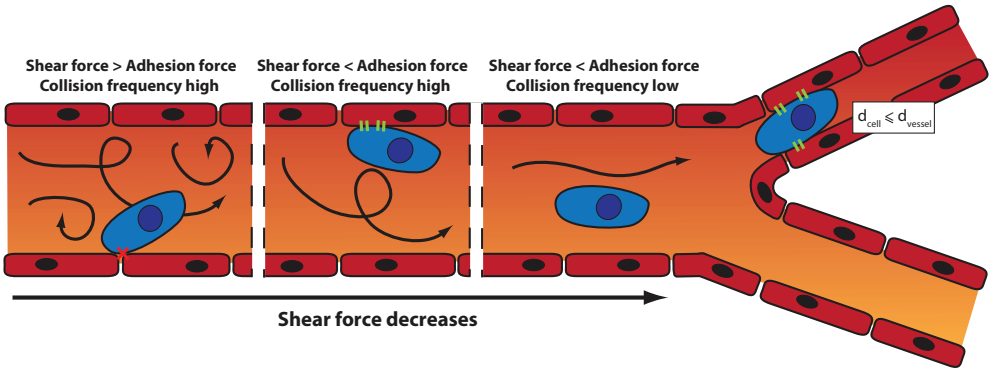

FIGURE 3 | Mechanisms of arrest of a CTC: the influence of the shear force and the blood vessel diameter on the site of CTC extravasation.

exerted inside the blood vessel (Zhu et al., 2008). When the shear force increases, the collisions between cells and the vessel wall increase, which in turn enhances the likelihood of cell adhesion. However, if the shear force is too high, turbulences may prevent the adhesion.

It is therefore possible to capture CTCs by designing a device with strong adhesive cues. Yoon et al. (2013) designed a microfluidic device consisting of graphene oxide nanosheets fixed onto a patterned gold surface to capture CTCs in early-stage cancer for analytical purposes (**Figure 1** Scheme II-4-a). The nanosheets were functionalized with epithelial cell adhesion molecule (EpCAM) antibody to capture CTCs. Blood samples were retrieved from healthy donors and mixed with labeled human breast cancer cell lines MCF-7 and Hs-578T and the human prostate cancer cell line PC-3. This microfluidic device captured more than 70% of the cancer cells in the prepared blood sample with high specificity. A similar principle was also implemented in the design of CELLSEARCH® CTC Test, the first and only clinically validated and FDA-approved blood test for enumerating CTCs (CELLSEARCH Circulating Tumor Cell, 2019). It allows for early assessment of patient prognosis as well as follow-up of the patient. The test constitutes the use of ferrofluid nanoparticles with EpCAM antibodies that bind to CTCs (**Figure 1** Scheme II-4-b). Once magnetically separated from the rest of the blood sample, cells are stained to discriminate CTCs from leukocytes that can copresent in the sample. Working within the same domain of research, Chen et al. (2016) designed a nanoroughened glass substrate to capture CTCs based on their stronger adhesion capacity compared with normal blood cells (**Figure 1** Scheme II-4-c). Such a working principle makes this device useful for capturing CTCs regardless of their surface marker expression profile, which is known to vary according to the type of cancer, patient demographics, and the state of the disease. It is indeed well discussed in the literature that the EMT process may lead to reduction in the epithelial cell adhesion molecule (EpCAM) expression in CTC (Hyun et al., 2016). The capture of CTC using EpCAM antibody alone may lead to an underestimation of the CTC number in the blood. With this device, more than 80% of cancer cells in whole blood samples from mice with induced breast cancer or lung cancer were captured independently of their EpCAM expression. Based on these findings, it is evident that a number of approaches can be adopted to capture CTCs to enable early detection of metastasis, although most of them are still far from translation to the clinic.

Extravasation and Secondary Tumor Formation

At the end of their time in blood circulation, the CTCs that survived and adhered to the blood vessel walls extravasate, and a fraction of these proceeds to form a secondary tumor. It has been shown experimentally that only about 0.01% of the cells in the circulation system eventually contribute to metastatic colonization (Fidler, 1970). The location at which they stop and grow into a secondary tumor is not believed to be randomly determined, and the reasons driving the selection of a particular site are still being investigated. In 1889, Paget et al. hypothesized that metastasizing cancer cells are like seeds that can only grow in the proper soil (Paget, 1889). Indeed, it has been observed that invasive cancer cells tend to migrate toward certain preferred sites of metastasis, a phenomenon that has been coined as "tissue tropism" (Seib et al., 2015). More recent studies revealed that the formation of certain microenvironments termed as pre-metastatic niches is crucial to the subsequent formation of metastatic tumors. These microenvironments consist of inflammatory immune cells, stromal cells, ECM proteins, tumor-secreted exosomes, and homing factors (Aguado et al., 2017). Tumor-secreted exosomes are sent to prime the niche at a target organ (often lungs, liver, brain, bone, and lymph nodes) by attracting bone marrow-derived cells (BMDCs) as well as increasing the proliferation of fibroblast-like stromal cells (Peinado et al., 2012). BMDCs include $CD11b^{+}$ myeloid cells, myeloid-derived suppressor cells, neutrophils, tumor-associated macrophages, and regulatory T cells. They are known to create an attractive site for metastasizing cells, and the presence of VEGFR1-positive BMDCs can serve as a predictor for the arrival of tumor cells (Kaplan et al., 2005). Moreover, the establishment of a pre-metastatic niche is associated with an increased secretion of inflammatory cytokines and chemokines (Hiratsuka et al., 2006; Darash-Yahana et al., 2009; Brennecke et al., 2014). The increasing understanding of

the pre-metastatic niches and their roles in welcoming metastatic dissemination has inspired scientists to create synthetic niches as a means to trap migrating cancer cells.

Creation of a Synthetic Pre-metastatic Niche to Trap CTCs

Many different strategies have been explored to engineer pre-metastatic niches. For example, Seib et al. (2015) developed a tumor trap for the metastasizing cells of breast and prostate cancers by imitating the red bone marrow microenvironment (**Figure 1** Scheme II-3-b). The strategy was adopted based on the knowledge that the bone was the preferred site of colonization in more than 60% of cases of metastasis for primary breast cancer and 73% for primary prostate cancer (Weiss, 1992). Evidence shows that red bone marrow attracts migrating cancer cells *via* chemotaxis with stromal derived factor-1 (SDF-1) (Taichman et al., 2002) and CXCL16 (Lee et al., 2013). It also provides adhesion sites that interact with tumor cell surface molecules such as annexin2 (Shiozawa et al., 2008), growth arrest-specific 6 (GASP-6) (Shiozawa et al., 2010), CD44 (Hill et al., 2006), integrins (such as VLA-4, VLA-5, and LFA-1), and cadherins. Moreover, the bone marrow microenvironment is composed of osteoblasts, osteoclasts, stromal cells, stem cells, and mineralized bone marrow surrounded by a rich vascular bed, making it a perfect site for tumor growth (Mishra et al., 2011). To imitate the red bone marrow, Seib et al. designed a silk fibroin scaffold loaded with bone morphogenetic protein 2 (BMP-2) that is capable of developing bone and marrow *in vivo*. After implantation into the mammary fat pads of mice with induced breast or prostate tumor, no effect on the primary tumor growth was observed. However, metastatic growth could be seen taking place in the functionalized scaffolds, suggesting that it is possible to lure metastasizing cells into a trap by imitating the bone marrow microenvironment. A similar strategy was adopted by Bersani et al. (2014). They utilized a polyacrylamide hydrogel coated with bone marrow stromal cells (BMSCs), which was able to capture metastasizing cells of prostate cancer.

De Vlieghere et al. (2015) took a slightly different approach to mimic a pre-metastatic niche by developing traps made of iron oxide-coated microparticles, encapsulating metabolically active cancer-associated fibroblasts (CAFs) (**Figure 1** Scheme II-3-c). The CAFs continuously deposited ECM composed of type I collagen and tenascine C, among others, creating an adhesive environment for disseminated cancer cells. The microparticles were implanted into the peritoneal cavities of mice with induced ovarian cancer. Twenty-four hours after the implantation, the microparticles were magnetically removed, and the adhesion of cancer cells on the microparticles was assessed. The treatment led to a delay in peritoneal metastasis and prolonged the animal survival.

Another variation in the strategy for recruiting metastasizing cancer cells was presented by Azarin et al. (2015). They developed a microporous scaffold from poly(lactide-co-glycolic acid) (PLGA) scaffold for *in vivo* capture of metastasizing breast cancer cells through the induction of a local immune response (**Figure 1** Scheme II-3-d). Indeed, it has been shown that immune cells are implicated in tumor cell recruitment (Qian et al., 2009; Qian et al., 2011). Here, they have either recruited immune cells into the scaffold by grafting the chemokine CCL22, which is known to induce migration of immune cells but not tumor cells, or incorporated the $Gr1^{hi}CD11b^{+}$ immune cells directly into the PLGA scaffold. By doing this, they were able to reduce the number of breast cancer cells that metastasized to the lung by 88%. Similarly, Rao et al. (2016) designed a poly(ε-caprolactone) (PCL)-based device with a slower degradation rate than PLGA scaffolds and investigated the immune response induced at the implantation site, the ability of the device to recruit metastatic cells for detection prior to colonization of organs as well as its influence on the survival of mice with induced breast cancer. Pelaez et al. (2018) further developed the strategy to enable the elimination of the attracted metastatic cells by noninvasive focal hyperthermia. To do so, they coupled metal discs to PCL microparticles to allow heat generation through electromagnetic induction using an oscillating magnetic field. The heat generation could be modulated conveniently by changing the size of the disc or the type of metal.

It has been shown that exosomes, which are vesicles involved in the transfer of information between cells, play a role in homing CTCs in the pre-metastatic niche (Peinado et al., 2012). De La Fuente et al. (2015) harnessed the potential of this knowledge and designed a three-dimensional scaffold with embedded exosomes extracted from the ascitic fluid of ovarian cancer patients (**Figure 1** Scheme II-3-e). The scaffold, called M-Trap, was implanted in the inner wall of the peritoneum of mice with a xenograft of human ovarian cancer in the peritoneal cavity. They showed that the scaffold could serve as the preferred site of metastasis, while a peritoneal carcinometastasis was observed in the absence of the M-Trap. Moreover, an increase in the mean survival was observed in the presence of the M-Trap (from 117.5 to 198.8 days), which was further improved by the removal of the scaffold (mean of survival of 309.4 days). The safety and performance of the M-Trap is currently being evaluated in a clinical trial involving female patients with stage IIIC ovarian cancer (ClinicalTrials.gov Identifier NCT03085238).

Chemoattraction of Tumor Cells

Migrating cells can make directional choices when presented with different migration pathways. *In vitro*, it has been shown that neutrophil-like cells can navigate through a microfabricated maze by following a chemical gradient (Skoge et al., 2016). Chemokines and their receptors are particularly involved in this navigation process. They are indeed responsible for the chemoattraction of various cells and could therefore be used to attract migrating tumor cells into a trap. Several receptors/chemokines have been identified to facilitate cancer cell migration. The most investigated one is SDF-1, also called CXCL12, which binds with high affinity to the CXCR4 and CXCR7 receptors. This chemokine is a pro-inflammatory mediator and is known to play a role in the recruitment of T cells, monocytes, and lympho-hemopoietic progenitor cells (Crump et al., 1997). Its overexpression has been linked to an increase in the invasiveness of ovarian cancer (Kajiyama et al., 2008), breast cancer (Bachelder et al., 2002; Zhan et al., 2016), and GBM (Barbero et al., 2003; Hira et al., 2017), among others [further details can be found elsewhere (Kryczek

et al., 2007)]. In addition, despite being less well studied, CXCL16 and its receptor CXCR6 are also suspected to play a role in the migration of tumor cells. Wang et al. (2008) have shown that the expression of CXCR6 increases with the grade of prostate cancer. These results were supported by Lu et al. (2008) who observed that metastatic cells from prostate cancer overexpress the CXCR6 receptor. Moreover, CXCL16 have been shown to induce the migration and enhance the proliferation of CXCR6-expressing cancer cells *in vitro* (Darash-Yahana et al., 2009).

With this knowledge, several groups have tried to stop the migration of tumor cells by inhibiting chemokine receptors, particularly the CXCR4 receptor. A reduction in the migration of cancer cells has been observed *in vitro* (Brennecke et al., 2014; Chittasupho et al., 2017; Zheng et al., 2017). However, this has not been successfully replicated *in vivo*. Brennecke et al. found that the use of CXCR4 antibody 12G5 can reduce the number of osteosarcoma pulmonary metastases having a diameter of <0.1 mm but not those of larger dimensions (Brennecke et al., 2014). This finding can be explained by the fact that chemoattraction of cancer cells can be mediated by several pairs of chemokine–receptor interaction (for example, SDF-1 can bind either CXCR4 or CXCR7 or both, and CXCR6 can be activated by CXCL16). In addition, cells can activate the so-called compensation mechanisms *in vivo* to maintain their migration capacity. Indeed, it has been observed that neural progenitor cells (NPCs) are able to migrate in response to SDF-1 *via* the activation of the CXCR7 receptor in response to the blockade of the CXCR4 receptor (Chen et al., 2015). Therefore, in order to stop the migration of tumor cells completely, all receptors implicated in *in vivo* chemoattraction should be identified and blocked, making the task nearly impossible. Moreover, this strategy could only work if the tumor cells have yet to begin migrating. In the particular case of GBM, cancer cells usually have already invaded the surrounding tissues at the time of diagnosis (Giese et al., 2003). Thus, it may be more useful to direct the migration of cells toward a desired location instead of blocking the migration process altogether.

Chemokines are already being used to attract cells into a scaffold for regenerative medicine purposes. The tumor trap concept can benefit from the existing knowledge in this field of application. Water-retaining polymer networks such as hydrogels and swellable matrices, which have been widely used in tissue engineering and regeneration, are pivotal platforms that are transferrable to the tumor trap application. For this purpose, biocompatible polymers capable of *in situ* formation of three-dimensional gels (Schesny et al., 2014; Shen et al., 2014; Addington et al., 2015) or matrices (Li et al., 2013; Yoon et al., 2013; Azarin et al., 2015; De Vlieghere et al., 2015; Ding et al., 2015; Autier et al., 2018) may be used to exert chemotaxis (based on a gradient of soluble attractant or repellant) or haptotaxis (based on a gradient of substrate-bound extracellular matrix proteins) (**Figure 4**). Of particular interest is the potential exploitation of the CXCR4-SDF-1 axis due to its prominent roles in regulating the migration of many types of cancer cells (Andreas et al., 2014; Schesny et al., 2014; Addington et al., 2015; Goffart et al., 2015). Examples of biomaterials used to deliver SDF-1 for regenerative medicine are presented in **Table 1**. Recently, the development of SDF-1-releasing scaffolds to attract tumor cells has received increasing attention. Giarra et al. (2018) designed a temperature-responsive gel loaded with SDF-1 based on methylcellulose (MC) or poloxamers with or without hyaluronic acid (HA) for the purpose of attracting CXCR4-expressing GBM cells (**Figure 1** Scheme II-3-f). Haji Mansor et al. (2018), on the other hand, encapsulated the chemokine in nanoparticles composed of PLGA and a (PEG)-PLGA copolymer to achieve sustained release (**Figure 1** Scheme II-3-g). However, in both papers, no *in vivo* assessment on the ability of SDF-1 to attract migrating cancer cells was performed.

Challenges Associated With the Clinical Translation of the Tumor Trapping Strategy

While promising preclinical results have been obtained from the use of tumor traps as a diagnostic and/or therapeutic tool, there are multiple issues that must be addressed before this approach can enter the clinic. Main concerns include identifying suitable means for *in vivo* monitoring of the recruitment of cancer cells into the scaffolds to allow one to decide on the optimal time point for killing the trapped cancer cells. Prolonged duration of cancer cell recruitment may lead to overcrowding of the tumor trap and subsequent cell escape, reducing the purpose of the synthetic niche to merely a "relay" for the cancer cells en route to their natural metastatic sites.

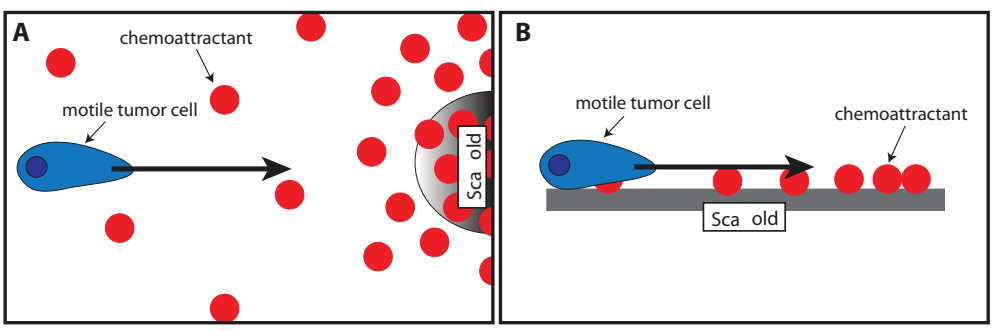

FIGURE 4 | Illustration of the use of scaffolds to attract motile tumor cells by chemotaxis **(A)** or haptotaxis **(B)**.

TABLE 1 | Strategies to load SDF-1 into different biomaterials.

Bonding strategy	Type of biomaterial	Composition	Target site for regeneration	Ref
Adsorption	Hydrogel	Hyaluronic acid	Cardiac tissue	(Purcell et al., 2012)
		PPCN	Wound healing	(Zhu et al., 2016)
	3D scaffold	Collagen	Cartilage	(Chen et al., 2015)
			Tendon	(Sun et al., 2018)
		Collagen/silk fibroin	Bone	(Hu et al., 2018)
		Hydroxyapatite	Bone	(Zhang et al., 2018)
		Decellularized skeletal muscle	Muscle	(Rajabi et al., 2018)
		Collagen/PLA	Bone	(Ritz et al., 2017)
		PLGA	Cartilage	(Wang et al., 2017)
	Membrane	PCL/gelatin	Bone	(Ji et al., 2013)
Immobilization through specific heparin-mediated interaction	Hydrogel	Heparin/PEG	Cardiac tissue	(Prokoph et al., 2012)
			Blood vessel	(Krieger et al., 2016)
			Cardiac tissue	(Baumann et al., 2013)
	3D scaffold	Heparin/PLCL	Blood vessel	(Shafiq et al., 2017)
		Heparin/PGS	Blood vessel	(Lee et al., 2013)
		Heparin/PLLA	Blood vessel	(Yu et al., 2012)
Systems with nano/ microparticles	Microspheres	Alginate	Bone	(Xu et al., 2018)
	Hydrogel/ Nanoparticles	Hydrogel: CS/GP nano: CS/CMCS	Bone	(Mi et al., 2017)
	Microcapsules	Dex-GMA/gelatin/ PNIPAAm	Wound healing	(Chen et al., 2013)
	Particles	PLGA	Cardiac tissue	(Zamani et al., 2015)

PPCN, poly (polyethylene glycol citrate-co-N-isopropylacrylamide); PLA, polylactide; PLGA, poly(lactic-co-glycolic) acid; PCL, polycaprolactone; PEG, poly(ethylene-glycol); PLCL, poly(L-lactide-co-e-caprolactone) (PLCL); PGS, poly(glycerol sebacate); PLLA, poly(l-lactic acid); CS, chitosan; GP, beta-glycerol phosphate disodium salt; CMCS, carboxymethyl-chitosan; Dex-GMA, glycidyl methacrylated dextran; PNIPAAm, poly(N-isopropylacrylamide).

The incorporation of chemoattractant molecules such as SDF-1 into the tumor trap may also introduce additional complexities. In particular, there are concerns regarding the selectivity of SDF-1-mediated chemotaxis. Indeed, in addition to its role in recruiting cancer cells to local and distant sites of colonization, SDF-1 is also implicated in the homing of other cell lines such as immune cells and stem cells (Crump et al., 1997; Wang et al., 2017; Hu et al., 2018). Moreover, the potential off-target effects may also be exacerbated by the fact that this chemokine is known to be involved in various processes that support tumor progression, angiogenesis, metastasis, and survival (Teicher and Fricker, 2010). It is therefore necessary to study in more detail the effect of injecting such proteins near tumor cells *in vivo* and to carefully evaluate the entire risks before moving to the clinic.

Further down the development timeline, the most effective way to kill the recruited cancer cells should be elucidated. It may be tempting to suggest direct removal of the trap to achieve an immediate eradication of the disease. However, this approach will necessitate an additional surgery, a requirement that may be very difficult to fulfill especially in patients who are terminally ill. A less invasive solution would be to use stereotactic radiotherapy (SRT). SRT is a treatment where radiation beam is directed to a well-defined spot, usually the tumor site, from many different angles around the body. The procedure ensures the targeted site receives much higher dose of radiation than the surrounding tissues. At the moment, SRT seems to be a viable option for killing the trapped cancer cells. This said, other selective approaches should also be considered and evaluated.

CONCLUSION

A good understanding of the escape pathways of a prey allows the hunter to capture it more efficiently; the same rule of thumb can be applied to tumor cells. Using this principle, it is possible to design tumor traps for diagnostic and/or therapeutic applications. For the latter purpose, it is necessary that the trapped cells are killed by the application of existing therapies. The different therapeutic strategies (surgery, chemotherapy, targeted therapy, …) may not be sufficient on their own to cure every cancer type, but they can be used in combination to achieve the best clinical outcomes. Jain et al. used a chemotherapeutic agent in the form of cyclopamine alongside their tumor trap to shrink down the size of GBM tumors (Jain et al., 2014). It would also be interesting to combine the trap with radiosensitizers, focus x-ray, or γ-ray microbeams. Since the trap would concentrate the tumor cells, the efficiency of chemo- and radiotherapies can potentially be improved, while the associated side effects are likely to decrease. Immunotherapy, which can be broadly described as the activation of immune cells to make them able to recognize and eliminate tumor cells, could also be used. Indeed, one of the major difficulties in immunotherapy is to make the cancer cells accessible to the activated immune cells. This is particularly true in the brain, as there is a need to overcome the blood–brain barrier (Lyon et al., 2017). If immune cells can be preloaded or attracted into the trap *via* chemoattraction, this will facilitate the killing of the trapped cancer cells. Indeed, immune cells are also sensitive to a gradient of chemokines such as SDF-1 (Krieger et al., 2016)

and can therefore be recruited into the trap together with the cancer cells of interest. Overall, this bio-integrative approach can be seen as counterintuitive insofar as the factors governing the trapping of tumor cells are also involved in other signaling pathways that may lead to effects that are opposite to the initial will (Komarova, 2015). Our current knowledge on the mechanisms driving the migration of cancerous cells might not be sufficient to develop a trap that only impacts tumor cells in a safe manner. The translation to the clinic will therefore require further investigations on the efficacy and safety of such systems. Nevertheless, as Albert Einstein pointed out, "we do not solve problems with the modes of thought that have engendered them," and this unique approach therefore deserves further investigations.

AUTHOR CONTRIBUTIONS

MN wrote the manuscript. CA-L and EG contributed to the conception and design of the work. MH, FB, CA-L and EG contributed to manuscript revision. All authors read and approved the submitted version.

FUNDING

This work was supported by the "Institut National de la Santé et de la Recherche Médicale" (INSERM), the University of Angers (Angers, France), the MINECO (SAF2017-83118-R), the Agencia Estatal de Investigacion (AEI, Spain), and the Fondo Europeo de Desarollo Regional (FEDER). It is also related to the LabEx IRON "Innovative Radiopharmaceuticals in Oncology and Neurology" as part of the French government "Investissements d'Avenir" program, to the INCa (Institut National du Cancer) MARENGO consortium "MicroRNA agonist and antagonist Nanomedicines for GliOblastoma treatment: from molecular programmation to preclinical validation" through the PL-BIO 2014-2020 grant and to the MuMoFRaT project "Multi-scale Modeling & simulation of the response to hypo-Fractionated Radiotherapy or repeated molecular radiation Therapies" supported by "La Région Pays-de-la-Loire" and by the Cancéropôle Grand-Ouest (tumor targeting and radiotherapy network). MN was a Ph.D. student involved in the Erasmus Mundus Joint Doctorate program for Nanomedicine and pharmaceutical innovation (EMJD NanoFar) and received a fellowship from "La Région Pays-de-la-Loire."

REFERENCES

Addington, C. P., Heffernan, J. M., Millar-Haskell, C. S., Tucker, E. W., Sirianni, R. W., and Stabenfeldt, S. E. (2015). Enhancing neural stem cell response to SDF-1alpha gradients through hyaluronic acid-laminin hydrogels. *Biomaterials* 72, 11–19. doi: 10.1016/j.biomaterials.2015.08.041

Aguado, B. A., Bushnell, G. G., Rao, S. S., Jeruss, J. S., and Shea, L. D. (2017). Engineering the pre-metastatic niche. *Nat. Biomed. Eng.* 1, 1–12. doi: 10.1038/s41551-017-0077

Andreas, K., Sittinger, M., and Ringe, J. (2014). Toward *in situ* tissue engineering: Chemokine-guided stem cell recruitment. *Trends Biotechnol.* 32, 483–492. doi: 10.1016/j.tibtech.2014.06.008

Autier, L., Clavreul, A., Cacicedo, M. L., Franconi, F., Sindji, L., Rousseau, A., et al. (2018). A new glioblastoma cell trap for implantation after surgical resection. *Acta Biomater.* 84, 268–279. doi: 10.1016/j.actbio.2018.11.027

Azarin, S. M., Yi, J., Gower, R. M., Aguado, B. A., Sullivan, M. E., Goodman, A. G., et al. (2015). *In vivo* capture and label-free detection of early metastatic cells. *Nat. Commun.* 6, 8094. doi: 10.1038/ncomms9094

Aznavoorian, S., Stracke, M. L., Krutzsch, H., Schiffmann, E., and Liotta, L. A. (1990). Signal transduction for chemotaxis and haptotaxis by matrix molecules in tumor cells. *J. Cell Biol.* 110, 1427–1438. doi: 10.1083/jcb.110.4.1427

Bachelder, R. E., Wendt, M. A., and Mercurio, A. M. (2002). Vascular endothelial growth factor promotes breast carcinoma invasion in an autocrine manner by regulating the chemokine receptor CXCR4. *Cancer Res.* 62, 7203–7206.

Barbero, S., Bonavia, R., Bajetto, A., Porcile, C., Pirani, P., Ravetti, J. L., et al. (2003). Stromal cell-derived factor 1alpha stimulates human glioblastoma cell growth through the activation of both extracellular signal-regulated kinases 1/2 and Akt. *Cancer Res.* 63, 1969–1974.

Baumann, P., Balasubramanian, V., Onaca-Fischer, O., Sienkiewicz, A., and Palivan, C. G. (2013). Light-responsive polymer nanoreactors: a source of reactive oxygen species on demand. *Nanoscale* 5, 217–224. doi: 10.1039/C2NR32380J

Bernstein, J. J., and Woodard, C. A. (1995). Glioblastoma cells do not intravasate into bloodvessels. *Neurosurgery* 36, 124–132. doi: 10.1227/00006123-199501000-00016

Bersani, F., Lee, J., Yu, M., Morris, R., Desai, R., Ramaswamy, S., et al. (2014). Bioengineered implantable scaffolds as a tool to study stromal-derived factors in metastatic cancer models. *Cancer Res.* 74, 7229–7238. doi: 10.1158/0008-5472.CAN-14-1809

Brennecke, P., Arlt, M. J. E., Campanile, C., Husmann, K., Gvozdenovic, A., Apuzzo, T., et al. (2014). CXCR4 antibody treatment suppresses metastatic spread to the lung of intratibial human osteosarcoma xenografts in mice. *Clin. Exp. Metastasis* 31, 339–349. doi: 10.1007/s10585-013-9632-3

Brustugun, O. T., Grønberg, B. H., Fjellbirkeland, L., Helbekkmo, N., Aanerud, M., Grimsrud, T. K., et al. (2018). Substantial nation-wide improvement in lung cancer relative survival in Norway from 2000 to 2016. *Lung Cancer* 122, 138–145. doi: 10.1016/j.lungcan.2018.06.003

CELLSEARCH Circulating Tumor Cell. (2019), https://www.cellsearchctc.com/ (accessed May 25, 2019).

Chen, F. M., Lu, H., Wu, L. A., Gao, L. N., An, Y., and Zhang, J. (2013). Surface-engineering of glycidyl methacrylated dextran/gelatin microcapsules with thermo-responsive poly(N-isopropylacrylamide) gates for controlled delivery of stromal cell-derived factor-1&alpha. *Biomaterials* 34, 6515–6527. doi: 10.1016/j.biomaterials.2013.05.014

Chen, P., Tao, J., Zhu, S., Cai, Y., Mao, Q., Yu, D., et al. (2015). Radially oriented collagen scaffold with SDF-1 promotes osteochondral repair by facilitating cell homing. *Biomaterials* 39, 114–123. doi: 10.1016/j.biomaterials.2014.10.049

Chen, Q., Zhang, M., Li, Y., Xu, D., Wang, Y., Song, A., et al. (2015). CXCR7 mediates neural progenitor cells migration to CXCL12 independent of CXCR4. *Stem Cells* 33, 2574–2585. doi: 10.1002/stem.2022

Chen, W., Allen, S. G., Reka, A. K., Qian, W., Han, S., Zhao, J., et al. (2016). Nanoroughened adhesion-based capture of circulating tumor cells with heterogeneous expression and metastatic characteristics. *BMC Cancer* 16, 614. doi: 10.1186/s12885-016-2638-x

Chiang, S. P. H., Cabrera, R. M., and Segall, J. E. (2016). Tumor cell intravasation. *Am. J. Physiol. Cell Physiol.* 311, C1–C14. doi: 10.1152/ajpcell.00238.2015

Chittasupho, C., Anuchapreeda, S., and Sarisuta, N. (2017). CXCR4 targeted dendrimer for anti-cancer drug delivery and breast cancer cell migration inhibition. *Eur. J. Pharm. Biopharm.* 119, 310–321. doi: 10.1016/j.ejpb.2017.07.003

Crump, M. P., Gong, J. H., Loetscher, P., Rajarathnam, K., Amara, A., Arenzana-Seisdedos, F., et al. (1997). Solution structure and basis for functional activity of stromal cell-derived factor-1; dissociation of CXCR4 activation from binding and inhibition of HIV-1. *EMBO J.* 16, 6996–7007. doi: 10.1093/emboj/16.23.6996

Darash-Yahana, M., Gillespie, J. W., Hewitt, S. M., Chen, Y. Y. K., Maeda, S., Stein, I., et al. (2009). The chemokine CXCL16 and its receptor, CXCR6, as markers

and promoters of inflammation-associated cancers. *PLoS One* 4, e6695. doi: 10.1371/journal.pone.0006695

De La Fuente, A., Alonso-Alconada, L., Costa, C., Cueva, J., Garcia-Caballero, T., Lopez-Lopez, R., et al. (2015). M-Trap: exosome-based capture of tumor cells as a new technology in peritoneal metastasis. *J. Natl. Cancer Inst.* 107, 1–10. doi: 10.1093/jnci/djv184

De Vlieghere, E., Gremonprez, F., Verset, L., Mariën, L., Jones, C. J., De Craene, B., et al. (2015). Tumor-environment biomimetics delay peritoneal metastasis formation by deceiving and redirecting disseminated cancer cells. *Biomaterials* 54, 148–157. doi: 10.1016/j.biomaterials.2015.03.012

Ding, Y., Wang, Y., Opoku-Damoah, Y., Wang, C., Shen, L., Yin, L., et al. (2015). Dual-functional bio-derived nanoparticulates for apoptotic antitumor therapy. *Biomaterials* 72, 90–103. doi: 10.1016/j.biomaterials.2015.08.051

Dougan, M., Dranoff, G., and Dougan, S. K. (2018). Cancer immunotherapy: beyond checkpoint blockade. *Annu. Rev. Cancer Biol.* 3, 55–75. doi: 10.1146/annurev-cancerbio-030518-055552

Fabian, D., Eibl, M. d. P. G. P. E., Alnahhas, I., Sebastian, N., Giglio, P., Puduvalli, V., et al. (2019). Treatment of glioblastoma (GBM) with the addition of tumor-treating fields (TTF): a review. *Cancers (Basel)* 11, 1–12. doi: 10.3390/cancers11020174

FDA. (2017a). FDA approval brings first gene therapy to the United States.

FDA. (2017b). FDA approves CAR-T cell therapy to treat adults with certain types of large B-cell lymphoma.

Feins, S., Kong, W., Williams, E. F., Milone, M. C., and Fraietta, J. A. (2019). An introduction to chimeric antigen receptor (CAR) T-cell immunotherapy for human cancer. *Am. J. Hematol.* 94, S3–S9. doi: 10.1002/ajh.25418

Fidler, I. J. (1970). Metastasis: quantitative analysis of distribution and fate of tumour emboli labeled with 125I-5-iodo-2[prime]-deoxyuridine. *J. Natl. Cancer Inst.* 45, 773–782.

Giarra, S., Ierano, C., Biondi, M., Napolitano, M., Campani, V., Pacelli, R., et al. (2018). Engineering of thermoresponsive gels as a fake metastatic niche. *Carbohydr. Polym.* 191, 112–118. doi: 10.1016/j.carbpol.2018.03.016

Giese, A., Bjerkvig, R., Berens, M. E., and Westphal, M. (2003). Cost of migration: invasion of malignant gliomas and implications for treatment. *J. Clin. Oncol.* 21, 1624–1636. doi: 10.1200/JCO.2003.05.063

Giladi, M., Schneiderman, R. S., Voloshin, T., Porat, Y., Munster, M., Blat, R., et al. (2015). Mitotic spindle disruption by alternating electric fields leads to improper chromosome segregation and mitotic catastrophe in cancer cells. *Sci. Rep.* 5, 1–16. doi: 10.1038/srep18046

Goffart, N., Kroonen, J., Di Valentin, E., Dedobbeleer, M., Denne, A., Martinive, P., et al. (2015). Adult mouse subventricular zones stimulate glioblastoma stem cells specific invasion through CXCL12/CXCR4 signaling. *Neuro Oncol.* 17, 81–94. doi: 10.1093/neuonc/nou144

Gritsenko, P. G., Ilina, O., and Friedl, P. (2012). Interstitial guidance of cancer invasion. *J. Pathol.* 226, 185–199. doi: 10.1002/path.3031

Haji Mansor, M., Najberg, M., Contini, A., Alvarez-Lorenzo, C., Garcion, E., Jérôme, C., et al. (2018). Development of a non-toxic and non-denaturing formulation process for encapsulation of SDF-1α into PLGA/PEG-PLGA nanoparticles to achieve sustained release. *Eur. J. Pharm. Biopharm.* 125, 38–50. doi: 10.1016/j.ejpb.2017.12.020

Hill, A., McFarlane, S., Johnston, P. G., and Waugh, D. J. J. (2006). The emerging role of CD44 in regulating skeletal micrometastasis. *Cancer Lett.* 237, 1–9. doi: 10.1016/j.canlet.2005.05.006

Hira, V. V. V., Verbovšek, U., Breznik, B., Srdič, M., Novinec, M., Kakar, H., et al. (2017). Cathepsin K cleavage of SDF-1α inhibits its chemotactic activity towards glioblastoma stem-like cells. *Biochim. Biophys. Acta - Mol. Cell Res.* 1864, 594–603. doi: 10.1016/j.bbamcr.2016.12.021

Hiratsuka, S., Watanabe, A., Aburatani, H., and Maru, Y. (2006). Tumour-mediated upregulation of chemoattractants and recruitment of myeloid cells predetermines lung metastasis. *Nat. Cell Biol.* 8, 1369–1375. doi: 10.1038/ncb1507

Hu, Y., Ran, J., Zheng, Z., Jin, Z., Chen, X., Yin, Z., et al. (2018). Exogenous stromal derived factor-1 releasing silk scaffold combined with intra-articular injection of progenitor cells promotes bone-ligament-bone regeneration. *Acta Biomater.* 71, 168–183. doi: 10.1016/j.actbio.2018.02.019

Hyun, K.-A., Koo, G.-B., Han, H., Sohn, J., Choi, W., Kim, S.-I., et al. (2016). Epithelial-to-mesenchymal transition leads to loss of EpCAM and different physical properties in circulating tumor cells from metastatic breast cancer. *Oncotarget* 7, 24677–24687. doi: 10.18632/oncotarget.8250

Iacobucci, G. (2019). Cancer survival in England: rates improve and variation falls. *BMJ* 365, l1532. doi: 10.1136/bmj.l1532

Jain, A., Betancur, M., Patel, G. D., Valmikinathan, C. M., Mukhatyar, V. J., Vakharia, A., et al. (2014). Guiding intracortical brain tumour cells to an extracortical cytotoxic hydrogel using aligned polymeric nanofibres. *Nat. Mater.* 13, 308–316. doi: 10.1038/nmat3878

Ji, W., Yang, F., Ma, J., Bouma, M. J., Boerman, O. C., Chen, Z., et al. (2013). Incorporation of stromal cell-derived factor-1α in PCL/gelatin electrospun membranes for guided bone regeneration. *Biomaterials* 34, 735–745. doi: 10.1016/j.biomaterials.2012.10.016

Kajiyama, H., Shibata, K., Terauchi, M., Ino, K., Nawa, A., and Kikkawa, F. (2008). Involvement of SDF-1alpha/CXCR4 axis in the enhanced peritoneal metastasis of epithelial ovarian carcinoma. *Int. J. Cancer* 122, 91–99. doi: 10.1002/ijc.23083

Kaplan, R. N., Riba, R. D., Zacharoulis, S., Bramley, A. H., Vincent, L., Costa, C., et al. (2005). VEGFR1-positive haematopoietic bone marrow progenitors initiate the pre-metastatic niche. *Nature* 438, 820–827. doi: 10.1038/nature04186

Kienast, Y., Von Baumgarten, L., Fuhrmann, M., Klinkert, W. E. F., Goldbrunner, R., Herms, J., et al. (2010). Real-time imaging reveals the single steps of brain metastasis formation. *Nat. Med.* 16, 116–122. doi: 10.1038/nm.2072

Kim, E. G., and Kim, K. M. (2015). Strategies and advancement in antibody-drug conjugate optimization for targeted cancer therapeutics. *Biomol. Ther. (Seoul)* 23, 493–509. doi: 10.4062/biomolther.2015.116

Komarova, N. L. (2015). Cancer: a moving target. *Nature* 525, 198–199. doi: 10.2469/cfm.v20.n1.10

Krieger, J. R., Ogle, M. E., McFaline-Figueroa, J., Segar, C. E., Temenoff, J. S., and Botchwey, E. A. (2016). Spatially localized recruitment of anti-inflammatory monocytes by SDF-1α-releasing hydrogels enhances microvascular network remodeling. *Biomaterials* 77, 280-290. doi: 10.1016/j.biomaterials.2015.10.045

Kryczek, I., Wei, S., Keller, E., Liu, R., and Zou, W. (2007). Stroma-derived factor (SDF-1 / CXCL12) and human tumor pathogenesis. *Am. J. Physiol. Cell Physiol.* 292, 987–995. doi: 10.1152/ajpcell.00406.2006

Kumar, S., and Weaver, V. M. (2009). Mechanics, malignancy, and metastasis: the force journey of a tumor cell. *Cancer Metastasis* 28, 113–127. doi: 10.1007/s10555-008-9173-4

Lee, J. T., Lee, S. D., Lee, J. Z., Chung, M. K., and Ha, H. K. (2013). Expression analysis and clinical significance of CXCL16/CXCR6 in patients with bladder cancer. *Oncol. Lett.* 5, 229–235. doi: 10.3892/ol.2012.976

Lee, K. W., Johnson, N. R., Gao, J., and Wang, Y. (2013). Human progenitor cell recruitment *via* SDF-1α coacervate-laden PGS vascular grafts. *Biomaterials* 34, 9877–9885. doi: 10.1016/j.biomaterials.2013.08.082

Levental, K. R., Yu, H., Kass, L., Lakins, J. N., Egeblad, M., Erler, J. T., et al. (2009). Matrix crosslinking forces tumor progression by enhancing integrin signaling. *Cell* 139, 891–906. doi: 10.1016/j.cell.2009.10.027

Li, W., Wang, J., Ren, J., and Qu, X. (2013). 3D graphene oxide-polymer hydrogel: near-infrared light-triggered active scaffold for reversible cell capture and on-demand release. *Adv. Mater.* 25, 6737–6743. doi: 10.1002/adma.201302810

Li, D., Cao, Y., Li, J., Xu, J., Liu, Q., and Sun, X. (2017). MiR-506 suppresses neuroblastoma metastasis by targeting ROCK1. *Oncol. Lett.* 13, 370–376. doi: 10.3892/ol.2016.5442

Li, Z., Song, W., Rubinstein, M., and Liu, D. (2018). Recent updates in cancer immunotherapy: a comprehensive review and perspective of the 2018 China Cancer Immunotherapy Workshop in Beijing. *J. Hematol. Oncol.* 11, 1–15. doi: 10.1186/s13045-018-0684-3

Liu, X., Chen, D., and Liu, G. (2014). Overexpression of RhoA promotes the proliferation and migration of cervical cancer cells. *Biosci. Biotechnol. Biochem.* 78, 1895–1901. doi: 10.1080/09168451.2014.943650

Lu, Y., Wang, J., Xu, Y., Koch, A. E., Cai, Z., Chen, X., et al. (2008). CXCL16 functions as a novel chemotactic factor for prostate cancer cells in vitro. *Mol. Cancer Res.* 6, 546–554. doi: 10.1158/1541-7786.MCR-07-0277

Lyon, J. G., Mokarram, N., Saxena, T., Carroll, S. L., and Bellamkonda, R. V. (2017). Engineering challenges for brain tumor immunotherapy. *Adv. Drug Deliv. Rev.* 114, 19–32. doi: 10.1016/j.addr.2017.06.006

MagForce, NanoTherm has the potential to tap into the US prostate cancer market as aunique focal treatment option, (2018).

Maier-Hauff, K., Ulrich, F., Nestler, D., Niehoff, H., Wust, P., Thiesen, B., et al. (2011). Efficacy and safety of intratumoral thermotherapy using magnetic iron-oxide nanoparticles combined with external beam radiotherapy on patients

with recurrent glioblastoma multiforme. *J. Neurooncol.* 103, 317–324. doi: 10.1007/s11060-010-0389-0

Mi, L., Liu, H., Gao, Y., Miao, H., and Ruan, J. (2017). Injectable nanoparticles/hydrogels composite as sustained release system with stromal cell-derived factor-1α for calvarial bone regeneration. *Int. J. Biol. Macromol.* 101, 341–347. doi: 10.1016/j.ijbiomac.2017.03.098

Mishra, A., Shiozawa, Y., Pienta, K. J., and Taichman, R. S. (2011). Homing of cancer cells to the bone. *Cancer Microenviron.* 4, 221–235. doi: 10.1007/s12307-011-0083-6

Nathanson, S. D. (2003). Insights into the mechanisms of lymph node metastasis. *Cancer* 98, 413–423. doi: 10.1002/cncr.11464

Paget, S. (1889). The distribution of secondary growths in cancer of the breast. *Lancet* 133, 571–573. doi: 10.1007/s12307-014-0163-5

Paszek, M. J., Zahir, N., Johnson, K. R., Lakins, J. N., Rozenberg, G. I., Gefen, A., et al. (2005). Tensional homeostasis and the malignant phenotype. *Cancer Cell* 8, 241–254. doi: 10.1016/j.ccr.2005.08.010

Paul, C. D., Mistriotis, P., and Konstantopoulos, K. (2017). Cancer cell motility: lessons from migration in confined spaces. *Nat. Rev. Cancer* 17, 131–140. doi: 10.1038/nrc.2016.123

Peinado, H., Alečković, M., Lavotshkin, S., Matei, I., Costa-Silva, B., Moreno-Bueno, G., et al. (2012). Melanoma exosomes educate bone marrow progenitor cells toward a pro-metastatic phenotype through MET. *Nat. Med.* 18, 883–891. doi: 10.1038/nm.2753

Pelaez, F., Manuchehrabadi, N., Roy, P., Natesan, H., Wang, Y., Racila, E., et al. (2018). Biomaterial scaffolds for non-invasive focal hyperthermia as a potential tool to ablate metastatic cancer cells. *Biomaterials* 166, 27–37. doi: 10.1016/j.biomaterials.2018.02.048

Polyak, K., and Weinberg, R. A. (2009). Transitions between epithelial and mesenchymal states: acquisition of malignant and stem cell traits. *Nat. Rev. Cancer* 9, 265–273. doi: 10.1038/nrc2620

Prokoph, S., Chavakis, E., Levental, K. R., Zieris, A., Freudenberg, U., Dimmeler, S., et al. (2012). Sustained delivery of SDF-1alpha from heparin-based hydrogels to attract circulating pro-angiogenic cells. *Biomaterials* 33, 4792–4800. doi: 10.1016/j.biomaterials.2012.03.039

Provenzano, P. P., Eliceiri, K. W., Campbell, J. M., Inman, D. R., White, J. G., and Keely, P. J. (2006). Collagen reorganization at the tumor-stromal interface facilitates local invasion. *BMC Med.* 4, 38. doi: 10.1186/1741-7015-4-38

Provenzano, P. P., Inman, D. R., Eliceiri, K. W., Trier, S. M., and Keely, P. J. (2008). Contact guidance mediated three-dimensional cell migration is regulated by Rho/ROCK-dependent matrix reorganization. *Biophys. J.* 95, 5374–5384. doi: 10.1529/biophysj.108.133116

Pulukuri, S., and Rao, J. (2008). Martix matalloproteinase-1 promotes prostate tumor growth and metastasis. *Int. J. Oncol.* 32, 757–765. doi: 10.3892/ijo.32.4.757

Purcell, B. P., Elser, J. A., Mu, A., Margulies, K. B., and Burdick, J. A. (2012). Synergistic effects of SDF-1α chemokine and hyaluronic acid release from degradable hydrogels on directing bone marrow derived cell homing to the myocardium. *Biomaterials* 33, 7849–7857. doi: 10.1016/j.biomaterials.2012.07.005

Qian, B., Deng, Y., Im, J. H., Muschel, R. J., Zou, Y., Li, J., et al. (2009). A distinct macrophage population mediates metastatic breast cancer cell extravasation, establishment and growth. *PLoS One* 4, e6562. doi: 10.1371/journal.pone.0006562

Qian, B.-Z., Li, J., Zhang, H., Kitamura, T., Zhang, J., Campion, L. R., et al. (2011). CCL2 recruits inflammatory monocytes to facilitate breast-tumour metastasis. *Nature* 475, 222–225. doi: 10.1038/nature10138

Rajabi, S., Jalili-Firoozinezhad, S., Ashtiani, M. K., Le Carrou, G., Tajbakhsh, S., and Baharvand, H. (2018). Effect of chemical immobilization of SDF-1α into muscle-derived scaffolds on angiogenesis and muscle progenitor recruitment. *J. Tissue Eng. Regen. Med.* 12, e438–e450. doi: 10.1002/term.2479

Rankin, E. B., and Giaccia, A. J. (2016). Hypoxic control of metastasis. *Science* 352, 175–180. doi: 10.1126/science.aaf4405

Rao, S. S., Bushnell, G. G., Azarin, S. M., Spicer, G., Aguado, B. A., Stoehr, J. R., et al. (2016). Enhanced survival with implantable scaffolds that capture metastatic breast cancer cells *in vivo*. *Cancer Res.* 76, 5209–5218. doi: 10.1158/0008-5472.CAN-15-2106

Ritz, U., Gerke, R., Götz, H., Stein, S., and Rommens, P. M. (2017). A new bone substitute developed from 3D-prints of polylactide (PLA) loaded with collagen i: an in vitro study. *Int. J. Mol. Sci.* 18, 2569–2583. doi: 10.3390/ijms18122569

Sambi, M., Bagheri, L., and Szewczuk, M. R. (2019). Current challenges in cancer immunotherapy: multimodal approaches to improve efficacy and patient response rates. *J. Oncol.* 2019, 1–12. doi: 10.1155/2019/4508794

Schesny, M. K., Monaghan, M., Bindermann, A. H., Freund, D., Seifert, M., Eble, J. A., et al. (2014). Preserved bioactivity and tunable release of a SDF1-GPVI bi-specific protein using photo-crosslinked PEGda hydrogels. *Biomaterials* 35, 7180–7187. doi: 10.1016/j.biomaterials.2014.04.116

Seib, F. P., Berry, J. E., Shiozawa, Y., Taichman, R. S., and Kaplan, D. L. (2015). Tissue engineering a surrogate niche for metastatic cancer cells. *Biomaterials* 51, 313–319. doi: 10.1016/j.biomaterials.2015.01.076

Shafiq, M., Kong, D., and Kim, S. H. (2017). SDF-1α peptide tethered polyester facilitates tissue repair by endogenous cell mobilization and recruitment. *J. Biomed. Mater. Res. A.* 105, 2670–2684. doi: 10.1002/jbm.a.36130

Shen, Y., Abaci, H. E., Krupsi, Y., Weng, L., Burdick, J. A., and Gerecht, S. (2014). Hyaluronic acid hydrogel stiffness and oxygen tension affect cancer cell fate and endothelial sprouting. *Biomater. Sci.* 2, 655–665. doi: 10.1039/c3bm60274e

Shiozawa, Y., Havens, A. M., Jung, Y., Ziegler, A. M., Pedersen, E. A., Wang, J., et al. (2008). Annexin II/annexin II receptor axis regulates adhesion, migration, homing, and growth of prostate cancer. *J. Cell. Biochem.* 105, 370–380. doi: 10.1002/jcb.21835

Shiozawa, Y., Pedersen, E. A., and Taichman, R. S. (2010). GAS6/Mer axis regulates the homing and survival of the E2A/PBX1-positive B-cell precursor acute lymphoblastic leukemia in the bone marrow niche. *Exp. Hematol.* 38, 132–140. doi: 10.1016/j.exphem.2009.11.002

Skoge, M., Wong, E., Hamza, B., Bae, A., Martel, J., Kfataria, R., et al. (2016). A worldwide competition to compare the speed and chemotactic accuracy of neutrophil-like cells. *PLoS One* 11, 1–19. doi: 10.1371/journal.pone.0154491

Strebhardt, K., and Ullrich, A. (2008). Paul Ehrlich's magic bullet concept: 100 years of progress. *Nat. Rev. Cancer* 8, 473–480. doi: 10.1038/nrc2394

Stupp, R., Taillibert, S., Kanner, A., Read, W., Steinberg, D. M., Lhermitte, B., et al. (2017). Effect of tumor-treating fields plus maintenance temozolomide vs maintenance temozolomide alone on survival in patients with glioblastoma a randomized clinical trial. *J. Am. Med. Assoc.* 318, 2306–2316. doi: 10.1001/jama.2017.18718

Sun, J., Mou, C., Shi, Q., Chen, B., Hou, X., Zhang, W., et al. (2018). Controlled release of collagen-binding SDF-1α from the collagen scaffold promoted tendon regeneration in a rat Achilles tendon defect model. *Biomaterials* 162, 22–33. doi: 10.1016/j.biomaterials.2018.02.008

Taichman, R. S., Cooper, C., Keller, E. T., Pienta, K. J., Taichman, N. S., and Mccauley, L. K. (2002). Use of the stromal cell-derived factor-1 / CXCR4 pathway in prostate cancer metastasis to bone. *Cancer Res.* 62 (6), 1832–1837.

Taphoorn, M. J. B., Dirven, L., Kanner, A. A., Lavy-Shahaf, G., Weinberg, U., Taillibert, S., et al. (2018). Influence of treatment with tumor-treating fields on health-related quality of life of patients with newly diagnosed glioblastoma a secondary analysis of a randomized clinical trial. *JAMA Oncol.* 4, 495–504. doi: 10.1001/jamaoncol.2017.5082

Teicher, B. A., and Fricker, S. P. (2010). CXCL12 (SDF-1)/CXCR4 pathway in cancer. *Clin. Cancer Res.* 16, 2927–2931. doi: 10.1158/1078-0432.CCR-09-2329

Trama, A., Bernasconi, A., McCabe, M. G., Guevara, M., Gatta, G., Botta, L., et al. (2019). Is the cancer survival improvement in European and American adolescent and young adults still lagging behind that in children? *Pediatr. Blood Cancer* 66, 1–9. doi: 10.1002/pbc.27407

van der Sanden, B., Appaix, F., Berger, F., Selek, L., Issartel, J.-P., and Wion, D. (2013). Translation of the ecological trap concept to glioma therapy: the cancer cell trap concept. *Future Oncol.* 9, 817–824. doi: 10.2217/fon.13.30

Wang, J., Lu, Y., Wang, J., Koch, A. E., Zhang, J., and Taichman, R. S. (2008). CXCR6 induces prostate cancer progression by the AKT/mammalian target of rapamycin signaling pathway. *Cancer Res.* 68, 10367–10376. doi: 10.1158/0008-5472.CAN-08-2780

Wang, C., Tong, X., and Yang, F. (2014). Bioengineered 3D brain tumor model to elucidate the effects of matrix stiffness on glioblastoma cell behavior using PEG-based hydrogels. *Mol. Pharm.* 11, 2115–2125. doi: 10.1021/mp5000828

Wang, Y., Sun, X., Lv, J., Zeng, L., Wei, X., and Wei, L. (2017). Stromal cell-derived factor-1 accelerates cartilage defect repairing by recruiting bone marrow mesenchymal stem cells and promoting chondrogenic differentiation. *Tissue Eng. Part A* 23, 1160–1168. doi: 10.1089/ten.tea.2017.0046

Weiss, L. (1992). Comments on hematogenous metastatic patterns in humans as revealed by autopsy. *Clin. Exp. Metastasis* 10, 191–199. doi: 10.1007/BF00132751

Wirtz, D., Konstantopoulos, K., and Searson, P.C.P.P.C. (2011). The physics of cancer: the role of physical interactions and mechanical forces in metastasis. *Nat. Rev. Cancer* 11, 522. doi: 10.1038/nrc3080

Wolf, K., Alexander, S., Schacht, V., Coussens, L. M., von Andrian, U. H., van Rheenen, J., et al. (2009). Collagen-based cell migration models in vitro and *in vivo*. *Semin. Cell Dev. Biol.* 20, 931–941. doi: 10.1016/j.semcdb.2009.08.005

Wolf, K., te Lindert, M., Krause, M., Alexander, S., te Riet, J., Willis, A. L., et al. (2013). Physical limits of cell migration: control by ECM space and nuclear deformation and tuning by proteolysis and traction force. *J. Cell Biol.* 201, 1069–1084. doi: 10.1083/jcb.201210152

Wong, S. Y., and Hynes, R. O. (2006). Lymphatic or hematogenous dissemination : perspective how does a metastatic tumor cell decide? *Cell Cycle* 5, 812–817. doi: 10.4161/cc.5.8.2646

Wozniak, M. A., Desai, R., Solski, P. A., Der, C. J., and Keely, P. J. (2003). ROCK-generated contractility regulates breast epithelial cell differentiation in response to the physical properties of a three-dimensional collagen matrix. *J. Cell Biol.* 163, 583–595. doi: 10.1083/jcb.200305010

Wu, X. Y., Liu, W. T., Wu, Z. F., Chen, C., Liu, J. Y., Wu, G. N., et al. (2016). Identification of HRAS as cancer-promoting gene in gastric carcinoma cell aggressiveness. *Am. J. Cancer Res.* 6, 1935–1948. doi: 10.1038/srep28044

Wyckoff, J. B., Jones, J. G., Condeelis, J. S., and Segall, J. E. (2000). A critical step in metastasis : *in vivo* analysis of intravasation at the primary tumor. *Cancer Res.* 60 (9), 2504–2511.

Wyckoff, J., Wang, W., Lin, E. Y., Wang, Y., Pixley, F., Stanley, E. R., et al., (2004). A paracrine loop between tumor cells and macrophages is required for tumor cell migration in mammary tumors. *Cancer Res.* 64, 7022–7029. doi: 10.1158/0008-5472.CAN-04-1449

Xu, C., Xu, J., Xiao, L., Li, Z., Xiao, Y., Dargusch, M., et al. (2018). Double-layered microsphere based dual growth factor delivery system for guided bone regeneration. *RSC Adv.* 8, 16503–16512. doi: 10.1039/C8RA02072H

Yoon, H. J., Kim, T. H., Zhang, Z., Azizi, E., Pham, T. M., Paoletti, C., et al. (2013). Sensitive capture of circulating tumour cells by functionalized graphene oxide nanosheets. *Nat. Nanotechnol.* 8, 735–741. doi: 10.1038/nnano.2013.194

Yu, J., Wang, A., Tang, Z., Henry, J., Li-Ping Lee, B., Zhu, Y., et al. (2012). The effect of stromal cell-derived factor-1α/heparin coating of biodegradable vascular grafts on the recruitment of both endothelial and smooth muscle progenitor cells for accelerated regeneration. *Biomaterials* 33, 8062–8074. doi: 10.1016/j.biomaterials.2012.07.042

Zamani, M., Prabhakaran, M. P., Thian, E. S., and Ramakrishna, S. (2015). Controlled delivery of stromal derived factor-1α from poly lactic-co-glycolic acid core-shell particles to recruit mesenchymal stem cells for cardiac regeneration. *J. Colloid Interface Sci.* 451, 144–152. doi: 10.1016/j.jcis.2015.04.005

Zeng, H., Chen, W., Zheng, R., Zhang, S., Ji, J. S., Zou, X., et al. (2018). Changing cancer survival in China during 2003–15: a pooled analysis of 17 population-based cancer registries. *Lancet Glob. Health* 6, e555–e567. doi: 10.1016/S2214-109X(18)30127-X

Zhan, Y., Zhang, H., Liu, R., Wang, W., Qi, J., and Zhang, Y. (2016). Eupolyphaga sinensis Walker ethanol extract suppresses cell growth and invasion in human breast cancer cells. *Integr. Cancer Ther.* 15, 102–112. doi: 10.1177/1534735415598224

Zhang, H., and Chen, J. (2018). Current status and future directions of cancer immunotherapy. *J. Cancer* 9, 1773–1781. doi: 10.7150/jca.24577

Zhang, B., Li, H., He, L., Han, Z., Zhou, T., Zhi, W., et al. (2018). Surface-decorated hydroxyapatite scaffold with on-demand delivery of dexamethasone and stromal cell derived factor-1 for enhanced osteogenesis. *Mater. Sci. Eng. C Mater. Biol. Appl.* 89, 355–370. doi: 10.1016/j.msec.2018.04.008

Zheng, N., Chen, J., Li, T., Liu, W., Liu, J., Chen, H., et al. (2017). Abortifacient metapristone (RU486 derivative) interrupts CXCL12/CXCR4 axis for ovarian metastatic chemoprevention. *Mol. Carcinog.* 56, 1896–1908. doi: 10.1002/mc.22645

Zheng, P. P., Kros, J. M., and Li, J. (2018). Approved CAR T cell therapies: ice bucket challenges on glaring safety risks and long-term impacts. *Drug Discov. Today*. 23, 1175–1182. doi: 10.1016/j.drudis.2018.02.012

Zhu, C., Yago, T., Lou, J., Zarnitsyna, V. I., and McEver, R. P. (2008). Mechanisms for flow-enhanced cell adhesion. *Ann. Biomed. Eng.* 36, 1–18. doi: 10.1007/s10439-008-9464-5

Zhu, Y., Hoshi, R., Chen, S., Yi, J., Duan, C., Galiano, R. D., et al. (2016). Sustained release of stromal cell derived factor-1 from an antioxidant thermoresponsive hydrogel enhances dermal wound healing in diabetes. *J. Control. Release* 238, 114–122. doi: 10.1016/j.jconrel.2016.07.043

Conflict of Interest Statement: The authors declare that the research was conducted in the absence of any commercial or financial relationships that could be construed as a potential conflict of interest.

frontiers in Oncology

REVIEW
published: 02 October 2019
doi: 10.3389/fonc.2019.00966

Convection-Enhanced Delivery: Connection to and Impact of Interstitial Fluid Flow

*Caleb A. Stine and Jennifer M. Munson**

Department of Biomedical Engineering and Mechanics, Virginia Polytechnic Institute and State University, Blacksburg, VA, United States

Convection-enhanced delivery (CED) is a method used to increase transport of therapeutics in and around brain tumors. CED works through locally applying a pressure differential to drive fluid flow throughout the tumor, such that convective forces dominate over diffusive transport. This allows therapies to bypass the blood brain barrier that would otherwise be too large or solely rely on passive diffusion. However, this also drives fluid flow out through the tumor bulk into surrounding brain parenchyma, which results in increased interstitial fluid (IF) flow, or fluid flow within extracellular spaces in the tissue. IF flow has been associated with altered transport of molecules, extracellular matrix rearrangement, and triggering of cellular motility through a number of mechanisms. Thus, the results of a simple method to increase drug delivery may have unintended consequences on tissue morphology. Clinically, prediction of dispersal of agents via CED is important to catheter design, placement, and implementation to optimize contact of tumor cells with therapeutic agent. Prediction software can aid in this problem, yet we wonder if there is a better way to predict therapeutic distribution based simply on IF flow pathways as determined from pre-intervention imaging. Overall, CED based therapy has seen limited success and we posit that integration and appreciation of altered IF flow may enhance outcomes. Thus, in this manuscript we both review the current state of the art in CED and IF flow mechanistic understanding and relate these two elements to each other in a clinical context.

Keywords: CED, glioma, brain, fluid flow, drug delivery, transport, cancer

OPEN ACCESS

Edited by:
Carmen Alvarez-Lorenzo, University of Santiago de Compostela, Spain

Reviewed by:
Raghu Raghavan, Therataxis, LLC, Baltimore, MD, United States
Ennio Tasciotti, Houston Methodist Research Institute, United States

****Correspondence:***
Jennifer M. Munson
munsonj@vt.edu

Specialty section:
This article was submitted to Pharmacology of Anti-Cancer Drugs, a section of the journal Frontiers in Oncology

Received: *01 March 2019*
Accepted: *11 September 2019*
Published: *02 October 2019*

Citation:
Stine CA and Munson JM (2019) Convection-Enhanced Delivery: Connection to and Impact of Interstitial Fluid Flow. Front. Oncol. 9:966. doi: 10.3389/fonc.2019.00966

INTRODUCTION

Convection-enhanced delivery (CED) is a technique that harnesses increased flow of fluid to increase transport of large molecules and drugs throughout a tissue. In brain cancer therapy, this technique has been implemented for decades but has not been adopted widely in the clinic. The ability of this therapy to move drugs around is useful, however there are a number of factors that can inhibit or obstruct the ability of this method to work appropriately. Fluid flow in the brain (healthy or diseased) is a constant force and it can affect not only the transport of drugs and molecules throughout the tumor and surrounding tissue, but also cause changes to tumor cells and surrounding cells that could worsen or alter disease progression. Specifically, interstitial fluid (IF) flow, or the fluid flow around cells within the porous extracellular matrix, interacts with cells to enact intracellular signaling events. CED, by its nature, increases this interstitial fluid flow (IFF) but the two are rarely discussed together. Thus, we hope to describe these flows in the context of both the natural flow in the brain and the changes in IF flow that may be attributed to the technique of CED.

THE FLUID FLOW NETWORK OF THE BRAIN: A SECONDARY SYSTEM OF REGULATION

Within the brain fluid flow is a tightly-controlled, yet complicated, process that occurs along defined pathways. A major driver of these flows is pressure: intracranial pressure resulting from the brain incompressibility of fluid within the confined space of the cranium and hydrostatic pressure arising from circulatory dynamics. This pressure includes the tissue and fluid components of the brain and is normally around 11 mmHg (1). Pressure is regulated by the flux of bulk fluid into and out of the brain and thus is directly linked to the fluid flow pathways and rates within the tissue. Intracranial pressure changes result in shifting or compression of at least one of the four principle components of the cranial fluid vault: blood, cerebrospinal fluid (CSF), IF, and brain tissue (2). Discrete pressures can be measured in the vasculature running throughout the brain. Contraction of ventricles within the heart create this hydrostatic pressure which is the main driver of convective flow in fluid movement through the arteries and across capillary walls. Thus, this vascular pressure also drives IF flows due to the resultant pressure differential between arteries and parenchymal space. While pressure provides the force for fluid movement, anatomic structures provide the pathways (summarized in **Figure 1**). A fundamental understanding of these pathways and the fluids that move within them is essential to appreciate the complex effects of introducing an exogenous convective force and fluid into the brain as therapy.

The Fluids, Structures, and Forces That Drive Flow

There are three main fluids that flow within the physiological domains of the brain: CSF, blood, and IF. Various groups have measured average flow velocities of blood, CSF, and IF (3–5). Ivanov et al. measured blood flow through cerebral capillaries in mice which was found to be 0.79 ± 0.03 mm/s. Using fluorescence intensity after bleaching on a rabbit ear, Chary and Jain measured interstitial flow to be 6×10^{-5} cm/s. CSF through the cerebral aqueduct was 5.27 ± 1.77 cm/s as reported by Mase et al. However, these flow rates can differ based on the localization within the tissue (i.e., major arteries vs. capillaries) and disease states.

CSF bathes the cortex and subarachnoid spaces acting as both a homeostatic regulator, distributing ions and nutrients and removing waste in the parenchyma, and as a hydraulic protector, providing buoyancy and cushioning for the brain. While there is still controversy surrounding the topic of CSF production and circulation (6, 7), general consensus is that the majority of CSF originates at the choroid plexus that line the lateral, third, and fourth ventricles (8–10). Once secreted, the CSF flows from the lateral ventricles through the interventricular foramen to the third ventricle. It then passes through the cerebral aqueduct and into the fourth ventricle before flowing into the spinal cord and subarachnoid spaces. The arachnoid villi, or arachnoid granulations, within the subarachnoid space provide a direct path for CSF to the systemic circulation through the superior sagittal sinus (11, 12). Experimental evidence suggests that another path exists through the cribriform plate. The CSF travels around olfactory nerve sheaths and is absorbed into the lymphatics within the submucosa of the olfactory epithelium (13, 14). More recently, CSF has been observed to drain into a recently (re) discovered lymphatic network within the meninges and into deep cervical lymph nodes (15, 16).

CSF flow is dynamic, driven by multiple pulsatile drivers within the central nervous system. Choroid plexus production of CSF, and subsequent velocity, has been linked to pulsatile blood flow and the cardiac cycle by Nilsson et al. (17). Phase contrast MRI indicates the pulsatile nature of CSF as it travels throughout the brain (18) indicating driving forces of heart rate (19, 20), respiration (21, 22), and ciliary beating of ependymal cells lining the ventricles and central canal of the spinal cord (23, 24). CSF flow is complicated and closely tied to other fluid movement within the brain.

Blood flow is a major driver of other fluid movement within the brain. Cerebral arteries run throughout the subarachnoid space and penetrate the cortex through the pia mater, forming what is known as the Virchow Robin space. This space is occluded from the parenchyma as the pial sheath surrounding the artery fuses with the basement membrane of the glia (6). As the arteries taper into arterioles and the complex capillary network within the parenchyma, glial cells and pericytes envelope the area around the endothelial cell layer of the blood vessels, collectively forming the blood brain barrier (BBB). Endothelial cells are especially important, forming tight junctions. The BBB limits solute transport into the brain based on size and polarity (25). The capillaries then converge to form venules and veins, leading back to the subarachnoid space, and eventually joining up with the jugular veins. To demonstrate the impact of arterial pulsation in driving transport within the brain, Rennels et al. showed that by blocking cerebral artery pulsation, horseradish peroxidase was prevented from rapid paravascular influx (20). Similarly, Hadaczek et al. infused fluorescent liposomes into rat striatum and measured distribution volumes between rats with high and low blood pressure rates (19). In rats with high blood pressure, infusate was distributed in significantly larger volumes. Thus, blood is a major driver of not only CSF flow, but also is the primary driver of endogenous IF movement.

IF, as the primary fluid within the parenchyma of the brain, is involved in cellular homeostasis and transport of nutrients. This IF is found in the spaces between the cells and extracellular matrix and is very similar in composition to CSF (26). IF originates from the blood brain barrier as the sodium-potassium pump provides a net secretion of fluid (filtered blood serum) into the parenchyma (27, 28). It may also arise as the byproduct of CSF mixing in the parenchyma as it travels via the glymphatic system.

Experimental evidence in mice suggests that CSF passes through the Virchow Robin space and enters spaces around the cerebral arteries within the cortex. In this para-arterial space, CSF passes around the astrocytic endfeet and into the interstitial space within the brain parenchyma, mixing with and becoming IF. Iliff et al. showed that IF is involved in the glymphatic system along with the CSF by injecting a tracer into the cortex and then fixing and imaging brain sections at different time points.

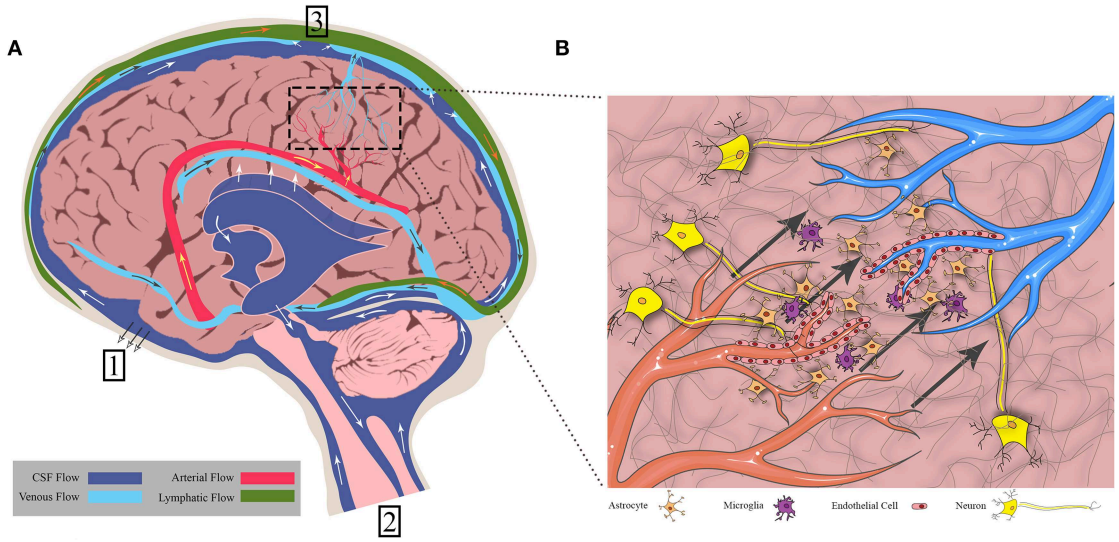

FIGURE 1 | Fluid flows throughout the brain in bulk flow pathways and in interstitial space within the cellular environment. **(A)** Bulk flow pathways include CSF through the ventricles and subarachnoid space, blood through the arteries and veins, and lymph through the meningeal lymphatics. Flow direction is shown by arrows. (1) CSF to cribriform plate (2) CSF to venous sinus through arachnoid villi (3) CSF to spinal cord. **(B)** Interstitial flow moves from cerebral arterioles to venules through the endothelial cells, crossing through extracellular matrix and cells such as neurons, astrocytes, and microglia. Figure not to scale.

They demonstrated that at <10 min after injection, the tracer was seen around arteries only, but after 1 h the tracer accumulated around venules as well. This indicates that IF and CSF drain via the same paravenous pathways after moving through the parenchyma. CSF and IF then collect in the corresponding paravenous spaces of the cerebral vein and, finally, either flow back to the subarachnoid space, enter the bloodstream, or drain to the cervical lymphatics (29). Interestingly, this system lines up nicely with the research done by Aspelund et al. (15) as the glymphatics would provide the link between upstream CSF and IF flow and downstream collection within the lymphatic vasculature (30). Recent criticisms debate the importance or independent existence of the glymphatic system (31, 32), but it would seem there is some means to linking the CSF and IF in the brain parenchyma. However, the degree to which they are independent vs. consistently mixed, is mostly semantic, as there are no independent barriers separating these two fluids (like with lymph and interstitial fluid for instance).

Though considered a convective force, there is supporting literature that IF flow is primarily a diffusional process (33–36) as the parenchyma has too high a hydraulic resistance for convection to occur. However, several groups have identified a convective component of IF (26, 27, 29). Abbott et al. (37) recently reviewed IF transport, which describes both contributors indicating that both convection and diffusion exist but may be dependent on anatomical location. White matter promotes convective flow as the fibers are aligned with lower amounts of dense matrix and cell bodies, whereas gray matter promotes diffusive flow (38). This has major implications for drug delivery as particles undergoing diffusion will be governed by size and particles undergoing convection will be governed by fluid flow velocity.

These pathways and fluids, in concert, offer a dynamic and complex network of flow within the brain. While we have yet to understand them altogether, significant work has been done to characterize and model the physiological state of these systems. This has led to a foundation from which abnormal flows can be studied, such as those arising in tumors, with the intention of more wholly understanding and developing therapeutic strategies against cancer.

Disruption of Fluid Flow in Diseased States: Focus on Glioblastoma

There has been considerable work to identify the impact that diseased states have on fluid transport and how this transport can, in turn, affect disease progression. Indeed, fluid flow in the brain is dynamic along many time scales, with velocity magnitudes that fluctuate with circadian rhythm (17, 39), decrease with age (40), and vary depending on changes in blood pressure (19). Flow has also been implicated in the progression of neurological disorders such as Alzheimer's (41). But perhaps the most drastic change to flow magnitudes is from the formation of brain tumors, which will be the focus of this review with specific emphasis on glioblastoma (GBM).

GBM has an overall survival from diagnosis of <2 years, making it the deadliest primary brain tumor. This type of primary brain cancer is known for its invasive nature and most commonly arises in the cortex of the brain, specifically the frontal and temporal lobes (42). Like fluid flow, the tumor is constrained by the fundamental architecture of the brain. Microscopically, the microenvironment that these tumors grow in is a complex assortment of cells, vasculature, and extracellular matrix (ECM) that contribute to altered molecular transport

and tumor progression (43). Glial and endothelial cells have been implicated in the progression of disease via invasion, maintenance of stem cell populations, and proliferation (44–50). The extracellular matrix is comprised of dense 3D networks composed of hydraulically resistant glycoproteins, proteoglycans, and hyaluronic acid (51) and contributes 20% of total brain volume (52). This fluid-rich, gel-like matrix has tortuous paths, with an estimated pore size between 20 and 60 nm that constrain and dictate the movement of molecules (36, 53). Conversely, fluid flow within the ECM can bend and stretch ECM molecules, altering the configuration of the microenvironment and triggering cellular mechanotransduction pathways (54, 55). A rich vasculature runs throughout the parenchyma yielding channels for fluid flow along glymphatic routes (56, 57).

In cancer, neo-vascularization causes a highly disorganized network of blood vessels. These vessels are also leaky due to increased permeability, are tortuous, and have blind ends (58). As blood and serum leak from the vasculature into the tumor and increase in volume, the IF pressure rises. In addition to increased fluid influx, the extracellular matrix undergoes massive reorganization by tumor cells and surrounding parenchymal cells (59, 60). This leads to decreased hydraulic conductivity and retention of fluids in the tumor bulk, further contributing to the increased IF pressure which can be as high as 45 mmHg inside some types of tumors (61). This pressure difference, specifically at the tumor border, drives flow from the tumor out into the surrounding parenchyma (62).

Dynamic contrast-enhanced imaging, which employs gadolinium contrast agents and time-lapse imaging, can be used to examine fluid movement into and within tumors. This technique is used clinically to examine blood vessel permeability and vascular transport in brain tumors. In an effort to observe the interstitial flow patterns in mouse models of glioma, Kingsmore et al. (63) adapted this technique by using concentration gradients of contrast to simultaneously calculate flow velocity and diffusion, yielding a map of the flow patterns within the tumor and surrounding interstitial space. Flow directionality is heterogeneous in and around the tumor, although there are converging regions that are believed to overlap with structures (like white matter tracts) within the brain. The average interstitial flow magnitude remains relatively restricted between 0 and 6 μm/s (when corrected). D'Esposito et al. (64) created a computational model to study intratumoral IF pressure of glioma in a mouse model. They removed the tumor postmortem and cleared the tumor and cortex of the mice, imaging the vasculature afterward. This was then used in a computational model which incorporated intravascular and interstitial compartments, vascular permeability, and blood and interstitial flow to yield quantitative information about perfusion, IF pressure, and IF velocity. Findings indicate a mean IF pressure within the tumor of 16 ± 10 mmHg, an IF velocity of <0.01 μm/s in the tumor center, and an interstitial velocity of 17 ± 4 μm/s at the tumor periphery (64). Similarly, interstitial flow of tumors in general has been modeled in numerous groups (65–68) and more recently in the context of chemokine convection (69). Incorporation of these natural flows into broader models of drug delivery should allow for better prediction of drug distribution, specifically in the context of manipulating fluid flow.

CONVECTION-ENHANCED DELIVERY TO DRIVE TISSUE TRANSPORT

The guiding principle behind CED is creating a positive pressure gradient to deposit treatment directly into the tumor or resection cavity and drive it through the surrounding parenchyma such that invaded cells might be accessed. This method was first described by Bobo et al. (70) in order to bypass the BBB and locally deliver chemotherapeutics or other anti-tumor agents. One such early example was the use of conjugated human transferrin to selectively target human glioma cells. Human transferrin is expressed ubiquitously in malignant tumors such as glioblastoma, but also in endothelial cells (71), creating an obstacle to intravenous delivery. CED was employed to deliver this type of drug and found to be efficacious in treating human glioma (72), eventually leading to clinical trials (73). CED uses catheters placed at specific locations to perfuse treatment directly in a, theoretically, spherical area. This method has been modeled mathematically, and at its core takes advantage of fundamental mass transport principles to increase convective over diffusive flux through the tissue.

CED is employed to solve drug delivery issues related not only to limited BBB permeability, but also to overcome high intratumoral pressures (sometimes termed the blood-tumor barrier) or limit systemic toxicity that may arise from some drugs. For example, Degen et al. conducted a study testing the dose effects of carboplatin and gemcitabine in a rat glioma model, utilizing CED or systemic delivery (74). They found that the perfusion of brain regions could be accomplished without toxicity and that the CED-treated groups had higher long-term survival. The positive pressure induced by CED drives flow through the tissue via convection-dominated transport until it reaches a certain limit governed by the infusion volume and rate. At this point, diffusion-dominated transport would govern. This means that near to the catheter, the velocity of flow is most important to the transport of the drug while farther away, the size of the drug is more important. Thus, CED is particularly beneficial to large molecule drugs, such as antibodies, nanoparticles, or conjugates (often imaging agents coupled with a drug or biomarker). Therefore, these types of therapies have been a major focus of preclinical and clinical CED application.

CED Has Shown Limited Clinical Success

Figure 2 shows a depiction of CED at the macroscopic level as it may be clinically implemented. Infusion rates range from 0.1 to 10 μL/min, and a single catheter can usually distribute drug up to a few millimeters as confirmed by imaging (75). Clinically, the therapeutic application is defined by two terms: volume of distribution (V_d), or amount of drug that is delivered, and volume of infusate (V_i), the amount of infusate (drug and carrier fluid) that is delivered. The ratio of V_d to V_i is used to

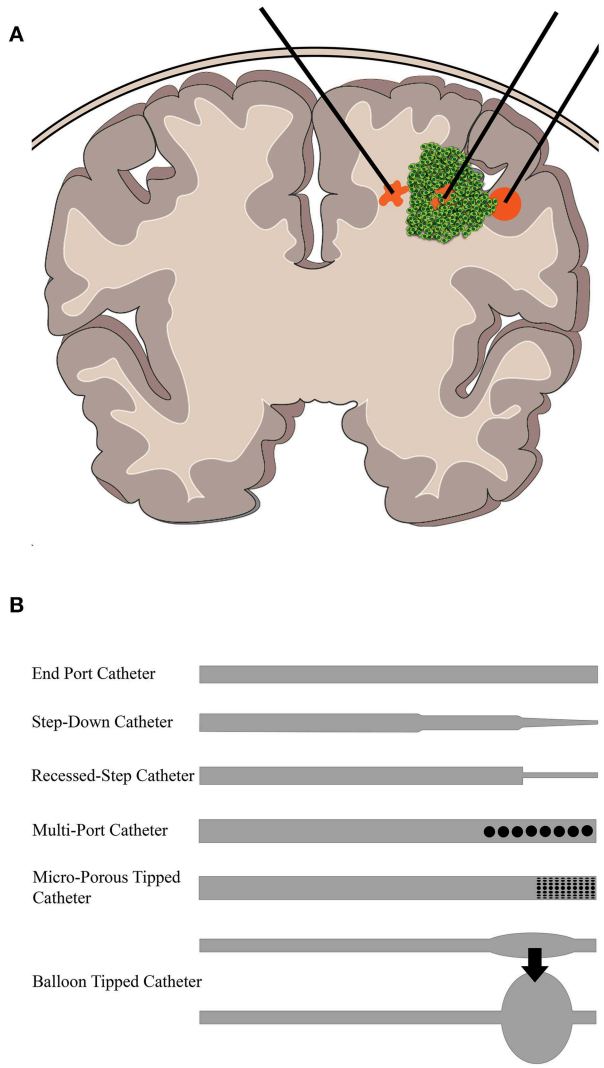

FIGURE 2 | Overview of CED into brain tumors. **(A)** CED is performed through catheters placed either intratumorally or intraparenchymally. The infusate profile will change depending on region of delivery (shown in orange). **(B)** Some example catheter designs that have been used to deliver CED.

describe how well CED delivers a specific drug, dependent on the drug and tissue being perfused. A higher ratio is desirable as this would indicate greater distribution of drug, all else being equal. An example is the ratio of gray matter, spinal cord, and peripheral nerves which range from 4:1 to 7:1 compared to the ratio of compacted white matter which ranges from 6:1 to 10:1 (76). This means that drug distribution is greater in the white matter than the gray matter, consistent with the increased permeability of that tissue, and thus conducts fluid flow at a different rate.

Catheter design, catheter placement, tumor location, tumor size, infusion rate, infusion frequency, drug type and concentration, and brain anatomy can all contribute to differential CED responses. When working with these parameters, it is often a balance between increasing the drug distribution profile within and around the tumor and limitations on the physical implementation of CED. For instance, increasing flow rates will undoubtedly increase the distribution of drug within and around the tumor while also reducing total infusion time for the patient. However, backflow, or the tendency of the infusate to travel back up between the catheter and the tissue, is directly impacted by the infusion rate (77). Thus, oftentimes, multiple catheters have been used to better distribute and increase infusion overall at lower rates, but this can be limited by surgical access and anatomy. As such, design of catheters has been a major area of research in CED. For instance, the development of a stepped catheter design which allows CED flow rates as high as 5 μL/min in mice (78) increases flow while limiting backflow. Other new catheter designs include hollow-fiber, multi-port, ultrafine, and balloon-tipped. Lewis et al. recently reviewed the history and evolution of catheter design for CED (79). Catheter placement and infusion rate varies among the clinical trials. This is due, in part, to the more personalized approach to catheter placement necessitated by the limitations presented by an individual tumor anatomy within the brain. Further, not only are catheters placed within tumors or resection cavities, but also within the surrounding parenchyma. This variability makes it difficult to compare parameters across clinical trials using CED. To aid in some of the ambiguity of the treatment, clinical imaging is often used in conjunction with CED. Intraoperative MRI is the primary modality. By incorporating a contrast agent into the infusate or as a drug conjugate, drug distribution can be monitored and analyzed in real-time and post-treatment (80, 81).

As mentioned, infusion rates are arguably one of the most important components to CED. We will discuss later how the infusion rate is responsible for mathematically driving drug distribution. Interestingly, while this is such an important factor, it is highly variable in clinical trials to date, ranging from 0.5 μL/min to (73, 82–102) 66 μL/min (**Table 1**). Further, the infusion time changes substantially between independent trials. Some trials infuse for days while others only for a few hours. Some infusions are continuous while others cycle. Lastly, the total volume infused varies from 2 to 108 mL which is unsurprising given the variance in flow rates and time intervals. This lack of standardization might be one of the reasons that CED has been unable to acquire clinical success, and part of the lack of standardization is that we still do not have a holistic understanding of how CED is affected by and exerts effects on the brain and tumor tissues.

Catheter placement is one of the most important steps in planning a CED intervention. Mathematical modeling and software have aided in this planning. One major factor in catheter placement is anatomical location of the tumor or location to be infused. Certain structures such as white matter tracts, ventricles, and ependymal surfaces have been known to cause failure of CED because of the impact they have on drug distribution (104, 105). The anisotropy of white matter tracts causes drug to preferentially flow through this bulk fluid pathway away from areas of therapeutic interest. Ventricles and ependymal surfaces can also act as sinks for the infusate, diminishing the Vd/Vi ratio.

TABLE 1 | Completed clinical trials of CED for human gliomas.

Source	Drug (concentration)	Flow rate	Complications	Success/failure rate	Catheter placement
Laske	Tf-CRM107 (0.1–>1 ug/ml)	0.5 uL/min increasing over 4 h to max of 4–10 ul/min for a total of 5 mL Infusion volumes increased up to 180 mL Infusions every 4–6 weeks until change seen	Reactive changes and edema (1 patient)	9/15 patients >= 50% decrease in tumor volume	1 to 3 catheters at selected sites in the tumor
Laske	Tf-CRM107 (0.67 ug/ml)	Up to 0.20 mL/h per catheter for 4–5 days until 40 mL delivered Second treatment 10 weeks after initial infusion	8/44 cerebral edema 3/44 seizure	Median survivial time 37 wks and mean survival time 45 weeks	2 catheters at selected sites in the tumor
Wersall	mAb 425	4 ml/h for 1 h	6/18 headache	Total median survival from diagnosis 39 week and from the start of mAb 18.5 week Expected median survival 24 week from start of therapy	3 to 4 catheters in the tumor-bed tissue
Rand	IL-4 pseudomonas exotoxin (0.2 μg/ml up to 6 μg/ml)	0.3–0.6 mL/h over a 4–8 day period (total infusion volume 30–185 mL)	2/9 hydrocephalus 3/9 cerebral edema	6/9 showed decreased enhancement after infusions but only one survived—the other tumors recurred	1 to 3 catheters at selected sites in the tumor based on shortest possible route. When three were used, middle inserted into center of tumor and other two placed on opposing side adjacent to largest volume of white matter
Voges	HSV-1-tk	0.025, 0.05, 0.1, 0.2, 0.4 mL/h, each at 2 h infusion time followed by 0.6 mL/h until final volume reached (30 or 60 mL)	–	Median survival time after infusion 28.1 weeks and median time to progression 8 weeks	Intracerebral
Weber	IL-4 pseudomonas exotoxin (6 μg/ml for 40 ml, 9 μg/ml for 40 ml, 15 μg/ml for 40 ml, or 9 μg/ml for 100 ml)	6.94 μL/min for 40 mL groups and 17.36 μl/min for 100 mL group. Delivered over 96 h.	26/31 seizures 10/31 (32%) cerebral edema (of those 10, 5 (50%) were serious)	Overall median survival 8.2 months with median survival of 5.8 months for GBM (highest 6-month survival for 6 μg/ml × 40 ml and 15 μg/ml × 40 ml)	1 to 3 catheters placed intratumorally
Lidar	Paclitaxel (3 patients 7.2 mg/6 mL, all others 3.6 mg/6.6 mL)	0.3 mL/h or 5 days in 24 h periods 20 cycles	2/15 edema 1/15 hydrocephalus	Median survival of 7.5 months	1 catheter placed intratumorally
Patel	Cotara (0.5–3 mCi/cm^3)	0.18 mL/h through each catheter over 1 or 2 days (total volume 4.5–18 mL). After infusion, 0.5 mL diluent flush infused at 0.18 ml/h. 39 received first infusion, 16 received a second infusion	10/51 brain edema (20%)	–	1 to 2 catheters near or at center of enhancing tumor
Kunwar (103)	IL-13-PE38QQR (0.25–2 μg/mL for intratumoral and 0.25–1 μg/mL for intraparenchymal)	Intratumoral—0.4 or 0.54 mL/h for 48–96 h total Intraparenchymal—0.75 mL/h for 96 h to 6 days total	27 headache (53%)—catheter placmt 6 aphasia (12%)—catheter placmt 21 headache (41%)—CED of drug 10 aphasia (20%)—CED of drug	–	1–2 for intratumoral and 1–3 catheters for intraparenchymal. One cohort with intratumoral placement followed by resection and then intraparenchymal administration. One cohort with intraparenchymal placement after tumor resection

(Continued)

TABLE 1 | Continued

Source	Drug (concentration)	Flow rate	Complications	Success/failure rate	Catheter placement
Vogelbaum (91)	IL-13-PE38QQR (0.25 or 0.5 μg/ml)	0.750 mL/h divided by # of catheters for 96 h	5 deep vein thrombosis (23%) 3 peripheral edema (14%) 3 aphasia (14%) 3 convulsion (14%)	–	2 to 4 catheters placed intraparenchymally
Sampson	TP-38 (25, 50, or 100 ng/mL)	0.4 mL/h for 50 h in each catheter (40 mL total)	Reflux and ineffective delivery in majority of patients (7/16 leak into subarachnoid space, 2/16 lead into ventricle, 4/16 pooling in necrotic area resection cavity, 3/16 successful infusion)	Overall median survival after therapy 28 weeks (20.1 for patients with residual disease and 33 for patients without residual disease)	2 catheters placed to target residual tumor or deep white matter adjacent to areas of previously resected tumor
Carpentier	CpG-ODN	0.333 mL/h for 6 h (2 mL infused total)	Seizure (5/31)	Median progression free survival 9.1 weeks and median overall survival 28 weeks	2 catheters placed intracerebrally
Kunwar (88)	IL-13-PE38QQR (0.5 μg/ml) vs. Gliadel wafers	0.75 mL/h over 96 h	10/183 brain edema 39/183 aphasia	Median survival 36.4 weeks compared to 35.4 weeks for gliadel wafers (for GBM confirmed group)	2–4 catheters placed intraparenchymally
Bruce	Topotecan (0.02, 0.04, 0.0667, 0.1, or 0.133 mg/mL)	200 μl/h in each catheter for 100 h (40 mL total)	5/18 headache 5/18 seizure	Median progression free survival 23 weeks and median overall survival 60 weeks	2 catheters placed into enhancing tumor or adjacent brain
Desjardins	Polio-rhinovirus chimera	500 μl/h over 6.5 h (3.25 mL total)	–	Median overall survival 12.5 mths compared to 11.3 mths historical and 6.6 mths NOVO-TTF-100 A treatment group	1 catheter placed intratumorally
Vogelbaum (96)	Topotecan (0.067 mg/mL)	0.396 mL/h over 96 h total (38 mL total)	–	–	2 catheters each with 4 microcatheters; 1 placed intratumorally and 1 placed intraparenchymally

Last, the drug that is delivered is extremely important to outcomes with CED and planning of infusions. Normally, when trying to deliver a drug through the vasculature and BBB, an advantage is to have it be as small as possible and potentially lipophilic so that it can pass through more easily and have a greater presence at the tumor site. CED bypasses the BBB completely, so this problem is now reversed; the drug is already where it needs to be, the issue is having it stay there. One study that examined this effect used topotecan and compared intracerebral delivery to intraperitoneal delivery using a rat glioma model (106). The authors found that the topotecan delivered systemically was able to cross the BBB, but there was a higher concentration of the topotecan in the brain and around the tumor when delivered via CED. They also observed a significant decrease in the tumor size of the CED group compared to the systemic delivery group. Because of this, drugs should have higher molecular weights and be hydrophilic if possible. Raghavan et al. (107) provide an interesting perspective into many of these clinical obstacles as well as relevant clinical scenarios in which CED could be improved upon. Some recent clinical studies with CED are highlighted in **Table 1** with discussion of some of these parameters.

CED Increases Drug Distribution in Interstitial Spaces

CED is governed by classical mass transport equations accounting for diffusive and convective flux. The changes in fluid velocity driven by CED and its impact on drug transport are best understood from this mathematical point of view. The main focus of CED is on the drug concentration profile that can be developed. This is based on the mass transport equation, which describes the change in concentration of a species over time. The general equation is dependent on diffusion and convection characteristics and is given by:

$$\frac{\partial c}{\partial t} = D\nabla^2 c - v \cdot \nabla c + R \tag{1}$$

Where the change in concentration over time ($\frac{\partial c}{\partial t}$) is solved from the diffusive component ($D\nabla^2 c$), convective component ($v \cdot \nabla c$), and rate of any reactions taking place. In other words, transport of a species (the infusate) depends on whether it is passively diffusing, being driven by a pressure differential (bulk flow), or being replenished or depleted by chemical reactions. In the tumor microenvironment, the pressure differential between the tumor and normal tissue creates a convective force throughout the interstitial space. Depending on the species being transported by this flow, there will also be diffusion taking place (as the concentration gradient spreads out) as well as reactions between the species and surrounding cells. With regards to CED, the concentration profile is often modeled as a sphere radiating outward from the catheter tip. In this context, the mass transport equation can be written with spherical coordinates:

$$\frac{\partial c}{\partial t} = D\left(\frac{1}{r^2}\frac{\partial}{\partial r}\left(r^2\frac{\partial c}{\partial r}\right) + \frac{1}{r^2 sin\theta}\frac{\partial}{\partial \theta}\left(sin\theta\frac{\partial c}{\partial \theta}\right) + \frac{1}{r^2\sin^2\theta}\frac{\partial^2 c}{\partial \varphi^2}\right) - v_r\frac{\partial c}{\partial r} - \frac{v_\theta}{r}\frac{\partial c}{\partial \theta} - \frac{v_\varphi}{rsin\theta}\frac{\partial c}{\partial \varphi} + R \tag{2}$$

Where r denotes the radius of the sphere from the catheter tip, θ an angle around the tip from the z axis, and φ an angle orthogonal to θ. Together, these describe the change in concentration of infusate over time in a spherical volume.

In order to solve for the convective component of the mass transport equation, the velocity of the infusate must be known. This can be solved from the generalized Navier-Stokes equation, which defines fluid flow rate based on the properties of that fluid and the surrounding space.

$$\rho\frac{dv}{dt} + \rho v \cdot \nabla v = -\nabla P + \mu\nabla^2 v + \rho g \tag{3}$$

In this equation, the first term describes the change in velocity of the fluid over time, the second term is the convective component of the velocity, ∇P defines the pressure gradient, $\mu\nabla^2 v$ is the viscous or diffusive component and ρg is the effect gravity has on the velocity. Together, these terms can be used to solve for the velocity profile of a fluid. Again, because CED theoretically supplies a spherical distribution of infusate at the location of the catheter tip spherical coordinates can be used, similar to Equation 2.

In regards to the fluid flow within the tumor microenvironment, Navier-Stokes can be simplified with the assumption of incompressible, creeping flow and being a Newtonian fluid to the Stokes equation. This can then be transitioned to Darcy's law by assuming viscous forces are linear with velocity. Darcy's law describes fluid moving through a porous medium, such as flow through the interstitial space of the brain parenchyma. This is especially useful in the context of glioblastoma as the pressure differential from the tumor causes flow through the interstitial space. Darcy's law is given by:

$$q = -\frac{k}{u}\left(\frac{\Delta p}{\Delta x}\right) \tag{4}$$

With this equation, the average velocity of the IF can be calculated based on the pressure differential (Δp), permeability of the parenchyma (k), viscosity of the fluid (μ), and a characteristic length of tissue through which the fluid is flowing (Δx). It is important to note that this gives a superficial velocity, not a discrete profile of the flow rate. This velocity can then be paired with the mass transport equation to solve for concentration of a drug over time. It is important to note, however, that this concentration profile cannot be solved without considering the convective component which is directly tied to the interstitial flow rate that the procedure is causing as well as the impact that the surrounding tissue is causing.

One last term to consider is the Péclet number:

$$Pe = \frac{L*v}{D} \tag{5}$$

Where L is the characteristic length, v is the flow velocity, and D is the mass diffusion coefficient. This term is a ratio of the convective component to the diffusive component for a given system. For a Péclet number less than one, diffusion dominates whereas a number greater than one means convection will dominate. This is important especially in the context of CED, where the main goal is to increase the convective component, by increasing the v in Equation 5, in order to obtain a larger distribution volume to the tissue. Under normal circumstances, the Péclet number in the interstitial space will be close to one, meaning that diffusion and convection components are about equal.

In the context of CED, the positive pressure induced inside the tumor from the catheter(s) would increase the pressure term in Darcy's Law, causing the velocity of the infusate through the interstitial space to increase. This velocity would also depend on the permeability of the parenchyma and tumor tissue, as the flow would have to travel through these media, and on the viscosity of the infusate. If the permeability of the tissue is higher there will be less resistance to flow, resulting in a higher flow rate as shown by Equation 4. A lower viscosity would similarly cause an increase in flow velocity, as a less viscous fluid is less resistant to deformation through shear stress. Once flow rate is determined, it can be used in the mass transport equation (v in Equation 1) to describe the convective component of drug delivery and in the Péclet number to describe how convection and diffusion are contributing. The transport of this mass is also affected by the diffusion coefficient of the drug and the reactions between the infusate and surrounding cellular environment. Together, these equations describe the drug concentration inside and around the tumor.

Advanced Mathematical Modeling

The equations laid out in the preceding section comprise the fundamental mathematical principles that govern CED, but they have been used well before this to study fluid flow and transport in brain and other tissues (108–110). Since Bobo et al. first proposed CED, there have been numerous mathematical models trying to predict drug transport, as there are obvious clinical benefits of doing so. Early models such as that by Morrison et al. (111, 112) took into account catheter diameter, volumetric inflow rate, hydraulic flow through tissue, and deformation of the tissue and were used to model backflow. Subsequent models have built off and adapted these precursors such as Raghavan et al. (113), which reformulated and extended the model by Morrison et al. more accurately predicting backflow surrounding a cylindrical catheter based on changes in volumetric flow rate. However, more complex analytical models have been and are being created that incorporate factors such as tissue edema, fluid pathways, tissue and tumor heterogeneity, and other structural and biophysical mediators to more accurately simulate *in vivo* conditions (114–120). These models have recognized and accounted for the role that interstitial flow and structural pathways play in the CED paradigm. When examining these mathematical models, consideration of whether they are modeling CED intraparenchymally or intratumorally is important to their application. Clinically, CED can be applied into tumors alone, into tumor+parenchyma, or into resected tumor cavities or surrounding parenchyma alone. Each of these tissues presents its own set of physical parameters and challenges to planning and treatment implementation. Most of the referenced models look at perfusion into the brain tissue and not the tumor itself, which has major limitations on the results owing to the differences in mechanical and biophysical properties.

Clinically, some mathematical models have been successful. Sampson et al. (121) tested an algorithm to predict patient-specific drug distributions in a retrospective study of a CED clinical trial. The algorithm aids in placing catheters such that drugs will be delivered successfully to specific anatomical regions of the brain. The software works by first delineating fluid-filled volumes and surfaces using a T2-weighted MRI to describe the anatomy of the brain. Manual segmentation of edematous brain regions is then performed so as to not confound the algorithm. Using infusate volume and catheter dimensions, length of backflow (flow back up the outside of the catheter) is calculated and then cross-referenced to any segmented surface or cavity that is within this length. If detected, the software gives a warning of potential poor catheter placement and the catheter can be repositioned. Once verified that backflow will not occur, the fluid distribution is calculated based on the mass transport equation (Equation 1) and Darcy's law (Equation 4). The result is a patient-specific 3D profile of the drug concentration. Rosenbluth et al. (122) later refined this approach by integrating diffusion tensor imaging to include more anatomical information. Rosenbluth et al. also developed an autosegmentation tool for use with CED (123).

The use of such software offers the ability to simulate drug distribution prior to application and has helped to enhance the reproducibility of drug delivery. However, these therapeutic approaches are still not offering the expected curative outcomes for many diseases, particularly in glioblastoma. One reason for this may be the focus on distribution volume of the drug (in terms of reducing backflow and creating more targeted zones of delivery) instead of the direct impact CED has on the flow pathways within the brain. Further, there currently exists no model of CED that incorporates the naturally-occurring fluid flow within the tissue which will have a major impact on the resultant flows from an imposed pressure gradient.

CED DIRECTLY CONTRIBUTES TO INCREASED IFF

The main focus of CED to date has been on delivering efficacious concentrations of drug in and around the tumor or resection site, but the downstream impact of this extrinsic force has not been considered. CED not only is an effort to bypass the BBB, but also to overcome the heightened intratumoral interstitial pressures. It is this same heightened pressure that drives IF flow at the tumor border into the surrounding parenchyma (61). The interstitial pressure in normal brain tissue is 0.8

mmHg, whereas it is 7 mmHg when a tumor is present (124). This increased interstitial pressure can lead to issues with CED. As mentioned, it can cause increased efflux of the CED-administered treatment back up the catheter track, reducing total delivered dose and hence, decreased clinical efficacy (80). Because CED introduces an additional hydrostatic pressure compared to a relatively normal pressure in adjacent tissue, IF flow will be induced or increased although we still don't know the downstream consequences as illustrated in **Figure 3**.

Like interstitial pressure, IFF rates are higher in tumor-bearing tissues as at border regions; though it can be nearly static in some regions of the tumor (63). Heightened interstitial or bulk flows can also affect CED success. In regions with low resistance to flow or along bulk fluid paths, drugs may move very quickly through the tissue reducing residence time around invaded tumor cells that are being targeted. The complex heterogeneity of tumors coupled with the anisotropy of the brain makes this balance complicated in application of flow.

CED is most often performed post-surgical resection, however, in some cases and oftentimes in canine glioma, CED is performed with the tumor in place. The inherent biophysical differences in these tissues makes exact modeling difficult, especially IF flow due to its dependence on the matrix permeability and fluid viscosity, both affected by therapeutic intervention. For instance, radiation therapy has been shown to degrade extracellular matrix in other tissues which will increase permeability of the extracellular matrix (125). As CED is most often performed on patients who have already received numerous rounds of standard of care and potentially experimental treatments, it can be difficult to generalize parameters based on healthy or even initially diagnosed patients. Strategies to use clinical imaging to identify these other properties can aid in these efforts for patient-specificity and potentially improve outcomes by identifying these parameters. Importantly, we can link the known CED derived transport to IF flow to better understand and model the effects of these changes in patients.

IF Flow Can Drive Tumor Invasion

The effects of IF flow on cancers in general was recently reviewed by Munson and Shieh (126). In glioma, two groups have shown that this IF flow causes glioma cells to invade (126–128). The flow is thought to mediate mechanisms whereby the tumor cells actively invade the healthy tissue and may contribute to the diffusive nature of these tumors which makes them particularly difficult to cure.

Two proposed mechanisms by which flow could be mediating tumor invasion in the brain include autologous chemotaxis and cellular mechanotransduction (127). Autologous chemotaxis is the process by which a cell migrates in the direction of autologous chemokine gradients formed by IF flow carrying secreted protein upstream of the cell body (129). In glioma, the receptor, CXCR4, and its ligand, CXCL12, have been

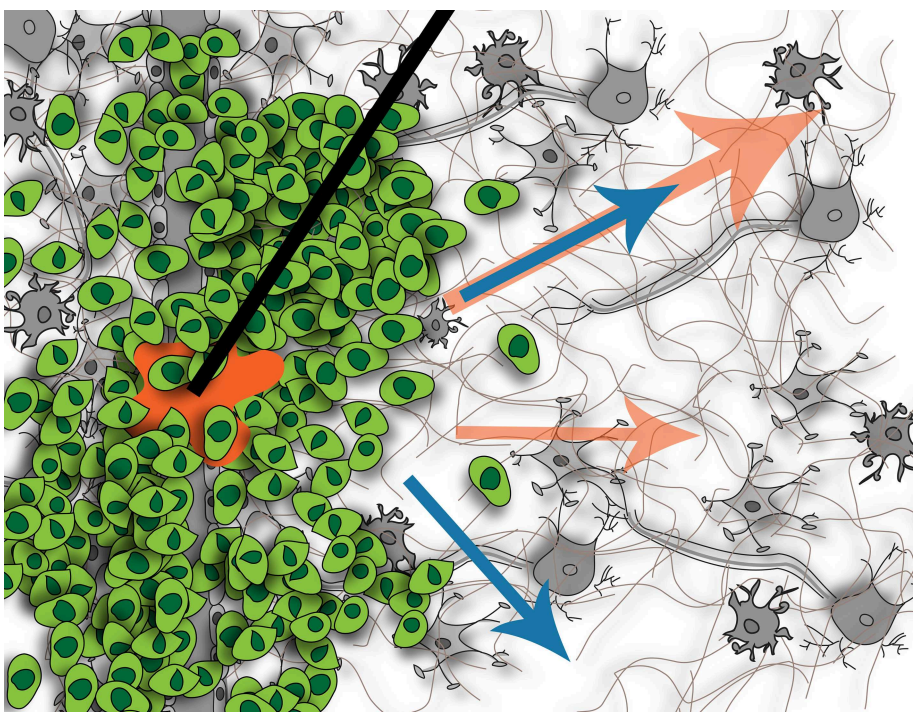

FIGURE 3 | Illustration of fluid flow resulting from tumor (blue arrows) and potential effects on flow when introducing CED (orange arrows). Without CED, the tumor causes interstitial flow from its border into the surrounding parenchyma, affecting cells located there. With CED, this interstitial flow will be increased but it is not known if this will create new pathways of flow or just increase existing ones, or what the downstream impact of this increased flow will be on the resident cells. Figure not to scale.

implicated in this mechanism in rat and patient glioma cells (127, 130). Mechanotransduction is the process by which cells sense and react to mechanical changes in their environment via extracellular matrix binding proteins. These cues can be induced by forces such as shear stress, compressive stress, or tensile stress (54). IF flow results in localized shear stress at the cell surface which directly signals to cytoskeletal binding proteins leading to glioma cell migration (128). One of the major receptors implicated in this mechanism is CD44 (127, 131), but other matrix-binding proteins may also be involved in mechanotransduction in the glioma microenvironment. Both CXCR4 and CD44 are highly upregulated in glioma, which further enhances the importance of studying flow in conjunction with these cancers. Paths of invasion within the brain occur in perivascular spaces around blood vessels (132), along white matter tracts (38), in perineuronal spaces, and along the meningeal layers lining the brain. Coincidentally these are regions with increased preferential bulk flow as shown by Geer and Grossman in their seminal work using convection-infused dye as a surrogate for heightened tumor pressure and tumor cells. Though these regions are subject to bulk flow as opposed to interstitial flow, much of the IF flow that is moving within the brain extracellular space eventually drains toward and along these major conduits, thus linking IF flow, bulk flow, and invasive pathways.

Recently, Cornelison et al. showed that CED therapy (at 1 μL/min) in a GL261 mouse model increased invasion of glioma cells, mediated by CXCR4. By blocking CXCR4 with AMD3100 this invasive response was effectively eliminated, suggesting that CED therapy could be more efficacious by considering the impact of fluid flow. This was the first direct proof *in vivo* that CED could lead to increased invasion. Interstitial flow in other tissues can also alter the surrounding tissues (55, 133). Interestingly, in the brains bearing GL261 tumors, not only was CXCR4 phosphorylation increased in the tumor cells with CED, but there was also observably more p-CXCR4 in the surrounding parenchymal tissue, implicating neuroglial cells have a role in possibly other flow-related signaling. These findings could have major implications on the outcome of the CED procedures, and potentially offer some partial explanation into why CED has not been shown to statistically significantly increase patient survival in clinical trials.

CHALLENGES AND OPPORTUNITIES OF CED: FOCUS ON IFF

We contend that a vital component to successful CED treatment is recognizing inherent fluid flow and pathways within the brain and their impact. Though these therapies have been implemented for decades, very few studies exist that probe the inherent contributions of the brain to CED outcomes (as opposed to CED on brain outcomes, or more often, tumor outcomes). We propose that not only are these conduits acting as passive sinks, but that the bulk fluid flow that moves along white matter tracts and within ventricles are active conduits for bulk movement of drug. Not only are these more obvious locations privy to this type of flow, but also the perineuronal or perivascular or glymphatic pathways as well. These more microscopic bulk flows offer pathways of fluid movement that can just as easily transport drug away from the tumor and quickly out of the brain. Increases in IF flow may be a good thing in this regard as keeping therapies within the interstitial spaces of the brain where they move more slowly through the complex extracellular space may offer opportunities to access more invasive cells or exert effects longer. Regardless, coupling and appreciating that there are multiple flows occurring along multiple length scales within the tissue is integral to success of a therapy that aims to alter flow. In our imaging studies, we found that though IF flow velocities were fairly consistent between animals, the intratumoral heterogeneity was high, especially in terms of direction of flow (63). Perhaps imaging flow within tissues may offer insight into CED based therapy distribution and outcomes that are not clearly apparent by simply observing the anatomy of tumor and surrounding brain.

These inherent flow pathways within the brain and natural or abnormal flows that develop due to a tumor are important when determining the appropriate design elements that are implemented. For instance, the design of catheters could account for these flow pathways by understanding the natural forces that they may be feeling beyond flow and could be designed to take advantage (coupled with placement) of inherent flows to minimize issues with backflow. Drug design and development could also take advantage of IF flow by carefully sizing particles based on the known properties of the tissue and the effect of the specific rate of IF flow within those tissues. Use of *in vitro* models of IFF in the brain (127) coupled with potential CED-based therapies could offer insight before implementation in the brain. Further, a major advance would be to continue to develop imaging modalities that can yield the parameters needed to best model fluid flow and drug distribution within individual tumors, allowing the complex computational models to better predict therapeutic delivery.

An appreciation of IF flow is also important due to its biological impact. As we mentioned, it has been shown that only a 10-fold increase in interstitial flow compared to normal physiological flow can trigger glioma cell invasion *in vitro* and *in vivo*. This response is troubling in the context of CED as the introduction of higher flows may lead to more invasion, or trigger specific invasion in already invaded tumor cells. The impact of magnitude is not yet known as IFF responses have only been studied as an on-off mechanism. A strong understanding of how tumor cells respond to heightened flows over a range is important to an understanding of the implications of CED and perhaps implementation of therapies (such as CXCR4 inhibitors or CD44 inhibitors) that can attenuate these responses. Additionally, the effect on surrounding tissues is totally unstudied, but important for a strong comprehension of how drugs may be interacting within the extracellular spaces both with other cells and with the matrix. These changes could limit drug distribution through cellular uptake and matrix binding.

In theory, CED should be a very effective treatment, if not curative. It removes many of the mysteries facing systemic delivery: known drug concentration in the tumor, defined delivery profiles, increased distribution to access invasive cells, and *in situ* and personalized treatment of patient tumors. However, in clinical trials—there has been no statistically significant difference between CED and the standard treatment modalities. This is perplexing, and we propose that there is still something we are not accounting for. Though IFF is likely not the complete picture, a better knowledge and appreciation for the inherent flows within these tissues seems one logical step to better understanding outcomes of a flow-based therapy.

AUTHOR CONTRIBUTIONS

JM and CS both planned, wrote, and edited the manuscript.

FUNDING

This work was supported by NIH R37CA222563 to JM.

REFERENCES

1. Albeck MJ, Børgesen SE, Gjerris F, Schmidt JF, Sørensen PS. Intracranial pressure and cerebrospinal fluid outflow conductance in healthy subjects. *J Neurosurg.* (1991) 74:597–600. doi: 10.3171/jns.1991.74.4.0597
2. Brock M, Furuse M, Weber R, Hasuo M, Dietz H. Brain tissue pressure gradients. In: Lundberg N, Pontén U, and Brock M, editors. *Intracranial Pressure II*. Berlin, Heidelberg: Springer Berlin Heidelberg (1975). p. 215–20. doi: 10.1007/978-3-642-66086-3_45
3. Chary SR, Jain R. Direct measurement of interstitial convection and diffusion of albumin in normal and neoplastic tissues by fluorescence photobleaching. *Proc Natl Acad Sci USA.* (1989) 86:5385–9. doi: 10.1073/pnas.86.14.5385
4. Ivanov KP, Kalinina MK, Levkovich YI. Blood flow velocity in capillaries of brain and muscles and its physiological significance. *Microvasc Res.* (1981) 22:143–55. doi: 10.1016/0026-2862(81)90084-4
5. Mase M, Yamada K, Banno T, Miyachi T, Ohara S, Matsumoto T. Quantitative analysis of csf flow dynamics using MRI in normal pressure hydrocephalus. *Intracr Pressure Neuromonit Brain Injury.* (1998) 71:350–3. doi: 10.1007/978-3-7091-6475-4_101
6. Brinker T, Stopa E, Morrison J, Klinge P. A new look at cerebrospinal fluid movement. *Fluids Barriers CNS.* (2014) 11:1–16. doi: 10.1186/2045-8118-11-10
7. Orešković D, Radoš M, Klarica M. Role of choroid plexus in cerebrospinal fluid hydrodynamics. *Neuroscience.* (2017) 354:69–87. doi: 10.1016/j.neuroscience.2017.04.025
8. Dandy WE. Internal hydrocephalus. An Experimental, Clinical and Pathological Study. *Also Am. J. Dis. Child.* (1914) 6:406–82. doi: 10.1001/archpedi.1914.02180010416002
9. Spector R, Keep RF, Robert Snodgrass S, Smith QR, Johanson CE. A balanced view of choroid plexus structure and function: Focus on adult humans. *Exp. Neurol.* (2015) 267:78–8(1913) 6. doi: 10.1016/j.expneurol.2015.02.032
10. Weed LH. Studies on cerebro-spinal fluid. No IV : the dual source of cerebro-spinal fluid. *J Med Res.* (1914) 31:93–118.
11. Kido DK, Gomez DG, Pavese AM, Potts DG. Human spinal arachnoid villi and granulations. *Neuroradiology.* (1976) 11:221–8. doi: 10.1007/BF00328377
12. Weller RO, Kida S, Zhang E-T. Pathways of fluid drainage from the brain - morphological aspects and immunological significance in rat and man. *Brain Pathol.* (1992) 2:277–84. doi: 10.1111/j.1750-3639.1992.tb00704.x
13. Kida S, Pantazis A, Weller RO. CSF drains directly from the subarachnoid space into nasal lymphatics in the rat. Anatomy, histology and immunological significance. *Neuropathol Appl Neurobiol.* (1993) 19:480–8. doi: 10.1111/j.1365-2990.1993.tb00476.x
14. Weller RO, Djuanda E, Yow HY, Carare RO. Lymphatic drainage of the brain and the pathophysiology of neurological disease. *Acta Neuropathol.* (2009) 117:1–14. doi: 10.1007/s00401-008-0457-0
15. Aspelund A, Wiig H, Antila S, Karaman S, Detmar M, Proulx ST, et al. A dural lymphatic vascular system that drains brain interstitial fluid and macromolecules. *J Exp Med.* (2015) 212:991–9. doi: 10.1084/jem.20142290
16. Louveau A, Smirnov I, Keyes TJ, Eccles JD, Rouhani SJ, Peske JD, et al. Structural and functional features of central nervous system lymphatic vessels. *Nature.* (2015) 523:337–41. doi: 10.1038/nature14432
17. Nilsson C, Stahlberg F, Thomsen C, Henriksen O, Herning M, Owman C. Circadian variation in human cerebrospinal fluid production measured by magnetic resonance imaging. *Am J Physiol Integr Comp Physiol.* (2017) 262:R20–4. doi: 10.1152/ajpregu.1992.262.1.R20
18. Battal B, Kocaoglu M, Bulakbasi N, Husmen G, Tuba Sanal H, Tayfun C. Cerebrospinal fluid flow imaging by using phase-contrast MR technique. *Br J Radiol.* (2011) 84:758–65. doi: 10.1259/bjr/66206791
19. Hadaczek P, Yamashita Y, Mirek H, Tamas L, Bohn MC, Noble C, et al. The "Perivascular pump" Driven by arterial pulsation is a powerful mechanism for the distribution of therapeutic molecules within the brain. *Mol Ther.* (2006) 14:69–78. doi: 10.1016/j.ymthe.2006.02.018
20. Rennels ML, Gregory TF, Blaumanis OR, Fujimoto K, Grady PA. Evidence for a "Paravascular" fluid circulation in the mammalian central nervous system, provided by the rapid distribution of tracer protein throughout the brain from the subarachnoid space. *Brain Res.* (1985) 326:47–63. doi: 10.1016/0006-8993(85)91383-6
21. Brinker T, Lüdemann W, Von Berens Rautenfeld D, Samii M. Dynamic properties of lymphatic pathways for the absorption of cerebrospinal fluid. *Acta Neuropathol.* (1997) 94:493–8. doi: 10.1007/s004010050738
22. Dreha-Kulaczewski S, Joseph AA, Merboldt K-D, Ludwig H-C, Gartner J, Frahm J. Inspiration is the major regulator of human CSF flow. *J Neurosci.* (2015) 35:2485–91. doi: 10.1523/JNEUROSCI.3246-14.2015
23. Faubel R, Westendorf C, Bodenschatz E, Eichele G. Cilia-based flow network in the brain ventricles. *Science.* (2016) 353:176–8. doi: 10.1126/science.aae0450
24. Mirzadeh Z, Han Y-G, Soriano-Navarro M, Garcia-Verdugo JM, Alvarez-Buylla A. Cilia organize ependymal planar polarity. *J Neurosci.* (2010) 30:2600–10. doi: 10.1523/JNEUROSCI.3744-09.2010
25. Banks WA. From blood-brain barrier to blood-brain interface: new opportunities for CNS drug delivery. *Nat Rev Drug Discov.* (2016) 15:275–92. doi: 10.1038/nrd.2015.21
26. Cserr HF, Patlak CS. Secretion and Bulk Flow of Interstitial Fluid. *Physiol Pharmacol Blood-Brain Barrier.* (1992) 245–61. doi: 10.1007/978-3-642-76894-1_9
27. Abbott NJ. Evidence for bulk flow of brain interstitial fluid: significance for physiology and pathology. *Neurochem Int.* (2004) 45:545–52. doi: 10.1016/j.neuint.2003.11.006
28. Cserr HF, Cooper DN, Milhorat TH. Flow of cerebral interstitial fluid as indicated by the removal of extracellular markers from rat caudate nucleus. *Exp Eye Res.* (1977) 25:461–73. doi: 10.1016/S0014-4835(77)80041-9
29. Iliff JJ, Wang M, Liao Y, Plogg BA, Peng W, Gundersen GA, et al. A paravascular pathway facilitates CSF flow through the brain parenchyma and the clearance of interstitial solutes, including amyloid B. *Sci Transl Med.* (2012) 4:147ra111. doi: 10.1126/scitranslmed.3003748
30. Louveau A, Plog BA, Antila S, Alitalo K, Nedergaard M, Kipnis J. Understanding the functions and relationships of the glymphatic system and meningeal lymphatics. *J Clin Invest.* (2017) 127:3210–9. doi: 10.1172/JCI90603
31. Albargothy NJ, Johnston DA, Macgregor-Sharp M, Weller RO, Verma A, Hawkes CA, et al. Convective influx / glymphatic system : tracers

injected into the CSF enter and leave the brain along separate periarterial basement membrane pathways. *Acta Neuropathol.* (2018) 136:139–52. doi: 10.1007/s00401-018-1862-7
32. Smith AJ, Verkman AS. The "glymphatic" mechanism for solute clearance in Alzheimer 's disease: game changer or unproven speculation? *FASEB J.* (2018) 32:543–51. doi: 10.1096/fj.201700999
33. Asgari M, De Zélicourt D, Kurtcuoglu V. Glymphatic solute transport does not require bulk flow. *Sci Rep.* (2016) 6:1–11. doi: 10.1038/srep38635
34. Holter KE, Kehlet B, Devor A, Sejnowski TJ, Dale AM, Omholt SW, et al. Interstitial solute transport in 3D reconstructed neuropil occurs by diffusion rather than bulk flow. *Proc Natl Acad Sci USA.* (2017) 114:9894–9. doi: 10.1073/pnas.1706942114
35. Smith AJ, Yao X, Dix JA, Jin BJ, Verkman AS. Test of the 'glymphatic' hypothesis demonstrates diffusive and aquaporin-4-independent solute transport in rodent brain parenchyma. *Elife.* (2017) 6:1–16. doi: 10.7554/eLife.27679
36. Wolak DJ, Thorne RG. Diffusion of macromolecules in the brain: implications for drug delivery. *Mol Pharm.* (2013) 10:1492–504. doi: 10.1021/mp300495e
37. Abbott NJ, Pizzo ME, Preston JE, Janigro D, Thorne RG. The role of brain barriers in fluid movement in the CNS: is there a 'glymphatic' system? *Acta Neuropathol.* (2018) 135:387–407. doi: 10.1007/s00401-018-1812-4
38. Geer CP, Grossman SA. Interstitial fluid flow along white matter tracts: a potentially important mechanism for the dissemination of primary brain tumors. *J Neurooncol.* (1997) 32:193–201. doi: 10.1023/A:1005761031077
39. Elvsåshagen T, Mutsaerts HJ, Zak N, Norbom LB, Quraishi SH, Pedersen PØ, et al. Cerebral blood flow changes after a day of wake, sleep, and sleep deprivation. *Neuroimage.* (2018) 186:497–509. doi: 10.1016/j.neuroimage.2018.11.032
40. Ma Q, Ineichen BV, Detmar M, Proulx ST. Outflow of cerebrospinal fluid is predominantly through lymphatic vessels and is reduced in aged mice. *Nat Commun.* (2017) 8:1434. doi: 10.1038/s41467-017-01484-6
41. Da Mesquita S, Louveau A, Vaccari A, Smirnov I, Cornelison RC, Kingsmore KM, et al. Functional aspects of meningeal lymphatics in ageing and Alzheimer's disease. *Nature.* (2018) 560:185–91. doi: 10.1038/s41586-018-0368-8
42. Larjavaara S, Mäntylä R, Salminen T, Haapasalo H, Raitanen J, Jääskeläinen J, et al. Incidence of gliomas by anatomic location. *Neuro. Oncol.* (2007) 9:319–25. doi: 10.1215/15228517-2007-016
43. Charles N, Holland E, Gilbertson R, Glass R, Kettenmann H. Tumor microenvironment in the brain. *Cancers.* (2012) 4:218–43. doi: 10.3390/cancers4010218
44. Attwell D, Buchan AM, Charpak S, Lauritzen M, MacVicar BA, Newman EA. Glial and neuronal control of brain blood flow. *Nature.* (2010) 468:232–43. doi: 10.1038/nature09613
45. Brandao M, Simon T, Critchley G, Giamas G. Astrocytes, the rising stars of the glioblastoma microenvironment. *Glia.* (2018) 67:1–12. doi: 10.1002/glia.23520
46. Chen W, Wang D, Du X, He Y, Chen S, Shao Q, et al. Glioma cells escaped from cytotoxicity of temozolomide and vincristine by communicating with human astrocytes. *Med Oncol.* (2015) 32:43. doi: 10.1007/s12032-015-0487-0
47. Infanger DW, Cho Y, Lopez BS, Mohanan S, Liu SC, Gursel D, et al. Glioblastoma stem cells are regulated by interleukin-8 signaling in a tumoral perivascular niche. *Cancer Res.* (2013) 73:7079–89. doi: 10.1158/0008-5472.CAN-13-1355
48. Mancino M, Ametller E, Gascón P, Almendro V. The neuronal influence on tumor progression. *Biochim Biophys Acta Rev Cancer.* (2011) 1816:105–18. doi: 10.1016/j.bbcan.2011.04.005
49. Rath BH, Fair JM, Jamal M, Camphausen K, Tofilon PJ. Astrocytes enhance the invasion potential of glioblastoma stem-like cells. *PLoS ONE.* (2013) 8:e54752. doi: 10.1371/journal.pone.0054752
50. Rolón-Reyes K, Kucheryavykh YV, Cubano LA, Inyushin M, Skatchkov SN, Eaton MJ, et al. Microglia activate migration of glioma cells through a Pyk2 intracellular pathway. *PLoS ONE.* (2015) 10:1–18. doi: 10.1371/journal.pone.0131059
51. Dauth S, Grevesse T, Pantazopoulos H, Campbell PH, Maoz BM, Berretta S, et al. Extracellular matrix protein expression is brain region dependent. *J Comp Neurol.* (2016) 524:1309–36. doi: 10.1002/cne.23965
52. Nicholson C. Reports on Progress in Physics Related content Diffusion and related transport mechanisms in brain tissue tissue (2001) 64:816–84. doi: 10.1088/0034-4885/64/7/202
53. Thorne RG, Nicholson C. *In vivo* diffusion analysis with quantum dots and dextrans predicts the width of brain extracellular space. *Proc Natl Acad Sci USA.* (2006) 103:5567–72. doi: 10.1073/pnas.0509425103
54. Butcher DT, Alliston T, Weaver VM. A tense situation: forcing tumour progression. *Nat Rev Cancer.* (2009) 9:108–22. doi: 10.1038/nrc2544
55. Rutkowski JM, Swartz MA. A driving force for change: interstitial flow as a morphoregulator. *Trends Cell Biol.* (2007) 17:44–50. doi: 10.1016/j.tcb.2006.11.007
56. Duvernoy H, Delon S, Vannson JL. The vascularization of the human cerebellar cortex. *Brain Res Bull.* (1983) 11:419–80. doi: 10.1016/0361-9230(83)90116-8
57. Wong AD, Ye M, Levy AF, Rothstein JD, Bergles DE, Searson PC. The blood-brain barrier: an engineering perspective. *Front Neuroeng.* (2013) 6:1–22. doi: 10.3389/fneng.2013.00007
58. Krishna Priya S, Nagare RP, Sneha VS, Sidhanth C, Bindhya S, Manasa P, et al. Tumour angiogenesis—origin of blood vessels. *Int J Cancer.* (2016) 139:729–35. doi: 10.1002/ijc.30067
59. Cha J, Kang SG, Kim P. Strategies of mesenchymal invasion of patient-derived brain tumors: microenvironmental adaptation. *Sci Rep.* (2016) 6:1–12. doi: 10.1038/srep24912
60. Lim E-J, Suh Y, Yoo K-C, Lee J-H, Kim I-G, Kim M-J, et al. Tumor-associated mesenchymal stem-like cells provide extracellular signaling cue for invasiveness of glioblastoma cells. *Oncotarget.* (2017) 8:1438–48. doi: 10.18632/oncotarget.13638
61. Jain RK. Vascular and interstitial barriers to delivery of therapeutic agents in tumors. *Cancer Metastasis Rev.* (1990) 9:253–66. doi: 10.1007/BF00046364
62. Soltani M, Chen P. Numerical modeling of interstitial fluid flow coupled with blood flow through a remodeled solid tumor microvascular network. *PLoS ONE.* (2013) 8:e67025. doi: 10.1371/journal.pone.0067025
63. Kingsmore KM, Vaccari A, Abler D, Cui SX, Epstein FH, Rockne RC, et al. MRI analysis to map interstitial flow in the brain tumor microenvironment. *APL Bioeng.* (2018) 2:031905. doi: 10.1063/1.5023503
64. d'Esposito A, Sweeney PW, Ali M, Saleh M, Ramasawmy R, Roberts TA, et al. Computational fluid dynamics with imaging of cleared tissue and of *in vivo* perfusion predicts drug uptake and treatment responses in tumours. *Nat. Biomed. Eng.* (2018) 2:773–87. doi: 10.1038/s41551-018-0306-y
65. Netti PA, Baxter LT, Boucher Y, Skalak R, Jain RK. Time-dependent behavior of interstitial fluid pressure in solid tumors: implications for drug delivery. *Cancer Res.* (1995) 55:5451–8.
66. Pathak AP, McNutt S, Shah T, Wildes F, Raman V, Bhujwalla ZM. *In vivo* "MRI phenotyping" Reveals changes in extracellular matrix transport and vascularization that mediate VEGF-driven increase in breast cancer metastasis. *PLoS ONE.* (2013) 8:1–11. doi: 10.1371/journal.pone.0063146
67. Soltani M, Chen P. Numerical modeling of fluid flow in solid tumors. *PLoS ONE.* (2011) 6:e20344. doi: 10.1371/journal.pone.0020344
68. Welter M, Rieger H. Interstitial fluid flow and drug delivery in vascularized tumors: a computational model. *PLoS ONE.* (2013) 8:e110568. doi: 10.1371/journal.pone.0070395
69. Raghavan R. Interstitial flow, pathological states, and stem cell delivery in the brain. *ResearchGate.* (2019). doi: 10.13140/RG.2.2.33787.57123. [Epub ahead of print].
70. Bobo RH, Laske DW, Akbasak A, Morrison PF, Dedrick RL, Oldfield EH. Convection-enhanced delivery of macromolecules in the brain. *Proc Natl Acad Sci USA.* (1994) 91:2076–80. doi: 10.1073/pnas.91.6.2076
71. Recht L, Torres CO, Smith TW, Raso V, Griffin TW. Transferrin receptor in normal and neoplastic brain tissue: implications for brain-tumor immunotherapy. *J Neurosurg.* (1990) 72:941–45. doi: 10.3171/jns.1990.72.6.0941
72. Laske DW, Ilercil O, Akbasak A, Youle RJ, Oldfield EH. Efficacy of direct intratumoral therapy with targeted protein toxins for solid human gliomas in nude mice. *J Neurosurg.* (1994) 80:520–26. doi: 10.3171/jns.1994.80.3.0520

73. Laske D, Youle R, Oldfield E. Tumor regression with regional distribution of the targeted toxin TF-CRM107 in patients with malignant brain tumors. *Nat Med.* (1997) 3:1362–8. doi: 10.1038/nm1297-1362
74. Degen JW, Walbridge S, Vortmeyer AO, Oldfield EH, Lonser RR. Safety and efficacy of convection-enhanced delivery of gemcitabine or carboplatin in a malignant glioma model in rats. *J Neurosurg.* (2003) 99:893–8. doi: 10.3171/jns.2003.99.5.0893
75. Mehta AM, Sonabend AM, Bruce JN. Convection-enhanced delivery. *Neurotherapeutics.* (2017) 14:358–71. doi: 10.1007/s13311-017-0520-4
76. Lonser RR, Sarntinoranont M, Morrison PF, Oldfield EH. Convection-enhanced delivery to the central nervous system. *J Neurosurg.* (2015) 122:697–706. doi: 10.3171/2014.10.JNS14229
77. Chen MY, Lonser RR, Governale LS, Morrison PF, Oldfield EH. Variables affecting convection-enhanced delivery to the striatum: a systematic examination of rate of infusion, cannula size, infusate concentration, and tissue—cannula sealing time. *J Neurosurg.* (2009) 90:315–20. doi: 10.3171/jns.1999.90.2.0315
78. Fiandaca MS, Varenika V, Eberling J, McKnight T, Bringas J, Pivirotto P, et al. Real-time MR imaging of adeno-associated viral vector delivery to the primate brain. *Neuroimage.* (2008) 47:T27–35. doi: 10.1016/j.neuroimage.2008.11.012
79. Lewis O, Woolley M, Johnson D, Rosser A, Barua NU, Bienemann AS, et al. Chronic, intermittent convection-enhanced delivery devices. *J Neurosci Methods.* (2016) 259:47–56. doi: 10.1016/j.jneumeth.2015.11.008
80. Raghavan R, Brady ML, Rodríguez-Ponce MI, Pedain C, Hartlep A, Sampson JH. Convection-enhanced delivery of therapeutics for brain disease, and its optimization. *Neurosurg Focus.* (2006) 20:E12. doi: 10.3171/foc.2006.20.4.7
81. Varenika V, LeCouteur R, Park J, Higgins R, Berger M, Bringas J, et al. Detection of infusate leakage in the brain using real-time imaging of convection-enhanced delivery. *J Neurosurg.* (2008) 109:874–80. doi: 10.3171/JNS/2008/109/11/0874
82. Anderson RCE, Yanes CL, Kennedy B, Canoll P, Needle M, Garvin J, et al. Convection-enhanced delivery of topotecan into diffuse intrinsic brainstem tumors in children. *J Neurosurg Pediatr.* (2012) 11:289–95. doi: 10.3171/2012.10.PEDS12142
83. Bogdahn U, Schmaus S, Poverennova I, Venkataramana NK, Oliushine V, Balasubramaniam A, et al. Targeted therapy for high-grade glioma with the TGF- 2 inhibitor trabedersen: results of a randomized and controlled phase IIb study. *Neuro Oncol.* (2010) 13:132–42. doi: 10.1093/neuonc/noq142
84. Bruce JN, Fine RL, Canoll P, Yun J, Kennedy BC, Rosenfeld SS, et al. Regression of recurrent malignant gliomas with convection-enhanced delivery of topotecan. *Neurosurgery.* (2011) 69:1272–9. doi: 10.1227/NEU.0b013e3182233e24
85. Carpentier A, Chinot O, Gorochov G, Barrie M, Metellus P, Richard M, et al. Intracerebral administration of CpG oligonucleotide for patients with recurrent glioblastoma: a phase II study. *Neuro Oncol.* (2011) 12:401–8. doi: 10.1093/neuonc/nop047
86. Kreitman RJ, Puri RK, Pastan I. A circularly permuted recombinant interleukin 4 toxin with increased activity. *Proc Natl Acad Sci USA.* (1994) 91:6889–93. doi: 10.1073/pnas.91.15.6889
87. Kunwar S, Prados MD, Chang SM, Berger MS, Lang FF, Piepmeier JM, et al. Direct intracerebral delivery of cintredekin besudotox (IL13-PE38QQR) in recurrent malignant glioma: a report by the cintredekin besudotox intraparenchymal study group. *J Clin Oncol.* (2007) 25:837–44. doi: 10.1200/JCO.2006.08.1117
88. Kunwar S, Westphal M, Chang S, Pedain C, Joshi BH, Piepmeier J, et al. Phase III randomized trial of CED of IL13-PE38QQR vs Gliadel wafers for recurrent glioblastoma. *Neuro Oncol.* (2010) 12:871–81. doi: 10.1093/neuonc/nop054
89. Lidar Z, Nass D, Mardor Y, Jonas T, Faibel M, Hadani M, et al. Convection-enhanced delivery of paclitaxel for the treatment of recurrent malignant glioma: a Phase I/II clinical study. *J Neurosurg.* (2009) 100:472–9. doi: 10.3171/jns.2004.100.3.0472
90. Lieberman DM, Morrison PF, Laske DW, Bankiewicz KS, Oldfield EH. Convection-enhanced distribution of large molecules in gray matter during interstitial drug infusion. *J Neurosurg.* (2009) 82:1021–9. doi: 10.3171/jns.1995.82.6.1021
91. Vogelbaum MA, Sampson J, Kunwar S, Chang S, Shaffrey M, Asher A, et al. Convection-enhanced delivery of cintredekin besudotox (Interleukin-13-PE38QQR) followed by radiation therapy with and without temozolomide in newly diagnosed malignant gliomas: phase 1 study of final safety results. *Neurosurgery.* (2007) 61:1031–8. doi: 10.1227/01.neu.0000303199.77370.9e
92. Patel SJ, Shapiro WR, Laske DW, Jensen RL, Asher AL, Wessels BW, et al. Safety and feasibility of convection-enhanced delivery of Cotara for the treatment of malignant glioma: initial experience in 51 patients. *Neurosurgery.* (2005) 56:1243–52. doi: 10.1227/01.NEU.0000159649.71890.30
93. Rand RW, Kreitman RJ, Patronas N, Varricchio F, Pastan I, Puri RK. Intratumoral administration of recombinant circularly permuted interleukin-4-Pseudomonas exotoxin in patients with high-grade glioma. *Clin Cancer Res.* (2000) 6:2157–65. Available online at: https://clincancerres.aacrjournals.org/
94. Saito R, Watanabe M, Kumabe T, Nagamatsu K, Sonoda Y, Tominaga T. Regression of recurrent glioblastoma infiltrating the brainstem after convection-enhanced delivery of nimustine hydrochloride. *J Neurosurg Pediatr.* (2016) 7:522–6. doi: 10.3171/2011.2.PEDS10407
95. Sampson JH, Provenzale JM, Kunwar S, Berger MS, Wong TZ, Petry NA, et al. Intracerebral infusion of an EGFR-targeted toxin in recurrent malignant brain tumors. *Neuro Oncol.* (2008) 10:320–9. doi: 10.1215/15228517-2008-012
96. Vogelbaum MA, Mohammadi AM, Brewer C, Ahluwalia MS, Peereboom DM, Barnett GH, et al. First-in-human evaluation of the Cleveland Multiport Catheter for convection-enhanced delivery of topotecan in recurrent high-grade glioma: results of pilot trial 1. *J Neurosurg.* (2018) 130:1–10. doi: 10.3171/2017.10.JNS171845
97. Voges J, Coenen HH, Wienhard K, Sturm V, Dittmar C, Kracht L, et al. Imaging-guided convection-enhanced delivery and gene therapy of glioblastoma. *Ann Neurol.* (2003) 54:479–87. doi: 10.1002/ana.10688
98. Weaver M, Laske DW. Transferrin receptor ligand-targeted toxin conjugate (Tf-CRM107) for therapy of malignant gliomas. *J Neurooncol.* (2003) 65:3–13. doi: 10.1023/A:1026246500788
99. Weber F, Asher A, Bucholz R, Berger M, Prados M, Chang S, et al. Safety, tolerability, and tumor response of IL4-Pseudomonas exotoxin (NBI-3001) in patients with recurrent malignant glioma. *J Neurooncol.* (2003) 64:125–37. doi: 10.1007/BF02700027
100. Weber FW, Floeth F, Asher A, Bucholz R, Berger M, Prados M, et al. Local convection enhanced, delivery of IL4-Pseudomonas exotoxin (NBI-3001) for treatment of patients with recurrent malignant glioma. *Acta Neurochir.* (2003) (Suppl) 88:93–103. doi: 10.1007/978-3-7091-6090-9_15
101. Wersäll P, Ohlsson I, Biberfeld P, Collins VP, Von Krusenstjerna S, Larsson S, et al. Intratumoral infusion of the monoclonal antibody, mAb 425, against the epidermal-growth-factor receptor in patients with advanced malignant glioma. *Cancer Immunol Immunother.* (1997) 44:157–64. doi: 10.1007/s002620050368
102. White E, Bienemann A, Megraw L, Bunnun C, Gill S. Evaluation and optimization of the administration of a selectively replicating herpes simplex viral vector to the brain by convection-enhanced delivery. *Cancer Gene Ther.* (2011) 18:358–69. doi: 10.1038/cgt.2011.2
103. Kunwar S, Chang S, Prados MD, Berger MS, Sampson JH, Croteau D, et al. Safety of intraparenchymal convection-enhanced delivery of cintredekin besudotox in early-phase studies. *Neurosurg. Focus.* (2006) 20:E15.
104. Jagannathan J, Oldfield EH, Walbridge S, Butman JA, Lonser RR. Effect of ependymal and pial surfaces on convectionenhanced delivery. *J Neurosurg.* (2008) 109:547–52. doi: 10.3171/JNS/2008/109/9/0547
105. Yin D, Bringas J, Berger MS, Fiandaca MS, Forsayeth J, Richardson RM, et al. Cannula placement for effective convection-enhanced delivery in the non-human primate thalamus and brainstem: implications for clinical delivery of therapeutics. *J Neurosurg.* (2010) 113:240–8. doi: 10.3171/2010.2.JNS091744
106. Kaiser MG, Parsa AT, Fine RL, Hall JS, Chakrabarti I, Bruce JN. Tissue distribution and antitumor activity of topotecan delivered by intracerebral clysis in a rat glioma model. *Neurosurgery.* (2000) 47:1391–9. doi: 10.1097/00006123-200012000-00026
107. Raghavan R, Brady M, Sampson J. Delivering therapy to target: improving the odds for successful drug development. *Ther Deliv.* (2016) 7:457–81. doi: 10.4155/tde-2016-0016

108. Basser PJ. Interstitial pressure, volume, and flow during infusion into brain tissue. *Microvasc Res.* (1992) 44:143–65. doi: 10.1016/0026-2862(92)90077-3
109. Baxter LT, Jain RK. Transport of fluid and macromolecules in tumors. I Role of interstitial pressure and convection. *Microvasc Res.* (1989) 37:77–104. doi: 10.1016/0026-2862(89)90074-5
110. Saltzman WM, Radomsky L. Drugs released from polymers: diffusion and elimination in brain tissue. *Chem Eng Sci.* (1991) 46:2429–44. doi: 10.1016/0009-2509(91)80036-X
111. Morrison PF, Laske DW, Oldfield EH, Dedrick RL, Bobo H. High-flow microinfusion: tissue penetration and pharmacodynamics. *Am J Physiol Integr Comp Physiol.* (1994) 266:R292–305. doi: 10.1152/ajpregu.1994.266.1.R292
112. Morrison PF, Chen MY, Chadwick RS, Lonser RR, Oldfield EH. Focal delivery during direct infusion to brain: role of flow rate, catheter diameter, and tissue mechanics. *Am J Physiol Integr Comp Physiol.* (1999) 277:R1218–29. doi: 10.1152/ajpregu.1999.277.4.R1218
113. Raghavan R, Mikaelian S, Brady M, Chen ZJ. Fluid infusions from catheters into elastic tissue: I. Azimuthally symmetric backflow in homogeneous media. *Phys Med Biol.* (2010) 55:281–304. doi: 10.1088/0031-9155/55/1/017
114. Chen X, Sarntinoranont M. Biphasic finite element model of solute transport for direct infusion into nervous tissue. *Ann Biomed Eng.* (2007) 35:2145–58. doi: 10.1007/s10439-007-9371-1
115. Kim JH, Astary GW, Chen X, Mareci TH, Sarntinoranont M. Voxelized model of interstitial transport in the rat spinal cord following direct infusion into white matter. *J Biomech Eng.* (2009) 131:071007. doi: 10.1115/1.3169248
116. Linninger AA, Somayaji MR, Erickson T, Guo X, Penn RD. Computational methods for predicting drug transport in anisotropic and heterogeneous brain tissue. *J Biomech.* (2008) 41:2176–87. doi: 10.1016/j.jbiomech.2008.04.025
117. Raghavan R, Brady M. Predictive models for pressure-driven fluid infusions into brain parenchyma. *Phys Med Biol.* (2011) 56:6179–204. doi: 10.1088/0031-9155/56/19/003
118. Smith JH, Humphrey JAC. Interstitial transport and transvascular fluid exchange during infusion into brain and tumor tissue. *Microvasc Res.* (2007) 73:58–73. doi: 10.1016/j.mvr.2006.07.001
119. Smith JH, Jaime García J. A non-linear biphasic model of flow-controlled infusions in brain: mass transport analyses. *J Biomech.* (2011) 44:524–31. doi: 10.1016/j.jbiomech.2010.09.010
120. Zhan W, Wang CH. Convection enhanced delivery of chemotherapeutic drugs into brain tumour. *J Control Release.* (2018) 271:74–87. doi: 10.1016/j.jconrel.2017.12.020
121. Sampson J, Raghavan R, Brady M, Provenzale J, Herndon J II, Croteau D, et al. Clinical utility of a patient-specific algorithm for simulating intracerebral drug infusions. *Neuro Oncol.* (2007) 9:343–53. doi: 10.1215/15228517-2007-007
122. Rosenbluth KH, Eschermann JF, Mittermeyer G, Thomson R, Mittermeyer S, Bankiewicz KS. Analysis of a simulation algorithm for direct brain drug delivery. *Neuroimage.* (2012) 59:2423–9. doi: 10.1016/j.neuroimage.2011.08.107
123. Rosenbluth KH, Gimenez F, Kells AP, Salegio EA, Mittermeyer GM, Modera K, et al. Automated segmentation tool for brain infusions. *PLoS ONE.* (2013) 8:e64452. doi: 10.1371/journal.pone.0064452
124. Boucher Y, Salehi H, Witwer B, Harsh GR, Jain RK. Interstitial fluid pressure in intracranial tumours in patients and in rodents. *Br J Cancer.* (1997) 75:829–36. doi: 10.1038/bjc.1997.148
125. Leroi N, Lallemand F, Coucke P, Noel A, Martinive P. Impacts of ionizing radiation on the different compartments of the tumor microenvironment. *Front Pharmacol.* (2016) 7:1–9. doi: 10.3389/fphar.2016.00078
126. Munson JM, Shieh AC. Interstitial fluid flow in cancer: implications for disease progression and treatment. *Cancer Manage Res.* (2014) 6:317–28. doi: 10.2147/CMAR.S65444
127. Kingsmore KM, Logsdon DK, Floyd DH, Peirce SM, Purow BW, Munson JM. Interstitial flow differentially increases patient-derived glioblastoma stem cell invasion: via CXCR4, CXCL12, and CD44-mediated mechanisms. *Integr Biol.* (2016) 8:1246–60. doi: 10.1039/c6ib00167j
128. Qazi H, Shi ZD, Tarbell JM. Fluid shear stress regulates the invasive potential of glioma cells via modulation of migratory activity and matrix metalloproteinase expression. *PLoS ONE.* (2011) 6:e20348. doi: 10.1371/journal.pone.0020348
129. Shields JD, Fleury ME, Yong C, Tomei AA, Randolph GJ, Swartz MA. Autologous chemotaxis as a mechanism of tumor cell homing to lymphatics via interstitial flow and autocrine CCR7 signaling. *Cancer Cell.* (2007) 11:526–38. doi: 10.1016/j.ccr.2007.04.020
130. Munson JM, Bellamkonda RV, Swartz MA. Interstitial flow in a 3d microenvironment increases glioma invasion by a cxcr4-dependent mechanism. *Cancer Res.* (2013) 73:1536–46. doi: 10.1158/0008-5472.CAN-12-2838
131. Qazi H, Palomino R, Shi ZD, Munn LLLL, Tarbell JMJM. Cancer cell glycocalyx mediates mechanotransduction and flow-regulated invasion. *Integr Biol.* (2013) 5:1334–43. doi: 10.1039/c3ib40057c
132. Cuddapah VA, Robel S, Watkins S, Sontheimer H. A neurocentric perspective on glioma invasion. *Nat Rev Neurosci.* (2014) 15:455–65. doi: 10.1038/nrn3765
133. Shieh AC. Biomechanical forces shape the tumor microenvironment. *Ann Biomed Eng.* (2011) 39:1379–89. doi: 10.1007/s10439-011-0252-2

Conflict of Interest: The authors declare that the research was conducted in the absence of any commercial or financial relationships that could be construed as a potential conflict of interest.

frontiers in Pharmacology

ORIGINAL RESEARCH
published: 06 February 2020
doi: 10.3389/fphar.2020.00008

A Novel C Type CpG Oligodeoxynucleotide Exhibits Immunostimulatory Activity *In Vitro* and Enhances Antitumor Effect *In Vivo*

Tete Li[1], Jing Wu[1], Shan Zhu[1], Guoxia Zang[1], Shuang Li[1], Xinping Lv[1], Wenjun Yue[1], Yuan Qiao[1], Jiuwei Cui[2], Yan Shao[3], Jun Zhang[3], Yong-Jun Liu[1] and Jingtao Chen[1]**

[1] Institute of Translational Medicine, The First Hospital of Jilin University, Changchun, China, [2] Cancer Center, The First Hospital of Jilin University, Changchun, China, [3] Changchun Huapu Biotechnology Co., Ltd., Changchun, China

Background: C type CpG oligodeoxynucleotides (CpG-C ODNs), possessing the features of both A type and B type CpG ODNs, exert a variety of immunostimulatory activities and have been demonstrated as an effective antitumor immunotherapy. Based on the structural characteristics, we designed 20 potential ODNs with the aim of synthesizing an optimal, novel CpG-C ODN specific to human and murine Toll-like receptor 9 (TLR9). We also sought to investigate the *in vitro* immunostimulatory and *in vivo* antitumor effects of the novel CpG-C ODN.

Methods: Twenty potential CpG-C ODNs were screened for their ability to secrete interferon (IFN)-α, and interleukin (IL)-6 and tumor necrosis factor (TNF)-α production for the three most promising sequences were assayed in human peripheral blood mononuclear cells (PBMCs) by enzyme-linked immunosorbent assay (ELISA) or cytometric bead array assay. The functions of human and mouse B cells, and cytokine production in mice induced by the most promising sequence, HP06T07, were determined by flow cytometry and ELISA. Growth and morphology of tumor tissues in *in vivo* murine models inoculated with CT26 cells were analyzed by a growth inhibition assay and immunohistochemistry, respectively.

Results: Among the 20 designed ODNs, HP06T07 significantly induced IFN-α, IL-6, and TNF-α secretion, and promoted B-cell activation and proliferation in a dose-dependent manner in human PBMCs and mouse splenocytes *in vitro*. Intratumoral injection of HP06T07 notably suppressed tumor growth and prolonged survival in the CT26 subcutaneous mouse model in a dose-dependent manner. HP06T07 administered nine times at 2-day intervals (I2) eradicated tumor growth at both primary and distant sites of CT26 tumors. HP06T07 restrained tumor growth by increasing the infiltration of T cells, NK cells, and plasmacytoid dendritic cells (pDCs).

Conclusions: HP06T07, a novel CpG-C ODN, shows potent immunostimulatory activity *in vitro* and suppresses tumor growth in the CT26 subcutaneous mouse model.

Keywords: cytosine-phosphate-guanosine dinucleotide-containing oligodeoxynucleotides, Toll-like receptor 9, plasmacytoid dendritic cells, B cells, antitumor immunotherapy

OPEN ACCESS

Edited by:
Carmen Alvarez-Lorenzo, University of Santiago de Compostela, Spain

Reviewed by:
Adán Pinto Fernández, University of Oxford, United Kingdom
Ivan Hirsch, Charles University, Czechia

***Correspondence:**
Yong-Jun Liu
yjliuanderson@yahoo.com
Jingtao Chen
jtchen@jlu.edu.cn

Specialty section:
This article was submitted to Pharmacology of Anti-Cancer Drugs, a section of the journal Frontiers in Pharmacology

Received: *14 February 2019*
Accepted: *03 January 2020*
Published: *06 February 2020*

Citation:
Li T, Wu J, Zhu S, Zang G, Li S, Lv X, Yue W, Qiao Y, Cui J, Shao Y, Zhang J, Liu Y-J and Chen J (2020) A Novel C Type CpG Oligodeoxynucleotide Exhibits Immunostimulatory Activity In Vitro and Enhances Antitumor Effect In Vivo. Front. Pharmacol. 11:8. doi: 10.3389/fphar.2020.00008

INTRODUCTION

Unmethylated cytosine-phosphate-guanosine dinucleotide (CpG)-containing oligodeoxynucleotides (ODNs), also known as immunostimulatory sequences (ISS), imitate the immunoenhancing activities of bacterial DNA (Krieg et al., 1995; Krieg, 2002). In addition, as ligands for Toll-like receptor 9 (TLR9), they directly activate plasmacytoid dendritic cells (pDCs) and B cells (Hemmi et al., 2000; Bauer et al., 2001).

Based on the chemical compositions, structures, and *in vitro* activities, CpG ODNs are divided structurally and functionally into three types: A, B, and C types [also known as D (CpG-A), K (CpG-B), and CpG-C types, respectively]. CpG-A ODNs, which naturally form a multimeric structure at ~20–100 nm under physiological conditions (Kerkmann et al., 2005), are characterized by a phosphodiester central CpG-containing palindromic motif, capped at the 3'-end by a phosphorothioate-modified poly G tail (Verthelyi et al., 2001). CpG-A ODNs can induce pDCs to produce large amounts of interferon (IFN)-α and tumor necrosis factor (TNF)-α, which in turn promotes higher IFN-α- and TNF-α-dependent NK cell activity (Marshall et al., 2003; Marschner et al., 2005; Marshall et al., 2006), $CD8^+$ T cell activation, and cytotoxicity (Huber and Farrar, 2011). However, they weakly stimulate TLR9-dependent nuclear factor (NF)-κB signaling, and the production of pro-inflammatory cytokines such as interleukin (IL)-6 (Marshall et al., 2003; Vollmer et al., 2004).

CpG-B ODNs contain phosphorothioate backbones and encode one or more CpG dinucleotides (Verthelyi et al., 2001; Kadowaki et al., 2001). CpG-B ODNs markedly induce B-cell activation and maturation by upregulating CD40/CD80/CD86, activate B-cell proliferation, and increase the production of cytokines such as IL-6 and TNF-α, while inducing a relatively small production of IFN-α (Krieg, 2012).

CpG-C ODNs have the characteristics of both CpG-A and CpG-B ODNs (Bao et al., 2006), and contain a full phosphorothioate backbone and a stimulatory palindromic CpG-containing motif (Sharma et al., 2008). In addition, CpG-C ODNs markedly induce cytokine secretion such as IFN-α, IL-6, and TNF-α, and stimulate the activation and proliferation of B cells (Krieg et al., 1995; Krieg, 2002; Liu et al., 2011; Li et al., 2017). Such strong stimulatory features of CpG-C ODNs show promise for using as a therapeutic immunopotentiator.

CpG-C ODNs have shown potent immune-enhancing effects that require unique sequence characteristics (Vollmer et al., 2004; Liu et al., 2011; de Titta et al., 2013). For instance, ODN 2395, a typical CpG-C ODN, has two major indispensable sequence characteristics: (a) one or more TCG elements close to, or at the 5′-end of the ODN, and (b) a palindromic sequence containing multiple CpG motifs at the 3′-end of the ODN (Vollmer et al., 2004). In addition, the hexameric motif 5′ GTCGTT in ODNs has also been demonstrated as the optimal sequence for CpG-C ODNs activities such as that of ODN 2395 (Vollmer et al., 2004). However, it has also been demonstrated that CpG-C ODNs such as C274, C695, and C792 that lack this sequence, also have very potent immunoenhancing effects (Fearon et al., 2003; Marshall et al., 2004; Marshall et al., 2005). In addition, the increasing IFN-α production correlates with longer palindromes (Marshall et al., 2005; Du et al., 2007).

CpG ODNs have been demonstrated to stimulate type-I helper T cells (Th1)-biased innate and adaptive immune responses in both pre-clinical and clinical studies (Klinman, 2004; Krieg, 2012). The stimulation is mediated by initiation of B-cell proliferation and activation (Krieg, 1996; Walker et al., 1999; Hartmann et al., 2000), enhancement of cytokine secretion (Krieg et al., 1999), or promotion of NK-cell cytotoxicity (Ballas et al., 1996). CpG ODNs have received widespread attention for using as vaccine adjuvants (Shirota and Klinman, 2014) and immunotherapeutic agents to treat various infections (Nijnik, 2013), allergies, and cancers (Klinman, 2004; van Duin et al., 2006). Extensive pre-clinical and clinical studies have provided evidence that CpG ODNs are an effective treatment option for cancers, owing to their ability to initiate immune activation in the tumor microenvironment, and break immunosuppression and tolerance (Whitmore et al., 2004). In mice, some studies have demonstrated that intratumoral injections of CpG ODNs can effectively delay tumor growth by stimulating innate and adaptive responses (Sharma et al., 2008; Marabelle et al., 2014). In humans, combining intratumoral CpG ODN with radiation has been demonstrated to be efficacious in patients with cutaneous T-cell lymphoma (Kim et al., 2012) and indolent B-cell lymphoma (Brody et al., 2010). In addition, CpG ODNs have been studied in combination with other drugs to treat cancers (Krieg, 2012; Scheiermann and Klinman, 2014), especially drugs of checkpoint inhibitors such as anti-programmed cell death 1 (PD-1) antibodies (Wang S. et al., 2016; Wang C. et al., 2016). In recent years, CpG-C ODNs, owing to the potent immunostimulatory activity, have been examined for cancer treatment. For example, SD101 (CpG-C ODN) represses tumor growth and reverts the resistance of anti-PD-1 antibodies by increasing leukocyte infiltration and type I IFN-regulated gene expression in a mouse model and a phase 1b/2 clinical experiment, respectively (Wang S. et al., 2016; Ribas et al., 2016).

In this study, we designed 20 potential ODNs based on the nucleotide sequence features of CpG-C ODNs with altered CpG motifs. The immunostimulatory properties of these CpG ODNs were comprehensively investigated to target the best novel CpG-C ODN that is specific to human and murine TLR9. We detected the abilities of the novel CpG-C ODN, HP06T07, to stimulate cytokine (IFN-α, IL-6, and TNF-α) secretion, and activation and proliferation of B cells in human peripheral blood mononuclear cells (PBMCs) and mouse splenocytes *in vitro*. In addition, we confirmed the antitumor effect of HP06T07 using the *in vivo* mouse CT26 tumor model.

MATERIALS AND METHODS

CpG ODNs

Single-stranded, phosphorothioated ODNs containing CpG sequences were synthesized by Ribo Life Science Company (Suzhou, China). ODN 1-20 (ODN 13 was renamed HP06T07) were the sequences modified based on the nucleotide sequence

characteristics of CpG-C ODNs. CpG-C control (GC) was used as the negative control for the CpG-C ODN. The positive controls were ODN 2216 (CpG-A), 2006 (CpG-B), and 2395 (CpG-C). All CpG ODNs were described in **Supplementary Table 1**. All CpG ODNs were dissolved in sterile endotoxin-free water.

Animals

Specific-pathogen-free female BALB/c and C57BL/6 mice (Vital River Laboratory Animal Technology Co., Beijing, China), between 6 and 8 weeks old, were used in the study, and were maintained in a pathogen-free animal facility at the Institute of Translational Medicine, The First Hospital, Jilin University. All animal experiments were performed in accordance with institutional guidelines and the protocols were approved by the ethics committee of the First Hospital of Jilin University, Changchun, China (approval no.: 2017-031).

Cells and Cell Culture

Human PBMCs were isolated using Ficoll (Corning, NY, USA) density gradient centrifugation of buffy coats obtained from healthy volunteers enrolled by the First Hospital of Jilin University. All volunteers signed an informed consent for use of their data for research purposes. The protocol used was approved by the institutional ethics committee (approval no.: 2017-031). Mouse splenocytes were isolated from 6- to 8-week-old BALB/c mice and cultured in RPMI-1640 medium (Corning, NY, USA) supplemented with 10% fetal bovine serum (FBS; Clark, USA) and 1% penicillin/streptomycin (TransGen Biotech, Beijing, China). The murine CT26 colon carcinoma cells were purchased from the American Type Culture Collection (Gaining Biological; Shanghai, China). The CT26 cells were cultured in RPMI-1640 medium supplemented with 10% FBS and 1% penicillin/streptomycin. All cells were cultured at 37°C in humidified air containing 5% CO_2.

Detection of Cytokines Using Enzyme-Linked Immunosorbent Assay (ELISA) and Cytometric Bead Array (CBA) Assay

Human PBMCs or mouse splenocytes were cultured at 0.2–1×10^6 cells/well in 96-well U-bottomed plates using different concentrations of CpG ODNs. After 16 h, the supernatants were harvested and assayed with the following ELISA kits: human IFN-α, mouse IL-6, mouse TNF-α (Mabtech, Sweden), and mouse IFN-α (eBioscience, Vienna, Australia). Human IL-6 and TNF-α were analyzed using CBA (BD Biosciences, San Jose, CA, USA). All kits were used according to the manufacturers' instructions and the results obtained were expressed as picogram per milliliter (pg/ml). For the CBA assays, 50 µl of diluted samples or recombinant standards were incubated with 50 µl mixed capture beads for 1 h at 25°C. Then, 50 µl phycoerythrin-conjugated detection antibodies were added for 2 h protected from light to form the sandwich complexes. After washing the samples to remove the unbound reagents, the concentrations of the cytokines were determined using a flow cytometer (FACS Array; BD Biosciences, San Jose, USA) and the obtained data were analyzed using the FCAP Array software (BD Biosciences, San Jose, CA, USA).

Flow Cytometry Analysis

After stimulation with or without CpG ODNs for 24 h, human PBMCs or mouse splenocytes were collected, pre-incubated with anti-mouse CD16/32 antibodies (BD Biosciences, San Jose, CA, USA), and the dead cells were excluded using an aqua dead cell staining kit (Invitrogen, San Diego, CA, USA). The cells were stained with the following antibodies: anti-human or anti-mouse CD45, CD3, CD19, CD80, and CD86 (BD Biosciences, San Jose, USA); incubated with the respective antibodies for 25 min at 4°C; and then washed twice. After performing FACS using LSRFortessa™ cytometer (BD Biosciences, San Jose, CA, USA), the results were analyzed using the FlowJo software (BD Biosciences, San Jose, CA, USA).

Cell Proliferation Assays

Human PBMCs or mouse splenocytes (5×10^5 cells) were suspended in phosphate-buffered saline (PBS) and then stained with 5-(and 6-) carboxyfluorescein diacetate succinimidyl ester (CFSE; Invitrogen, San Diego, CA, USA) at 37°C for 7 min, protected from light. Pre-cooled RPMI-1640 medium containing FBS was then added to the cells to stop the staining process. After three rounds of washing, cells were incubated with or without CpG ODNs at 37°C for 72 h, and harvested for staining with other antibodies. All flow cytometry data were acquired using the LSRFortessa™ cytometer and were analyzed using the FlowJo software. Decreased CFSE content indicated proliferating cells.

Syngeneic Mouse Models

For the CT26 mouse model, 2×10^5 CT26 tumor cells were injected subcutaneously into the right hind flank of the 6- to 8-week-old BALB/c mice on day 0 and 1×10^5 CT26 cells injected into the left side on day 4. When tumor sizes reached a maximum of 0.6–0.8 cm in diameter, 50 µl HP06T07, GC or PBS was injected into the right side of the tumors. Tumor sizes on both sides of mice were monitored using a digital caliper (AIRAJ, China) every 2–3 days, and the tumor volumes were calculated using the formula: volume (mm^3) = (length × width × width)/2. When the tumor volumes exceeded 3,000 mm^3, mice were euthanized.

Immunohistochemistry

Mice were euthanized on day 28, and tumors on the right and left sides were harvested, fixed in 4% paraformaldehyde for 24 h, and paraffin-embedded for immunohistochemistry using a method reported previously (Gur et al., 2011). Paraffin-embedded spleen sections were stained with rabbit anti-mouse CD3ϵ (99940S; 1:150; Cell Signaling Technology, Danvers, MA, USA), CD19 (90176S; 1:800; Cell Signaling Technology, Danvers, MA, USA), NCR1 (ab214468; 1:600; Abcam, Cambridge, MA, USA), and rat anti-mouse PDCA-1 (DDX0390P-100; 1:100; Novus biologicals, Littleton, CO, USA) antibodies overnight, washed with Tris-buffered saline, and then incubated with goat anti-rat/rabbit (Fuzhou Maxim Biotechnology Development Co., Ltd., Fuzhou, China) and 3,3'-diaminobenzidine (DAB) substrate (Fuzhou Maxim Biotechnology Development Co., Ltd., Fuzhou, China). Images were captured using a light microscope (BX51N-34-FL-1-

D, Olympus Corporation, Tokyo, Japan) and processed by CellSens Dimension software (Universal Imaging).

Statistical Analysis

Data were analyzed using GraphPad Prism software (San Diego, CA, USA) and expressed as means ± standard error of the mean (SEM). Log-rank test was performed to compare survival curves between groups. Statistical significance of the differences between the experimental groups was determined using the Student's t-test or two-way analysis of variance (ANOVA), followed by Bonferroni test for multiple comparisons. P values < 0.05 were considered significant ($^{*}P < 0.05$, $^{**}P < 0.01$, $^{***}P < 0.001$, and $^{****}p < 0.0001$).

RESULTS

The Production of IFN-α, IL-6, and TNF-α by Human PBMCs Is Effectively Induced by CpG-C ODNs

CpG-C ODNs induce IFN-α production by pDCs (Marshall et al., 2003). ELISA results showed that ODN 9, ODN 10, and ODN 13 (the principal ODNs that renamed HP06T07) markedly induced IFN-α in a dose-dependent manner, and the induced IFN-α peaked at a CpG ODN concentration of 0.33 or 1 μM. Other CpG ODNs also stimulated IFN-α production to a certain degree, but their effects were weaker than those of ODN 9, ODN 10, and HP06T07 (**Figure 1A** and **Table S1**).

The cytokine-inducing activities of these three CpG ODNs were evaluated using ELISA or CBA with the typical CpG-C ODN, ODN 2395, as the positive control to evaluate cytokine production. ODN 2006, a CpG-B ODN, was used as the negative control for IFN-α secretion, and as a positive control for IL-6 and TNF-α production. The results showed that ODN 2395 markedly induced IFN-α, IL-6, and TNF-α production, while ODN 2006 effectively induced IL-6 and TNF-α; no obvious IFN-α secretion was observed as mentioned above. Compared to ODN 9, ODN 10, and the controls, ODN 2006 and ODN 2395, the most upregulation of IFN-α, IL-6, and TNF-α was caused by HP06T07 (**Figures 1B–D**). Owing to the potent cytokine induction by HP06T07, it was used in subsequent experiments to confirm its function *in vitro* and *in vivo*.

Activation and Proliferation of Human B Cells Are Enhanced by HP06T07

CpG-C ODNs not only induce the production of cytokines, but promote B-cell activation and proliferation (Marshall et al., 2003). Flow cytometry analysis revealed that GC had no obvious effect on CD80 and CD86 expression in B cells. ODN 2395 significantly promoted CD80 and CD86 expression in B cells to increase their activation and maturation in a dose-dependent manner. HP06T07 also significantly promoted CD80 and CD86 expression in B cells in a dose-dependent manner (**Figures 2A–D**). In addition, the proliferation of B cells was determined using CFSE incorporation after stimulation for 3 days. Similar to the activation and maturation of B cells, HP06T07 and ODN 2395 increased the proliferation of B cells in a dose-dependent manner, whereas GC had no effect on B-cell proliferation (**Figures 2E, F**). All CpG ODNs had no direct effect on the proliferation of T cells (**Figures 2G, H**).

In addition, all CpG ODNs had no effect on IFN-α, IL-6, and TNF-α production (**Figures S1C–E**) and CD80 and CD86 expression (**Figures S1F, G**) in human monocyte-derived dendritic cells (MDDCs; **Figures S1A, B**) that did not express TLR9, suggesting that HP06T07 was specific to human TLR9.

Secretion of Cytokines and Functions of B Cells in Mouse Splenocytes Are Effectively Increased by HP06T07

HP06T07 markedly stimulated human PBMCs to secrete IFN-α, IL-6, and TNF-α, and enhanced B-cell activation and proliferation. To confirm the immune-enhancing function of HP06T07 in mice, similar studies were performed. In evaluating the production of cytokines, ELISA revealed that similar to the effect on human PBMCs, HP06T07 induced higher IFN-α, IL-6, and TNF-α secretion than ODN 2395, whereas GC did not induce the secretion of these cytokines (**Figures 3A–C**).

We additionally detected the activation and proliferation of B cells in mouse splenocytes stimulated by CpG ODNs. Mouse splenocytes were stimulated with or without HP06T07, ODN 2395, and the negative control GC; all were triple diluted (0.01, 0.03, 0.11, 0.33, 1, and 3 μM). As observed with human B cells, ODN 2395 induced B cells to express CD80 and CD86 (**Figures 3D–G**), and promoted B-cell proliferation (**Figures 3H, I**). GC had no effect on B-cell activities. HP06T07 enhanced B-cell activation and proliferation with higher values observed than ODN 2395 (**Figures 3D–I**). Furthermore, all CpG ODNs did not affect the proliferation of T cells (**Figures 3J, K**).

We next investigated mouse TLR9 (mTLR9) activation by HP06T07 using HEK-Blue™-mTLR9 cells (**Figure S1H**) and the parental cell line HEK-Blue™ Null1 cells (**Figure S1I**). HP06T07 more markedly augmented the activation of mTLR9 at a low concentration than ODN2395 did, while GC had no effect in HEK-Blue™-mTLR9 cells (**Figure S1H**). All CpG ODNs had no effect in HEK-Blue™ Null1 cells that did not express mTLR9 (**Figures S1I–K**). These results suggested that the novel CpG-C ODN, HP06T07, was specific to mTLR9.

In Vivo Treatment With Different Doses and Administration Regimen of HP06T07 Restrains CT26 Tumor Growth

The above results showed that the HP06T07 designed as a CpG-C ODN clearly promoted B-cell functions and enhanced the secretion of cytokines including IFN-α, IL-6, and TNF-α. To further evaluate whether intratumoral treatment with HP06T07 suppresses tumor growth, and confirm the optimal dose, CT26 cells were implanted in both flanks of BALB/c mice. Firstly, the CT26 tumor-bearing mice were divided into six groups and intratumorally injected with PBS, the CpG-C negative control GC, and four doses of HP06T07 (0.3, 1, 2.5, and 5 mg/kg) in the right flank on day 8, 11, 14, 17, and 20 (**Figure 4A**). Tumor growth and mouse weights were then monitored (**Figures 4B–E**). HP06T07 significantly suppressed tumor growth in a dose-dependent manner on the right injected and left uninjected sites. In addition, HP06T07 (5 mg/kg) showed the most obvious immunotherapeutic effect (**Figures 4B, C**). The survival study illustrated that HP06T07 improved the survival

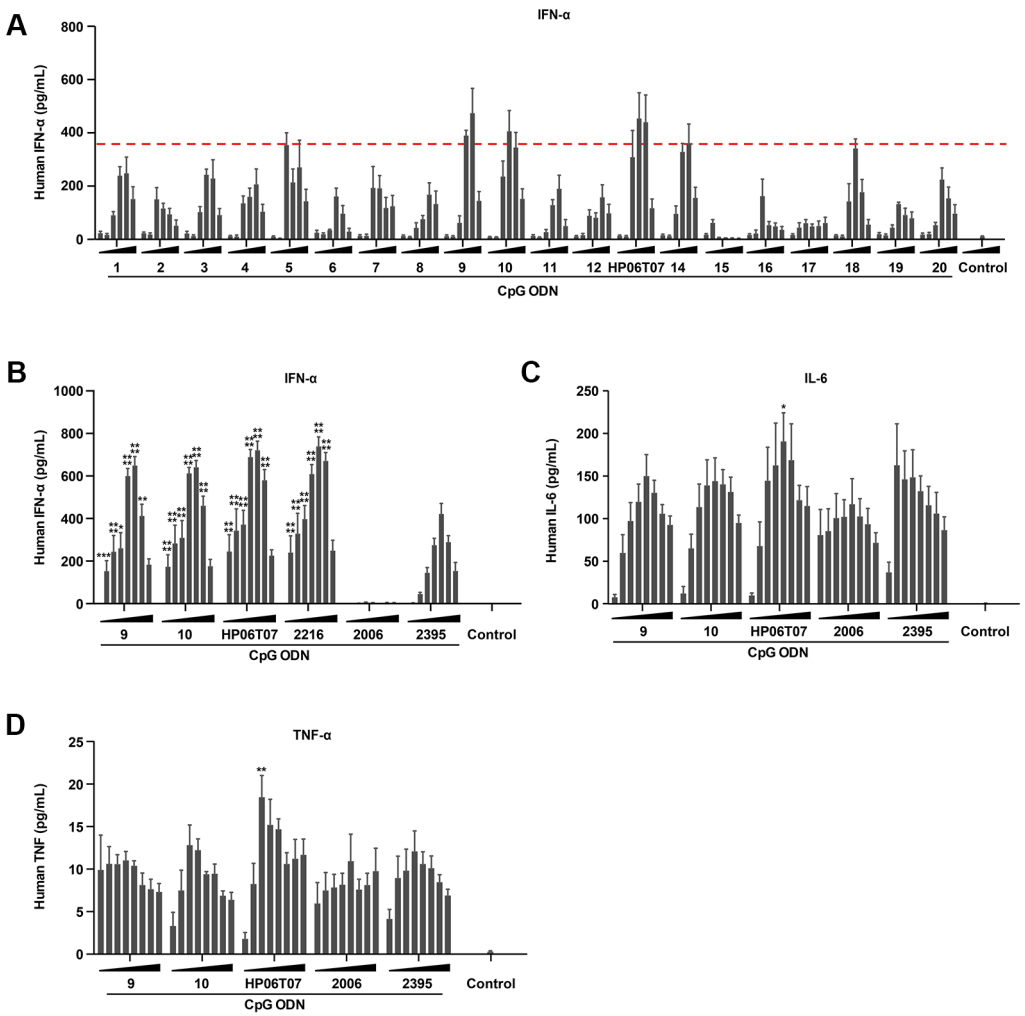

FIGURE1 | The production of IFN-α, IL-6, and TNF-α by human PBMCs is effectively induced by CpG-C ODNs. **(A)** Human PBMCs (2×10^5) were cultured with or without the 20 designed CpG-C ODNs at different concentrations (0.01, 0.03, 0.1, 0.3, 1, and 3 μM) for 16 h. Supernatants were harvested and assayed for IFN-α using ELISA. **(B–D)** Human PBMCs (2×10^5) were incubated with or without ODN 9, 10, 13 (the principal ODNs that renamed HP06T07), 2216, 2006, and 2395 at different concentrations (0.025, 0.05, 0.1, 0.2, 0.4, 0.8, 1.6, and 3.2 μM) for 16 h. Supernatants were harvested and assayed for IFN-α **(B)** using ELISA, and IL-6 **(C)** and TNF-α **(D)** *via* CBA. All data are presented as means ± SEM of three technical replicates from two donors per group. Statistical significance of differences between ODN 2395 and other treated groups were determined ($^{*}P < 0.05$, $^{**}P < 0.01$, $^{***}P < 0.001$, and $^{****}P < 0.0001$).

of mice bearing CT26 tumors (**Figure 4D**). HP06T07 did not reduce the weight of the mice, suggesting that HP06T07 does not induce major side effects (**Figure 4E**). Furthermore, HP06T07 (5 mg/kg) significantly suppressed tumor growth more than ODN 2395 (5 mg/kg) treatment did (**Figure 4F**).

In addition, bilateral CT26 tumor models were treated with 3 mg/kg HP06T07 at different administration intervals and times (**Figure 5A**), which repressed tumor progression to some extent. The consecutive administration of HP06T07 nine times at 2-day intervals (I2), had the best antitumor effect in delaying CT26 tumor growth at both primary and distant sites (**Figures 5B, C**). HP06T07 administered four times at 5-day intervals (I5) also exhibited antitumor effect. HP06T07 administered six times at 3-day intervals (I3), and five times at 6-day intervals (I4) displayed similar antitumor effect, but weaker than those of I2 and I5 (**Figures 5B, C**). Overall, HP06T07 did not decrease mouse weights (**Figure 5D**).

Treatment With HP06T07 Induces Accumulation of T Cells, NK Cells, and pDCs

To characterize the antitumor effects of HP06T07 on tumor-infiltrating immune cells, tumors of mice treated with HP06T07 or PBS administered six times at 3-day intervals (I3) were harvested 2 days after the last treatment. Immunohistochemistry of tumor sections from right side of HP06T07-treated mice showed $CD3^+$ cells (**Figure 6A**), whereas the control mice showed few $CD3^+$ cells. In addition, HP06T07 promoted the infiltration of $NCR1^+$ (**Figure 6B**) and $PDCA\text{-}1^+$ (**Figure 6C**) cells, compared to the PBS-treated group. No significant changes in $CD19^+$, a B-cell

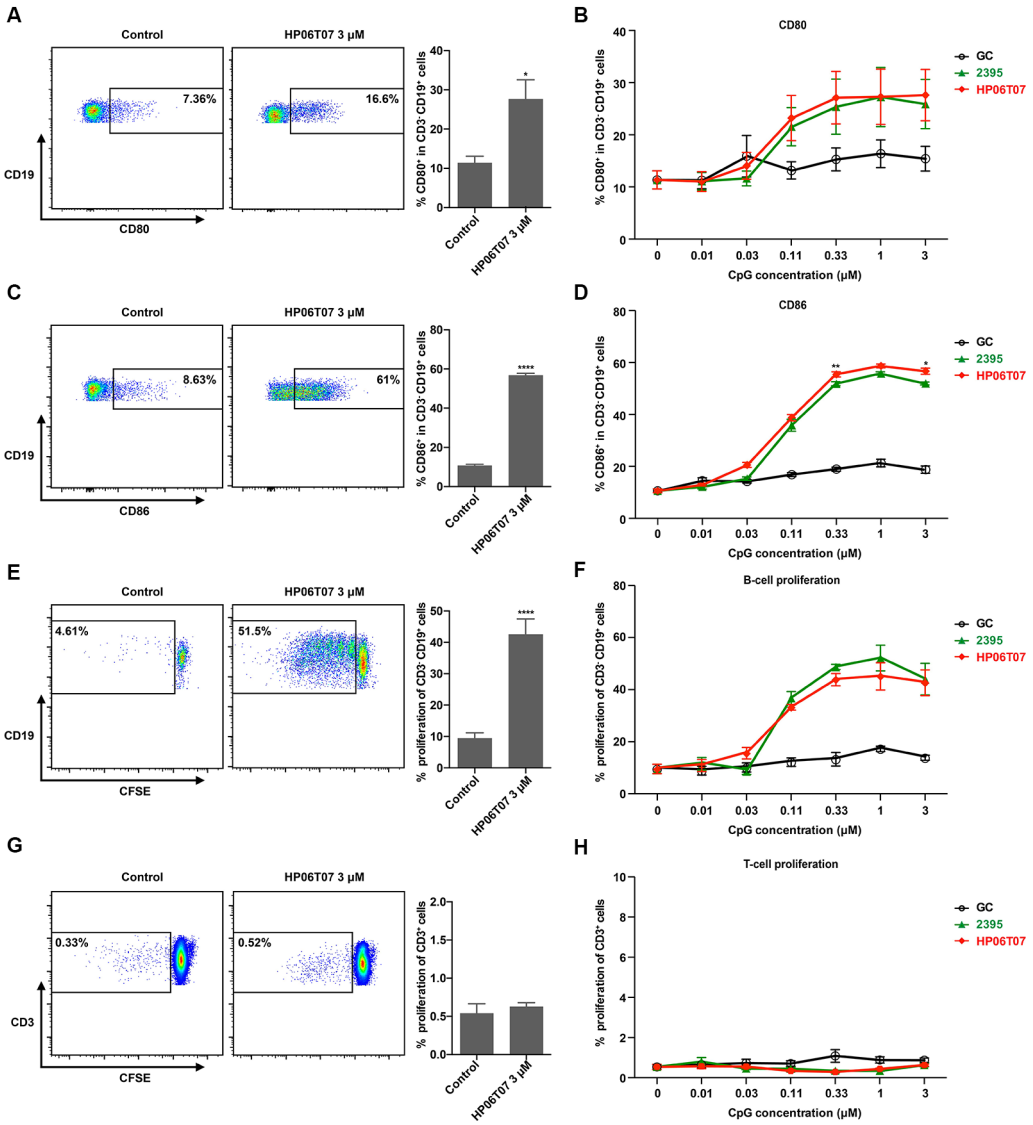

FIGURE 2 | Activation and proliferation of human B cells are enhanced by HP06T07. Human PBMCs (5×10^5) cultured with or without HP06T07 (red), ODN 2395 (green), and negative control GC (black) at different concentrations (0.01, 0.03, 0.1, 0.3, 1, and 3 μM) for 24 h. Cells were collected, and the dead cells were excluded using an aqua dead cell stain kit. Cells were then stained with CD3, CD19, CD80, and CD86. Representative plots and histograms of CD80 **(A)** and CD86 **(C)** expression analyzed using flow cytometry (gated on $CD3^-$ $CD19^+$ B cells). **(B, D)** Expression of CD80 and CD86 on $CD3^-$ $CD19^+$ B cells. **(E–H)** Human PBMCs (5×10^5) incorporated with CFSE and cultured with or without HP06T07, ODN 2395, and the negative control GC at different concentrations (0.01, 0.03, 0.1, 0.3, 1, and 3 μM) for 3 days. $CD19^+$ B cell **(E, F)** and $CD3^+$ T cell **(G, H)** proliferation was measured by decreasing the CFSE content. All data are presented as means ± SEM of three technical replicates from two donors per group. Statistical significance of differences between HP06T07 and ODN 2395 groups were determined ($^*P < 0.05$, $^{**}P < 0.01$, and $^{****}P < 0.0001$).

specific surface antigen, were observed in tumors between the HP06T07- and PBS-treated groups (**Figure 6D**). These results demonstrated that HP06T07 increased the infiltration of T cells, NK cells, and pDCs.

DISCUSSION

In this study, we aimed to screen novel CpG-C ODNs developed with proprietary intellectual property rights. To this end, *in vitro* and *in vivo* experimental studies were performed to evaluate the immunostimulatory properties of the novel CpG-C ODN that is specific for humans and mice, from the 20 potential ODNs designed based on the nucleotide sequence characteristics of CpG-C ODNs.

The data clearly indicate that HP06T07 is an effective CpG-C ODN. CpG-C ODNs markedly induce IFN-α, IL-6, and TNF-α secretion and stimulate B cells (Marshall et al., 2003). Firstly, the designed HP06T07 significantly induced IFN-α

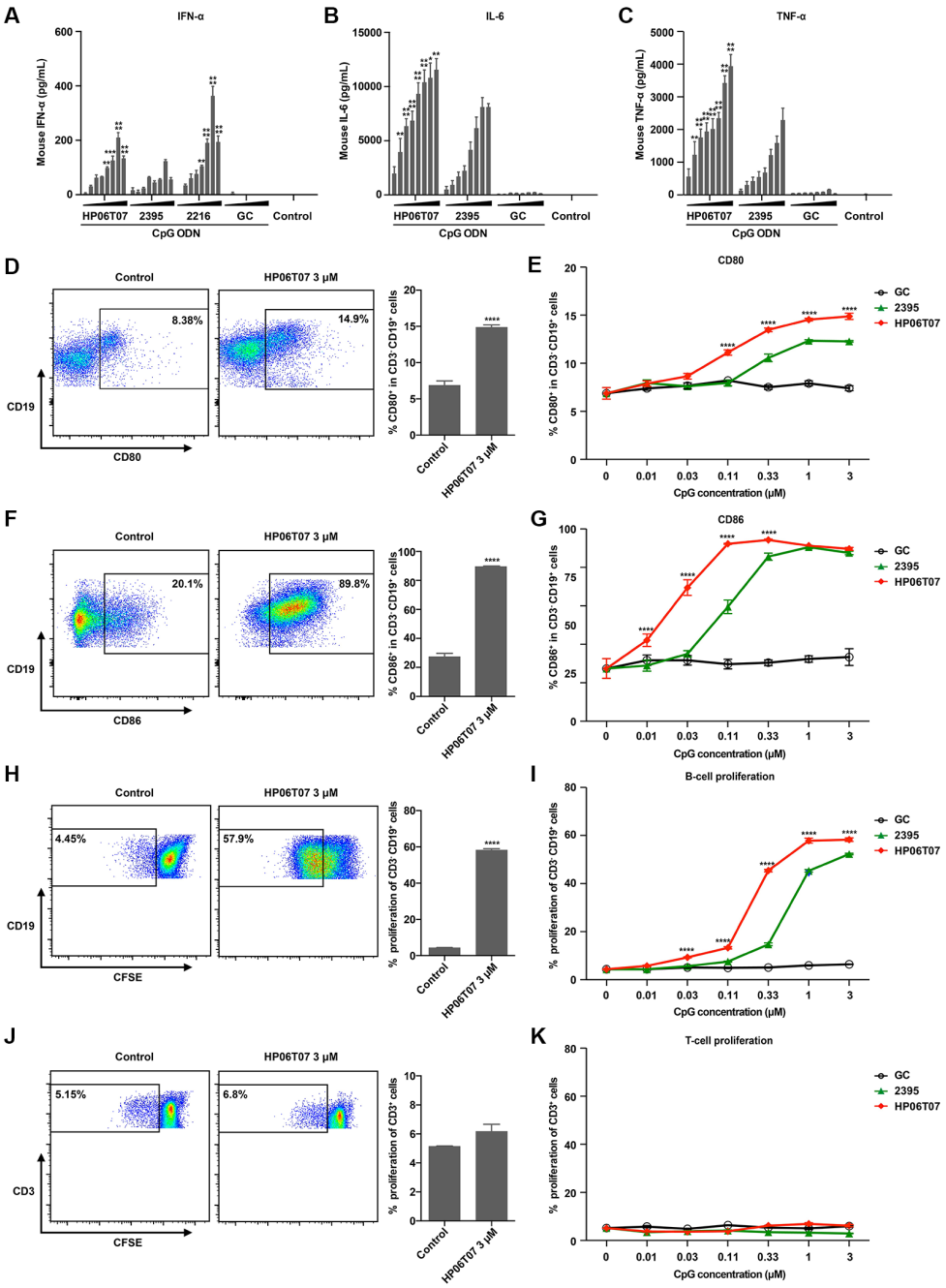

FIGURE 3 | Secretion of cytokines and functions of B cells in mouse splenocytes are effectively increased by HP06T07. **(A)** Mouse splenocytes (1×10^6) were cultured with or without HP06T07 (red), ODN 2395 (green), negative control GC (black), and ODN 2216, at different concentrations (0.025, 0.05, 0.1, 0.2, 0.4, 0.8, 1.6, and 3.2 μM) for 16 h. Supernatants were harvested and assayed for IFN-α *via* ELISA. **(B–C)** Mouse splenocytes (5×10^5) were stimulated with or without HP06T07, ODN 2395 and negative control GC at different concentrations (0.025, 0.05, 0.1, 0.2, 0.4, 0.8, 1.6, and 3.2 μM) for 16 h. Supernatants were harvested and assayed for IL-6 **(B)** and TNF-α **(C)** using ELISA. **(D–G)** Mouse splenocytes (5×10^5) were cultured with or without HP06T07, ODN 2395, and negative control GC at different concentrations (0.01, 0.03, 0.1, 0.3, 1, and 3 μM) for 24 h. Dead cells were excluded using the aqua dead stain kit and cells were stained with CD3, CD19, CD80, and CD86. Representative plots and histograms of CD80 **(D)** and CD86 **(F)** expression were analyzed using flow cytometry (gated on $CD3^-$ $CD19^+$ B cells). **(E, G)** Expression of CD80 and CD86 on $CD3^-$ $CD19^+$ B cells. **(H–K)** Mouse splenocytes (5×10^5) were incorporated with CFSE and cultured with or without HP06T07, ODN 2395, and negative control GC at different concentrations (0.01, 0.03, 0.1, 0.3, 1, and 3 μM) for 3 days. $CD19^+$ B cell **(H, I)** and $CD3^+$ T cell **(J, K)** proliferation was measured by decreasing CFSE content. All data are presented as means ± SEM of two to three technical replicates from two independent experiments per group. Statistical significance of differences between HP06T07 or ODN 2216 and ODN 2395 groups were determined (**P < 0.01, ***P < 0.001, and ****P < 0.0001).

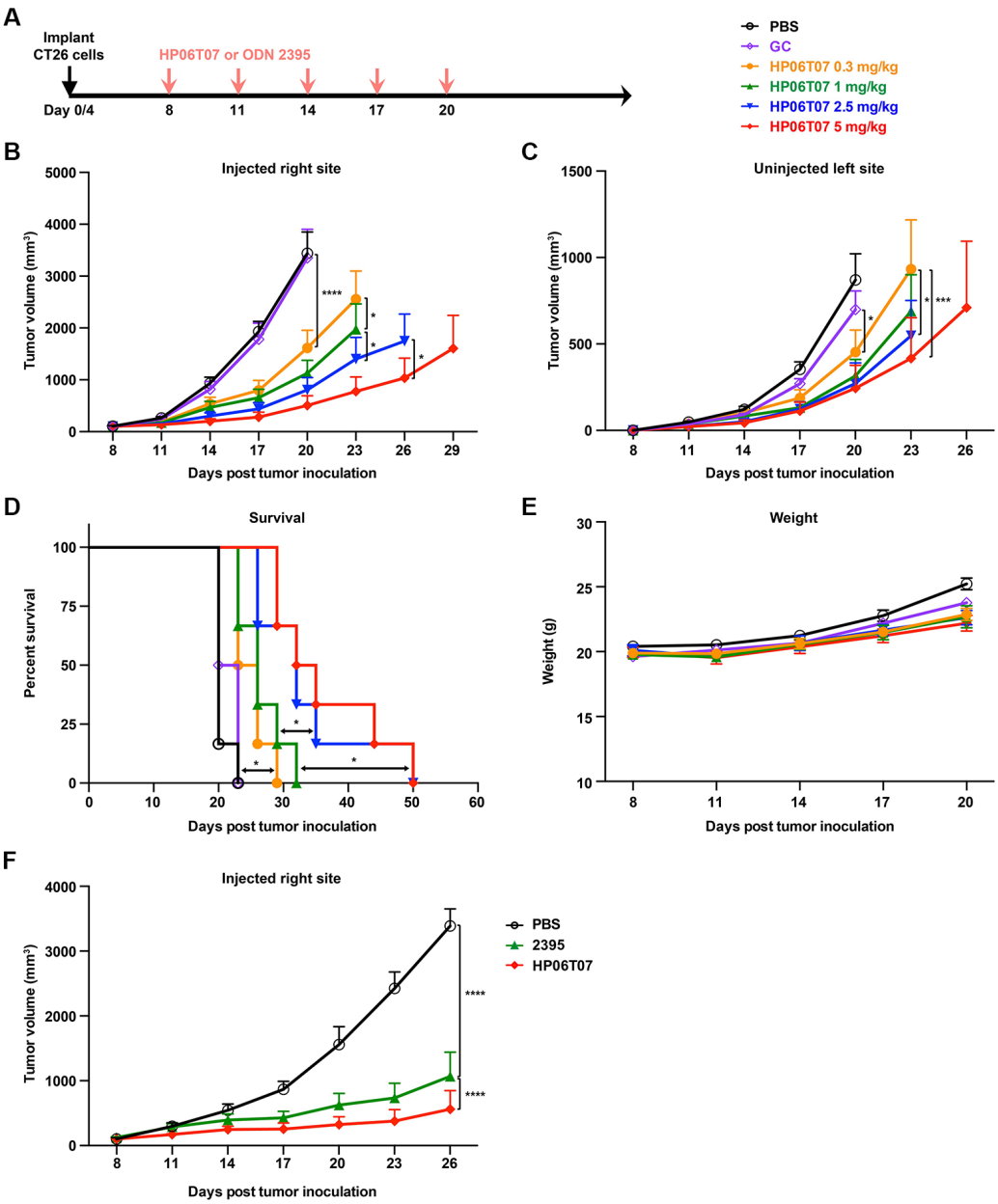

FIGURE 4 | *In vivo* treatment with different doses of HP06T07 exhibits diverse immunotherapeutic effect on CT26 tumors. **(A)** Experimental protocol for HP06T07 treatment with different doses or ODN 2395 treatment. CT26 (2×10^5) cells were implanted subcutaneously into right flanks of 6- to 8-week-old BALB/c mice on day 0, and the CT26 (1×10^5) cells injected into the left side on day 4. When tumor sizes reached a maximum of 0.6–0.8 cm in diameter (day 8), different doses of HP06T07 (0.3, 1, 2.5, and 5 mg/kg; yellow, green, blue, and red, respectively) or GC (2.5 mg/kg; purple) were intratumorally injected into the right side of tumors on day 8, 11, 14, 17, and 20. Tumor sizes on both sides of mice were monitored using a digital caliper, every 3 days. **(B)** Tumor volumes of injected right site of tumors over time. **(C)** Tumor volumes of uninjected left site of tumors over time. **(D)** Overall survival over time. **(E)** Mouse weights over time. **(F)** Tumor volumes of injected right site of tumors in mouse treated with or without 5 mg/kg HP06T07 (red) or ODN2395 (green). All data are means ± SEM (n = 6/group). Statistical significance of differences was determined (*P < 0.05, *P < 0.01, ***P < 0.001, and ****P < 0.0001).

secretion from human PBMCs and mouse splenocytes compared to the control formulation (**Figures 1A, B** and **3A**). Secondly, HP06T07 enhanced IL-6 and TNF-α production in human and mouse cells *in vitro* (**Figures 1C, D** and **3B, C**). HP06T07 also markedly increased CD80 and CD86 expression in human and murine B cells (**Figures 2A–D** and **3D–G**), and promoted B cell proliferation (**Figures 2E, F** and **3H, I**). Thus, the data obtained clearly demonstrated that HP06T07 is an effective immunostimulatory human and murine CpG-C ODN.

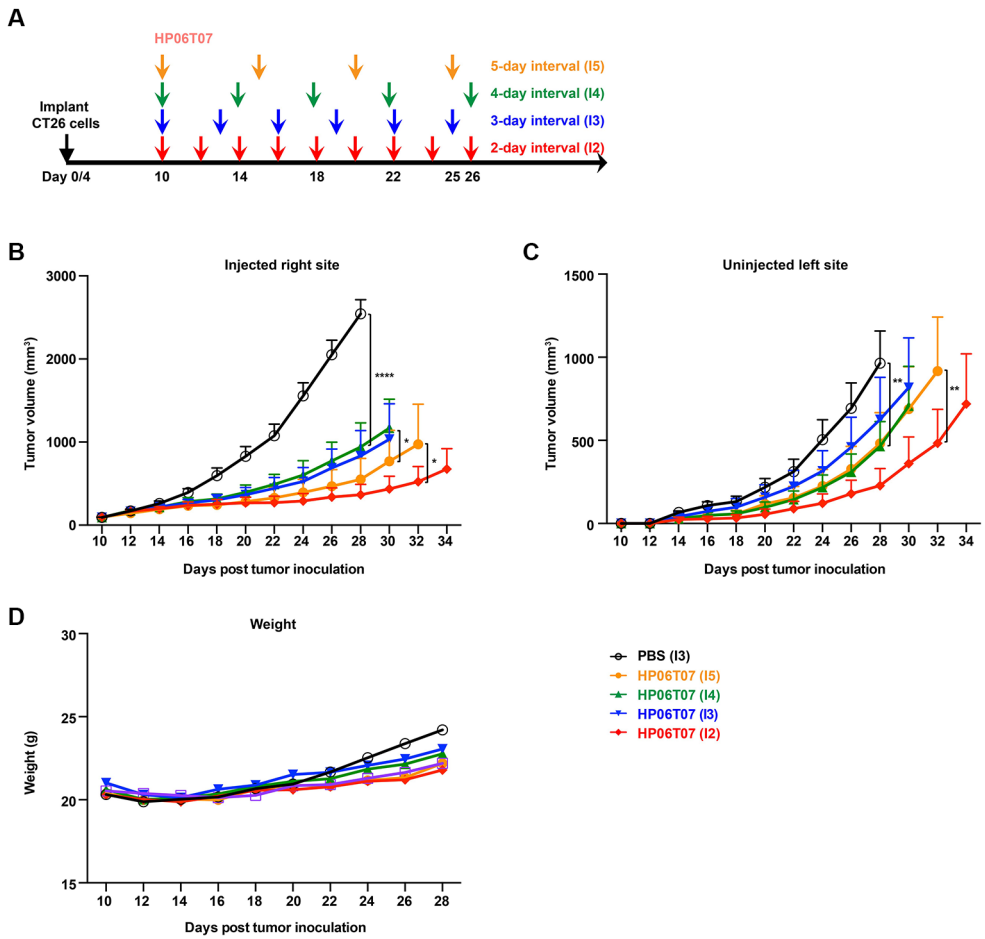

FIGURE 5 | *In vivo* treatment with different administration regimens of HP06T07 suppresses tumor growth. **(A)** Experimental protocol of HP06T07 treatment with different administration regimens. CT26 (2×10^5) cells were implanted subcutaneously into the right flank of 6- to 8-week-old BALB/c mice on day 0, and on day 4 in left flank using the CT26 (1×10^5) cells. When tumor sizes reached a maximum of 0.6–0.8 cm in diameter (day 10), 3 mg/kg HP06T07 was intratumorally injected into right side of tumors at 50 μl, and was administered consecutively four times at 5-day intervals (days 10, 15, 20, and 25; I5; yellow), five times at 4-day intervals (day 10, 14, 18, 22, and 26; I4; green), six times at 3-day intervals (day 10, 13, 16, 19, 22, and 25; I3; blue) or nine times at 2-day intervals (day 10, 12, 14, 16, 18, 20, 22, 24, and 26; I2; red). Tumor sizes on both sides of mice were monitored using digital calipers, every 2 days. Tumor growth on injected right **(B)** and uninjected left **(C)** sites was monitored. **(D)** Mouse weights over time. All data are means ± SEM (n = 8/group). Statistical significance of differences was determined ($^{*}P < 0.05$, $^{**}P < 0.001$, and $^{****}P < 0.0001$).

The detection of cytokine production is a conventional method for the screening of CpG ODNs. In this study, IFN-α production was first checked to screen 20 potential CpG-C ODNs except CpG-B ODNs. We found that ODN 9, ODN 10, and HP06T07 significantly induced IFN-α secretion in human PBMCs. IFN-α has many biological functions including promoting the proliferation of Th1 (Belardelli, 1995), increasing the tumor-specific cytolytic T cell activity (von Hoegen et al., 1990), and suppressing tumor growth and tumor angiogenesis (Okada et al., 2001). Therefore, these three most promising ODNs were selected for a further study to detect IL-6 and TNF-α production. We found that HP06T07 markedly promoted IL-6 and TNF-α production. Thus, HP06T07 was deemed the most promising CpG-C ODN. In addition, HP06T07 enhanced the functions of B cells in human and mouse, and increased cytokine production in mouse. Thus, HP06T07 is an effective CpG-C ODN specific for humans and mice.

HP06T07, a 29-nucleotide phosphorothioate oligodeoxynucleotide, significantly induced the secretion of cytokines in human PBMCs and mouse splenocytes *in vitro*. However, certain cytokines could be produced by several immune cells. For example, IFN-α is predominantly secreted by pDCs (Liu, 2005); however, other immune cells such as macrophages and T cells also produce IFN-α. TNF-α is produced by pDCs, B cells, and monocytes/macrophages, among other cells (Campbell et al., 2009). In the present study, we determined the concentration of the cytokines stimulated by HP06T07 in human PBMCs and mouse splenocytes; however, we were unable to identify the cells induced by CpG ODNs. Thus, flow cytometry or sorted pDCs

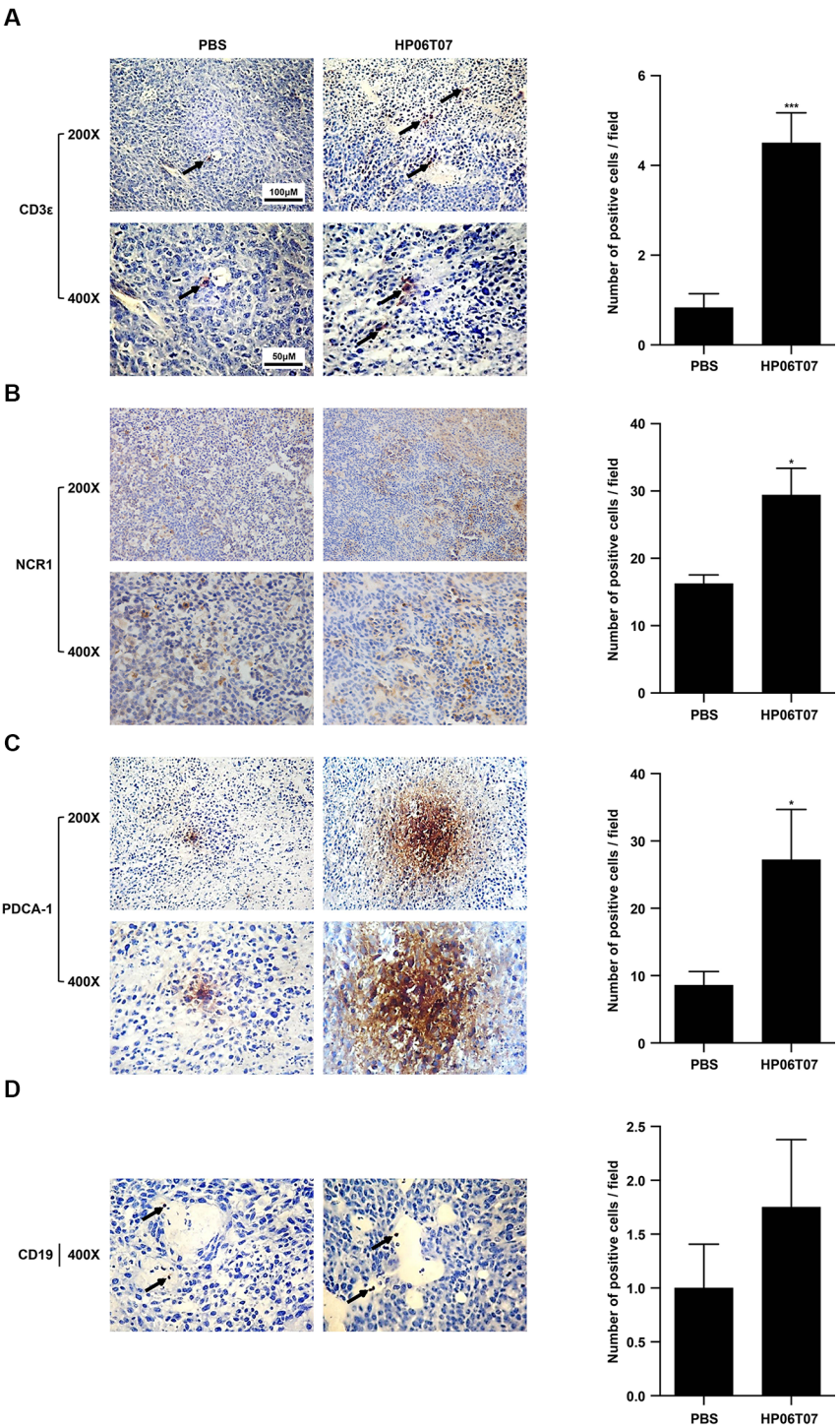

FIGURE 6 | Treatment with HP06T07 induces accumulation of T cells, NK cells, and pDCs. Three mg/kg HP06T07 or PBS was intratumorally injected into right sides of tumors at 50 μl and was administered consecutively six times at 3-day intervals (day 10, 13, 16, 19, 22, and 25; l3). Two days after last treatment, tumors on the right sides of mice were harvested, embedded with paraffin, and stained with anti-mouse CD3ε **(A)**, NK cell marker NCR1 **(B)**, pDCs marker PDCA-1 **(C)**, and CD19 **(D)**. Positive cells were detected with alkaline phosphatase-conjugated goat anti-rat/rabbit IgG according to the manufacturer's instructions. Representative images from one of three HP06T07- or PBS-treated mice are shown. Arrows indicate infiltration of immune cells. Original magnification, 200× and 400×. Histogram results were expressed as mean ± SEM of positive cells/field evaluated at 400× images (n = 4–6/group). Statistical significance of differences was determined (*$P < 0.05$ and ***$P < 0.001$).

and B cells should be used as more precise methods to further determine the cell-specific activation of HP06T07 in future studies.

In our *in vivo* experiments, tumor growth in CT26 subcutaneous model treated with different concentrations of HP06T07 delivered to the tumor was notably suppressed in a dose-dependent manner (**Figure 4**). These results indicated that HP06T07 owing to its powerful immunostimulatory effect, has efficient antitumor activity and is expected to be one of the most potent monotherapies for cancers. The effects of the intratumoral injection aligns with previous reports that *in situ* vaccination with CpG-C ODN significantly inhibited the occurrence and development of tumors (Sato-Kaneko et al., 2017; Sagiv-Barfi et al., 2018). We also investigated the antitumor effect of different administration regimens (intervals and times) of HP06T07 (**Figure 5**). We demonstrated that HP06T07 administered at I2 and I5 had the best antitumor effect by delaying CT26 tumor growth on both right and left sites (**Figure 5**). Therefore, intensive monotherapy with HP06T07 either continuously or at regular intervals achieved superior therapeutic effects.

In vivo treatment with different doses and administration regimen of HP06T07 did not decrease mouse weights. However, the HP06T07-treated groups appeared to experience slightly less weight gain than the PBS-treated group. The reason might be that HP06T07 significantly suppressed tumor growth to keep tumors at small volumes, while the tumor in the PBS-treated group could not be controlled and thus, kept increasing. Consequently, the overall mouse weights (pure mouse weights and tumor weights) in the PBS-treated group were obviously increased especially when tumor volumes exceeded 1,000 mm^3.

Intratumoral injection of HP06T07 enhanced the infiltration of $CD3^+$ T cells, $NCR1^+$ NK cells, and PDCA-1^+ pDCs as shown by immunohistochemistry (**Figure 6**). CD3 is commonly used as a T-cell-specific marker. NKp46, a major killer receptor, is expressed exclusively by NK and NK-like cells for which an orthologous protein, NCR1, has been found in mice (Gur et al., 2010). Thus, NCR1 is considered as the most specific mouse NK cell marker (Gur et al., 2011). B220 (CD45R) and PDCA-1 (BST2) are important specific phenotype markers of pDCs (Narendra et al., 2014; Kostarnoy et al., 2017). However, B220 was expressed not only on pDCs, but also on B cells and activated T cells (Simon et al., 2018). Therefore, PDCA-1 was considered the more accurate and specific marker. CD19 is usually used as a B-cell marker. In our studies, $CD19^+$ cells were few and scattered, and no significant difference occurred between HP06T07-treated and PBS-treated groups. In our *in vitro* experiments, however, HP06T07 significantly promoted B-cell proliferation. A possible reason to explain this contradiction might be that the B cells were only a small population of immune cells in the subcutaneous tumor tissues, making them difficult to detect using immunohistochemistry. Flow cytometry analysis to detect the infiltrations and functions of immune cells might solve this problem in the future.

HP06T07 significantly suppressed tumor growth on the right injected and left uninjected sites, suggesting that intratumoral injection of HP06T07 triggered systemic antitumor immune responses. This is consistent with previous reports in which CpG ODNs inhibited growth of tumors on both sides in CT26, MCA38, TSA, and A20 mouse models (Wang S. et al., 2016; Sagiv-Barfi et al., 2018). HP06T07 promoted the accumulation of T cells, B cells, NK cells, and pDCs. However, the exact and in-depth mechanism of the antitumor effect of HP06T07 was not identified in the present study. Thus, immune system responses and other mechanisms that might be involved in the treatment with HP06T07 still require elucidation by further investigations.

CONCLUSIONS

We have demonstrated that the novel CpG-C ODN, HP06T07, significantly induces B-cell functions, and IFN-α, IL-6, and TNF-α secretion in human and mouse *in vitro*. In addition, intratumoral injection of HP06T07 suppressed tumor growth at both primary and distant sites of CT26 tumors. In the future, with more studies, HP06T07 may be an excellent candidate for cancer therapy when used as a monotherapy or co-therapy.

DATA AVAILABILITY STATEMENT

The raw data analyzed during the current study are available from the corresponding authors upon reasonable request.

ETHICS STATEMENT

This study was carried out in accordance with the recommendations of institutional guidelines, the ethics committee of the First Hospital of Jilin University with written informed consent from all subjects. All subjects gave written informed consent in accordance with the Declaration of Helsinki. The protocol was approved by the ethics committee of the First Hospital of Jilin University, Changchun, China (approval no.: 2017-031).

AUTHOR CONTRIBUTIONS

TL, SZ, GZ, SL, and YQ performed the *in vitro* experiments, analyzed the data, and revised the manuscript. TL, JW, XL, and WY performed the *in vivo* experiments and analyzed the data. TL, JWC, YS, and JZ assisted in the writing of the discussion and revised the manuscript. Y-JL and JTC conceived the study, revised the data, and wrote the manuscript. All authors read and approved the final manuscript.

FUNDING

This study was financially supported by the National Natural Science Foundation of China (Grant 81870152, 81571534); the

National Major Scientific and Technological Special Project for "Significant New Drugs Development" during the Twelfth Five-year Plan Period (Grant 2013ZX09102032); the Key Scientific Project of Jilin Province (Grant 20140204024YY); the Scientific and Technological Developing Plan of Jilin Province (Grant 20180101097JC); the Jilin Provincial Key Laboratory of Biotherapy (20170622011JC); the Fundamental Research Funds for the Central Universities, and the Program for JLU Science and Technology Innovative Research Team (No. 2017TD-08); the 13th Five-Year Science and Technology Research and Planning Project of the Education Department of Jilin Province (JJKH20190043KJ).

ACKNOWLEDGMENTS

We would like to thank Pharmaron for their excellent technical assistance.

SUPPLEMENTARY MATERIAL

The Supplementary Material for this article can be found online at: https://www.frontiersin.org/articles/10.3389/fphar.2020.00008/full#supplementary-material

REFERENCES

Ballas, Z. K., Rasmussen, W. L., and Krieg, A. M. (1996). Induction of NK activity in murine and human cells by CpG motifs in oligodeoxynucleotides and bacterial DNA. *J. Immunol.* 157, 1840–1845.

Bao, M., Zhang, Y., Wan, M., Dai, L., Hu, X., Wu, X., et al. (2006). Anti-SARS-CoV immunity induced by a novel CpG oligodeoxynucleotide. *Clin. Immunol.* 118, 180–187. doi: 10.1016/j.clim.2005.09.014

Bauer, S., Kirschning, C. J., Hacker, H., Redecke, V., Hausmann, S., Akira, S., et al. (2001). Human TLR9 confers responsiveness to bacterial DNA *via* species-specific CpG motif recognition. *Proc. Natl. Acad. Sci. USA.* 98, 9237–9242. doi: 10.1073/pnas.161293498

Belardelli, F. (1995). Role of interferons and other cytokines in the regulation of the immune response. *APMIS.* 103, 161–179.

Brody, J. D., Ai, W. Z., Czerwinski, D. K., Torchia, J. A., Levy, M., Advani, R. H., et al. (2010). In situ vaccination with a TLR9 agonist induces systemic lymphoma regression: a phase I/II study. *J. Clin. Oncol.* 28, 4324–4332. doi: 10.1200/JCO.2010.28.9793

Campbell, J. D., Cho, Y., Foster, M. L., Kanzler, H., Kachura, M. A., Lum, J. A., et al. (2009). CpG-containing immunostimulatory DNA sequences elicit TNF-alpha-dependent toxicity in rodents but not in humans. *J. Clin. Invest.* 119, 2564–2576. doi: 10.1172/JCI38294

de Titta, A., Ballester, M., Julier, Z., Nembrini, C., Jeanbart, L., van der Vlies, A. J., et al. (2013). Nanoparticle conjugation of CpG enhances adjuvancy for cellular immunity and memory recall at low dose. *Proc. Natl. Acad. Sci. USA.* 110, 19902–19907. doi: 10.1073/pnas.1313152110

Du, H. Y., Xia, S. Y., Song, H. F., Li, N., Shang, M. M., Zou, J., et al. (2007). Structure-efficacy relationships of immunostimulatory activity of CpG-containing oligodeoxynucleotides on mouse spleen cells. *Acta Pharmacol. Sinica.* 28, 1637–1644. doi: 10.1111/j.1745-7254.2007.00628.x

Fearon, K., Marshall, J. D., Abbate, C., Subramanian, S., Yee, P., Gregorio, J., et al. (2003). A minimal human immunostimulatory CpG motif that potently induces IFN-gamma and IFN-alpha production. *Eur. J. Immunol.* 33, 2114–2122. doi: 10.1002/eji.200323948

Gur, C., Porgador, A., Elboim, M., Gazit, R., Mizrahi, S., Stern-Ginossar, N., et al. (2010). The activating receptor NKp46 is essential for the development of type 1 diabetes. *Nat. Immunol.* 11, 121–128. doi: 10.1038/ni.1834

Gur, C., Enk, J., Kassem, S. A., Suissa, Y., Magenheim, J., Stolovich-Rain, M., et al. (2011). Recognition and killing of human and murine pancreatic beta cells by the NK receptor NKp46. *J. Immunol.* 187, 3096–3103. doi: 10.4049/jimmunol.1101269

Hartmann, G., Weeratna, R. D., Ballas, Z. K., Payette, P., Blackwell, S., Suparto, I., et al. (2000). Delineation of a CpG phosphorothioate oligodeoxynucleotide for activating primate immune responses *in vitro* and *in vivo*. *J. Immunol.* 164, 1617–1624.

Hemmi, H., Takeuchi, O., Kawai, T., Kaisho, T., Sato, S., Sanjo, H., et al. (2000). A Toll-like receptor recognizes bacterial DNA. *Nature.* 408, 740–745. doi: 10.1038/35047123

Huber, J. P., and Farrar, J. D. (2011). Regulation of effector and memory T-cell functions by type I interferon. *Immunology.* 132, 466–474. doi: 10.1111/j.1365-2567.2011.03412.x

Kadowaki, N., Antonenko, S., and Liu, Y. J. (2001). Distinct CpG DNA and polyinosinic-polycytidylic acid double-stranded RNA, respectively, stimulate CD11c- type 2 dendritic cell precursors and CD11c+ dendritic cells to produce type I IFN. *J. Immunol.* 166, 2291–2295.

Kerkmann, M., Costa, L. T., Richter, C., Rothenfusser, S., Battiany, J., Hornung, V., et al. (2005). Spontaneous formation of nucleic acid-based nanoparticles is responsible for high interferon-alpha induction by CpG-A in plasmacytoid dendritic cells. *J. Biol. Chem.* 280, 8086–8093. doi: 10.1074/jbc.M410868200

Kim, Y. H., Gratzinger, D., Harrison, C., Brody, J. D., Czerwinski, D. K., Ai, W. Z., et al. (2012). In situ vaccination against mycosis fungoides by intratumoral injection of a TLR9 agonist combined with radiation: a phase 1/2 study. *Blood.* 119, 355–363. doi: 10.1182/blood-2011-05-355222

Klinman, D. M. (2004). Immunotherapeutic uses of CpG oligodeoxynucleotides. *Nat. Rev. Immunol.* 4, 249–258. doi: 10.1038/nri1329

Kostarnoy, A. V., Gancheva, P. G., Lepenies, B., Tukhvatulin, A. I., Dzharullaeva, A. S., Polyakov, N. B., et al. (2017). Receptor Mincle promotes skin allergies and is capable of recognizing cholesterol sulfate. *Proc. Natl. Acad. Sci. USA.* 114, E2758–E2765. doi: 10.1073/pnas.1611665114

Krieg, A. M., Yi, A. K., Matson, S., Waldschmidt, T. J., Bishop, G. A., Teasdale, R., et al. (1995). CpG motifs in bacterial DNA trigger direct B-cell activation. *Nature.* 374, 546–549. doi: 10.1038/374546a0

Krieg, A. M., Yi, A. K., and Hartmann, G. (1999). Mechanisms and therapeutic applications of immune stimulatory CpG DNA. *Pharmacol. Ther.* 84, 113–120.

Krieg, A. M. (1996). An innate immune defense mechanism based on the recognition of CpG motifs in microbial DNA. *J. Lab. Clin. Med.* 128, 128–133.

Krieg, A. M. (2002). CpG motifs in bacterial DNA and their immune effects. *Annu. Rev. Immunol.* 20, 709–760. doi: 10.1146/annurev.immunol.20.100301.064842

Krieg, A. M. (2012). CpG still rocks! Update on an accidental drug. *Nucleic Acid. Ther.* 22, 77–89. doi: 10.1089/nat.2012.0340

Li, S., Wu, J., Zhu, S., Liu, Y. J., and Chen, J. (2017). Disease-associated plasmacytoid dendritic cells. *Front. Immunol.* 8, 1268. doi: 10.3389/fimmu.2017.01268

Liu, Y., Luo, X., Yang, C., Yu, S., and Xu, H. (2011). Three CpG oligodeoxynucleotide classes differentially enhance antigen-specific humoral and cellular immune responses in mice. *Vaccine.* 29, 5778–5784. doi: 10.1016/j.vaccine.2011.05.087

Liu, Y. J. (2005). IPC: professional type 1 interferon-producing cells and plasmacytoid dendritic cell precursors. *Annu. Rev. Immunol.* 23, 275–306. doi: 10.1146/annurev.immunol.23.021704.115633

Marabelle, A., Kohrt, H., Caux, C., and Levy, R. (2014). Intratumoral immunization: a new paradigm for cancer therapy. *Clin. Cancer Res.* 20, 1747–1756. doi: 10.1158/1078-0432.CCR-13-2116

Marschner, A., Rothenfusser, S., Hornung, V., Prell, D., Krug, A., Kerkmann, M., et al. (2005). CpG ODN enhance antigen-specific NKT cell activation *via* plasmacytoid dendritic cells. *Eur. J. Immunol.* 35, 2347–2357. doi: 10.1002/eji.200425721

Marshall, J. D., Fearon, K., Abbate, C., Subramanian, S., Yee, P., Gregorio, J., et al. (2003). Identification of a novel CpG DNA class and motif that optimally stimulate B cell and plasmacytoid dendritic cell functions. *J. Leukoc. Biol.* 73, 781–792.

Marshall, J. D., Higgins, D., Abbate, C., Yee, P., Teshima, G., Ott, G., et al. (2004). Polymyxin B enhances ISS-mediated immune responses across multiple species. *Cell Immunol.* 229, 93–105. doi: 10.1016/j.cellimm.2004.04.009

Marshall, J. D., Fearon, K. L., Higgins, D., Hessel, E. M., Kanzler, H., Abbate, C., et al. (2005). Superior activity of the type C class of ISS *in vitro* and *in vivo* across multiple species. *DNA Cell Biol.* 24, 63–72. doi: 10.1089/dna.2005.24.63

Marshall, J. D., Heeke, D. S., Abbate, C., Yee, P., and Van Nest, G. (2006). Induction of interferon-gamma from natural killer cells by immunostimulatory CpG DNA is mediated through plasmacytoid-dendritic-cell-produced interferon-alpha and tumour necrosis factor-alpha. *Immunology.* 117, 38–46. doi: 10.1111/j.1365-2567.2005.02261.x

Narendra, S. C., Chalise, J. P., Höök, N., and Magnusson, M. (2014). Dendritic cells activated by double-stranded RNA induce arthritis *via* autocrine type I IFN signaling. *J. Leukoc. Biol.* 95, 661–666. doi: 10.1189/jlb.0613320

Nijnik, A. (2013). Immunomodulatory approaches for prevention and treatment of infectious diseases. *Curr. Opin. Microbiol.* 16, 590–595. doi: 10.1016/j.mib.2013.06.011

Okada, H., Villa, L., Attanucci, J., Erff, M., Fellows, W. K., Lotze, M. T., et al. (2001). Cytokine gene therapy of gliomas: effective induction of therapeutic immunity to intracranial tumors by peripheral immunization with interleukin-4 transduced glioma cells. *Gene Ther.* 8, 1157–1166. doi: 10.1038/sj.gt.3301496

Ribas, A., Gonzalez, R., Drabick, J., Kummar, S., Agarwala, S., Nemunaitis, J., et al. (2016). Phase 1b/2, open-label, multicenter, dose escalation and expansion trial of intratumoral SD 101 in combination with pembrolizumab in patients with metastatic melanoma. *Ann. Oncol.* 27 (suppl_6), 1067P.

Sagiv-Barfi, I., Czerwinski, D. K., Levy, S., Alam, I. S., Mayer, A. T., Gambhir, S. S., et al. (2018). Eradication of spontaneous malignancy by local immunotherapy. *Sci. Transl. Med.* 10, eaan4488. doi: 10.1126/scitranslmed.aan4488

Sato-Kaneko, F., Yao, S., Ahmadi, A., Zhang, S. S., Hosoya, T., Kaneda, M. M., et al. (2017). Combination immunotherapy with TLR agonists and checkpoint inhibitors suppresses head and neck cancer. *JCI Insight* 2, e93397. doi: 10.1172/jci.insight.93397

Scheiermann, J., and Klinman, D. M. (2014). Clinical evaluation of CpG oligonucleotides as adjuvants for vaccines targeting infectious diseases and cancer. *Vaccine.* 32, 6377–6389. doi: 10.1016/j.vaccine.2014.06.065

Sharma, S., Dominguez, A. L., Hoelzinger, D. B., and Lustgarten, J. (2008). CpG-ODN but not other TLR-ligands restore the antitumor responses in old mice: the implications for vaccinations in the aged. *Cancer Immunol. Immun.* 57, 549–561. doi: 10.1007/s00262-007-0393-1

Shirota, H., and Klinman, D. M. (2014). Recent progress concerning CpG DNA and its use as a vaccine adjuvant. *Expert Rev. Vaccines.* 13, 299–312. doi: 10.1586/14760584.2014.863715

Simon, M., Ipek, R., Homola, G. A., Rovituso, D. M., Schampel, A., Kleinschnitz, C., et al. (2018). Anti-CD52 antibody treatment depletes B cell aggregates in the central nervous system in a mouse model of multiple sclerosis. *J. Neuroinflammation.* 15, 225. doi: 10.1186/s12974-018-1263-9

van Duin, D., Medzhitov, R., and Shaw, A. C. (2006). Triggering TLR signaling in vaccination. *Trends. Immunol.* 27, 49–55. doi: 10.1016/j.it.2005.11.005

Verthelyi, D., Ishii, K. J., Gursel, M., Takeshita, F., and Klinman, D. M. (2001). Human peripheral blood cells differentially recognize and respond to two distinct CPG motifs. *J. Immunol.* 166, 2372–2377.

Vollmer, J., Weeratna, R., Payette, P., Jurk, M., Schetter, C., Laucht, M., et al. (2004). Characterization of three CpG oligodeoxynucleotide classes with distinct immunostimulatory activities. *Eur. J. Immunol.* 34, 251–262. doi: 10.1002/eji.200324032

von Hoegen, P., Zawatzky, R., and Schirrmacher, V. (1990). Modification of tumor cells by a low dose of Newcastle disease virus. III. Potentiation of tumor-specific cytolytic T cell activity *via* induction of interferon-alpha/beta. *Cell Immunol.* 126, 80–90.

Walker, P. S., Scharton-Kersten, T., Krieg, A. M., Love-Homan, L., Rowton, E. D., Udey, M. C., et al. (1999). Immunostimulatory oligodeoxynucleotides promote protective immunity and provide systemic therapy for leishmaniasis *via* IL-12- and IFN-gamma-dependent mechanisms. *Proc. Natl. Acad. Sci. USA.* 96, 6970–6975.

Wang, C., Sun, W., Wright, G., Wang, A. Z., and Gu, Z. (2016). Inflammation-Triggered Cancer Immunotherapy by Programmed Delivery of CpG and Anti-PD1 Antibody. *Adv. Mater.* 28, 8912–8920. doi: 10.1002/adma.201506312

Wang, S., Campos, J., Gallotta, M., Gong, M., Crain, C., Naik, E., et al. (2016). Intratumoral injection of a CpG oligonucleotide reverts resistance to PD-1 blockade by expanding multifunctional CD8+ T cells. *Proc. Natl. Acad. Sci. USA.* 113, E7240–E7249. doi: 10.1073/pnas.1608555113

Whitmore, M. M., DeVeer, M. J., Edling, A., Oates, R. K., Simons, B., Lindner, D., et al. (2004). Synergistic activation of innate immunity by double-stranded RNA and CpG DNA promotes enhanced antitumor activity. *Cancer Res.* 64, 5850–5860. doi: 10.1158/0008-5472.CAN-04-0063

Conflict of Interest: Authors YS and JZ were employed by company Changchun Huapu Biotechnology Co., Ltd.

The remaining authors declare that the research was conducted in the absence of any commercial or financial relationships that could be construed as a potential conflict of interest.

frontiers in Pharmacology

REVIEW
published: 08 April 2020
doi: 10.3389/fphar.2020.00368

Targeting Tumor Associated Macrophages to Overcome Conventional Treatment Resistance in Glioblastoma

Hélène Grégoire[1], *Loris Roncali*[1], *Audrey Rousseau*[1,2], *Michel Chérel*[3], *Yves Delneste*[1,4], *Pascale Jeannin*[1,4], *François Hindré*[1,5] *and Emmanuel Garcion*[1,6*]

[1] CRCINA, INSERM, Université de Nantes, Université d'Angers, Angers, France, [2] Département de Pathologie Cellulaire et Tissulaire, CHU Angers, Angers, France, [3] CRCINA, INSERM, Université d'Angers, Université de Nantes, Nantes, France, [4] Laboratoire d'Immunologie et Allergologie, CHU d'Angers, Angers, France, [5] PRIMEX, Plateforme de radiobiologie et d'imagerie expérimentale, SFR ICAT, Université d'Angers, Angers, France, [6] PACeM, Plateforme d'analyses cellulaires et moléculaires, SFR ICAT, Université d'Angers, Angers, France

OPEN ACCESS

Edited by:
Robert Clarke,
Georgetown University,
United States

Reviewed by:
David Soto-Pantoja,
Wake Forest School of Medicine,
United States
Biana Godin,
Houston Methodist Research Institute,
United States

***Correspondence:**
Emmanuel Garcion
emmanuel.garcion@univ-angers.fr

Specialty section:
This article was submitted to Pharmacology of Anti-Cancer Drugs, a section of the journal Frontiers in Pharmacology

Received: 23 December 2019
Accepted: 10 March 2020
Published: 08 April 2020

Citation:
Grégoire H, Roncali L, Rousseau A, Chérel M, Delneste Y, Jeannin P, Hindré F and Garcion E (2020) Targeting Tumor Associated Macrophages to Overcome Conventional Treatment Resistance in Glioblastoma. Front. Pharmacol. 11:368. doi: 10.3389/fphar.2020.00368

Glioblastoma (GB) is the most common and devastating form of brain cancer. Despite conventional treatments, progression or recurrences are systematic. In recent years, immunotherapies have emerged as an effective treatment in a number of cancers, leaving the question of their usefulness also faced with the particular case of brain tumors. The challenge here is major not only because the brain is the seat of our consciousness but also because of its isolation by the blood-brain barrier and the presence of a unique microenvironment that constitutes the central nervous system (CNS) with very specific constituent or patrolling cells. Much of the microenvironment is made up of immune cells or inflammation. Among these, tumor-associated macrophages (TAMs) are of significant interest as they are often involved in facilitating tumor progression as well as the development of resistance to standard therapies. In this review, the ubiquity of TAMs in GB will be discussed while the specific case of microglia resident in the brain will be also emphasized. In addition, the roles of TAMs as accomplices in the progression of GB and resistance to treatment will be presented. Finally, clinical trials targeting TAMs as a means of treating cancer will be discussed.

Keywords: glioblastoma, macrophages, microglia, resistance, radiation, crosstalks, tumor-associated macrophage

INTRODUCTION

Glioblastoma (GB) is the most frequent and malignant form of brain tumors. It is associated with a poor prognosis and the median overall survival of GB patients is about 15 months after standard of care (Stupp et al., 2009). Conventional treatments consist of maximal safe resection followed by external radiotherapy and concomitant chemotherapy based on the use of the alkylating agent temozolomide (TMZ) (Stupp et al., 2005). However, recurrence inevitably occurs. Currently, no therapy can completely cure GB; current treatments can only marginally improve the overall survival of patients. The current

strategy focuses mostly on targeting the tumor cells, failing to account for other cellular constituents present in the tumor. Hence, to cure and achieve a complete resection of GB tumors, new therapeutic strategies are in great demand.

GB is a highly heterogeneous tumor, with diverse co-existing cell types that include tumor cells, endothelial cells, fibroblasts and different cell types from the immune system (Charles et al., 2011; Quail and Joyce, 2017). A particular emphasis has been placed on the immune system and especially on tumor-associated macrophages (TAMs) as they are the dominant infiltrating immune cell population in GB. These cells interact with tumor cells to promote tumor growth and progression (Feng et al., 2015). The host defense is composed of both innate and adaptative immune cells and they are both involved in cancer immune surveillance in early stages of the disease. However, the tumor is able to escape this immune surveillance during its development. At that point, the tumor can recruit immune cells and change their original function to be one of its accomplices (Brown et al., 2018; Finn, 2018). Tumor cells can inhibit the cytotoxic function of the immune system by secreting immunosuppressive factors or recruiting immunosuppressive inflammatory cells. In relation to this, macrophages appear to be a promising target to improve the effectiveness of actual therapy as more and more information on their physiological and pathological roles in the brain is being uncovered.

Macrophages are the most abundant infiltrating immune cells in GB. Their function is different from their homolog in healthy tissues (Nishie et al., 1999; Hussain et al., 2006). They are able to discriminate the components of the self from the non-self (microbes) but also the altered components of the self. When recognizing the non-self or altered self-components, they can begin their process of elimination. Macrophages located in the tumor microenvironment are called tumor-associated macrophages. Under normal physiological conditions, macrophages are implicated in different processes such as organ development, tissue homeostasis, host defense against infections. These cells can also participate in metabolic disorders, immune diseases and cancer development (Sica et al., 2015). Normally, the myeloid population is the major player of the innate immune system and represents up to 30% of the tumor mass (Rossi et al., 1987; Graeber et al., 2002). Both the activation status and the number of TAMs present in the tumor microenvironment seem to influence GB prognosis (Komohara et al., 2008; Lu-Emerson et al., 2013; Pyonteck et al., 2013).

Macrophages are characterized by their plasticity and heterogeneity. They can be activated by different types of stimuli (growth factors, cytokines, microbial products, nucleotides) which in turn will affect macrophages differently (Poh and Ernst, 2018). *In vitro*, the stimulation of macrophages by interferon-γ (IFN–γ) and/or lipopolysaccharides (LPS) induces the classical (M1) macrophage polarization (Nielsen and Schmid, 2017). M1 macrophages favor the generation of T helper Type 1 (Th1) lymphocytes. Classically activated macrophages are good effectors to fight malignant tumors and are associated with chronic inflammation (Atri et al., 2018). Those macrophages are characterized by a high expression of IL-12, IL-23, and a low expression of IL-10. They can also produce high levels of pro-inflammatory cytokines IL-1β, tumor necrosis factor α (TNF-α), and IL-6, and increase the expression of inducible nitric oxide synthase (iNOS, NOSII) and reactive oxygen species (ROS). Another known stimulus for M1 macrophages is GM-CSF (Granulocyte Macrophage Colony-Stimulating Factor). It activates STAT5, which leads to the activation of the PI3K-AKT pathway (Jeannin et al., 2018).

On the contrary, macrophages stimulated *in vitro* by IL-4 and/or IL-13 are called alternatively activated (M2) macrophages (Murray et al., 2014). They are known effectors for promoting Th2 lymphocytes. They are involved in angiogenesis and tumor progression (Martinez and Gordon, 2014). This phenotype is associated with a low expression of IL-12, IL-23, and a high expression of IL-10 and TGF-β. Furthermore, M2 macrophages also have high levels of arginase 1 (Arg1), mannose receptors and scavenger receptors. M-CSF (Macrophage Colony-Stimulating Factor) and IL-34 also induce a M2 phenotype. M-CSF and IL-34 express the same receptor named CD115 and activate the MAP kinases signaling pathway (Jeannin et al., 2018).

Although the traditional M1/M2 dichotomy is useful for understanding the functionality of TAMs, recent analyzes, in particular of single-cell, revealed a spectrum of activation states much more complex than these traditional polarizations (Locati et al., 2020). Hence, macrophages in cancer are double-edged swords exerting pro- and antitumor functions. More than a real opposition, the M1/M2 signature crystallize a continuum of two extremes capable of specific adaptations (eg., chromatin remodeling, epigenetic marks, trained immunity, metabolic reprogramming,…) to various loco-regional cues (eg., cytokines, chemokines, miRNA, or immune checkpoints). In addition, proliferating monocytes could persist in a state of self-renewal within tumor tissues, rather than immediately differentiate into macrophages indicating a much higher complexity (Lin et al., 2019). It should again be emphasized that the M1 and M2 markers are distinct across species and in particular between humans and mice (eg., in human NOSII and Arg1 do not account for M1 and M2 macrophages, respectively) (Thomas and Mattila, 2014). In this regard, there are no specific surface markers in humans except a privileged panel of produced cytokines.

TAMs that are described in the tumor have in most cases pro-tumorigenic functions that promote tumor growth, invasion, angiogenesis, and tumor metastasis. In the GB microenvironment, both TAMs derive from blood monocytes; some originate from resident macrophages called microglia. Hence, macrophages appear to be an attractive target for new therapeutic strategies (Noy and Pollard, 2014).

The goal of this review is to discuss whether macrophages are worth considering as therapeutic targets in GB and to summarize the existing drugs targeting macrophages. In the second part of this review, the presence of microglia in brain tumor will be discussed. Then, the roles of TAMs in regulating the tumor

development, progression, and the response to conventional therapy will be reviewed. Finally, a survey of clinical trials testing drugs against macrophages in cancer will be presented.

THE PRESENCE OF TAMS IN GB: REALITY OR NOT?

The World Health Organization (WHO) classification of Central Nervous System (CNS) tumors was restructured in 2016. Diagnoses are based on both molecular alterations and histopathologic features (integrated diagnosis) in contrast to the 2007 WHO classification that only included histopathologic features (Louis et al., 2007; Louis et al., 2016). The tumor is essentially defined by the characteristics of the tumor cells that compose it, independently of the ecosystem in which they evolve and which they could themselves modify. GB also consists of many different noncancerous cells. The following cells are known to define the tumor microenvironment: endothelial cells, pericytes, fibroblasts, and immune cells in addition to cancer cells (Quail and Joyce, 2013).

The tumor microenvironment is now emerging as an important regulator of cancer progression (Quail and Joyce, 2017). Data from the literature seem to suggest that distinct molecular profiles in GB are correlated with differences in their microenvironment (Zhernakova et al., 2018). Even if the WHO classification now includes molecular data, no information on the tumor microenvironment has been integrated so far. Despite the fact that a solid tumor has never been seen without infiltrating immune cells, current diagnostic guidelines often forget voluntarily to take this into account. Although this does not necessarily modify the diagnosis as it is perceived today, it could be useful as regards the consideration of patient management and escape or not to new well identified therapies. The presence of TAMs has already been well described in GB (Saha et al., 2017; Séhédic et al., 2017; Roesch et al., 2018). In a mouse model, TAMs were observed in perivascular areas in the tumor and seem to be implicated in gliomagenesis Feng et al., 2015. Interestingly, their localization in the tumor appears to depend on their phenotypes Schiffer et al., 2018. In 2012, a meta-analysis showed that a high density of TAMs appeared to be associated with a poor prognosis in head and neck, ovarian and breast cancer and with a better prognosis in colorectal cancer (Zhang et al., 2012; Yuan et al., 2017; Zhao et al., 2017). Further evidence revealed that human GB display a mixed population of M1/M2 macrophages, and the ratio M1:M2 correlated with survival in IDH1 R132H wild type GB (Zeiner et al., 2018). In high-grade gliomas, M2 macrophages were correlated with an unfavorable prognostic (Sørensen et al., 2018). Caponegro et al. also described a correlation between the presence of TAMs and a poorest prognosis in GB (Caponegro et al., 2018). Furthermore, a study based on magnetic resonance imaging in GB showed that highly aggressive tumors were also correlated with the presence of TAMs (Zhou et al., 2018). Taking into account these findings, the presence of TAMs in GB has been well proven. Macrophages are important for the progression of GB and assessing them may give more information on the prognosis.

MICROGLIA: THE RESIDENT MACROPHAGES OF THE CNS

Microglia are the resident macrophages of the CNS and a healthy CNS macrophage population consists only of resident microglia. The blood brain barrier is impaired in neuropathological diseases, thus allowing an infiltration of monocytes form peripheral blood. In GB, both resident microglia and peripheral macrophages can be detected (Lisi et al., 2017). It is crucial to understand their molecular differences and their specific roles in the tumor. Resident microglia and newly recruited macrophages, hereafter referred to as peripheral macrophages have a distinct origin, as microglia arise from the yolk sac primitive macrophages (Ginhoux et al., 2013; Ginhoux and Guilliams, 2016). Although their origin differs, they share common histologic characteristics. Differentiating between microglia and peripheral macrophages is a difficult task, since they share common surface markers. The name TAM may very well include both resident microglia and monocyte-derived macrophages (Szulzewsky et al., 2015; Kloepper et al., 2016). In order to separate macrophages of hematopoietic origin from resident microglia, CD45 was used in flow cytometry analysis (Badie et al., 2000). However, resident microglia can upregulate their CD45 expression, making them indistinguishable from peripheral macrophages (Müller et al., 2015). Using a genetically engineered mouse, it was demonstrated that peripheral macrophages represent the majority of TAMs in the tumor, and resident microglia form a minor TAM population (Chen et al., 2017). Moreover, resident microglia and peripheral macrophages have different preferential localizations. Peripheral macrophages mostly appear in perivascular areas while resident macrophages are usually located in the peritumoral zone. A recent study showed that only a small batch of common genes toward species (rat, mice, human) differentiates GB-induced polarization of resident microglia (Walentynowicz et al., 2018). Although many studies tried to decipher the origin of TAMs in the tumor, no clear answer has yet been obtained.

Resident microglia are described to be involved in many processes including tumor growth and progression (Bryukhovetskiy et al., 2016; Matias et al., 2018). Microglia were shown to contribute to the invasiveness of GB by upregulating serpin family A member 3 (SERPINA3) expression in GB stem cells (GSCs), that is implicated in the remodeling of the extracellular matrix (Li et al., 2018). Resident microglia were also shown to mediate GB progression and stemness through the activation of interferon regulatory factor 7 (IRF7) that generates an inflammatory environment (Li Z. et al., 2017). Resident microglia are also involved in antitumor immunity processes through the expression of toll-like receptor 2 (TLR2) that down regulates their major histocompatibility complex class II (MHCII) expression (Qian et al., 2018). In a murine model, enhancer of zeste homolog 2 (EZH2) expression in GB was shown to be involved in the polarization of TAMs toward the M2 phenotype, creating an immune deficient environment (Yin et al., 2017). A 6 cytokine-related gene signature in resident microglia was shown to be sufficient to predict survival and identify M2 cells in GB (Cai et al., 2015). Both resident and peripheral macrophages are uniquely involved

in supporting GB growth and progression. Hence, if we wish to target TAMs as a mean to treat GB, we must first characterize this population as peripheral macrophages and/or resident microglia and counter their exact roles in GB initiation and maintenance.

TUMOR-ASSOCIATED MACROPHAGES: A PARTNER IN CRIME FOR TUMOR CELLS

A tumor can influence its microenvironment, and inversely. Thus, the interactions between the tumor cells and the nearby non-tumor cells are crucial to promote tumor angiogenesis, peripheral immune tolerance, and tumor growth. As previously said, TAMs are highly represented inside the tumor microenvironment. They are known for their heterogeneous phenotype, which by simplification can be with either anti-tumor (M1-like) or pro-tumor functions (M2-like). As TAMs are highly plastic cells, they can program themselves into both subpopulations. This gives them the ability to have different functions in different tumor areas and at different times during the tumor development.

Biology of the Tumor

Tumor Cells

The effect of TAMs on tumor cells is dependent on their type of activation. The reprogrammed M1 TAMs suppress the growth of GB cells (Li T. et al., 2017) meanwhile the M2 macrophages are described to favor tumor growth and resistance to therapy (Xue et al., 2017).

A macrophage with pro-tumor function in the tumor microenvironment is a macrophage that enhances tumor initiation and growth. TAMs and tumor cells actively communicate with each other leading to tumor progression. Their communication is mediated by interleukins IL-6 and IL-10 and transforming growth factor-β1 (TGF-β1) (Wagner et al., 1999; Ye et al., 2012). These cytokines activate signaling pathways in the tumor cells that boost processes such as proliferation, invasion and vascularization (**Figure 1**). TGF-β1 secretion by TAMs is responsible for the recruitment of cancer stem-like cells (CSCs) expressing CD133. Another consequence of TGF-β1 secretion is the production of metalloproteinase 9 (MMP-9) by CSCs rendering them highly invasive (Ye et al., 2012). TAMs are able to secrete pleiotrophin (PTN); CSCs express the PTN receptor PTPRZ1 on their cell surface. Once PTN is recognized by its receptor, it stimulates CSCs maintenance and tumorigenic potential, and therefore promotes GB growth (Shi et al., 2017). PTN- expressing TAMs also express CD163 which is an M2 lineage marker. Wang et al. showed that macrophages support GB invasiveness through the CCL4-CCR5 axis that enhances MMP-9 expression (Wang et al., 2016). Hypoxia was also shown to positively contribute to this mechanism by enhancing CCL4 and CCR5 expression. An increase of TAMs in a mouse model was shown to decrease the survival of the mice associated with a reduction of CD8+ T cells (Chae et al., 2015). On top of that, EGFR activation level correlates with TAM infiltration. Consequently, EGF can induce an upregulation of vascular cell adhesion molecule-1 (VCAM-1) that favors the interaction between TAMs and tumor cells, which in turn promoted tumor cell invasion (Zheng et al., 2013). MerTK (Myeloid-Epithelial-Reproductive Tyrosine Kinase) is a tyrosine kinase expressed by macrophages that suppresses the innate immune response. Its expression was shown to be higher in tumor recurrences. TAMs that express MerTK are also associated with tumor growth and resistance to treatment, making MerTK a potential therapeutic target (Wu et al., 2018). The molecular crosstalk between tumor cells and macrophages appears to be important for tumor growth and malignant progression. Therefore, modulating the exchange between those two cell populations may be therapeutically relevant.

Angiogenesis

GB is a highly hypoxic tumor with prominent necrotic regions due to the rapid proliferation of GB cells. The cell composition of the tumor core is quite different from that of the peritumoral area. The tumor core is more hypoxic, contains more $CD163^+$ TAMs and has a higher expression of VEGF-A (Tamura et al., 2018) (a major factor for vascularization). A downstream effect of hypoxia and necrosis is an increase in vascular proliferation. In the tumor microenvironment, TAMs are located near blood vessels. In mice, endothelial cells produce IL-6 that induces the expression of Arg1 and thus the alternative phenotype in TAMs (Wang et al., 2018). This alternative activation is mediated by the hypoxia-inducible factor-2α (HIF-2α). Wang et al. targeted IL-6 expression in a mouse model and improved the survival of GB-bearing mice. VEGF was shown to be implicated in promoting pro-angiogenic functions of TAMs in a GB rodent model (Turkowski et al., 2018). Gliomas overexpressing VEGF were correlated with an increase in the expression of MHCI and MHCII on macrophages. Endothelial cells and TAMs interaction leads to angiogenesis through the expression of TGF-β1 and integrin αvβ3, which induces the activation of the SRC-PI3K-YAP signaling (Cui et al., 2018) (**Figure 1**). The pro-angiogenic properties of TAMs are mediated by the protein CRCR1. This protein activates the PDGFB–PDGFRβ pathways and promotes pericytes recruitment, migration, and tumor angiogenesis (Zhu C. et al., 2017). In sum, TAMs have a proangiogenic function in GB. Thus, targeting macrophages may improve the response to anti-angiogenic therapies (Deng et al., 2017; Gagner et al., 2017). Indeed, blocking the macrophages recruitment by combining the chemokine SDF-1 and VEGF inhibitors was more effective and decreased tumor invasiveness and vascular density.

Immune Environment

Each tumor is characterized by an immune suppressive environment that forms one hallmark of cancer (Hanahan et al., 2011). This is in part due to the presence of TAMs in tumors but also to a complex regulation of the expression of immune and inflammatory genes by the global tumor ecosystem. It was found that IKKβ levels were reduced in GB; consequently, the NF-κB expression was decreased leading to defective immune and inflammatory gene expression in macrophages (Mieczkowski et al., 2015). NF-κB signaling is required for macrophage polarization and immune suppression in GB, making NF-κB a suitable target to improve overall survival in

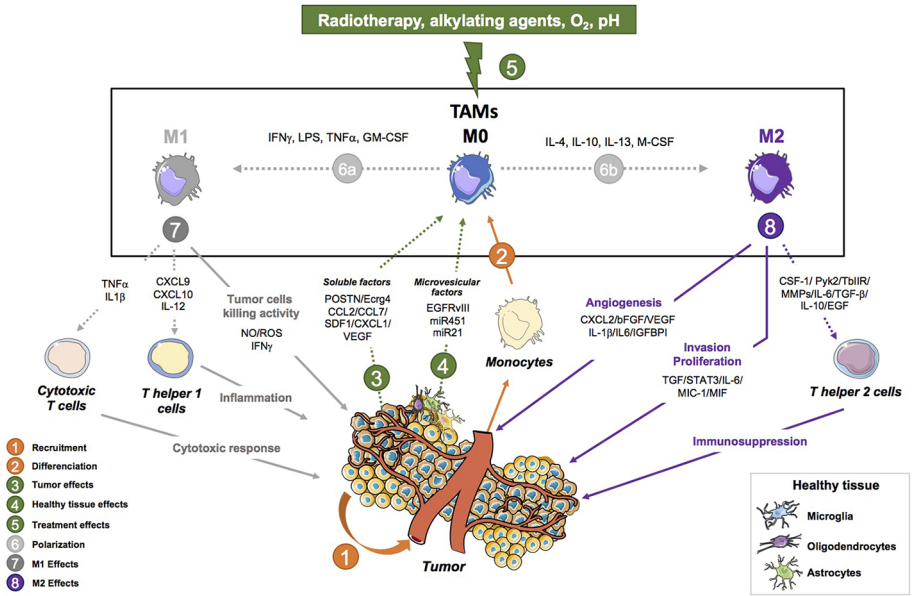

FIGURE 1 | Tumor-associated macrophage activities in glioblastoma progression. This figure shows the pro-tumoral (angiogenesis, invasion, proliferation and immunosuppressive properties) and anti-tumor (Tumor cell killing, Th1 response and anti-tumor activity) activities of tumor-associated macrophages (TAMs) in brain tumors. (1) Monocytes are recruited to the tumor where they differentiate into macrophages. The tumor is involved in their programming as it sends different signals to induce a specific phenotype in favor of the tumor. (2) TAMs that are recruited can either polarize into a continuum of macrophage states that are described with two extremes: an M1 (2a) or an M2 (2b) phenotype depending on the signal they receive (IFNγ/LPS/GM-CSF for M1 and IL-4/IL-13/M-CSF for M2) Pyonteck et al., 2013; Kast et al., 2017; Roesch et al., 2018. (3) M1-like TAMs are macrophages with anti-tumor properties such as tumor cell kill abilities mediated by the production of NO, ROS, IFNγ Kennedy et al., 2013; Leblond et al., 2017. They also mediate the Th1 response in the tumor through the activation of Th helper cells by secreting CXCL9, CXCL10, IL-12 Poon et al., 2017. Finally, they also display an anti-tumor activity by activating cytotoxic T cells *via* TNFα and IL1β. (4) M2-like TAMs have pro tumoral properties such as enhancing the invasive and proliferative ability of GB cells by secreting CSF-1, MMPs, Pyk2, TGFβIIR, TGFβ, IL-6, IL-10, and EGF. They can also mediate the immunosuppressive environment through the expression of IL-6, MIC-1, MIF, STAT3, and TGFβ. Finally, TAMs also regulate angiogenesis through the following factors: IL-6, MIC-1, MIF, STAT3, and TGFβ. (5) The tumor controls the polarization of TAMs through the production of soluble factors (CCL2/CCL7/SDF-1/CX3CL1/VEGF/POSTN/Ecrg4) Feng et al., 2015; Hambardzumyan et al., 2015; Lee et al., 2015; Zhou et al., 2015; Chang et al., 2016; Chen and Hambardzumyan, 2018; Turkowski et al., 2018 and microvesicle factors (EGFRvIII, miR451, miR21) Van Der Vos et al., 2016; Manda et al., 2018. (6) The tumor is also able to send signals to recruit new peripherical macrophages. (7) Environmental cues including radiotherapy, chemotherapy, O_2 level, pH are involved in the programing and functions of macrophages Hardee et al., 2012. (8) Healthy brain cells and TAMs probably interact and are involved in the programming of TAMs. Their interaction has yet to be studied. CCL2, C-C motif chemokine ligand 2; CCL7, C-C motif chemokine ligand 7; CSF-1, colony stimulating factor 1; CXCL2, C-X3-C motif chemokine ligand 2; CX3CL1, C-X3- C motif chemokine ligand 1; Ecrg4, esophageal cancer-related gene 4; EGF, endothelial growth fact; IGFBP1, insulin-like growth factor-binding protein 1; IL-1β, interleukin-1 beta; IL-10, interleukin-10; IL-6, interleukin-6; MIC-1, macrophage inhibitory cytokine 1; MIF, macrophage migration inhibitory factor; MMPs, matrix metalloproteinases; POSTN, periostin; Pyk2, proline rich tyrosine kinase 2; SDF-1, stromal cell-derived factor 1; STAT3, signal transducer and activator of transcription3; TGF-β, transforming growth factor-beta; TGFβIIR, TGF-beta type II receptor; VEGF, vascular endothelial growth factor; βFGF, basic fibroblast growth factor.

GB (Achyut et al., 2017). TAMs strongly inhibit the proliferation of antitumor T cells in the tumor microenvironment (Kumar et al., 2017). It was shown that an inhibition of transcription factors such as NF-κB, a mediator of M2 macrophages polarization, led to slower tumor growth and prolonged survival in a mouse model. It also decreased T cell induction which made the tumor less immunosuppressive (Barberi et al., 2018). Targeting NF-κB may improve the effectiveness of the current standard therapies.

TAMs express IL-4Rα that promotes immunosuppression. In mice, they also express Arg1 that is critical for T cell inhibition (Kohanbash et al., 2013). Chemokine ligand 22 (CCL22) is produced by TAMs and its expression is associated with a low survival rate and $CD4^+$ T cell activation (Zhou et al., 2015). One of the key regulators of the immunosuppressive environment in GB is fibrinogen-like protein 2 (FGL2). Its expression was correlated with a higher number of $CD4^+$ T cells and M2 macrophages (Latha et al., 2018). The colony stimulating factor receptor (CSF1R) is required for the recruitment of TAMs in the tumor microenvironment. It is also involved in promoting the polarization of macrophages toward the M2 phenotype. Inhibition of CSF1R attenuates the recruitment of TAMs and also increases the $CD8^+$ T cell infiltration (Strachan et al., 2013) (**Figure 1**). Another regulator of the immune microenvironment is the receptor tyrosine kinase AXL that is expressed in TAMs (Sadahiro et al., 2018). Its inhibition in a GB mouse model was

associated with prolonged survival. Furthermore, myeloid derived suppressor cells (MDSC) such as TAMs have been described to be activated by GB CSCs through MIF expression, having then an immunosuppressive activity on $CD8^+$ T cells, notably through the Arg1 expression in mice models (Flavahan et al., 2016). Overall, targeting TAMs may disturb the immunosuppressive environment of the tumor, allowing the immune cells to function more effectively.

Loco-Regional Cues for Metabolic Reprogramming

A peculiarity of GB is that it affects the seat of our consciousness, the CNS, whose immune status remains privileged due notably to the presence of the blood-brain barrier (BBB) and of unique resident cells (microglia, astrocytes, endothelial cells) (cf. **Box 1**). Although a precise control of the inflammatory or immune infiltrate is realized, the physiological and anatomical characteristics of the CNS is fed by the field of new recent knowledge, such as the identification of direct vascular channels connecting skull bone marrow to the brain surface enabling myeloid cell migration (Herisson et al., 2018), and make evolve our representation of its immune status. It should be stressed, however, that depending on the therapeutic strategy envisaged, the drug used can have a distinct impact when used according to a peripheral or loco-regional mode of administration (cf. **Tables 1**–**3**). Hence, if TAMs influence immune and adaptive signaling, reciprocally, loco-regional metabolic signals produced in tumor environments (glucose, glutamine, cystéine, lactate, IDO, adenosine, itaconic acid, acidic pH) impacted the polarization fate and immunosuppressive functions of TAMs, thus possibly resulting in immune tolerance and treatment resistance in GB (for review, see Won et al., 2019). Hence, tolerance can be reversed at both the promoters and enhancers of tolerized genes involved in metabolism and lipid biosynthesis, leading to transcriptional programs that rewired the intracellular signaling of innate immune cells thus increasing the capability of macrophages to respond to stimulation (for review see, Locati et al., 2020). In line with this, it has been observed that inhibition of fatty acid synthase (FAS), which catalyzes the synthesis of long-chain fatty acids, prevents the pro-inflammatory response in macrophages (Carroll et al., 2018). Interestingly, using metabolic profiling, it was found that exposure to β-amyloid triggers acute reactive microglial inflammation accompanied by metabolic reprogramming from oxidative phosphorylation to glycolysis while metabolic boosting with recombinant interferon-γ treatment reversed the defective glycolytic metabolism and inflammatory functions of microglia (Baik et al., 2019). Such microglial metabolic switch may also have a strong impact on GB development.

TAMs and Therapeutics

TAMs and Surgical Resection

Surgical resection is the current standard treatment for GB. However, limited data on the biological consequences of surgical resection have been published so far. It was reported that surgical resection increases proliferation and angiogenesis (Kong et al., 2010). After surgical resection, TAMs were shown to express higher levels of CD163, a M2 macrophage marker, and their localization was close to the site of recurrence (Zhu H. et al., 2017). Both TAMs and oligodendrocyte progenitor cells are localized near the tumor periphery. They enhance the stemness and chemo-radioresistance in GB cells (Hide et al., 2018). It was shown that tumor phenotypes associated with telomerase overexpression and TAMs infiltration were more complicated to resect, probably due to improvement of GB cell migratory capabilities (Hung et al., 2016). The inability to surgically remove the whole tumor contributes to the poor prognosis and recurrence of GB.

TAMs and Radiotherapy

Macrophages inside the tumor mass are involved in multiple phenomena that include radiation resistance. Radiation therapy itself induces changes in the tumor microenvironment and renders the tumor more aggressive. In fact, recurrence mostly appears near the irradiated area (Gupta and Burns, 2018). Radiotherapy induces a rapid inflammatory response leading to TAMs recruitment. This inflammatory response is correlated with a short survival time (Tabatabaei et al., 2017). TAMs participate in the induction of GB cell differentiation to a mesenchymal state through NF-κB production, an event that correlated with radiation resistance (Bhat et al., 2013). Recently, Leblond et al. showed that M1 macrophages are more sensitive to radiation than M2 macrophages (Leblond et al., 2017). The proportion of M2 macrophages in irradiated tissues is thus increased. Moreover, M2 macrophages were described to contribute to relapses in oral cancer by promoting vascularization after radiation treatment (Okubo

BOX 1 | Non-cancerous brain cells alter macrophages polarization and functions.

Tumor cells cooperate with its surroundings such as the tumor microenvironment. The brain is also the home of specific cell types with their own characteristics and functions; although those cells are not part of the tumor, they can also interact with it. The interaction between cells residing in the brain and TAMs are very poorly understood in cancer but has been studied in depth in other pathologies, which will be quickly reviewed in this box. Both neurons and astrocytes can produce CX3CL1R, the receptor for CX3CL1 found on microglia Matias et al., 2018. CX3CL1 promotes TAM recruitment and increases the expression of MMPs and thus invasive properties. When an ischaemic stroke happens, ischaemic neurons are able to prime microglia toward an M1 phenotype during an injury Hu et al., 2012. Another cell type is oligodendrocyte which accounts for the formation of the myelin sheath in the CNS. It was found that macrophages and oligodendrocyte progenitor cells colocalized near the tumor border. At this site of colocalization, those cells induced stemness and resistance to therapy in GB cells Hide et al., 2018. In the peripheral nervous system, Schwann cells are the cells responsible for myelin sheath formation. Schwann cells were shown to promote cancer invasion by direct contact with tumor cells Deborde et al., 2016. The mechanism involved in this process remains unclear. In neurofibromas (peripheral nerve sheath tumors due to NF1 loss in Schwann cells), macrophages were shown to be abundant Stratton et al., 2018. In this case, Schwann cells and macrophages communicate with each other and are involved in the regulation of inflammatory gene expression. As Schwann cells and oligodendrocytes share a common function in normal tissue, it may be interesting to further study the involvement of oligodendrocytes in GB. Non-cancerous cells of the CNS and peripheral nervous system interact with macrophages and lead them to polarize toward a specific phenotype.

TABLE 1 | Clinical trials targeting the recruitment of macrophages.

Target	Drugs	Inhibitor type	Clinical trial	Tumor type	Benefit
CCL2-CCR2 axis	Carlumab	mAb	NCT00992186 (2009) (completed, has results)	Metastatic Castrate-Resistant Prostate Cancer	Information about the disease's progression
			NCT01204996 (2010) (Completed)	Solid Tumors	
			NCT00537368 (2007) (Completed)	Solid Tumors	
	PF-04136309	Small molecule	NCT02732938 (2016) (Terminated)	Metastatic Pancreatic Cancer	Unknown
	MLN1202	mAb	NCT01015560 (2009) (Completed with results)	Bone Metastases	Well tolerated
	CCX872-B	Small molecule	NCT03778879 (2018) (Not yet recruiting)	Pancreatic Adenocarcinoma	Unknown
	BMS-813160	Small molecule	NCT03496662 (2018) (Recruiting)	Pancreatic Ductal Adenocarcinoma (PDAC)	Unknown
CD47	Hu5F9-G4	mAb	NCT02953509 (2016) (Recruiting)	B-cell Non-Hodgkin's Lymphoma	Unknown
			NCT03248479 (2017) (Recruiting)	Haematological Malignancies	
			NCT02216409 (2014) (Active, not recruiting)	Haematological Malignancies	
			NCT02678338 (2016) (Recruiting)	Haematological Malignancies	
			NCT02953782 (2016) (Recruiting)	Colorectal Cancer	
	TTI-621	Small molecule	NCT03530683 (2018) (Recruiting)	Refractory Lymphoma, Myeloma	Unknown
			NCT02663518 (2016) (Recruiting)	Hematologic Malignancies and Selected Solid Tumors	
	ALX148	Small molecule	NCT03013218 (2017) (Recruiting)	Solid Tumors and Lymphoma	Unknown
	SRF231	mAb	NCT03512340 (2018) (Recruiting)	Solid and Hematologic Cancers	Unknown
	CC-90002	mAb	NCT02367196 (2015) (Recruiting)	Solid and Hematologic Cancers	Unknown
	IBI188	mAb	NCT03763149 (2018) (Not yet recruiting)	Malignant Tumors and Lymphomas Advanced Malignancies	Unknown
			NCT03717103 (2018) (Recruiting)		

et al., 2016). In a radioresistant GB model, the total RNA was sequenced and it was found that there was a positive regulation of macrophage chemotaxis following radiation (Doan et al., 2018). Also, in a murine glioma model, an increase in SDF-1α at the tumor invasion front after radiotherapy was correlated with the recruitment of TAMs and radioresistance (Wang et al., 2013). Irradiation of the tumor leads to the alteration of multiple pathways. In particular, it modifies the macrophage activation type, rendering them more supportive of tumor growth.

TAMs and Chemotherapy

The standard treatment of GB affects the molecular profiles of the tumor. Temozolomide (TMZ) is commonly used to treat GB. TAMs that express CD74 were described to be involved in TMZ resistance by inducing AKT and Erk1/2 activation in tumor cells (Kitange et al., 2010). Gene expression profiling showed that the tumor that recurred after treatment did not match the primary treatment-naïve tumor. After treatment, the polarization toward the M2 phenotype was upregulated (Hudson et al., 2018). Tumor protein 53 (p53) is involved in promoting the development of the tumor. GB with the p53 isoform Δ133p53β had increased $CD163^+$ macrophages (Kazantseva et al., 2018). Moreover, Δ133p53β supports cancer stemness (Arsic et al., 2015). In addition, it is correlated with resistance to TMZ (Kazantseva et al., 2018). GB is able to evade the toxic effects of chemotherapy, but it can equally evade the action of the immune system. Hence, a cocktail of multiple drugs targeting different pathways may provide the most effective therapy for GB and improve overall survival.

CURRENT THERAPIES TARGETING TUMOR-ASSOCIATED MACROPHAGES IN CANCER

Targeting the Recruitment of TAMs

One strategy to target TAMs is to block their recruitment to the tumor site. It can be achieved by targeting the chemokine ligand 2 (CCL2) - chemokine receptor 2 (CCR2) axis. CCL2 is an inflammatory chemokine that can recruit macrophages and Treg lymphocytes leading to an immunosuppressive environment (Chang et al., 2016). To achieve this, a human IgG1k mAb called Carlumab was developed. A survey of clinical trials involving the CCL2-CCR2 axis is provided in **Table 1**.

A phase 2 study showed that this antibody was well-tolerated. However, it did not block the CCL2-CCR2 axis or have any antitumor activity as a single agent in metastatic prostate cancer (Pienta et al., 2013) (NCT00992186). When Carlumab was combined with four other chemotherapies, the treatment was still well tolerated but the suppression of CCL2-CCR2 axis remained elusive (Brana et al., 2015) (NCT01204996). In other studies, Carlumab was shown to transiently suppress CCL2 and had a preliminary antitumor activity (Sandhu et al., 2013) (NCT00537368, 2007). PF-04136309 combined with

TABLE 2 | Clinical trials with toll-like receptor (TLR) agonists for macrophages reprogramming.

Target	Drugs	Inhibitor type	Clinical trial	Tumor type	Benefit
CD40	APX005M	mAb	NCT03502330 (2018) (Recruiting) NCT02482168 (2015) (Active, not recruiting) NCT03123783 (2017) (Recruiting) NCT03389802 (2018) (Recruiting) NCT03165994 (2017) (Recruiting)	Non-small Cell Lung Cancer, Renal Cell Carcinoma Solid tumors Non-small Cell Lung Cancer or Metastatic Melanoma Pediatric CNS Tumors Resectable Esophageal and Gastroesophageal Junction Cancers	Unknown
	Selicrelumab	mAb	NCT02304393 (2014) (Recruiting)	Locally Advanced and/or Metastatic Solid Tumors	Unknown
	ChiLob 7/4	mAb	NCT01561911 (2012) (Completed)	Non-Hodgkin Lymphoma	Unknown
	CP-870,893	mAb	NCT00607048 (Completed)	Non-Hodgkin Lymphoma	Unknown
	CDX-1140	Small molecule	NCT03329950 (Recruiting)	Advanced Malignancies	Unknown
TLR7	LHC165	Small molecule	NCT03301896 (2017) (Recruiting)	Advanced Malignancies	Unknown
	Imiquimod	Small molecule	NCT01421017 (2011) (Completed) NCT00899574 (2009) (Completed with results)	Breast Cancer With Skin Metastases Chest Wall Recurrence or Skin Metastases	Well tolerated. Partial response: tumor regression and immune response
	NKTR-262	Small molecule	NCT03435640 (2018) (Recruiting)	Locally Advanced or Metastatic Solid Tumor Malignancies	Unknown
	IMO-8400	Small molecule	NCT02252146, (Completed with results)	Diffuse Large B Cell Lymphoma (DLBCL)	Lack of efficacy
	Resiquimod	Small molecule	NCT00821652 (2009) (Completed)	Surgically resected Stage IIB, IIC, Stage III or Stage IV (AJCC criteria) Melanoma	Unknown
	DSP-0509	Small molecule	NCT03416335 (2018) (Recruiting)	Advanced Solid Tumors	Unknown
TLR8	VTX-2337	Small molecule	NCT02431559 (2015) (Completed) NCT01294293, (Completed) NCT01334177, (Completed) NCT02452697 (2015) (Recruiting)	Platinum-Resistant Ovarian Cancer Ovarian Epithelial, Fallopian Tube, or Peritoneal Cavity Cancer Ovarian Epithelial, Fallopian Tube, or Peritoneal Cavity Cancer Myeloid and Lymphoid Malignancies	Unknown
TLR9	EMD 1201081	Small molecule	NCT01040832 (2009) (Completed with results)	Recurrent or Metastatic Squamous Cell Carcinoma of the Head and Neck	EMD 1201081 was well tolerated in combination with cetuximab, but no clinical efficacy was observed Ruzsa et al., 2014
	DUK-CPG-001	Small molecule	NCT02452697 (2015) (Recruiting)	Myeloid and Lymphoid Malignancies	Unknown
	IMO-2055	Small molecule	NCT00719199 (2008) (Completed) NCT00633529 (2008) (Completed)	Colorectal Cancer NSCLC	Unknown
	CMP-001	Small molecule	NCT03618641 (2018) (Recruiting) NCT03507699 (2018) (Recruiting)	Stage IIIB/C/D Melanoma Patients With Clinically Apparent Lymph Node Disease Metastatic Colorectal Cancer	Unknown
	SD-101	Small molecule	NCT03007732 (2017) (Recruiting) NCT03410901 (Recruiting) NCT02927964 (2016) (Recruiting) NCT02254772 (2014) (Completed with results)	Hormone-Naïve Oligometastatic Prostate Cancer Low-Grade B-Cell Non-Hodgkin Lymphoma Refractory Grade 1-3A Follicular Lymphoma Recurrent Low-Grade B-Cell Lymphoma	Well tolerated but progression of the tumor was observed

chemotherapy was also shown to be well-tolerated and led to a tumor response (Nywening et al., 2016).

Reprogramming of TAMs Toward an Antitumoral Phenotype

As mentioned previously, TAMs can exist in different functional states between the M1 and M2 phenotypes, making them highly heterogeneous and plastic cells (Biswas and Mantovani, 2010). Thus, they can be either pro- or anti-tumoral (Wynn et al., 2013). Reprogramming the TAMs toward a tumoricidal or a tumor-inhibition state may be a plausible therapeutic strategy. Different strategies are being studied in the clinic. These are reported in **Table 2** (please refer also to **Box 2**).

Inhibition of CD47

Inhibition of CD47 is a strategy that can facilitate phagocytosis of tumor cells by macrophages. Indeed, CD47 expressed by cancer cells inhibits phagocytosis through its interaction with signal

TABLE 3 | Clinical trials using drugs to deplete macrophages from the tumor's microenvironment.

Target	Drugs	Inhibitor type	Clinical trial		Benefit
CSF1R	Pexidartinib	Small molecule	NCT02777710 (2016) (Recruiting)	Metastatic/Advanced Pancreatic or Colorectal Cancers	Unknown
	DCC-3014	Small molecule	NCT03069469 (2017) (Recruiting)	Advanced Malignancies	Unknown
	LY3022855	mAb	NCT03153410 (2017) (Recruiting)	Pancreas Adenocarcinoma	Unknown
			NCT02718911 (2016) (Completed)	Advanced Solid Tumors	
				Melanoma	
			NCT03101254 (2017) (Recruiting)		
	PLX3397	Small molecule	NCT01004861 (2009) (Completed)	Solid Tumors	Unknown
				Melanoma and Other Solid Tumors	
			NCT02452424 (2015) (Completed)	Recurrent Glioblastoma	
				Pigmented Villonodular Synovitis (PVNS) or Giant Cell	
			NCT01349036 (2011) (Completed)	Tumor of the Tendon Sheath (GCT-TS)	
			NCT02371369 (2015) (Active, not recruiting)		
	MCS110	Small molecule	NCT03694977 (2018) (Not yet recruiting)	Gastric Cancer	Unknown
	IMC-CS4	Small molecule	NCT01346358 (2011) (Completed)	Advanced Solid Tumors	Unknown
	Cabiralizumab	mAb	NCT03697564 (2018) (Not yet recruiting)	Stage IV Pancreatic Cancer	Unknown
			NCT02526017 (2015) (Active, not recruiting)		
	SNDX-6352	mAb	NCT03238027 (2017) (Recruiting)	Solid Tumors	Unknown
	JNJ-40346527	Small molecule	NCT03557970 (2018) (Not yet recruiting)	Acute Myeloid Leukemia	Unknown
	ARRY-382	Small molecule	NCT02880371, (Recruiting)	Acute Myeloid Leukemia	Unknown
			NCT01316822 (2011) (Completed)	Advanced or Metastatic Cancers	
	BLZ945	Small molecule	NCT02829723 (2016) (Recruiting)	Advanced Solid Tumors	Unknown
	RO5509554	Small molecule	NCT01494688 (2011) (Completed)	Advanced Solid Tumors	Unknown
NA	Clodronate	Bisphosphonate	NCT01198457 (2010) (Completed)	Breast Neoplasms, Prostatic Neoplasms, Multiple Myeloma	Treatment with clodronate suggests a benefit in recurrence rates for postmenopausal women with breast cancer Paterson et al., 2012
			NCT00009945 (2010) (2003) (Completed with results)	Stage I or Stage II Breast Cancer	
				Bone neoplasms	
			NCT00909142 (2009) (Completed)	Hormone Refractory Metastatic Prostate Cancer	
				Primary Breast Cancer	
			NCT00003232 (2004) (Completed)		
			NCT00127205 (2005) (Active, not recruiting)		
	Zoledronate	Bisphosphonate	NCT00301873 (2006) (Completed, has results)	Primary Malignant Glioma	
			NCT00885326 (2009) (Active, not recruiting)	High-Risk Neuroblastoma	
			NCT01345019 (2011), (Active, not recruiting)	Multiple Myeloma	

regulatory protein-α (SIRPα) expressed by macrophages thus sending out a "do not eat me" signal. Alternatively, CD47 can serve as a receptor for thrombospondin 1 (TSP1) to trigger specific signaling. Many tumors are described to overexpress CD47 (Zhang et al., 2015; Zhao et al., 2016). Inhibition of CD47 in a preclinical model showed a modification of microglia phenotypes in GB that was correlated with better survival (Hutter et al., 2019). Furthermore, *in vivo,* the anti-CD47 treatment is able to shift the macrophage phenotype toward an M1 type (Zhang et al., 2016) and induces anti-tumor effects (Li F. et al., 2017). The preclinical study of Hu5F9-G4 in pediatric malignant primary brain model demonstrated that this CD47 inhibitor is a safe and effective therapeutic agent (Gholamin et al., 2017). Hu5F9-G4 was also shown to be well tolerated in a clinical trial (Sikic et al., 2018) (NCT02216409, **Table 2**). TTI-621, a small molecule inhibiting CD47, is being investigated in an ongoing clinical trial. Interestingly, however, it has recently been observed that CD47 inhibition may result in cancer cell resistance to chemotherapy through escape to senescence (Guillon et al., 2019).

Activation of CD40

CD40 is expressed on monocytes, macrophages, dendritic cells, and B cells. It is a receptor that belongs to the TNF receptor superfamily. Many clinical trials targeting CD40 notably through agonistic or activating antibodies are ongoing (**Table 3**). In a mouse model, targeting CD40 was useful in producing antitumor effects that greatly improved the overall survival (Shoji et al.,

BOX 2 | The content of exosomes as a therapeutic target to control TAMs phenotype.

Exosomes are microvesicles (30-120μm) that are secreted through exocytosis by various cells. They exert a variety of biological effects. GB cells can secrete exosomes that carry proteins such as EGFR variant III (EGFRvIII) Manda et al., 2018. The content of exosomes was shown to be different depending on partial pressure in O_2 as cancer cells can adapt to their surroundings Zhang et al., 2017. Exosomes can mediate immunosuppressive properties in GB through their internalization in monocytes. Once they are internalized, they cause a rearrangement of the monocyte cytoskeleton and induce an M2 phenotype Gabrusiewicz et al., 2018. Vos et al. visualized the effect of GB-derived exosomes on TAMs and observed a shift of their cytokine profile to an immune-suppressive profile Van Der Vos et al., 2016. They also observed an elevation of miR-21 expression in TAMs associated with a decrease in c-Myc mRNA levels. GB-derived exosomes were shown to modify the expression of cell surface proteins and cytokines (IL-6 and VEGF), and to increase phagocytic activity in macrophages De Vrij et al., 2015. Also, blood samples from patients with GB were analyzed and shown to harbor GB-derived exosomes containing immunoglobulin (Ig) G2 and IgG4 antibody isotypes Harshyne et al., 2016. Those exosomes were able to induce the expression of CD163, associated with the M2 phenotype. Exosomes appear to be important for the communication between tumor cells and TAMs in GB. As key players from the tumor ecosystem, targeting them may impair the regulatory effects of GB cells on TAM immunosuppressive properties.

2016). Targeting CD40 modulated the immune cell number and led to an antitumor response (Vonderheide et al., 2013; Nowak et al., 2015). In a mouse model, the combination of CSF1R inhibition and CD40 activation induced the reprogramming of TAMs (Hoves et al., 2018), thus allowing the protective response of T cells (Perry et al., 2018).

TLR Agonist

Toll-like receptors (TLRs) are normally activated by microbial moieties (including nucleic acids) allowing macrophages to acquire a M1 phenotype. Using a TLR agonist to reprogram macrophages was thus of interest in cancer treatment (Feng et al., 2019). Numerous TLR7 ligands, TLR9 ligands, and one TLR8 ligand have been tested for their antitumoral properties in clinical trials (**Table 2**). For example, the TLR7 agonist Imiquimod has been tested. It was well tolerated and associated to tumor regression and increased lymphocytic infiltrate (Adams et al., 2013) (NCT00899574). The TLR7 agonist 852A was also well tolerated with reversible side effects (Dudek et al., 2007). IMO-2055, a TLR9 agonist, demonstrated a possible antitumor activity when combined with erlotinib and bevacizumab (Smith et al., 2014) (NCT00633529).

Depletion of TAMs

The activation of TAMs is dependent on the CSF1R signaling pathway. Therefore, CSF1R may be a way to target macrophages specifically. Many small molecules and antibodies were developed against CSF1R, and numerous clinical trials have been completed or are ongoing (**Table 3**). PLX3397 is a small molecule targeting CSF1R, it reduced the number of TAMs in a preclinical GB model and showed an antitumor activity (Coniglio and Segall, 2013; Yan et al., 2017). In clinical studies, PLX3397 was also well tolerated and showed anti-tumor responses after treatment (Tap et al., 2015) (NCT01004861). PLX3397 was also well tolerated but showed no efficacy in GB (Butowski et al., 2016) (NCT01349036). BLZ945, another small molecule inhibitor of CSF1R, can alter the polarization of TAMs in glioma (Pyonteck et al., 2013). It is currently being assessed in a clinical trial.

Another way to deplete the number of TAMs in the tumor is to use bisphosphonates. They are described for both direct and indirect anti-tumor effects such as induction of tumor apoptosis and inhibition of cell adhesion. More importantly, they alter the behavior of TAMs (Van Acker et al., 2016). Bisphosphonates are divided in two classes depending on their structure and mechanism of action. Clodronate belongs to the first group while zoledronate belongs to the second group. Both zoledronate and clodronate are still being assessed in clinical trials (**Table 3**).

CONCLUSION

In GB microenvironment, both resident and peripheral macrophages are present and there is an urgent need to understand their specific roles in tumor progression and resistance to treatment. It is obvious that macrophages may be a useful target to improve the outcome of cancer. Currently, many drugs targeting macrophages are being tested in the clinic. However, only a few are tested specifically in GB. The immune landscape in GB, and in cancer in general, has to be investigated further as there is a lack of efficacy in the clinic when only TAMs are targeted. The targeting of TAMs must be implemented hand in hand with the standard treatment to potentially improve the overall effect. In summary, TAMs seem to be a promising target to overcome resistance that arises in GB.

AUTHOR CONTRIBUTIONS

HG, LR and EG wrote the manuscript. FH and EG contributed to the conception and design of the work. HG, LR, AR, MC, YD, PJ, FH, and EG contributed to manuscript amendments and revisions. All authors read and approved the submitted version.

FUNDING

This work was supported by the French national research agency (ANR) through the LabEx IRON << *Innovative Radiopharmaceuticals in Oncology and Neurology*>> as part of the French government "Investissements d'Avenir" program (ANR-11-LABX-0018). It was also supported by the ANR under the frame of EuroNanoMed III (project GLIOSILK). The work was additionally funded by the "Institut National de la Santé et de la Recherche Médicale" (INSERM) and by the University of Angers (Angers, France). It was also related to: (i) the PL-BIO 2014-2020 INCa (Institut National du Cancer) consortium MARENGO <<*; MicroRNA agonist and antagonist Nanomedicines for*

GliOblastoma treatment: from molecular programmation to preclinical validation>>, (ii) to the MuMoFRaT project << *Multi-scale Modeling & simulation of the response to hypo-Fractionated Radiotherapy or repeated molecular radiation Therapies*>> supported by "La Région Pays-de-la-Loire" and by the Cancéropôle Grand-Ouest (Vectorization, imaging and radiotherapies network), (iii) the LabEX IGO and the ANR through the investment of the future program ANR-11-LABX-0016-01, (iv) the SIRIC ILIAD program supported by INCa, and (v) the Ministry of Health and the Institute for Health and Medical Research (Inserm) (contract INCa-DGOS-Inserm_12558). HG and LR were PhD fellows funded by the LabEx IRON and by the LabEx IRON-2 and the University of Angers, respectively.

REFERENCES

Achyut, B. R., Angara, K., Jain, M., Borin, T. F., Rashid, M. H., Iskander, A. S. M., et al. (2017). Canonical NFκB signaling in myeloid cells is required for the glioblastoma growth. *Sci. Rep.* 7, 1–12. doi: 10.1038/s41598-017-14079-4

Adams, S., Kozhaya, L., Martiniuk, F., Meng, T., Chiriboga, L., Liebes, L., et al. (2013). Rejection of Skin Metastases in Patients With Breast Cancer. *Clin. Cancer Res.* 18, 6748–6757. doi: 10.1158/1078-0432.CCR-12-1149

Arsic, N., Gadea, G., Lagerqvist, E. L., Busson, M., Cahuzac, N., Brock, C., et al. (2015). The p53 isoform Δ133p53β promotes cancer stem cell potential. *Stem Cell Rep.* 4, 531–540. doi: 10.1016/j.stemcr.2015.02.001

Atri, C., Guerfali, F. Z., and Laouini, D. (2018). Role of Human Macrophage Polarization in Inflammation during Infectious Diseases. *Int. J. Mol. Sci.* 19, 1801. doi: 10.3390/ijms19061801

Badie, B., Schartner, J., Vorpahl, J., and Preston, K. (2000). Interferon-γ Induces Apoptosis and Augments the Expression of Fas and Fas Ligand by Microglia in Vitro. *Exp. Neurol.* 162, 290–296. doi: 10.1006/exnr.1999.7345

Baik, S. H., Kang, S., Lee, W., Choi, H., Chung, S., Kim, J., et al. (2019). A Breakdown in Metabolic Reprogramming Causes Microglia Dysfunction in Alzheimer's Disease. *Cell Metab*. doi: 10.1016/j.cmet.2019.06.005

Barberi, T., Martin, A., Suresh, R., Barakat, D. J., Harris-Bookman, S., Drake, C. G., et al. (2018). Absence of host NF-κB p50 induces murine glioblastoma tumor regression, increases survival, and decreases T-cell induction of tumor-associated macrophage M2 polarization. *Cancer Immunol. Immunother.* 67, 1491–1503. doi: 10.1007/s00262-018-2184-2

Bhat, K. P. L., Balasubramaniyan, V., Vaillant, B., Ezhilarasan, R., Hummelink, K., Hollingsworth, F., et al. (2013). Mesenchymal Differentiation Mediated by NF-κB Promotes Radiation Resistance in Glioblastoma. *Cancer Cell* 24, 331–346. doi: 10.1016/j.ccr.2013.08.001

Biswas, S. K., and Mantovani, A. (2010). Macrophage plasticity and interaction with lymphocyte subsets: Cancer as a paradigm. *Nat. Immunol.* 11, 889–896. doi: 10.1038/ni.1937

Brana, I., Calles, A., LoRusso, P. M., Yee, L. K., Puchalski, T. A., Seetharam, S., et al. (2015). Carlumab, an anti-C-C chemokine ligand 2 monoclonal antibody, in combination with four chemotherapy regimens for the treatment of patients with solid tumors: an open-label, multicenter phase 1b study. *Targeting Oncol.* 10, 111–123. doi: 10.1007/s11523-014-0320-2

Brown, N. F., Carter, T. J., Ottaviani, D., and Mulholland, P. (2018). Harnessing the immune system in glioblastoma. *Br. J. Cancer* 119, 1171–1181. doi: 10.1038/s41416-018-0258-8

Bryukhovetskiy, I. S., Dyuizen, I. V., Shevchenko, V. E., Bryukhovetskiy, A. S., Mischenko, P. V., Milkina, E. V., et al. (2016). Hematopoietic stem cells as a tool for the treatment of glioblastoma multiforme. *Mol. Med. Rep.* 14, 4511–4520. doi: 10.3892/mmr.2016.5852

Butowski, N., Colman, H., De Groot, J. F., Omuro, A. M., Nayak, L., Wen, P. Y., et al. (2016). Orally administered colony stimulating factor 1 receptor inhibitor PLX3397 in recurrent glioblastoma: An Ivy Foundation Early Phase Clinical Trials Consortium phase II study. *Neuro. Oncol.* 18, 557–564. doi: 10.1093/neuonc/nov245

Cai, J., Zhang, W., Yang, P., Wang, Y., Li, M., Zhang, C., et al. (2015). Identification of a 6-cytokine prognostic signature in patients with primary glioblastoma harboring M2 microglia/macrophage phenotype relevance. *PloS One* 10, e0126022–e0126022. doi: 10.1371/journal.pone.0126022

Caponegro, M. D., Moffitt, R. A., and Tsirka, S. E. (2018). Expression of neuropilin-1 is linked to glioma associated microglia and macrophages and correlates with unfavorable prognosis in high grade gliomas. *Oncotarget* 9, 35655–35665. doi: 10.18632/oncotarget.26273

Carroll, R. G., Zasłona, Z., Galván-Peña, S., Koppe, E. L., Sévin, D. C., Angiari, S., et al. (2018). An unexpected link between fatty acid synthase and cholesterol synthesis in proinflammatory macrophage activation. *J. Biol. Chem.* doi: 10.1074/jbc.RA118.001921

Chae, M., Peterson, T. E., Balgeman, A., Chen, S., Zhang, L., Renner, D. N., et al. (2015). Increasing glioma-associated monocytes leads to increased intratumoral and systemic myeloid-derived suppressor cells in a murine model. *Neuro. Oncol.* 17, 978–991. doi: 10.1093/neuonc/nou343

Chang, A. L., Miska, J., Wainwright, D. A., Dey, M., Rivetta, C. V., Yu, D., et al. (2016). CCL2 Produced by the Glioma Microenvironment Is Essential for the Recruitment of Regulatory T Cells and Myeloid-Derived Suppressor Cells. *Cancer Res.* 76, 5671–5682. doi: 10.1158/0008-5472.CAN-16-0144

Charles, N. A., Holland, E. C., Gilbertson, R., Glass, R., and Kettenmann, H. (2011). The brain tumor microenvironment. *Glia* 59, 1169–1180. doi: 10.1002/glia.21136

Chen, Z., and Hambardzumyan, D. (2018). Immune Microenvironment in Glioblastoma Subtypes. *Front. Immunol.* 9, 1004. doi: 10.3389/fimmu.2018.01004

Chen, Z., Feng, X., Herting, C. J., Garcia, V. A., Nie, K., Pong, W. W., et al. (2017). Cellular and Molecular Identity of Tumor-Associated Macrophages in Glioblastoma. *Cancer Res.* 77, 2266–2278. doi: 10.1158/0008-5472.CAN-16-2310

Coniglio, S. J., and Segall, J. E. (2013). Review: Molecular mechanism of microglia stimulated glioblastoma invasion. *Matrix Biol.* 32, 372–380. doi: 10.1016/j.matbio.2013.07.008

Cui, X., Morales, R. T. T., Qian, W., Wang, H., Gagner, J. P., Dolgalev, I., et al. (2018). Hacking macrophage-associated immunosuppression for regulating glioblastoma angiogenesis. *Biomaterials* 161, 164–178. doi: 10.1016/j.biomaterials.2018.01.053

De Vrij, J., Niek Maas, S. L., Kwappenberg, K. M. C., Schnoor, R., Kleijn, A., Dekker, L., et al. (2015). Glioblastoma-derived extracellular vesicles modify the phenotype of monocytic cells. *Int. J. Cancer* 137, 1630–1642. doi: 10.1002/ijc.29521

Deborde, S., Hall, A., Wong, R.J., Deborde, S., Omelchenko, T., Lyubchik, A., et al. (2016). Schwann cells induce cancer cell dispersion and invasion Find the latest version : Schwann cells induce cancer cell dispersion and invasion. *J. Clin. Invest.* 126, 1538–1554. doi: 10.1172/JCI82658

Deng, L., Stafford, J. H., Liu, S. C., Chernikova, S. B., Merchant, M., Recht, L., et al. (2017). SDF-1 Blockade Enhances Anti-VEGF Therapy of Glioblastoma and Can Be Monitored by MRI. *Neoplasia (United States)* 19, 1–7. doi: 10.1016/j.neo.2016.11.010

Doan, N. B., Nguyen, H. S., Alhajala, H. S., Jaber, B., Al-Gizawiy, M. M., Ahn, E.-Y. E., et al. (2018). Identification of radiation responsive genes and transcriptome profiling via complete RNA sequencing in a stable radioresistant U87 glioblastoma model. *Oncotarget* 9, 23532–23542. doi: 10.18632/oncotarget.25247

Dudek, A. Z., Yunis, C., Harrison, L. I., Kumar, S., Hawkinson, R., Cooley, S., et al. (2007). First in human phase I trial of 852A, a novel systemic toll-like receptor 7 agonist, to activate innate immune responses in patients with advanced cancer. *Clin. Cancer Res.* 13, 7119–7125. doi: 10.1158/1078-0432.CCR-07-1443

Feng, X., Szulzewsky, F., Yerevanian, A., Chen, Z., Heinzmann, D., Rasmussen, R. D., et al. (2015). Loss of CX3CR1 increases accumulation of inflammatory monocytes and promotes gliomagenesis. *Oncotarget* 6, 15077–15094. doi: 10.18632/oncotarget.3730

Feng, Y., Mu, R., Wang, Z., Xing, P., Zhang, J., Dong, L., et al. (2019). A toll-like receptor agonist mimicking microbial signal to generate tumor-suppressive macrophages. *Nat. Commun.* 10, 2272. doi: 10.1038/s41467-019-10354-2

Finn, O. J. A. (2018). Believer's Overview of Cancer Immunosurveillance and Immunotherapy. *J. Immunol.* 200, 385–391. doi: 10.4049/jimmunol.1701302

Flavahan, W. A., Nakano, I., Rich, J. N., Otvos, B., Silver, D. J., Sinyuk, M., et al. (2016). Cancer Stem Cell-Secreted Macrophage Migration Inhibitory Factor

Stimulates Myeloid Derived Suppressor Cell Function and Facilitates Glioblastoma Immune Evasion. *Stem Cells* 34, 2026–2039. doi: 10.1002/stem.2393

Gabrusiewicz, K., Li, X., Wei, J., Hashimoto, Y., Marisetty, A. L., Ott, M., et al. (2018). Glioblastoma stem cell-derived exosomes induce M2 macrophages and PD-L1 expression on human monocytes. *Oncoimmunology* 7 (e1412909), 1–10. doi: 10.1080/2162402X.2017.1412909

Gagner, J. P., Sarfraz, Y., Ortenzi, V., Alotaibi, F. M., Chiriboga, L. A., Tayyib, A. T., et al. (2017). Multifaceted C-X-C Chemokine Receptor 4 (CXCR4) Inhibition Interferes with Anti–Vascular Endothelial Growth Factor Therapy–Induced Glioma Dissemination. *Am. J. Pathol.* 187, 2080–2094. doi: 10.1016/j.ajpath.2017.04.020

Gholamin, S., Mitra, S. S., Feroze, A. H., Liu, J., Kahn, S. A., Zhang, M., et al. (2017). Disrupting the CD47-SIRPα anti-phagocytic axis by a humanized anti-CD47 antibody is an efficacious treatment for malignant pediatric brain tumors. *Sci. Transl. Med.* 9, 1–14. doi: 10.1126/scitranslmed.aaf2968

Ginhoux, F., and Guilliams, M. (2016). Tissue-Resident Macrophage Ontogeny and Homeostasis. *Immunity* 44, 439–449. doi: 10.1016/j.immuni.2016.02.024

Ginhoux, F., Lim, S., Hoeffel, G., Low, D., and Huber, T. (2013). Origin and differentiation of microglia. *Front. Cell. Neurosci.* 7, 45. doi: 10.3389/fncel.2013.00045

Graeber, M. B., Scheithauer, B. W., and Kreutzberg, G. W. (2002). Microglia in brain tumors. *Glia* 40, 252–259. doi: 10.1002/glia.10147

Guillon, J., Petit, C., Moreau, M., Toutain, B., Henry, C., Roché, H., et al. (2019). Regulation of senescence escape by TSP1 and CD47 following chemotherapy treatment. *Cell Death Dis*. doi: 10.1038/s41419-019-1406-7

Gupta, K., and Burns, T. C. (2018). Radiation-Induced Alterations in the Recurrent Glioblastoma Microenvironment: Therapeutic Implications. *Front. Oncol.* 8, 503. doi: 10.3389/fonc.2018.00503

Hambardzumyan, D., Gutmann, D. H., and Kettenmann, H. (2015). The role of microglia and macrophages in glioma maintenance and progression. *Nat. Neurosci.* 19, 20. doi: 10.1038/nn.4185

Hanahan, D., Weinberg, R. A., Adams, J. M., Cory, S., Aguirre-Ghiso, J. A., Ahmed, Z., et al. (2011). Hallmarks of cancer: the next generation. *Cell* 144, 646–674. doi: 10.1016/j.cell.2011.02.013

Hardee, M. E., Marciscano, A. E., Medina-Ramirez, C. M., Zagzag, D., Narayana, A., Lonning, S. M., et al. (2012). Resistance of glioblastoma-initiating cells to radiation mediated by the tumor microenvironment can be abolished by inhibiting transforming growth factor-β. *Cancer Res.* 72, 4119–4129. doi: 10.1158/0008-5472.CAN-12-0546

Harshyne, L. A., Nasca, B. J., Kenyon, L. C., Andrews, D. W., and Hooper, D. C. (2016). Serum exosomes and cytokines promote a T-helper cell type 2 environment in the peripheral blood of glioblastoma patients. *Neuro. Oncol.* 18, 206–215. doi: 10.1093/neuonc/nov107

Herisson, F., Frodermann, V., Courties, G., Rohde, D., Sun, Y., Vandoorne, K., et al. (2018). Direct vascular channels connect skull bone marrow and the brain surface enabling myeloid cell migration. *Nat. Neurosci.* doi: 10.1038/s41593-018-0213-2

Hide, T., Komohara, Y., Miyasato, Y., Nakamura, H., Makino, K., Takeya, M., et al. (2018). Oligodendrocyte Progenitor Cells and Macrophages/Microglia Produce Glioma Stem Cell Niches at the Tumor Border. *EBioMedicine* 30, 94–104. doi: 10.1016/j.ebiom.2018.02.024

Hoves, S., Ooi, C.-H., Wolter, C., Sade, H., Bissinger, S., Schmittnaegel, M., et al. (2018). Rapid activation of tumor-associated macrophages boosts preexisting tumor immunity. *J. Exp. Med.* doi: 10.1084/jem.20171440

Hu, X., Li, P., Guo, Y., Wang, H., Leak, R. K., Chen, S., et al. (2012). Microglia/macrophage polarization dynamics reveal novel mechanism of injury expansion after focal cerebral ischemia. *Stroke* 43, 3063–3070. doi: 10.1161/STROKEAHA.112.659656

Hudson, A. L., Parker, N. R., Khong, P., Parkinson, J. F., Dwight, T., Ikin, R. J., et al. (2018). Glioblastoma Recurrence Correlates With Increased APE1 and Polarization Toward an Immuno-Suppressive Microenvironment. *Front. Oncol.* 8 (314), 1–10. doi: 10.3389/fonc.2018.00314

Hung, N. A., Eiholzer, R. A., Kirs, S., Zhou, J., Ward-Hartstonge, K., Wiles, A. K., et al. (2016). Telomere profiles and tumor-associated macrophages with different immune signatures affect prognosis in glioblastoma. *Mod. Pathol.* 29, 212–226. doi: 10.1038/modpathol.2015.156

Hussain, S. F., Yang, D., Suki, D., Aldape, K., Grimm, E., and Heimberger, A. B. (2006). The role of human glioma-infiltrating microglia/macrophages in mediating antitumor immune responses. *Neuro. Oncol.* 8, 261–279. doi: 10.1215/15228517-2006-008

Hutter, G., Theruvath, J., Graef, C. M., Zhang, M., Schoen, M. K., Manz, E. M., et al. (2019). Microglia are effector cells of CD47-SIRPα antiphagocytic axis disruption against glioblastoma. *Proc. Natl. Acad. Sci. U. S. A.* 116, 997–1006. doi: 10.1073/pnas.1721434116

Jeannin, P., Paolini, L., Adam, C., and Delneste, Y. (2018). The roles of CSFs on the functional polarization of tumor-associated macrophages. *FEBS J.* 285, 680–699. doi: 10.1111/febs.14343

Kast, R. E., Hill, Q. A., Wion, D., Mellstedt, H., Focosi, D., Karpel-Massler, G., et al. (2017). Glioblastoma-synthesized G-CSF and GM-CSF contribute to growth and immunosuppression: Potential therapeutic benefit from dapsone, fenofibrate, and ribavirin. *Tumor Biol.* 39, 1–10. doi: 10.1177/1010428317699797

Kazantseva, M., Eiholzer, R. A., Mehta, S., Taha, A., Bowie, S., Roth, I., et al. (2018). Elevation of the TP53 isoform Δ133p53β in glioblastomas: an alternative to mutant p53 in promoting tumor development. *J. Pathol.* 246, 77–88. doi: 10.1002/path.5111

Kennedy, B. C., Showers, C. R., Anderson, D. E., Anderson, L., Canoll, P., Bruce, J. N., et al. (2013). Tumor-associated macrophages in glioma: friend or foe? *J. Oncol.* 2013, 486912. doi: 10.1155/2013/486912

Kitange, G. J., Carlson, B. L., Schroeder, M. A., Decker, P. A., Morlan, B. W., Wu, W., et al. (2010). Expression of CD74 in high grade gliomas: a potential role in temozolomide resistance. *J. Neurooncol.* 100, 177–186. doi: 10.1007/s11060-010-0186-9

Kloepper, J., Riedemann, L., Amoozgar, Z., Seano, G., Susek, K., Yu, V., et al. (2016). Ang-2/VEGF bispecific antibody reprograms macrophages and resident microglia to anti-tumor phenotype and prolongs glioblastoma survival. *Proc. Natl. Acad. Sci.* 113, 4476 LP– 4481. doi: 10.1073/pnas.1525360113

Kohanbash, G., McKaveney, K., Sakaki, M., Ueda, R., Mintz, A. H., Amankulor, N., et al. (2013). GM-CSF promotes the immunosuppressive activity of glioma-infiltrating myeloid cells through interleukin-4 receptor-α. *Cancer Res.* 73, 6413–6423. doi: 10.1158/0008-5472.CAN-12-4124

Komohara, Y., Ohnishi, K., Kuratsu, J., and Takeya, M. (2008). Possible involvement of the M2 anti-inflammatory macrophage phenotype in growth of human gliomas. *J. Pathol.* 216, 15–24. doi: 10.1002/path.2370

Kong, B., Michalski, C. W., Friess, H., and Kleeff, J. (2010). Surgical procedure as an inducer of tumor angiogenesis. *Exp. Oncol.* 32, 186–189.

Kumar, R., De Mooij, T., Peterson, T. E., Kaptzan, T., Johnson, A. J., Daniels, D. J., et al. (2017). Modulating glioma-mediated myeloid-derived suppressor cell development with sulforaphane. *PloS One* 12, 1–26. doi: 10.1371/journal.pone.0179012

Latha, K., Yan, J., Yang, Y., Gressot, L. V., Kong, L.-Y., Manyam, G., et al. (2018). The Role of Fibrinogen-Like Protein 2 on Immunosuppression and Malignant Progression in Glioma. *JN7CI J. Natl. Cancer Inst.* 111, 1–9. doi: 10.1093/jnci/djy107

Leblond, M. M., Pérès, E. A., Helaine, C., Gérault, A. N., Moulin, D., Anfray, C., et al. (2017). M2 macrophages are more resistant than M1 macrophages following radiation therapy in the context of glioblastoma. *Oncotarget* 8, 72597–72612. doi: 10.18632/oncotarget.19994

Lee, J., Dang, X., Borboa, A., Coimbra, R., Baird, A., and Eliceiri, B. P. (2015). Thrombin-processed Ecrg4 recruits myeloid cells and induces antitumorigenic inflammation. *Neuro. Oncol.* 17, 685–696. doi: 10.1093/neuonc/nou302

Li, Z., Huang, Q., Chen, H., Lin, Z., Zhao, M., and Jiang, Z. (2017). Interferon Regulatory Factor 7 Promoted Glioblastoma Progression and Stemness by Modulating IL-6 Expression in Microglia. *J. Cancer* 8, 207–219. doi: 10.7150/jca.16415

Li, T.-F., Li, K., Wang, C., Liu, X., Wen, Y., Xu, Y.-H., et al. (2017). Harnessing the cross-talk between tumor cells and tumor-associated macrophages with a nano-drug for modulation of glioblastoma immune microenvironment. *J. Control. Release* 268, 128–146. doi: 10.1016/j.jconrel.2017.10.024

Li,F., Lv, B., Liu, Y., Hua, T., Han, J., Sun, C., et al. (2017). Blocking the CD47-SIRPα axis by delivery of anti-CD47 antibody induces antitumor effects in glioma and glioma stem cells. *Oncoimmunology* 7, e1391973–e1391973. doi: 10.1080/2162402X.2017.1391973

Li, Y., Dong, X., Cai, J., Yin, S., Sun, Y., Yang, D., et al. (2018). SERPINA3 induced by astroglia/microglia co-culture facilitates glioblastoma stem-like cell invasion. *Oncol. Lett.* 15, 285–291. doi: 10.3892/ol.2017.7275

Lin, J. D., Nishi, H., Poles, J., Niu, X., McCauley, C., Rahman, K., et al. (2019). Single-cell analysis of fate-mapped macrophages reveals heterogeneity, including stem-like properties, during atherosclerosis progression and regression. *JCI Insight* 4 (e124574), 1–15. doi: 10.1172/jci.insight.124574

Lisi, L., Ciotti, G. M. P., Braun, D., Kalinin, S., Currò, D., Dello Russo, C., et al. (2017). Expression of iNOS, CD163 and ARG-1 taken as M1 and M2 markers of microglial polarization in human glioblastoma and the surrounding normal parenchyma. *Neurosci. Lett.* 645, 106–112. doi: 10.1016/j.neulet.2017.02.076

Locati,M., Curtale,G., and Mantovani, A. (2020). Diversity, Mechanisms, and Significance of Macrophage Plasticity. *Annu. Rev. Pathol. Mech. Dis* 15, 123–147. doi: 10.1146/annurev-pathmechdis-012418-012718

Louis, D. N., Ohgaki, H., Wiestler, O. D., Cavenee, W. K., Burger, P. C., Jouvet, A., et al. (2007). The 2007 WHO classification of tumours of the central nervous system. *Acta Neuropathol.* 114, 97–109. doi: 10.1007/s00401-007-0243-4

Louis, D. N., Perry, A., Reifenberger, G., von Deimling, A., Figarella-Branger, D., Cavenee, W. K., et al. (2016). The 2016 World Health Organization Classification of Tumors of the Central Nervous System: a summary. *Acta Neuropathol.* 131, 803–820. doi: 10.1007/s00401-016-1545-1

Lu-Emerson, C., Snuderl, M., Kirkpatrick, N. D., Goveia, J., Davidson, C., Huang, Y., et al. (2013). Increase in tumor-associated macrophages after antiangiogenic therapy is associated with poor survival among patients with recurrent glioblastoma. *Neuro. Oncol.* 15, 1079–1087. doi: 10.1093/neuonc/not082

Müller, A., Brandenburg, S., Turkowski, K., Müller, S., and Vajkoczy, P. (2015). Resident microglia, and not peripheral macrophages, are the main source of brain tumor mononuclear cells. *Int. J. Cancer* 137, 278–288. doi: 10.1002/ijc.29379

Martinez, F. O., and Gordon, S. (2014). The M1 and M2 paradigm of macrophage activation: time for reassessment. *F1000Prime Rep.* 6, 13. doi: 10.12703/P6-13

Matias, D., Balça-Silva, J., da Graça, G. C., Wanjiru, C. M., Macharia, L. W., Nascimento, C. P., et al. (2018). Microglia/Astrocytes–Glioblastoma Crosstalk: Crucial Molecular Mechanisms and Microenvironmental Factors. *Front. Cell. Neurosci.* 12, 235. doi: 10.3389/fncel.2018.00235

Mieczkowski, J., Kocyk, M., Nauman, P., Gabrusiewicz, K., Sielska, M., Przanowski, P., et al. (2015). Down-regulation of IKKβ expression in glioma-infiltrating microglia/macrophages is associated with defective inflammatory/immune gene responses in glioblastoma. *Oncotarget* 6, 33077–33090. doi: 10.18632/oncotarget.5310

Murray, P. J., Allen, J. E., Biswas, S. K., Fisher, E. A., Gilroy, D. W., Goerdt, S., et al. (2014). Macrophage activation and polarization: nomenclature and experimental guidelines. *Immunity* 41, 14–20. doi: 10.1016/j.immuni.2014.06.008

NCT00003232 (2004). Combination Chemotherapy in Treating Pain in Patients With Hormone Refractory Metastatic Prostate Cancer. ClinicalTrials.gov. Available at https://clinicaltrials.gov/ct2/show/NCT00003232

NCT00009945 (2003). Clodronate With or Without Chemotherapy and/or Hormonal Therapy in Treating Women With Stage I or Stage II Breast Cancer. ClinicalTrials.gov. Available at: https://clinicaltrials.gov/ct2/show/NCT00009945

NCT00127205 (2005). S0307 Phase III Trial of Bisphosphonates as Adjuvant Therapy for Primary Breast Cancer. ClinicalTrials.gov. Available at: https://clinicaltrials.gov/ct2/show/NCT00127205

NCT00301873 (2006). Zoledronate in Preventing Osteoporosis in Patients With Primary Malignant Glioma. ClinicalTrials.gov. Available at: https://clinicaltrials.gov/ct2/show/NCT00301873

NCT00537368 (2007). First Study of the Safety of CNTO 888 in Patients With Solid Tumors. ClinicalTrials.gov. Available at: https://clinicaltrials.gov/ct2/show/NCT00537368

NCT00633529 (2008). Safety of Adding IMO-2055 to Erlotinib + Bevacizumab in 2nd Line Treatment for Patients With NSCLC. ClinicalTrials.gov. Available at: https://clinicaltrials.gov/ct2/show/NCT00633529

NCT00719199 (2008). Study of FOLFIRI Plus Cetuximab Plus IMO-2055 in Patients With Colorectal Cancer. ClinicalTrials.gov. Available at: https://clinicaltrials.gov/ct2/show/NCT00719199

NCT00821652 (2009). Randomized, Double Blind, Placebo-controlled Topical Resiquimod Adjuvant for NY-ESO-1 Protein Vaccination. ClinicalTrials.gov. Available at: https://clinicaltrials.gov/ct2/show/NCT00821652

NCT00885326 (2009). N2007-02:Bevacizumab,Cyclophosphamide,& Zoledronic Acid in Patients W/ Recurrent or Refractory High-Risk Neuroblastoma. ClinicalTrials.gov. Available at: https://clinicaltrials.gov/ct2/show/NCT00885326

NCT00899574 (2009). Imiquimod for Breast Cancer Patients With Chest Wall Recurrence or Skin Metastases. ClinicalTrials.gov. Available at: https://clinicaltrials.gov/ct2/show/NCT00899574

NCT00909142 (2009). Bonefos and the Consumption of Analgesics (BICAM). ClinicalTrials.gov. Available at: https://clinicaltrials.gov/ct2/show/NCT00909142

NCT00992186 (2009). A Study of the Safety and Efficacy of Single-agent Carlumab (an Anti-Chemokine Ligand 2 [CCL2]) in Participants With Metastatic Castrate-Resistant Prostate Cancer. ClinicalTrials.gov.Available at: https://clinicaltrials.gov/ct2/show/NCT00992186

NCT01004861 (2009). Safety Study of PLX108-01 in Patients With Solid Tumors. ClinicalTrials.gov. Available at: https://clinicaltrials.gov/ct2/show/NCT01004861

NCT01015560 (2009). S0916, MLN1202 in Treating Patients With Bone Metastases. ClinicalTrials.gov. Available at: https://clinicaltrials.gov/ct2/show/NCT01015560

NCT01040832 (2009). EMD 1201081 in Combination With Cetuximab in Second-Line Cetuximab-Naïve Subjects With Recurrent or Metastatic Squamous Cell Carcinoma of the Head and Neck. ClinicalTrials.gov. Available at: https://clinicaltrials.gov/ct2/show/NCT01040832

NCT01198457 (2010). Study to Investigate Adherence of Patients to Clodronate (Bonefos) Treatment (BONA). ClinicalTrials.gov. Available at: https://clinicaltrials.gov/ct2/show/NCT01198457

NCT01204996 (2010). A Study of the Safety and Efficacy of CNTO 888 in Combination With SoC (Standard of Care) Chemotherapy in Patients With Solid Tumors. ClinicalTrials.gov. Available at: https://clinicaltrials.gov/ct2/show/NCT01204996

NCT01294293 and NCT01334177 (2011). TLR8 Agonist VTX-2337 and Pegylated Liposomal Doxorubicin Hydrochloride or Paclitaxel in Treating Patients With Recurrent or Persistent Ovarian Epithelial, Fallopian Tube, or Peritoneal Cavity Cancer. ClinicalTrials.gov. Available at: https://clinicaltrials.gov/ct2/show/NCT01294293

NCT01316822 (2011). A Study of ARRY-382 in Patients With Selected Advanced or Metastatic Cancers. ClinicalTrials.gov. Available at: https://clinicaltrials.gov/ct2/show/NCT01316822

NCT01345019 (2011). Denosumab Compared to Zoledronic Acid in the Treatment of Bone Disease in Patients With Multiple Myeloma. ClinicalTrials.gov.

NCT01346358 (2011). A Study of IMC-CS4 in Subjects With Advanced Solid Tumors. ClinicalTrials.gov. Available at: https://clinicaltrials.gov/ct2/show/NCT01346358

NCT01349036 (2011). A Phase 2 Study of PLX3397 in Patients With Recurrent Glioblastoma. ClinicalTrials.gov. Available at: https://clinicaltrials.gov/ct2/show/NCT01349036

NCT01421017 (2011). Toll-like Receptor (TLR) 7 Agonist, Cyclophosphamide, and Radiotherapy for Breast Cancer With Skin Metastases. ClinicalTrials.gov. Available at: https://clinicaltrials.gov/ct2/show/NCT01421017

NCT01494688 (2011). A Study of RO5509554 as Monotherapy and in Combination With Paclitaxel in Participants With Advanced Solid Tumors. ClinicalTrials.gov. Available at: https://clinicaltrials.gov/ct2/show/NCT01494688

NCT01561911 and NCT00607048. (2012) A Phase I Study of the Chimeric Anti-CD40 Monoclonal Antibody ChiLob 7/4 to Treat Advanced Malignancies Refractory to Conventional Anti-cancer Treatment. ClinicalTrials.gov. Available at: https://clinicaltrials.gov/ct2/show/NCT01561911

NCT02216409 (2014). Phase 1 Trial of Hu5F9-G4, a CD47-targeting Antibody. ClinicalTrials.gov. Available at https://clinicaltrials.gov/ct2/show/NCT02216409

NCT02252146. Dose Escalation Study in Patients With Relapsed or Refractory DLBCL and MyD88 L265P Mutation. ClinicalTrials.gov.

NCT02254772 (2014). A Phase I/II Study of Intratumoral Injection of SD-101. ClinicalTrials.gov. Available at: https://clinicaltrials.gov/ct2/show/NCT02254772

NCT02304393 (2014). A Study of Selicrelumab (RO7009789) in Combination With Atezolizumab in Participants With Locally Advanced and/or Metastatic Solid Tumors. ClinicalTrials.gov.Available at: https://clinicaltrials.gov/ct2/show/NCT02304393

NCT02367196 (2015). A Phase 1, Dose Finding Study of CC-90002 in Subjects With Advanced Solid and Hematologic Cancers. ClinicalTrials.gov. Available at https://clinicaltrials.gov/ct2/show/NCT02367196

NCT02371369 (2015). Phase 3 Study of Pexidartinib for Pigmented Villonodular Synovitis (PVNS) or Giant Cell Tumor of the Tendon Sheath (GCT-TS) (ENLIVEN). ClinicalTrials.gov. Available at: https://clinicaltrials.gov/ct2/show/NCT02371369

NCT02431559 (2015). A Phase 1/2 Study of Motolimod (VTX-2337) and MEDI4736 in Subjects With Recurrent, Platinum-Resistant Ovarian Cancer for Whom Pegylated Liposomal Doxorubicin (PLD) is Indicated. ClinicalTrials.gov. Available at: https://clinicaltrials.gov/ct2/show/NCT02431559

NCT02452424 (2015). A Combination Clinical Study of PLX3397 and Pembrolizumab To Treat Advanced Melanoma and Other Solid Tumors. ClinicalTrials.gov. Available at: https://clinicaltrials.gov/ct2/show/NCT02452424

NCT02452697 (2015). Ph2 NK Cell Enriched DCIs w/wo RLR9 Agonist, DUK-CPG-001 From Donors Following Allogeneic SCT (NK-DCI). ClinicalTrials.gov. Available at: https://clinicaltrials.gov/ct2/show/NCT02452697

NCT02482168 (2015). Study of the CD40 Agonistic Monoclonal Antibody APX005M. ClinicalTrials.gov. Available at: https://clinicaltrials.gov/ct2/show/NCT02482168

NCT02526017 (2015). *Study of Cabiralizumab in Combination With Nivolumab in Patients With Selected Advanced Cancers (FPA008-003)*. ClinicalTrials.gov. Available at: https://clinicaltrials.gov/ct2/show/NCT02526017

NCT02663518 (2016). A Trial of TTI-621 for Patients With Hematologic Malignancies and Selected Solid Tumors. ClinicalTrials.gov. Available at: https://clinicaltrials.gov/ct2/show/NCT02663518

NCT02678338 (2016). CAMELLIA: Anti-CD47 Antibody Therapy in Haematological Malignancies. ClinicalTrials.gov. Available at: https://clinicaltrials.gov/ct2/show/NCT02678338

NCT02718911 (2016). A Study of LY3022855 in Combination With Durvalumab or Tremelimumab in Participants With Advanced Solid Tumors. ClinicalTrials.gov. Available at: https://clinicaltrials.gov/ct2/show/NCT02718911

NCT02732938 (2016). Ph1b/2 Study of PF-04136309 in Combination With Gem/Nab-P in First-line Metastatic Pancreatic Patients (CCR2i). ClinicalTrials.gov. Available at: https://clinicaltrials.gov/ct2/show/NCT02732938

NCT02777710 (2016). Evaluation of Safety and Activity of an Anti-PDL1 Antibody (DURVALUMAB) Combined With CSF-1R TKI (PEXIDARTINIB) in Patients With Metastatic/Advanced Pancreatic or Colorectal Cancers (MEDIPLEX). ClinicalTrials.gov. Available at: https://clinicaltrials.gov/ct2/show/NCT02777710

NCT02829723 (2016). Phase I/II Study of BLZ945 Single Agent or BLZ945 in Combination With PDR001 in Advanced Solid Tumors. ClinicalTrials.gov. Available at: https://clinicaltrials.gov/ct2/show/NCT02829723

NCT02927964 (2016). TLR9 Agonist SD-101, Ibrutinib, and Radiation Therapy in Treating Patients With Relapsed or Refractory Grade 1-3A Follicular Lymphoma. ClinicalTrials.gov. Available at: https://clinicaltrials.gov/ct2/show/NCT02927964

NCT02953509 (2016). Trial of Hu5F9-G4 in Combination With Rituximab in Relapsed/Refractory B-cell Non-Hodgkin's Lymphoma. ClinicalTrials.gov. Available at: https://clinicaltrials.gov/ct2/show/NCT02953509

NCT02953782 (2016). Trial of Hu5F9-G4 in Combination With Cetuximab in Patients With Solid Tumors and Advanced Colorectal Cancer. ClinicalTrials.gov. Available at: https://clinicaltrials.gov/ct2/show/NCT02953782

NCT03007732 (2017). Pembrolizumab in Combination With Intratumoral SD-101 Therapy. ClinicalTrials.gov. Available at: https://clinicaltrials.gov/ct2/show/NCT03007732

NCT03013218 (2017). A Study of ALX148 in Patients With Advanced Solid Tumors and Lymphoma. ClinicalTrials.gov. Available at: https://clinicaltrials.gov/ct2/show/NCT03013218

NCT03069469 (2017). Study of DCC-3014 in Patients With Advanced Malignancies. ClinicalTrials.gov. Available at: https://clinicaltrials.gov/ct2/show/NCT03069469

NCT03101254 (2017). LY3022855 With BRAF/MEK Inhibition in Patients With Melanoma. ClinicalTrials.gov. Available at: https://clinicaltrials.gov/ct2/show/NCT03101254

NCT03123783 (2017). CD40 Agonistic Antibody APX005M in Combination With Nivolumab. ClinicalTrials.gov.

NCT03153410 (2017). Pilot Study With CY, Pembrolizumab, GVAX, and IMC-CS4 (LY3022855) in Patients With Borderline Resectable Adenocarcinoma of the Pancreas. ClinicalTrials.gov. Available at: https://clinicaltrials.gov/ct2/show/NCT03153410

NCT03165994 (2017). APX005M With Concurrent Chemoradiation for Resectable Esophageal and Gastroesophageal Junction Cancers. ClinicalTrials.gov. Available at: https://clinicaltrials.gov/ct2/show/NCT03165994

NCT03238027 (2017). A Phase 1 Study to Investigate SNDX-6352 Alone or in Combination With Durvalumab in Patients With Solid Tumors. ClinicalTrials.gov. Available at: https://clinicaltrials.gov/ct2/show/NCT03238027

NCT03248479 (2017). Hu5F9-G4 Monotherapy or Hu5F9-G4 in Combination With Azacitidine in Patients With Hematological Malignancies. ClinicalTrials.gov. Available at: https://clinicaltrials.gov/ct2/show/NCT03248479

NCT03301896 (2017). Study of the Safety and Efficacy of LHC165 Single Agent and in Combination With PDR001 in Patients With Advanced Malignancies. ClinicalTrials.gov. Available at: https://clinicaltrials.gov/ct2/show/NCT03301896

NCT03329950 (2017). A Study of CDX-1140 as Monotherapy or in Combination in Patients With Advanced Malignancies. ClinicalTrials.gov. Available at: https://clinicaltrials.gov/ct2/show/NCT03329950

NCT03389802 (2018). Phase I Study of APX005M in Pediatric CNS Tumors. ClinicalTrials.gov. Available at: https://clinicaltrials.gov/ct2/show/NCT03389802

NCT03410901 (2018). TLR9 Agonist SD-101, Anti-OX40 Antibody BMS 986178, and Radiation Therapy in Treating Patients With Low-Grade B-Cell Non-Hodgkin Lymphomas. ClinicalTrials.gov. Available at: https://clinicaltrials.gov/ct2/show/NCT03410901

NCT03416335 (2018). A Study of DSP-0509 in Patients With Advanced Solid Tumors to Determine the Safety and the Pharmacokinetic Profile. ClinicalTrials.gov. Available at: https://clinicaltrials.gov/ct2/show/NCT03416335

NCT03435640 (2018). A Study of NKTR-262 in Combination With NKTR-214 and With NKTR-214 Plus Nivolumab in Patients With Locally Advanced or Metastatic Solid Tumor Malignancies (REVEAL). ClinicalTrials.gov. Available at: https://clinicaltrials.gov/ct2/show/NCT03435640

NCT03496662 (2018). BMS-813160 With Nivolumab and Gemcitabine and Nab-paclitaxel in Borderline Resectable and Locally Advanced Pancreatic Ductal Adenocarcinoma (PDAC). ClinicalTrials.gov. Available at: https://clinicaltrials.gov/ct2/show/NCT03496662

NCT03502330 (2018). APX005M With Nivolumab and Cabiralizumab in Advanced Melanoma, Non-small Cell Lung Cancer or Renal Cell Carcinoma. ClinicalTrials.gov. Available at: https://clinicaltrials.gov/ct2/show/NCT03502330

NCT03507699 (2018). Combined Immunotherapy and Radiosurgery for Metastatic Colorectal Cancer. ClinicalTrials.gov. Available at: https://clinicaltrials.gov/ct2/show/NCT03507699

NCT03512340 (2018). Study of SRF231 in Patients With Advanced Solid and Hematologic Cancers. ClinicalTrials.gov. Available at: https://clinicaltrials.gov/ct2/show/NCT03512340

NCT03530683 (2018). A Trial of TTI-622 in Patients With Advanced Relapsed or Refractory Lymphoma or Myeloma (TTI-622-01). ClinicalTrials.gov. Available at: https://clinicaltrials.gov/ct2/show/NCT03530683

NCT03557970 and NCT02880371 (2018). CSF1R Inhibitor JNJ-40346527 in Treating Participants With Relapsed or Refractory Acute Myeloid Leukemia. ClinicalTrials.gov. Available at: https://clinicaltrials.gov/ct2/show/NCT03557970

NCT03618641 (2018). CMP-001 in Combo With Nivolumab in Stage IIIB/C/D Melanoma Patients With Clinically Apparent Lymph Node Disease. ClinicalTrials.gov. Available at: https://clinicaltrials.gov/ct2/show/NCT03618641

NCT03694977 (2018). Biomarker Study of PDR001 in Combination With MCS110 in Gastric Cancer. ClinicalTrials.gov. Available at: https://clinicaltrials.gov/ct2/show/NCT03694977

NCT03697564 (2018). Nivolumab + Cabiralizumab + Gemcitabine Versus Gemcitabine in Patients With Stage IV Pancreatic Cancer Achieving Disease Control in Response to First-line Chemotherapy (GemCaN Trial). ClinicalTrials.gov.Available at: https://clinicaltrials.gov/ct2/show/NCT03697564

NCT03717103 (2018). A Phase 1 Study Evaluating the Safety, Tolerability, and Initial Efficacy of Recombinant Human Anti-cluster Differentiation Antigen 47 (CD47) Monoclonal Antibody Injection (IBI188) in Patients With Advanced Malignancies. ClinicalTrials.gov. Available at: https://clinicaltrials.gov/ct2/show/NCT03717103

NCT03763149 (2018). A Study Evaluating the Safety, Tolerability, and Initial Efficacy of Recombinant Human Anti-cluster Differentiation Antigen 47 (CD47) Monoclonal Antibody Injection (IBI188) in Patients With Advanced Malignant Tumors and Lymphomas. ClinicalTrials.gov.

NCT03778879 (2018). Pre-operative Stereotactic Body Radiation Therapy for Pancreatic Adenocarcinoma With or Without CCX872-B. ClinicalTrials.gov. Available at: https://clinicaltrials.gov/ct2/show/NCT03778879

Nielsen, S. R., and Schmid, M. C. (2017). Macrophages as Key Drivers of Cancer Progression and Metastasis. *Mediators Inflamm.* 2017. 9624760, 1–11. doi: 10.1155/2017/9624760

Nishie, A., Ono, M., Shono, T., Fukushi, J., Otsubo, M., Onoue, H., et al. (1999). Macrophage Infiltration and Heme Oxygenase-1 Expression Correlate with Angiogenesis in Human Gliomas. *Clin. Cancer Res.* 5, 1107 LP–1113.

Nowak, A. K., Millward, M. J., Cook, A. M., McDonnell, A. M., Creaney, J., Lake, R. A., et al. (2015). A phase 1b clinical trial of the CD40-activating antibody CP-870,893 in combination with cisplatin and pemetrexed in malignant pleural mesothelioma. *Ann. Oncol.* 26, 2483–2490. doi: 10.1093/annonc/mdv387

Noy, R., and Pollard, J. W. (2014). Tumor-Associated Macrophages: From Mechanisms to Therapy. *Immunity* 41, 49–61. doi: 10.1016/j.immuni.2014.06.010

Nywening, T. M., Wang-Gillam, A., Sanford, D. E., Belt, B. A., Panni, R. Z., Cusworth, B. M., et al. (2016). Targeting tumour-associated macrophages with CCR2 inhibition in combination with FOLFIRINOX in patients with borderline resectable and locally advanced pancreatic cancer: a single-centre, open-label, dose-finding, non-randomised, phase 1b trial. *Lancet Oncol.* 17, 651–662. doi: 10.1016/S1470-2045(16)00078-4

Okubo, M., Kioi, M., Nakashima, H., Sugiura, K., Mitsudo, K., Aoki, I., et al. (2016). M2-polarized macrophages contribute to neovasculogenesis, leading to relapse of oral cancer following radiation. *Sci. Rep.* 6, 1–12. doi: 10.1038/srep27548

Paterson, A. H. G., Anderson, S. J., Lembersky, B. C., Fehrenbacher, L., Falkson, C. I., King, K. M., et al. (2012). Oral clodronate for adjuvant treatment of operable breast cancer (National Surgical Adjuvant Breast and Bowel Project protocol B-34): a multicentre, placebo-controlled, randomised trial. *Lancet Oncol.* 13, 734–742. doi: 10.1016/S1470-2045(12)70226-7

Perry, C. J., et al. (2018). Myeloid-targeted immunotherapies act in synergy to induce inflammation and antitumor immunity. *J. Exp. Med.* 215, 877–893. doi: 10.1084/jem.20171435

Perry, C. J., Muñoz-Rojas, A. R., Meeth, K. M., Kellman, L. N., Amezquita, R. A., Thakral, D., et al. (2013). Phase 2 study of carlumab (CNTO 888), a human monoclonal antibody against CC-chemokine ligand 2 (CCL2), in metastatic castration-resistant prostate cancer. *Invest. New Drugs* 31, 760–768. doi: 10.1007/s10637-012-9869-8

Poh, A. R., and Ernst, M. (2018). Targeting Macrophages in Cancer: From Bench to Bedside. *Front. Oncol.* 8, 49. doi: 10.3389/fonc.2018.00049

Poon, C. C., Sarkar, S., Yong, V. W., and Kelly, J. J. P. (2017). Glioblastoma-associated microglia and macrophages: Targets for therapies to improve prognosis. *Brain* 140, 1548–1560. doi: 10.1093/brain/aww355

Pyonteck, S. M., Akkari, L., Schuhmacher, A. J., Bowman, R. L., Sevenich, L., Quail, D. F., et al. (2013). CSF-1R inhibition alters macrophage polarization and blocks glioma progression. *Nat. Med.* 19, 1264. doi: 10.1038/nm.3337

Qian, J., Luo, F., Yang, J., Liu, J., Liu, R., Wang, L., et al. (2018). TLR2 Promotes Glioma Immune Evasion by Downregulating MHC Class II Molecules in Microglia. *Cancer Immunol. Res.* 6, 1220 LP–1233. doi: 10.1158/2326-6066.CIR-18-0020

Quail, D. F., and Joyce, J. A. (2013). Microenvironmental regulation of tumor progression and metastasis. *Nat. Med.* 19, 1423–1437. doi: 10.1038/nm.3394

Quail, D. F., and Joyce, J. A. (2017). The Microenvironmental Landscape of Brain Tumors. *Cancer Cell* 31, 326–341. doi: 10.1016/j.ccell.2017.02.009

Manda, S. V., Kataria, Y., Tatireddy, B. R., Ramakrishnan, B., Ratnam, B. G., Lath, R., et al. (2018). Exosomes as a biomarker platform for detecting epidermal growth factor receptor–positive high-grade gliomas. *J. Neurosurg.* 128, 1091–1101. doi: 10.3171/2016.11.jns161187

Roesch, S., Rapp, C., Dettling, S., and Herold-Mende, C. (2018). When Immune Cells Turn Bad-Tumor-Associated Microglia/Macrophages in Glioma. *Int. J. Mol. Sci.* 19, 436. doi: 10.3390/ijms19020436

Rossi, M. L., Hughes, J. T., Esiri, M. M., Coakham, H. B., and Brownell, D. B. (1987). Immunohistological study of mononuclear cell infiltrate in malignant gliomas. *Acta Neuropathol.* 74, 269–277. doi: 10.1007/BF00688191

Ruzsa, A., Sen, M., Evans, M., Lee, L. W., Hideghety, K., Rottey, S., et al. (2014). Phase 2, open-label, 1:1 randomized controlled trial exploring the efficacy of EMD 1201081 in combination with cetuximab in second-line cetuximab-naïve patients with recurrent or metastatic squamous cell carcinoma of the head and neck (R/M SCCHN). *Invest. New Drugs* 32, 1278–1284. doi: 10.1007/s10637-014-0117-2

Séhédic, D., Chourpa, I., Tétaud, C., Griveau, A., Loussouarn, C., Avril, S., et al. (2017). Locoregional confinement and major clinical benefit of188re-loaded CXCR4-targeted nanocarriers in an orthotopic human to mouse model of glioblastoma. *Theranostics* 7, 4517–4536. doi: 10.7150/thno.19403

Sørensen, M. D., Dahlrot, R. H., Boldt, H. B., Hansen, S., and Kristensen, B. W. (2018). Tumour-associated microglia/macrophages predict poor prognosis in high-grade gliomas and correlate with an aggressive tumour subtype. *Neuropathol. Appl. Neurobiol.* 44, 185–206. doi: 10.1111/nan.12428

Sadahiro, H., Kang, K.-D., Gibson, J. T., Minata, M., Yu, H., Shi, J., et al. (2018). Activation of the Receptor Tyrosine Kinase AXL Regulates the Immune Microenvironment in Glioblastoma. *Cancer Res.* 78, 3002 LP–3013. doi: 10.1158/0008-5472.CAN-17-2433

Saha, D., Martuza, R. L., and Rabkin, S. D. (2017). Macrophage Polarization Contributes to Glioblastoma Eradication by Combination Immunovirotherapy and Immune Checkpoint Blockade. *Cancer Cell* 32, 253–267.e5. doi: 10.1016/j.ccell.2017.07.006

Sandhu, S. K., Papadopoulos, K., Fong, P. C., Patnaik, A., Messiou, C., Olmos, D., et al. (2013). A first-in-human, first-in-class, phase i study of carlumab (CNTO 888), a human monoclonal antibody against CC-chemokine ligand 2 in patients with solid tumors. *Cancer Chemother. Pharmacol.* 71, 1041–1050. doi: 10.1007/s00280-013-2099-8

Schiffer, D., Annovazzi, L., Casalone, C., Corona, C., and Mellai, M. (2018). Glioblastoma: Microenvironment and Niche Concept. *Cancers* 11 (5), 1–17. doi: 10.3390/cancers11010005

Shi, Y., Ping, Y.-F., Zhou, W., He, Z.-C., Chen, C., Bian, B.-S.-J., et al. (2017). Tumour-associated macrophages secrete pleiotrophin to promote PTPRZ1 signalling in glioblastoma stem cells for tumour growth. *Nat. Commun.* 8, 15080. doi: 10.1038/ncomms15080

Shoji,T., Saito, R., Chonan, M., Shibahara, I., Sato, A., Kanamori, M., et al. (2016). Local convection-enhanced delivery of an anti-CD40 agonistic monoclonal antibody induces antitumor effects in mouse glioma models. *Neuro. Oncol.* 18, 1120–1128. doi: 10.1093/neuonc/now023

Sica, A., Erreni, M., Allavena, P., and Porta, C. (2015). Macrophage polarization in pathology. *Cell. Mol. Life Sci.* 72, 4111–4126. doi: 10.1007/s00018-015-1995-y

Sikic, B. I., Lakhani, N. J., Patnaik, A., Shah, S., Chandana, S. R., Rasco, D. W., et al. (2018). A first-in-class, first-in-human phase 1 pharmacokinetic (PK) and pharmacodynamic (PD) study of Hu5F9-G4, an anti-CD47 monoclonal antibody (mAb), in patients with advanced solid tumors. *J. Clin. Oncol.* 36, 3002. doi: 10.1200/JCO.2018.36.15_suppl.3002

Smith, D. A., Conkling, P., Richards, D. A., Nemunaitis, J. J., Boyd, T. E., Mita, A. C., et al. (2014). Antitumor activity and safety of combination therapy with the Toll-like receptor 9 agonist IMO-2055, erlotinib, and bevacizumab in advanced or metastatic

non-small cell lung cancer patients who have progressed following chemotherapy. *Cancer Immunol. Immunother.* 63, 787–796. doi: 10.1007/s00262-014-1547-6

Strachan, D. C., Ruffell, B., Oei, Y., Bissell, M. J., Coussens, L. M., Pryer, N., et al. (2013). CSF1R inhibition delays cervical and mammary tumor growth in murine models by attenuating the turnover of tumor-associated macrophages and enhancing infiltration by CD8+T cells. *Oncoimmunology* 2, 1–12. doi: 10.4161/onci.26968

Stratton, J. A., Holmes, A., Rosin, N. L., Sinha, S., Vohra, M., Burma, N. E., et al. (2018). Macrophages Regulate Schwann Cell Maturation after Nerve Injury. *Cell Rep.* 24, 2561–2572.e6. doi: 10.1016/j.celrep.2018.08.004

Stupp, R., Mason, W. P., van den Bent, M. J., Weller, M., Fisher, B., Taphoorn, M. J. B., et al. (2005). Radiotherapy plus Concomitant and Adjuvant Temozolomide for Glioblastoma. *N. Engl. J. Med.* 352, 987–996. doi: 10.1056/NEJMoa043330

Stupp, R., Hegi, M. E., Mason, W. P., van den Bent, M. J., Taphoorn, M. J. B., Janzer, R. C., et al. (2009). Effects of radiotherapy with concomitant and adjuvant temozolomide versus radiotherapy alone on survival in glioblastoma in a randomised phase III study: 5-year analysis of the EORTC-NCIC trial. *Lancet Oncol.* 10, 459–466. doi: 10.1016/S1470-2045(09)70025-7

Szulzewsky, F., Pelz, A., Feng, X., Synowitz, M., Markovic, D., Langmann, T., et al. (2015). Glioma-associated microglia/macrophages display an expression profile different from M1 and M2 polarization and highly express Gpnmb and Spp1. *PloS One* 10, e0116644–e0116644. doi: 10.1371/journal.pone.0116644

Tabatabaei,P., Visse, E., Bergström, P., Brännström, T., Siesjö, P., and Bergenheim, A. T. (2017). Radiotherapy induces an immediate inflammatory reaction in malignant glioma: a clinical microdialysis study. *J. Neurooncol.* 131, 83–92. doi: 10.1007/s11060-016-2271-1

Tamura, R., Ohara, K., Sasaki, H., Morimoto, Y., Kosugi, K., Yoshida, K., et al. (2018). Difference in Immunosuppressive Cells Between Peritumoral Area and Tumor Core in Glioblastoma. *World Neurosurg.* 120, e601–e610. doi: 10.1016/j.wneu.2018.08.133

Tap, W. D., Wainberg, Z. A., Anthony, S. P., Ibrahim, P. N., Zhang, C., Healey, J. H., et al. (2015). Structure-Guided Blockade of CSF1R Kinase in Tenosynovial Giant-Cell Tumor. *N. Engl. J. Med.* 373, 428–437. doi: 10.1056/NEJMoa1411366

Thomas, A. C., and Mattila, J. T. (2014). 'Of mice and men': arginine metabolism in macrophages. *Front. Immunol.* 5, 479. doi: 10.3389/fimmu.2014.00479

Turkowski, K., Brandenburg, S., Mueller, A., Kremenetskaia, I., Bungert, A. D., Blank, A., et al. (2018). VEGF as a modulator of the innate immune response in glioblastoma. *Glia* 66, 161–174. doi: 10.1002/glia.23234

Van Acker, H. H., Anguille, S., Willemen, Y., Smits, E. L., and Van Tendeloo, V. F. (2016). Bisphosphonates for cancer treatment: Mechanisms of action and lessons from clinical trials. *Pharmacol. Ther.* 158, 24–40. doi: 10.1016/j.pharmthera.2015.11.008

Van Der Vos, K. E., Abels, E. R., Zhang, X., Lai, C., Carrizosa, E., Oakley, D., et al. (2016). Directly visualized glioblastoma-derived extracellular vesicles transfer RNA to microglia/macrophages in the brain. *Neuro. Oncol.* 18, 58–69. doi: 10.1093/neuonc/nov244

Vonderheide, R. H., Burg, J. M., Mick, R., Trosko, J. A., Li, D., Shaik, M. N., et al. (2013). Phase i study of the CD40 agonist antibody CP-870,893 combined with carboplatin and paclitaxel in patients with advanced solid tumors. *Oncoimmunology* 2, 1–10. doi: 10.4161/onci.23033

Wagner, S., Czub, S., Greif, M., Vince, G. H., Suss, N., Kerkau, S., et al. (1999). Microglial/macrophage expression of interleukin 10 in human glioblastomas. *Int. J. Cancer* 82, 12–16. doi: 10.1002/(SICI)1097-0215(19990702)82:1<12::AID-IJC3>3.0.CO;2-O

Walentynowicz, K. A., Ochocka, N., Pasierbinska, M., Wojnicki, K., Stepniak, K., Mieczkowski, J., et al. (2018). In Search for Reliable Markers of Glioma-Induced Polarization of Microglia. *Front. Immunol.* 9, 1329. doi: 10.3389/fimmu.2018.01329

Wang, S. C., Yu, C. F., Hong, J. H., Tsai, C. S., and Chiang, C. S. (2013). Radiation Therapy-Induced Tumor Invasiveness Is Associated with SDF-1-Regulated Macrophage Mobilization and Vasculogenesis. *PloS One* 8 (e69182), 1–10. doi: 10.1371/journal.pone.0069182

Wang, Y., Liu, T., Yang, N., Xu, S., Li, X., and Wang, D. (2016). Hypoxia and macrophages promote glioblastoma invasion by the CCL4-CCR5 axis. *Oncol. Rep.* 36, 3522–3528. doi: 10.3892/or.2016.5171

Wang, Q., He, Z., Huang, M., Liu, T., Wang, Y., Xu, H., et al. (2018). Vascular niche IL-6 induces alternative macrophage activation in glioblastoma through HIF-2α. *Nat. Commun.* 9, 559. doi: 10.1038/s41467-018-03050-0

Won, W.-J., Deshane, J. S., Leavenworth, J. W., Oliva, C. R., and Griguer, C. E. (2019). Metabolic and functional reprogramming of myeloid-derived suppressor cells and their therapeutic control in glioblastoma. *Cell Stress.* 3, 47–65 doi: 10.15698/cst2019.02.176

Wu, J., Frady, L. N., Bash, R. E., Cohen, S. M., Schorzman, A. N., Su, Y.-T., et al. (2018). MerTK as a therapeutic target in glioblastoma. *Neuro. Oncol.* 20, 92–102. doi: 10.1093/neuonc/nox111

Wynn, T. A., Chawla, A., and Pollard, J. W. (2013). Origins and Hallmarks of Macrophages: Development, Homeostasis, and Disease. *Nature* 496, 445–455. doi: 10.1038/nature12034

Xue, N., Zhou, Q., Ji, M., Jin, J., Lai, F., Chen, J., et al. (2017). Chlorogenic acid inhibits glioblastoma growth through repolarizating macrophage from M2 to M1 phenotype. *Sci. Rep.* 7, 39011. doi: 10.1038/srep39011

Yan, D., Kowal, J., Akkari, L., Schuhmacher, A. J., Huse, J. T., West, B. L., et al. (2017). Inhibition of colony stimulating factor-1 receptor abrogates microenvironment-mediated therapeutic resistance in gliomas. *Oncogene* 36, 6049–6058. doi: 10.1038/onc.2017.261

Ye, X., Xu, S., Xin, Y., Yu, S., Ping, Y., Chen, L., et al. (2012). Tumor-Associated Microglia/Macrophages Enhance the Invasion of Glioma Stem-like Cells via TGF-β1 Signaling Pathway. *J. Immunol.* 189, 444 LP–44 453. doi: 10.4049/jimmunol.1103248

Yin, Y., Qiu, S., Li, X., Huang, B., Xu, Y., and Peng, Y. (2017). EZH2 suppression in glioblastoma shifts microglia toward M1 phenotype in tumor microenvironment. *J. Neuroinflammation* 14, 220. doi: 10.1186/s12974-017-0993-4

Yuan, D., Zhao, Y., Banks, W. A., Bullock, K. M., Haney, M., Batrakova, E., et al. (2017). Macrophage exosomes as natural nanocarriers for protein delivery to inflamed brain. *Biomaterials* 142, 1–12. doi: 10.1016/j.biomaterials.2017.07.011

Zeiner, P. S., Preusse, C., Golebiewska, A., Zinke, J., Iriondo, A., Muller, A., et al. (2018). Distribution and prognostic impact of microglia/macrophage subpopulations in gliomas. *Brain Pathol.* 29, 513–529. doi: 10.1111/bpa.12690

Zhang, Q., et al. (2012). Prognostic significance of tumor-associated macrophages in solid tumor: a meta-analysis of the literature. *PloS One* 7, e50946–e50946. doi: 10.1371/journal.pone.0050946

Zhang, H., Lu, H., Xiang, L., Bullen, J. W., Zhang, C., Samanta, D., et al. (2015). HIF-1 regulates CD47 expression in breast cancer cells to promote evasion of phagocytosis and maintenance of cancer stem cells. *Proc. Natl. Acad. Sci.* 112, E6215–E6223. doi: 10.1073/pnas.1520032112

Zhang, M., Hutter, G., Kahn, S. A., Azad, T. D., Gholamin, S., Xu, C. Y., et al. (2016). Anti-CD47 Treatment Stimulates Phagocytosis of Glioblastoma by M1 and M2 Polarized Macrophages and Promotes M1 Polarized Macrophages In Vivo. *PloS One* 11, e0153550–e0153550. doi: 10.1371/journal.pone.0153550

Zhang, G., Zhang, Y., Cheng, S., Wu, Z., Liu, F., and Zhang, J. (2017). CD133 positive U87 glioblastoma cells-derived exosomal microRNAs in hypoxia-versus normoxia-microenviroment. *J. Neurooncol.* 135, 37–46. doi: 10.1007/s11060-017-2566-x

Zhao, H., Wang, J., Kong, X., Li, E., Liu, Y., Du, X., et al. (2016). CD47 promotes tumor invasion and metastasis in non-small cell lung cancer. *Sci. Rep.* 6 (29719), 1–11. doi: 10.1038/srep29719

Zhao, X., Qu, J., Sun, Y., Wang, J., Liu, X., Wang, F., et al. (2017). Prognostic significance of tumor-associated macrophages in breast cancer: a meta-analysis of the literature. *Oncotarget* 8, 30576–30586. doi: 10.18632/oncotarget.15736

Zheng, Y., Yang, W., Aldape, K., He, J., and Lu, Z. (2013). Epidermal growth factor (EGF)-enhanced vascular cell adhesion molecule-1 (VCAM-1) expression promotes macrophage and glioblastoma cell interaction and tumor cell invasion. *J. Biol. Chem.* 288, 31488–31495. doi: 10.1074/jbc.M113.499020

Zhernakova, A., Garmaeva, S., Fu, J., Chen, L., and Wijmenga, C. (2018). A system biology perspective on environment–host–microbe interactions. *Hum. Mol. Genet.* 27, R187–R194. doi: 10.1093/hmg/ddy137

Zhou, M., Bracci, P. M., McCoy, L. S., Hsuang, G., Wiemels, J. L., Rice, T., et al. (2015). Serum macrophage-derived chemokine/CCL22 levels are associated with glioma risk, CD4 T cell lymphopenia and survival time. *Int. J. Cancer* 137, 826–836. doi: 10.1002/ijc.29441

Zhou, W., Ke, S. Q., Huang, Z., Flavahan, W., Fang, X., Paul, J., et al. (2015). Periostin secreted by glioblastoma stem cells recruits M2 tumour-associated macrophages and promotes malignant growth. *Nat. Cell Biol.* 17, 170–182. doi: 10.1038/ncb3090

Zhou, J., Reddy, M. V., Wilson, B. K. J., Blair, D. A., Taha, A., Frampton, C. M., et al. (2018). MR Imaging Characteristics Associate with Tumor-Associated Macrophages in Glioblastoma and Provide an Improved Signature for Survival Prognostication. *Am. J. Neuroradiol.* 39, 252 LP–25 259. doi: 10.3174/ajnr.A5441

Zhu, C., Chrifi, I., Mustafa, D., Van Der Weiden, M., Leenen, P. J. M., Duncker, D. J., et al. (2017). CECR1-mediated cross talk between macrophages and vascular mural cells promotes neovascularization in malignant glioma. *Oncogene* 36, 5356–5368. doi: 10.1038/onc.2017.145

Zhu, H., Leiss, L., Yang, N., Rygh, C. B., Mitra, S. S., Cheshier, S. H., et al. (2017). Surgical debulking promotes recruitment of macrophages and triggers glioblastoma phagocytosis in combination with CD47 blocking immunotherapy. *Oncotarget* 8, 12145–12157. doi: 10.18632/oncotarget.14553

Conflict of Interest: The authors declare that the research was conducted in the absence of any commercial or financial relationships that could be construed as a potential conflict of interest.

Advantages of publishing in Frontiers

OPEN ACCESS
Articles are free to read for greatest visibility and readership

FAST PUBLICATION
Around 90 days from submission to decision

HIGH QUALITY PEER-REVIEW
Rigorous, collaborative, and constructive peer-review

TRANSPARENT PEER-REVIEW
Editors and reviewers acknowledged by name on published articles

Frontiers
Avenue du Tribunal-Fédéral 34
1005 Lausanne | Switzerland

Visit us: www.frontiersin.org
Contact us: frontiersin.org/about/contact

REPRODUCIBILITY OF RESEARCH
Support open data and methods to enhance research reproducibility

DIGITAL PUBLISHING
Articles designed for optimal readership across devices

FOLLOW US
@frontiersin

IMPACT METRICS
Advanced article metrics track visibility across digital media

EXTENSIVE PROMOTION
Marketing and promotion of impactful research

LOOP RESEARCH NETWORK
Our network increases your article's readership